COMMUNICATIONS

COMMUNICATIONS

Dear readers,

This issue of the Communications – Scientific Letters of the University of Zilina is mainly devoted to materials engineering.

Utility parameters of machines and equipment increase in majority of technical disciplines; in parallel with that there is demand on reduction of their mass. Development in the field of construction materials directs thus to another increasing of strength characteristics, brittle damage resistance, improvement of surface properties, technological properties, etc.

Trend growth of all technical discipline is dependent on development of construction materials. The prestige experimental workplaces of universities and research institutions, both national and international, deal with material research. The editorial board addressed the institutions whose activities on the material research are significant.

Let me thank all of them (Charles University in Prague, Prague, CZ; University of Defence, Brno, CZ; Brno University of Technology, Brno, CZ; SVUM a.s., Prague, CZ; VSB – Technical University of Ostrava, Ostrava, CZ; Institute of Technology and Businesses in Ceske Budejovice, Ceske Budejovice, CZ; Clausthal University of Technology, DE; Universita Degli Studi di Parma, IT; Politecnico di Milano, IT; National Institute of Research and Development for Technical Physics Iasi, RU; Kyrgyz State Technical University, Bishkek, KG; Czestochowa University of Technology, PL; Technical University of Kosice, SK; University of Zilina, SK) who contributed to the Communications – Scientific Letters of the University of Zilina, No. 4, 2012.

Otakar Bokuvka

https://doi.org/10.26552/com.C.2012.4.6-10

Jan Kohout *

CHANGES OF MATERIAL PROPERTIES OF SILUMIN DURING AGE-HARDENING

Simple phenomenological description of age-hardening kinetics of supersaturated solid solution is presented using the sum of exponential functions with negative arguments containing rate constants whose temperature dependence is described by the Arrhenius equation. To determine the number of exponentials in the sum is very important: it should be sufficiently high to obtain accurate description of kinetics and sufficiently low to keep the simplicity and practical applicability of this description. The HB hardness and growth changes (i.e. relative length increase) of silumin during age-hardening are studied separately and then commonly as various manifestations of the same hardening.

Keywords: *aluminium alloys; silumin; ageing; hardening; kinetics; hardness; growth*

1. Introduction

Description even of simple phase transformation based on diffusion processes is quite complicated because it consists of several different stages: nucleation of germs of new phase, their free growth, growth after the areas of new phase reach one another, conversion of the residues of old phrase. Age-hardening of supersaturated solid solutions represents the sequence of several phase or structural changes; therefore its kinetics is very complicated and it is usually described only graphically. The author tried to use kinetic equations of simple chemical reactions in this case. As the hardening processes take place one after another, the equations of consecutive reactions were used with success for beryllium bronze hardening [1] and for exposure of bearing steels at elevated temperatures [2]. Further studies [3] of steels for rolling bearing steels showed that the consecutive reactions can be replaced by concurrent (parallel) reactions with substantially simpler form of kinetic equations if rate constants differ in orders. In the simplest case of the first order reactions the kinetic equation consists of the sum of exponential functions. This sum was used in this paper for the description of hardness changes and growth (i.e. relative length increase) during age-hardening of silumin, which is often used also in special technology.

All structural changes in supersaturated solution are the consequence of diffusion, which belongs among physical processes. Therefore the application of the equations of chemical reactions can be found rather unusual. However, both the changes – physical as well as chemical – have two basic common features:

a) in both cases the driving force of processes is determined by the decrease of total energy of structure or system towards its minimum characterising the equilibrium state,

b) structural changes in materials as well as chemical reactions are the processes when certain barrier has to be overcome.

Item a) in the simplest approach (driving force is proportional to the distance from equilibrium state) leads to the kinetic equations of exponential type, the barrier processes mentioned in b) lead to the description of temperature dependence of rate constants by the Arrhenius equation – regardless structural changes or chemical reactions are considered.

2. Basic precondition of the description

Presented procedure is based on very natural precondition: all processes taking place in studied temperature range are qualitatively the same and differ only quantitatively in their rates (described by the Arrhenius equation). This precondition seems to be contrary to usual approach when different temperature ranges are connected with certain processes (see e.g. four stages of martensite annealing). Nevertheless, the contradiction is only apparent: for chosen narrow temperature interval only one of the processes predominates in usual time dwells and the exhibition of all others is small or negligible (either they took place intensively in very short times, i.e. before considered temporal interval, or they will be considerable in times substantially longer than the interval covers). This is direct consequence of the order difference of rate constants of individual processes, which appear in arguments of exponential functions.

3. Experimental material

Presentation of supposed procedure was made using experimental results from book [4] for 355.0 silumin (signed by the Alu-

* **Jan Kohout**
Department of Mathematics and Physics, Faculty of Military Technology, University of Defence, Brno, Czech Republic,
E-mail: jan.kohout@unob.cz

minium Association Casting Alloy Designation System) (see p. 182, Fig. D.2.19) delivered in T4 state (solution treated and aged). This silumin with nominal chemical composition 5.0 wt.% Si, 1.25 wt.% Cu and 0.5 wt.% Mg corresponds to EN AC-45000 (EN AC-AlSi5Cu1Mg) subeutectic silumin [5] according to European standards. Solution heat treatment was made at 527 °C during 12 hours, finished by boiling water quench. Age-hardening of cylinder rods with 28.575 mm in diameter and 304.8 mm in length was made at temperatures 149, 177, 204, 227, 260 and 343 °C (300, 350, 400, 440, 500 and 650 °F in the original [4]). The results of both HB hardness and growth were used in this paper only for times at temperatures 10 000 hours or shorter.

4. Regression calculations

As mentioned above, the kinetic equations of concurrent chemical reactions (the simplest, i.e. of first order), which describe also consecutive reactions if their rate constants differ in orders. Concentration c of newly created reactant changes in time according to equation

$$c(t) = c_f\left[1 - \exp(-kt)\right] \tag{1}$$

where c_f is final concentration of newly created reactant and k is rate constant of the reaction. If the proportionality among structural changes and property changes is supposed, then the property change can be described by the sum of such equations

$$\Delta p(t,T) = \sum_{i=1}^{n} a_i \left\{1 - \exp\left[k_i(T)\cdot t\right]\right\} \tag{2}$$

where k_i are rate constants depending on temperature and a_i are coefficients with the same dimension as the property p whose changes are studied – these coefficients describe supposed proportionality among structural changes and property changes (if not only change but *total* value of the property is considered, additional constant a_0 is added in Eq. (2) – here $a_0 = 0$ is used for growth and $a_0 \neq 0$ is used for HB hardness). These coefficients a_i for $i = 1, ..., n$ represent maximum changes which can arise in connection with the i-th addend in Eq. (1) (in *correct* case corresponding to the i-th process taking place in material). Temperature dependence of rate constants is described by the Arrhenius equation which was used in the form

$$k_i(T) = k_i(T_0)\exp\left[-\frac{\varepsilon_i}{\kappa}\left(\frac{1}{T} - \frac{1}{T_0}\right)\right] \tag{3}$$

more suitable for regression calculations. T_0 represents firmly chosen suitable *reference temperature*, here it is $T_0 = 500$ K ≈ 227 °C representing approximately the midpoint of interval of ageing temperatures, and ε_i are activation energies of individual processes. The Boltzmann constant κ can be replaced by the universal gas constant R if the activation energies of moles are considered.

Description of kinetics using regression function (2) stops to be only phenomenological if individual addends in (2) can be assigned to individual processes taking place in materials during structural changes. As studied silumin contains besides aluminium and silicon also copper and magnesium, all following schemes of decomposition should be taken into account during hardening

$$\alpha \rightarrow \text{GPI} \rightarrow \text{GPII} \rightarrow \beta' \rightarrow \beta(MgSi_2) \tag{4}$$

$$\alpha \rightarrow \text{GPI} \rightarrow \text{GPII} \rightarrow \theta' \rightarrow \theta(CuAl_2) \tag{5}$$

$$\alpha \rightarrow \text{GPI} \rightarrow \text{GPII} \rightarrow S' \rightarrow S(CuAl_2Mg) \tag{6}$$

Although some authors (e.g. [5]) do not distinguish stages GPI and GPII, many different processes are to be considered during age-hardening of studied silumin, i.e. number n in Eq. (2) can reach quite high integers.

All regression calculations were done using MS Excel together with its supplement *Solver* whose adjustment for strongly nonlinear problems with regression parameters differing in many orders is necessary [6]. Only in some cases special regression procedure written in *Pascal* [7] was used which is better than MS Excel if extremely high interrelations between some pairs of regression parameters exist and in addition it gives also standard deviations of regression parameters.

5. Results of regression calculations

The basic problem of using regression function (2) is to determine optimum number of addends n. There are three possibilities how to determine it:

a) from theory of decomposition of studied supersaturated solid solution (if sufficiently deeply developed),
b) according to the number of stages and phase or structural components, which can be experimentally distinguished during age-hardening in hardened alloy,
c) phenomenologically according to the temporal course of studied properties.

In the case when quite complicated alloy (containing three metals and semimetal) is studied and not own but the results of other authors are used for regression without any information about structural development during age-hardening, only item c) remains to be applied.

Regression of growth of this silumin was solved already in previous paper [8] where the values $n = 2$ to 8 were studied. This paper shows which features of the family of kinetic curves are successively described when number n is increasing. For $n = 6$ certain optimum is reached: all basic features of kinetic curves are covered and increasing n gets no substantial improvement, only instability of regression calculations appears. The result of growth regression is presented in Fig. 1.

HB hardness kinetic curves of this silumin are studied newly in this paper (for similar 356.0 silumin were studied in paper [9]). Experience from previous regressions shows that $n = 4$ is the lowest meaningful number of addends in regression function (2) which can cover basic features of the family of those kinetic curves. Also

in this case number n was increased and also for $n = 6$ above mentioned optimum was reached as a compromise between success rate and complexity of the description of kinetic curves. The result of HB hardness regression using regression function (2) with added $a_0 = 71.77$ (initial value of hardness before age-hardening) is presented in Fig. 2.

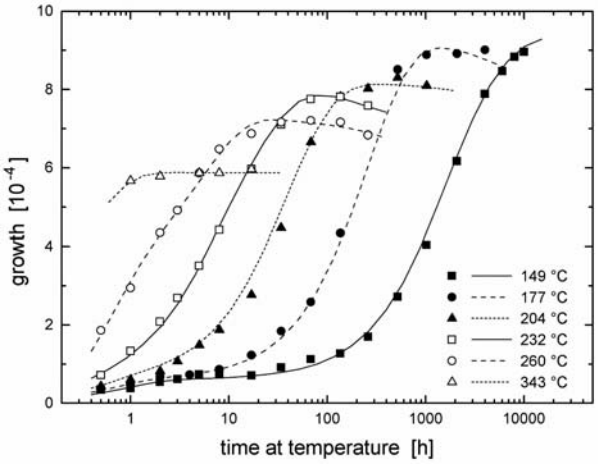

Fig. 1 Regression of growth kinetic curves using regression function (2)

6. Common regression of kinetic curves of more properties

In regression function (2) only parameters a_i (representing proportionality between the proportion of considered structural component in the whole structure mixture and the change of considered property) are connected with considered property, all other parameters (k_i, ε_i) are connected directly with structural changes, therefore they are common for all properties. This fact was used in common regression of growth and HB hardness. While in the case of *separate* regressions of growth and HB hardness with 6 addends in regression function 18 + 18 = 36 parameters are necessary, in the case of *common* regression only 24 parameters are sufficient. But not only reduction of the number of regression parameters is important – more important is the fact that common parameters can be determined with higher reliability and accuracy. Also assignment of addends in regression function (2) to processes in age-hardened silumin can be easier and more reliable in this case.

Basic problem of common regression is the generalized criterion of regression. Usual regression criterion is a minimum sum of squares of differences between corresponding couple measured value – fitted value of considered property. In the case of common regression when different quantities with values differing in orders are fitted (growth measured in 10^{-4} order and HB hardness measured in 10^{1} order), this criterion cannot be directly applied because the quantity with higher values would influence the sum of squares much more strongly than the quantity with lower values. In regression programs it can be solved by rescaling of values or by weighted sums of squares, which are in fact two sides of the same coin, but constants for rescaling or weight change can be determined by various ways and no unequivocal and universally accepted criterion for choosing the best one exists. In MS Excel supplement *Solver*, which can minimize arbitrary cell by changing other arbitrarily

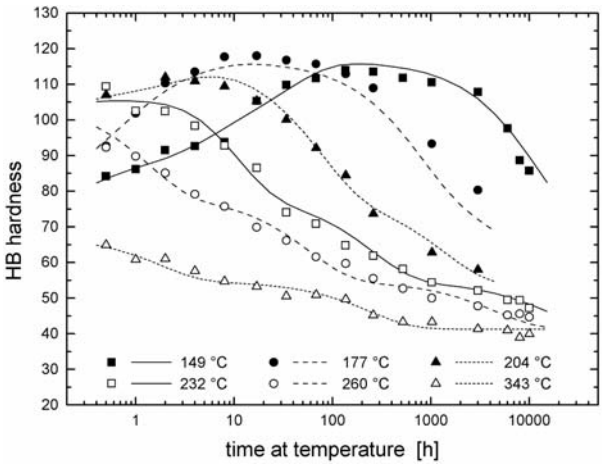

Fig. 2 Regression of HB hardness kinetic curves using regression function (2)

chosen cells, the criterion is very natural: the product of the sum of squares corresponding to HB hardness and sum of squares corresponding to growth is minimized. This approach is independent of scaling of fitted quantities. Common regression of growth and HB hardness with the lowest product of corresponding sums of squares is presented in Fig. 3.

Regression calculations in the case of 24 parameters with regression functions of *double-exponential* type (addends in kinetic equations as well as the Arrhenius equation are of exponential type) represent a very badly conditioned task (especially for experimental curves with high dispersion and low jaggedness). High degree of nonlinearity of regression functions leads to many local minima of regression criterion. Fortunately, most of them can be simply identified by very poor fit of measured dependences or by clearly incorrect final values of regression parameters (e.g. negative or zero values of quantities which must be positive, see rate constants, activation energies etc.). Very specific behaviour of *iteration path* is due to the construction of regression criterion as the product of sums of squares corresponding to hardness and to growth. Depending on initial values of regression parameters, in some cases the fit of growth is improving very quickly i.e. corresponding sum of squares decreases very quickly in initial iterations of regression calculations), while the fit of hardness is improving slowly and does not reach sufficient level (see Fig. 3, corresponding row in Table 1 is *common fit (G)*, while in other cases the situation is opposite (see Fig. 4, corresponding row in Table 1 is *common fit (H)*. As it was already mentioned, the best fit (according to the *product* of corresponding sums of squares) is presented in Fig. 3.

Comparison of sums of squares for separate fit and common fits — Table 1

Sum of squares	Growth	Hardness	Product
Separate fits	2.190	483.8	(1060)
Common fit (G)	3.489	870.1	3043
Common fit (H)	7.192	604.5	4783

The regression curve with the worst fit corresponds to the highest temperature (see hardness in Fig. 3 not respecting the jaggedness of experimental dependence as well as growth in Fig. 4 systematically shifted to higher values). All other hardening temperatures are chosen with the step of approx. 28 °C (50 °F), only the *distance* of the highest temperature is triple. Omitting this temperature, the fit would be much better but it exceeds the limited extent of this paper.

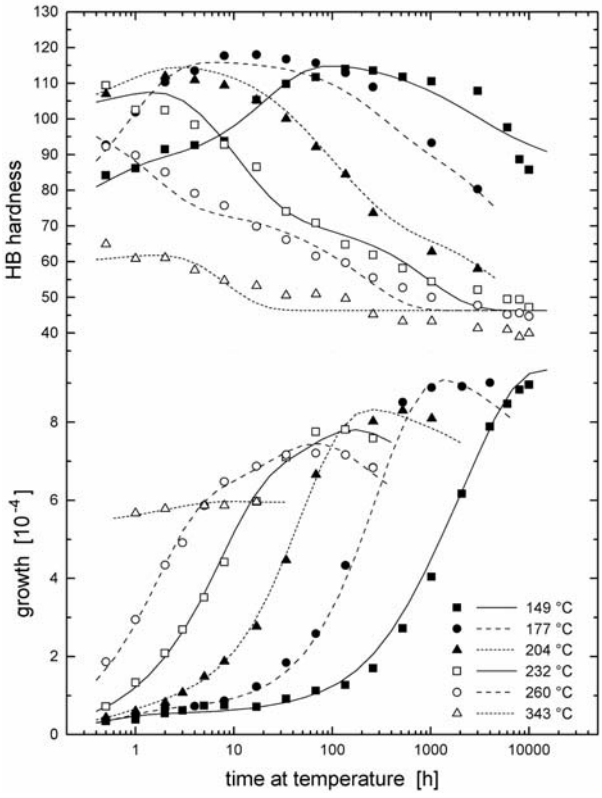

Fig. 3 Common regression of HB hardness kinetic curves and growth kinetic curves using regression function (2) – best fit of growth

The most important characteristics of individual processes, i.e. their activation energies (in kJ/mol), are presented in Table 2. From their values the processes could be identified, which is now only in progress.

Activation energies of individual processes (in ascending order) — Table 2

ε_i [kJ/mol]	ε_1	ε_2	ε_3	ε_4	ε_5	ε_6
Separate fit G – Fig. 1	14.9	88.6	146.9	243.8	250.0	269.3
Separate fit H – Fig. 2	15.6	22.0	96.6	119.8	149.2	215.2
Common fit (G) – Fig. 3	15.5	50.3	116.1	127.1	169.3	193.6
Common fit (H) – Fig. 4	9.6	81.4	100.0	130.2	147.3	184.8

7. Discussion

Generalized criterion of common regression (minimum product of corresponding sums of squares) can be directly implemented in MS Excel, but not in commercial regression programs. Instead of criterion S_1S_2 also the criterion $\sqrt{S_1S_2}$ could be considered but it leads to the same results as the previous one. In the case when the fit of one of quantities in common regression is substantially faster than of the other, the criterion $S_1^x S_2^{1-x}$ with suitably chosen $0 < < x < 1$ can be considered. Some interesting results have already been obtained with this criterion but systematic study has not yet been done.

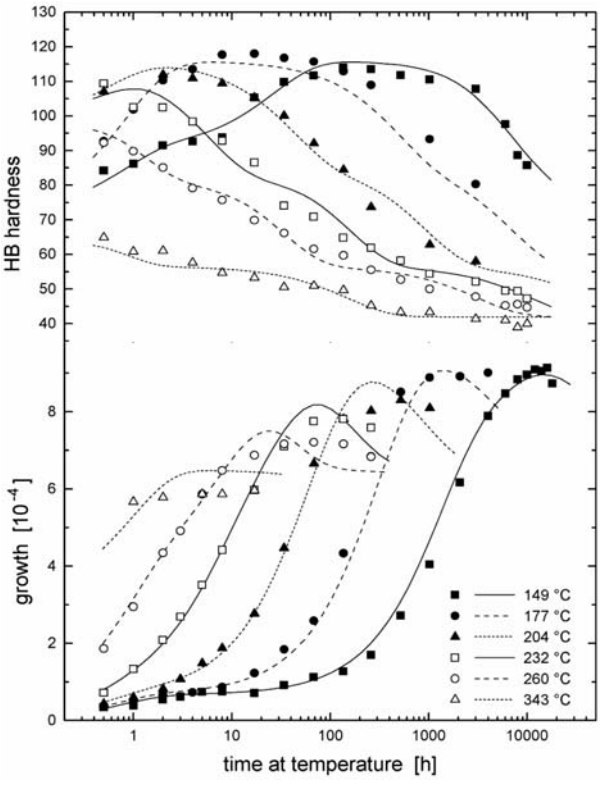

Fig. 4 Common regression of HB hardness kinetic curves and growth kinetic curves using regression function (2) – best fit of hardness

The results of regression show that the condition for replacing consecutive reactions by concurrent (parallel) reactions (i.e. rate constants differing in orders) is mostly fulfilled. Rate constants with extreme values (the lowest one and the highest one) are usually determined with lower accuracy than the others. Therefore, the hardening should be studied in sufficiently wide temporal as well as temperature ranges.

Up to now the author has no reliable tool for common regression giving with the values of regression parameters also their standard deviations. This problem will be solved in near future.

For the development of mentioned approach the simpler alloys should be used, with deep parallel study of microstructure, reliable identification of structural components and unequivocal assignation between addends in Eq. (2) and individual processes taking place in studied material during age-hardening. The proposal of such project will be submitted in next years – after the verification that the approach is really able to give effective and reliable results.

8. Conclusions

The sum of exponential functions with negative arguments containing rate constants, for whose temperature dependence the Arrhenius equation is used, proves to be a very good tool for the description of age-hardening kinetics of supersaturated solid solutions. It can be used not only for separate regression of the family of kinetic curves corresponding to the chosen studied property, but it can be successfully used in common regression of kinetic curves of more properties when rate constants and activation energies are common for all studied properties.

Acknowledgements

The research described in this paper was supported by the Organization Development Project (the project of the Department of Mathematics and Physics) awarded by the Ministry of Defence of the Czech Republic. Moreover the author is obliged to the authors whose experimental results were used for demonstration of the presented procedure.

References

[1] KOHOUT, J.: Modelling of Kinetics of Beryllium Bronze Hardening *(in Czech), Materials Engineering,* 2005, vol. 12, No. 3, pp. 133–137.
[2] KOHOUT, J.: Dimensional Degradation of Rolling Bearing Steels at Elevated Temperatures, *Degradacia vlastnosti konstrukcnych materalov [Degradation of Structural Materials Properties]*, Eds Bokuvka, O., Palcek, P.: Zilinska univerzita, 2003, pp. 155–160 *(in Czech).*
[3] KOHOUT, J.: Modelling of Changes in Properties of Alloys at Elevated Temperatures. *Mater. Sci. and Eng. A,* 2007, vol. A462, No. 1–2, pp. 159–163.
[4] KAUFMAN, J. G., ROOY, E. L.: *Aluminium Alloy Castings. Properties, Processes and Applications,* 3rd edition. Metals Park (OH): ASM International, 2007.
[5] MICHNA, S. et al.: *Encyklopedie hliniku [Aluminium encyclopaedia]*, Presov : Adin, 2005 *(in Czech).*
[6] KOHOUT, J., VECHET, S.: Regression not only S-N Curves in MS Excel from A to Z, *Letna skola unavy materialov 2006 [Summer School of Materials Fatigue 2006]*, Eds Bokuvka, O. and Palcek, P.: Zilinska univerzita, 2006, pp. 145–154 *(in Czech).*
[7] CELY, J.: *Programove moduly pro fyzikalni vypocty [Programme Modules for Calculations in Physics],* Brno : Rektorat UJEP, 1985 *(in Czech).*
[8] KOHOUT, J.: Description of Kinetics of Dimensional Changes of Silumin During Age-Hardening, *Degradacia vlastnosti konstrukcnych materialov [Degradation of Structural Materials Properties],* Eds Bokuvka, O., Palcek, P.: Zilinska univerzita, 2011, pp. 75–80.
[9] KOHOUT, J.: Kinetics of Hardness Changes During Age-Hardening of Silumin, *Materials Engineering,* 2011, vol. 18, No. 4, pp. 134–139.

https://doi.org/10.26552/com.C.2012.4.11-18

Hurtalova Lenka – Tillova Eva – Chalupova Maria *

MECHANICAL PROPERTIES OF HEAT TREATED SECONDARY AlSi12Cu1Fe CAST ALLOY AT ROOM TEMPERATURE

The contribution describes changes of mechanical properties (strength tensile, absorbed energy and Brinell hardness) in secondary (recycled) eutectic aluminium-silicon cast alloy – AlSi12Cu1Fe during solution treatment. This work presents the influences of the solution treatment by 525 °C, 545 °C and 565 °C with the holding time 2, 4, 8, 16 and 32 hours, water quenching at 40 °C and natural aging with holding time 24 hours. Mechanical properties were measured in line with STN EN ISO at room temperature. Solution treatment has led to changes in mechanical properties, caused by the changes in microstructure including the spheroidization and coarsening of eutectic silicon, gradual disintegration, shortening and thinning of intermetallic phases.

Keywords: solution treatment, mechanical properties, cast Al-Si eutectic alloy

1. Introduction

Many mechanical components, especially those for cars and rail vehicles, are made of Al-Si alloy thanks to the great potential of these materials as replacements for heavier materials (steel, cast iron or copper) [1, 2]. Aluminium alloys are the ideal replacement materials in car due to good formability, good corrosion resistance, high strength stiffness to weight ratio and recycling possibilities [3, 4].

In recent years, however, plenty of aluminium alloys waste has increased, therefore secondary (recycled) aluminium alloys are used to replace primary alloys. The use of secondary aluminium alloys is important, because the production of primary aluminium alloys consumes about 45 kWh/kg of metal and the production of secondary only about 2.8 kWh/kg of metal. Aluminium industry has the advantage of maximizing the amount of recycled metal, taking into account energy-savings and the reduction of dependence upon overseas sources. The remelting of recycled metal saves almost 95 % of the energy needed to produce prime aluminium from ore, and reductions in pollution and greenhouse emissions from mining, ore refining, and melting. Increasing the use of recycled metal is quite important from an ecological standpoint, since producing aluminium by recycling creates only about 5 % as much CO_2 as by primary production [5–7]. The utilization of secondary aluminium alloys has increased in recent years also due to its comparable properties with primary aluminium alloys [8].

Eutectic Al-Si alloys offer excellent fluidity, low density, high wear resistance and low expansivity and therefore are used for complex shape casting, thin-walled casting, pistons for rotors, compressor and so on [9, 10]. For example, eutectic Al-Si cast alloys used in the piston of petrol engines manufacturing, those the operating temperature at the top of pistons is 300 – 400 °C, must have good mechanical properties in order to fulfil the requirements for materials for pistons [9].

The mechanical properties of Al-Si alloys depend, besides Si, Cu, Mg and Fe-content, on the distribution and the shape of the silicon particles and changes in morphology of eutectic Si and intermetallic phases in secondary eutectic Al-Si cast alloy. Therefore it's necessary to understand the effects of the main alloying elements on the microstructure and mechanical properties [11–14].

The morphology of structure parameters can be affected for example with using heat treatment, modifying and grain refining. T4 heat treatment was used in this work. It consists of [15–19]:

- solution treatment, that is necessary to produce a solid solution. Production of a solid solution consists of keeping the Aluminium alloy at a sufficiently high temperature and for such a time so as to attain an almost homogeneous solid solution. The holding time on temperature is required to achieve dissolution of the undissolved or precipitated soluble phase constituents and to attain a reasonable degree of homogeneity;
- rapid water quenching to retain the maximum concentration of hardening constituent in solid solution;
- natural aging to obtain the desired mechanical properties in the casting.

The alloy and its heat treatment presented in this work are the part of a larger research project which was conducted to investigate and to provide better understanding of the influence of heat treatment and structure parameters on mechanical properties in recycled (secondary) aluminium cast alloy.

* **Hurtalova Lenka, Tillova Eva, Chalupova Maria**
Department of Materials Engineering, Faculty of Mechanical Engineering, University of Zilina, Slovakia, E-mail: lenka.hurtalova@fstroj.uniza.sk

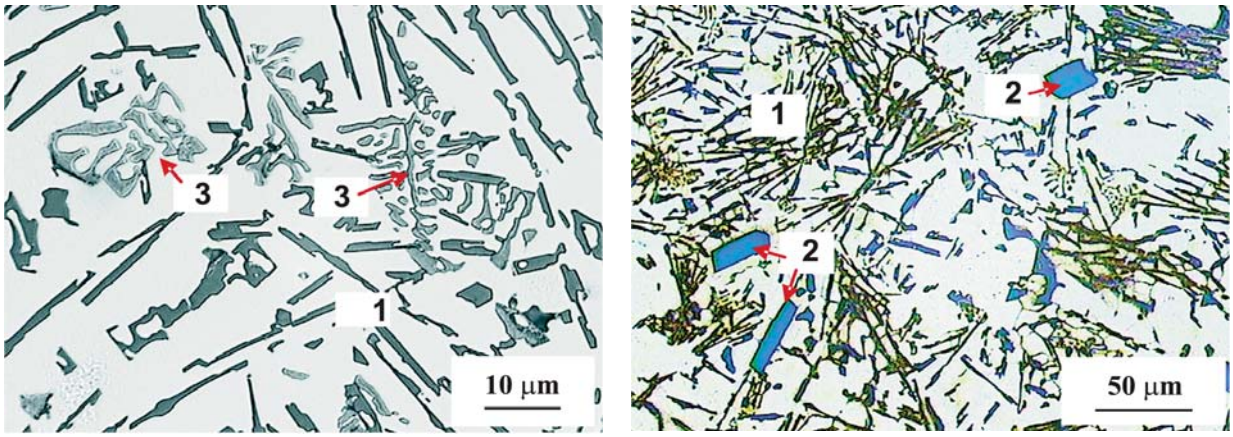

etch. Dix-Keller *etch. Weck-Aluminium*

Fig. 1 As - cast structure of AlSi12Cu1Fe cast alloy

2. Experimental material

Secondary AlSi12Cu1Fe cast alloy was used as an experimental material. The secondary alloy (prepared by recycling of aluminium scrap) was received in the form of 12.5 kg ingots. Experimental material was molten into the chill (chill casting). The melting temperature was maintained at 760 °C ± 5 °C. Molten metal was purified with salt AlCu4B6 before casting and was not modified or grain refined. The chemical analysis of AlSi12Cu1Fe cast alloy was carried out using an arc spark spectroscopy and the chemical composition is: 12.3 % Si, 0.8 % Cu, 0.7 % Fe, 0.35 % Mg, 0.22 % Mn, 0.43 % Zn, 0.01 % Sn, 0.05 % Pb, 0.03 % Ti, 0.03 % Ni and 0.02 % Cr.

In that the eutectic reaction occurs at 577 °C and from 11.3 to 12.6 % Si content in the eutectic AlSi12Cu1Fe cast alloy can be regarded as an eutectic alloy. Metallographic samples for the study were cut from the selected tensile specimens (after testing) and hot mounted for metallographic preparation. The microstructures were studied using an optical microscope Neophot 32 and scanning electron microscope (SEM) VEGA LMU II upon deep etching. The samples were prepared by standard metallographic procedures (wet ground on SiC papers, DP polished with 3 μm diamond pastes followed by Struers Op-S and etched for study at an optical microscope by standard etcher Dix-Keller, HNO_3, H_2SO_4 or colour etcher Weck-Aluminium, MA). Colour etching was used to highlight the phases that were not visible very well on the samples which were etched by standard etcher (black-white etcher). By the colour etching the surface of metallographic samples reacts to colour etcher so that on the surface there is transparent film formation, function which interference coating is [20]. The thickness of this transparent film depends on chemical composition of material.

Some samples were also deep-etched for 30 s in HCl solution in order to reveal the three-dimensional morphology of the silicon phase and intermetallic phases [21, 22]. The specimen preparation procedure for deep-etching consists of dissolving the aluminium matrix in a reagent that will not attack the eutectic components or intermetallic phases. The residuals of the etching products should be removed by intensive rinsing in alcohol. The preliminary preparation of the specimen is not necessary, but removing the superficial deformed or contaminated layer can shorten the process. Three-dimensional morphology was observed in such prepared samples, on a scanning electron microscope.

In the experimental cast alloy (AlSi12Cu1Fe), which has 12.3 % Si, the microstructure (Fig. 1) consists of eutectics (eutectic Si in α-phase (1)), primary Si particles (2) and intermetallic phases (3). It is necessary to achieve maximum performance of casting to affect the morphology of eutectic silicon, which is excreted in the form of large needles [10]. Morphology, distribution and size of Si markedly affect mechanical properties. In that Si can be influenced by the heat treatment without modifying, therefore the experimental alloy was heat treated. The heat treatment of experimental cast samples consists of solution treatment by temperatures 525 °C, 545 °C and 565 °C with the holding time 2, 4, 8, 16 and 32 hours, water quenching at 40 °C and natural aging at room temperature with the holding time 24 hours.

3. Results and discussion

3.1 Mechanical properties

The samples were subjected for mechanical test (tensile test, impact test and Brinell hardness test) after solution treatment.

Hardness measurement was performed by a Brinell hardness tester with the load of 62.5 kp, 2.5 mm diameter ball and the dwell time of 15 s. The Brinell hardness value at each state was obtained by the average of at least six measurements. Fig. 2 shows the variation in hardness of samples with heat treatments time 2, 4, 8, 16 and 32 hours by different temperatures. It can be seen that Brinell hardness is increased during holding time up to 2 hours for all the used temperatures of solution treatment. After this first peak Brinell hardness is decreased for all the temperatures of solution treat-

ments. On the curve by temperature 545 °C of solution treatment two maximums can be seen. The second maximum can be seen after the holding time 16 hours.

For the samples which were heat treated by temperature 525 °C and 565 °C, the second maximum can not be seen (the Brinell hardness is only decreased). The highest Brinell hardness was 110 HBW for the temperature of solution treatment 545 °C with the holding time 2 hours.

The samples were subjected for tensile and impact tests in order to investigate all changes of mechanical properties during solution treatment. The results are shown in Figs. 3 and 5.

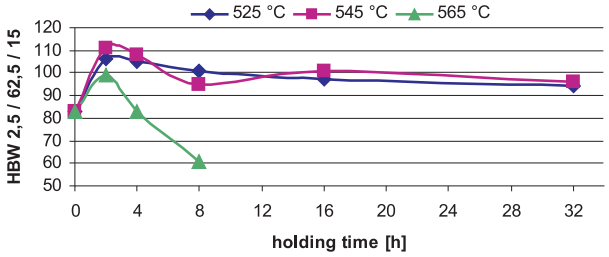

Fig. 2 Influence of solution treatment on Brinell hardness

Fig. 3 shows the influence of heat treatment on strength tensile. It can be found out that by the temperature 525 °C strength tensile is increased for all holding times of solution treatment besides 32 hours. By the temperature 545 °C the first maximum can be seen after the holding time 2 hours, then strength tensile goes down a little. On this temperature the second maximum can be seen after the holding time 16 hours after that the strength tensile decreases a little.

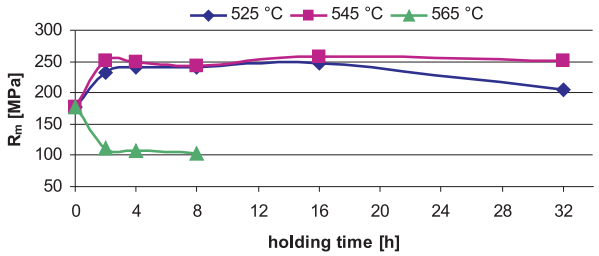

Fig. 3 Influence of solution treatment on strength tensile

After the solution treatment at the temperature 565 °C can be seen that strength tensile is lesser than strength tensile in as-cast. While at as-cast the strength tensile was 177 MPa, after the solution treatment at 565 °C with the holding time from 2 to 8 it ranged from 103 to 110 MPa. The decrease in strength tensile by this temperature is probably related to a high temperature of the solution treatment; because the temperature of eutectic reaction of Al-Si alloys is 577 °C. The results of strength tensile on the samples that were heat treated by the temperature 565 °C with the holding time 16 and 32 hours was immeasurable, because this temperature led to distortion of the testing samples (Fig. 4a).

In Fig. 3 it can be seen that strength tensile is increased during the temperatures 525 °C and 545 °C of the solution treatment. The highest strength tensile was 257 MPa for the temperature of solution treatment 545 °C with the holding time 16 hours.

Fig. 5 shows graphic dependence of material resistance on impact strength. By the temperature 525 °C we can observe that impact strength for all holding times of the solution treatment is increased (from 8 to 22 J). After the solution treatment at temperature 545 °C the first maximum can be seen after the holding time 8 hours, and then impact strength goes down a little. After that the impact strength is increased.

a) testing sample of strength tensile

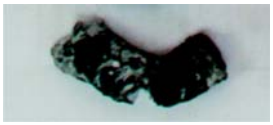

b) testing sample of impact strength

Fig. 4 Testing samples distortions (565 °C/16 hours)

By the temperature 565 °C can be seen that impact strength is increased only after the holding time from 2 hours, then the impact strength is decreased. The decrease of impact strength by this temperature is probably related to a high temperature of the solution treatment, which causes destruction of the testing samples (Fig. 4b) as by samples of strength tensile. The highest impact strength was 33 J for the temperature of solution treatment 545 °C with the holding time 32 hours.

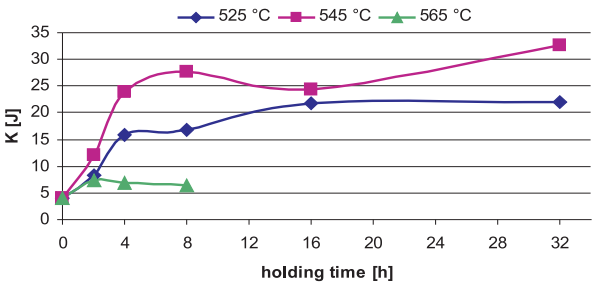

Fig. 5 Influence of solution treatment on impact strength

The mechanical properties of cast component are determined largely by the shape and distribution of Si particles in α-matrix. The optimum tensile, impact and fatigue properties are obtained with small, spherical and evenly distributed particles. Silicon also imparts heat treating ability to the casting through the formation of compounds with Mg, Fe and Cu.

3.2 Microstructural control

The samples were subjected for metallographic study after the mechanical test. The microstructure evolution was carried out by using a light microscope and scanning electron microscope.

Eutectic and primary Si was studied on a light microscope, because mechanical properties of cast component are determined largely by the shape and distribution of Si particles in the matrix. Si particles represent a large volume fraction of the eutectic alloy's microstructure and, therefore, are very important to affect their morphology. Small, spherical and evenly distributed particles provide the optimum tensile, impact and fatigue properties of aluminium material [15, 17].

Eutectic Si and minimum primary Si particles were observed in the structure of experimental material (Fig. 6). Secondary AlSi12Cu1Fe cast alloy was not modified or grain refined and so eutectic Si particles without heat treatment (as-cast state) are in a form of large hexagonal platelets (Fig. 6b), which are in the form of needles on a scratch pattern (Fig. 6a). Primary Si particles without heat treatment are in the form of prism (Fig. 6c) that are in the form of polygon with sharp ends on a scratch pattern (Fig. 6a). This morphology of Si particles is not good because these particles are brittle and can crack exposing the soft Al matrix. Therefore, the experimental cast samples were heat treated.

The kinetics of Si morphology transformation is influenced by the solution treatment [23]. The effect of solution treatment on morphology of eutectic Si, for all the temperatures and holding times of solution treatment, is demonstrated in Fig. 7. After the solution treatment at the temperature of 525 °C it was noted that the platelets of eutectic Si were fragmentized into smaller round needles (Fig. 7a). The temperature 525 °C is low for Si-spheroidization.

The spheroidization process was dominated by the temperature 545 °C of solution treatment. Eutectic Si needles (in as-cast state)

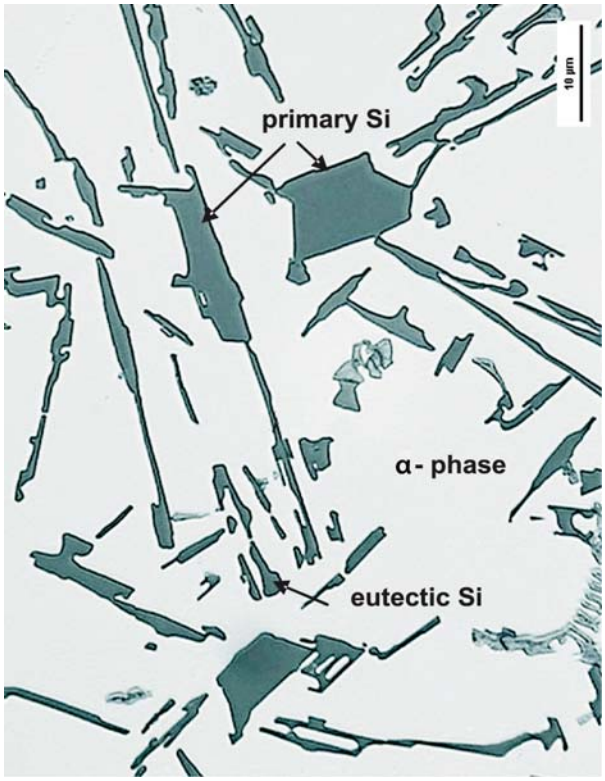

a) etch. Dix-Keller

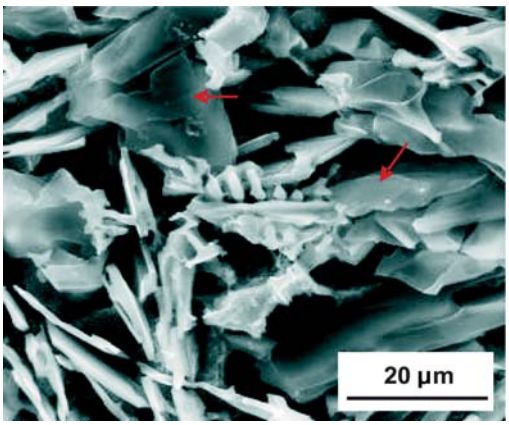

b) eutectic Si, deep etching, etch. HCl, SEM

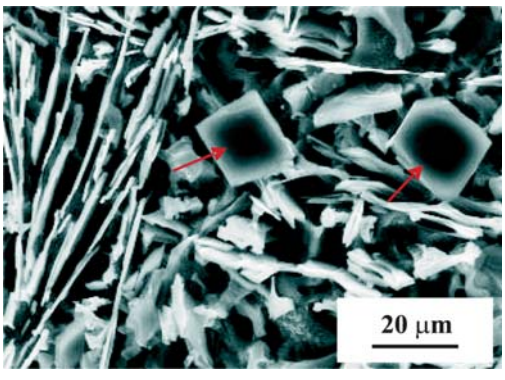

c) primary Si, deep etching, etch. HCl, SEM

Fig. 6 Morphology of Silicon in as-cast state

a) 525 °C

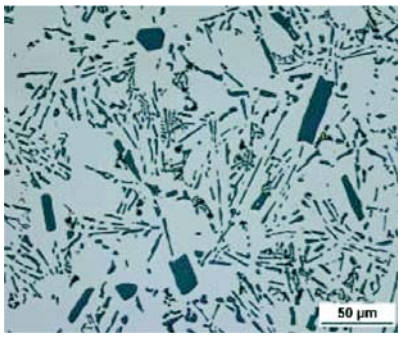

2 hours

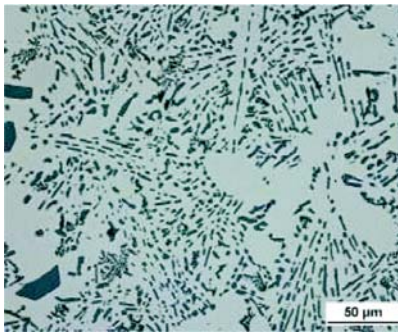

4 hours

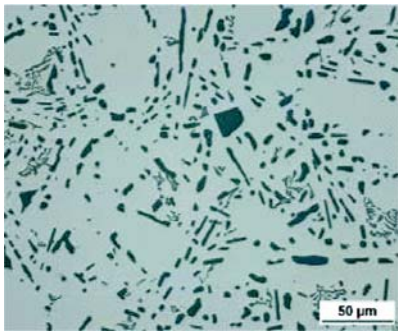

8 hours

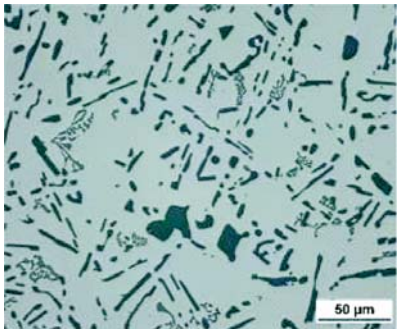

16 hours

a) 545 °C

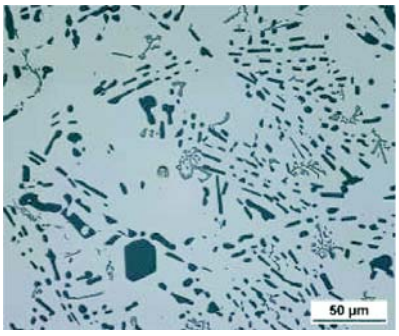

2 hours

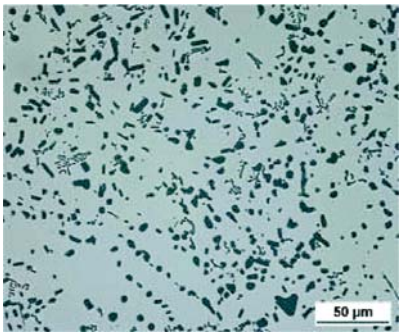

4 hours

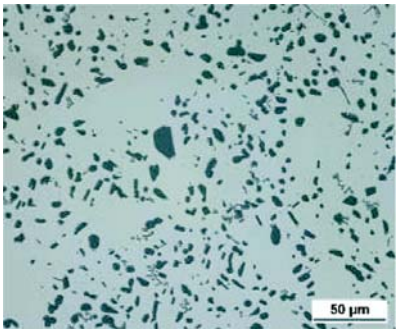

8 hours

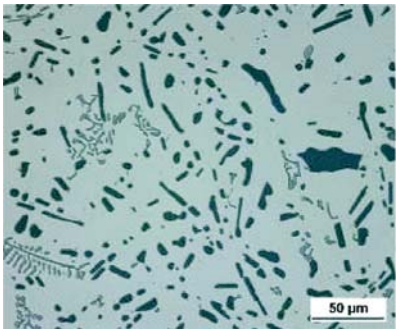

16 hours

a) 565 °C

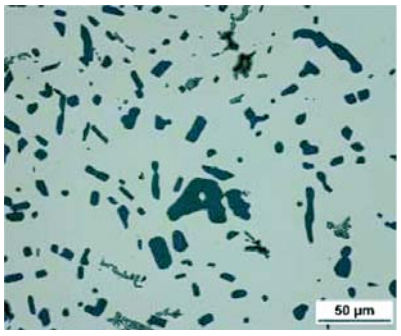

2 hours

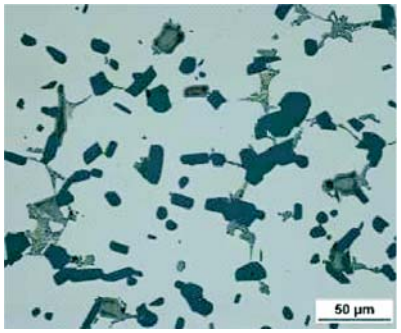

4 hours

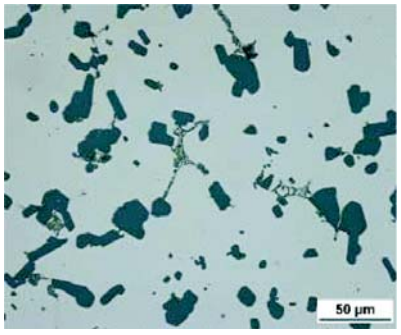

8 hours

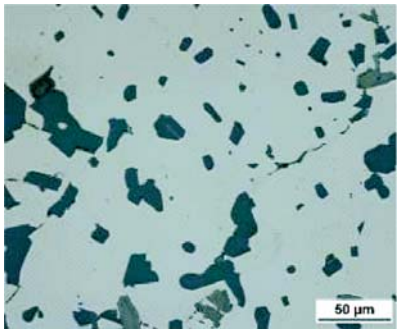

16 hours

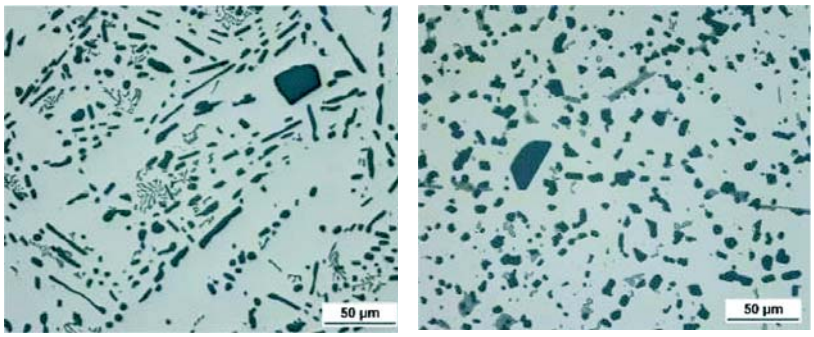

32 hours 32 hours

Fig. 7 Effect of solution treatment on morphology of Si particles, etch. Dix- Keller

are fragmented into smaller segments (at 545 °C) and these smaller Si particles were spheroidized to a rounded shape by the holding time 4 hours (Fig. 7b). After the holding time 16 and 32 hours, there is a change of morphology of eutectic Si particles, these spheroidized particles coarsen little by little (Fig. 7b). The solution treatment at the temperature 565 °C caused changes in morphology of eutectic Si particles, too. Eutectic Si particles gradually coarsen (Fig. 7c) and, therefore, this temperature of solution treatment (565 °C) is not convenient for heat treatment of experimental material. After the solution treatment we could observe that the primary Si particles rounded and reduced their size after all the temperatures and holding times of solution treatment – Figs. 7a, 7b and 7c.

3.3 Quantitative assesment of Si particles after solution treatment

The quantitative analysis was used to quantify the change of silicon morphology (size) in the microstructure during heat treatment. Quantitative analysis [24–26] was carried out on an Image Analyzer to quantify Si (average area Si particle and shape factor) by magnification 250 and 500 x. Fig. 8 shows the average area of Si particles obtained in the solution heat treated samples. This graphic relation is in line with the work of Paray and Gruzleski [23]. The average area of Si particles is decreased with increasing holding time of solution temperatures to 4 hours, after this holding time average area of Si particles is increased. The minimum value

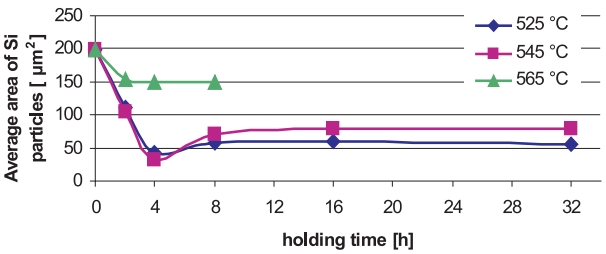

Fig. 8 Influence of solution treatment on average area of Si particles

of average Si particles was observed by the temperature 545 °C with the holding time 4 hours (33 µm^2). It's probably caused by spheroidization of silicon on this temperature.

Fig. 9 shows the changes in the average area of primary Si particles during the solution treatment. The minimum average area of primary Si particles was observed after the solution treatment by the temperature 525 °C with the holding time 16 hours (147 µm^2). By the increasing of the solution temperature the average area of primary Si particles was from 154 to 370 µm^2. After the solution treatment 565 °C the average area of primary Si was higher in comparison with other temperature of solution treatment because this temperature is not convenient for the heat treatment of experimental material.

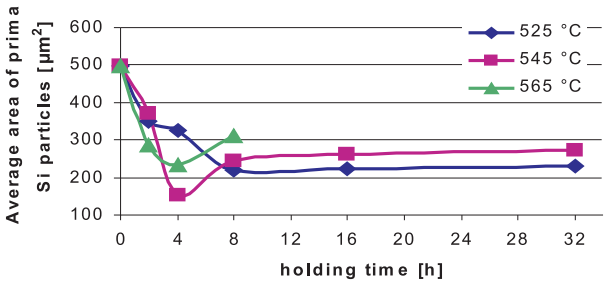

Fig. 9 Influence of solution treatment on average area of primary Si particles

4. Conclusions

In the present study, the effects of time and temperature of the solution heat treatment on mechanical properties in secondary eutectic AlSi12Cu1Fe cast alloy were investigated. These alloys are used for automotive applications and, therefore, their mechanical properties are very important. The results are summarized as follows:

- The mechanical properties are highly influenced by the temperature of solution treatment. Recycled AlSi12Cu1Fe cast alloy has in as-cast 83 HBW, R_m = 177 MPa and impact strength 3 J. Evaluation of mechanical properties has shown that the highest

mechanical properties are at the temperature 545 °C: Brinell hardness is after the holding time 2 hours 110 HBW, the strength tensile is after the holding time 16 hours 257 MPa and the impact strength is after the holding time 32 hours 33 J.

- Evaluation of microstructure, especially Si particles has shown that eutectic Si particles have spheroidized on the form of perfectly rounded grain at the temperature 545 °C with the holding time 4 hours. The temperature 525 °C was too low for spheroidization and temperature 565 °C was too high. Primary Si particles after the solution treatment, for all temperatures of treatment, rounded and reduced their size.
- Quantitative assessment has shown that minimum average area of Si particles was after the solution treatment by the temperature 545 °C with the holding time 4 hours. By this temperature the average area was from 33 to 127 μm^2.
- On the basis of the evaluation of mechanical properties and microstructure of AlSi12Cu1Fe cast alloy can say that the optimal mode of solution heat treatment for this secondary aluminium cast alloy is the solution treatment by the temperature 545 °C with the holding time up to 4 hours because it most improves mechanical properties thanks to spheroidization of eutectic Si to rounded shape and the values of tensile strength (250 MPa), Brinell hardness (cca 103 HB) and impact strength (24 J) are comparable with mechanical properties of heat treated primary cast alloy (R_m = 240 MPa; 70 HB).
- The solution treatment at 565 °C has caused distortion of the testing samples, local melting process and is not applicable for the secondary alloy with 12.3 % Si.

Acknowledgements

This work has been supported by Scientific Grant Agency of Ministry of Education of Slovak Republic and Slovak Academy of Sciences, No1/0841/11, No 1/0460/11 and No 1/0797/12.

References

[1] WANG, E. R., HUI, X. D., WANG, S. S., ZHAO, Y. F., CHEN, G. L.: Improved Mechanical Properties in cast Al-Si Alloys by Combined Alloying of Fe and Cu. *Materials Science and Engineering A 527*, 2010, pp. 7878–7884.

[2] MA, Z., SAMUEL, E., MOHAMED, A. M. A., SAMUEL, A. M., SAMUEL, F. H., DOTY, H. W.: Influence of Aging Treatments and Alloying Additives on the Hardness of Al-11Si-2.5Cu-Mg Alloys. *Materials and Design 31,* 2010, pp. 3791–3803.

[3] MILLER, W. S., ZHUANG, L., BOTTEMA, J., WITTEBROOD, A. J., SMET, P. DE, HASZLER, A., VIEREGGE, A.: Recent Development in Aluminium Alloys for the Automotive Industry. *Materials Science and Engineering,* A280, 2000, pp. 37–49.

[4] WITTHAYA, E., VIBOONPUN, N.: *Effect of Solution Treatment Time on Microstructure and Hardness of Al-Si-Cu-Ni Alloy,* from http://www2.mtec.or.th/th/seminar/Msativ/pdf/H01.pdf

[5] SENCAKOVA, L., VIRCIKOVA, E.: Life Cycle Assessment of Primary Aluminium Production. *Acta Metallurgica Slovaca,* 13, 3, 2007, pp. 412–419.

[6] DAS, K. S.: Designing Aluminum Alloys for a Recycling Friendly World. *Materials Science Forum,* vol. 519–521, 2006, pp. 1239–1244.

[7] DAS, K. S., GREN, J. A. S.: Aluminum Industry and Climate Change-Assessment and Responses. *Jom,* 62, 2, 2010, pp. 27–31.

[8] HURTALOVA, L., TILLOVA, E. CHALUPOVA, M.: Optical and Electron Microscopy Study of the Mechanical Properties Improvement on Recycled AlSi9Cu3 Cast Alloy Along the Hardening. *Intern. Virtual Journal for Science,* Technique and Innovations for the Industry, MTM, vol. 7, 2011, pp. 48–51.

[9] WANG, E. R., HUI, X. D., CHEN, G. L.: Eutectic Al-Si-Cu-Fe-Mn Alloys with Enhanced Mechanical Properties at Room and Elevated Temperature. *Materials and Design* 32, 2011, pp. 4333–4340.

[10] TILLOVA, E., CHALUPOVA, M.: *Strukturna analyza (Structural Analysis).* Edis Zilina, 2009.

[11] TAVITAS-MEDRANO, J. F., MOHAMED, A. M., GRUZLESKI, E. J., SAMUEL, H. F., DOTY, W. H.: Precipitation - hardening in Cast Al-Si-Cu-Mg Alloys. *J. of Materials Science,* 2009, vol. 45, No. 3, pp. 641–651.

[12] WARMUZEK, M.: *Aluminium/Silicon Alloys:* Atlas of Microfractographs, Introduction to Aluminium – Silicon Casting Alloys, 2004.

[13] MOUSTAFA, M. A., SAMUEL, F. H., Doty, W. H.: Effect of Solution Heat Treatment and Additives on the Microstructure of Al-Si (A413.1) Automotive Alloys. *J. Materials Sci.,* (2003), 38 (22), pp. 4507–4522.

[14] SAMUEL, A. M., SAMUEL, F. H., DOTY, W. H.: Observations on the Formation of 13-AlFeSi Phase in 319 Type Al-Si Alloys. *J. Materials Sci.* 31, 1996, pp. 5529–5539.

[15] SJOLANDER, E., SEIFEDDINE, S.: The Heat Treatment of Al-Si-Cu-Mg Casting Alloys. *J. of Materials Processing Technology,* 2010, pp. 249–1259.

[16] TASH, M., SAMUEL, H. F., MUCCIARDI, F., DOTY, W. H.: Effect of Metallurgical Parameters on the Hardness and Microstructural Characterization of As-cast and Heat-Treated 356 and 319 Aluminium Alloys. *Materials Science and Engineering,* A443, 2007, pp. 185–201.

[17] ABDULWAHAB, M.: Studies of the Mechanical Properties of Age-hardened Al-Si-Fe-Mn Alloy. *Australian J. of Basic and Applied Sciences 2* (4), 2008, pp. 839–843.

[18] JOHANSEN, H. G.: *Structural Aluminium Materials.* TALAT Lecture 2202 – Basic Level, 1994, pp. 2–28.

[19] TRENDA, G.: Solutions for Ductile Die Casting, from http://foundry-planet.com/fileadmin/redakteur/werbepartner/sag/SolutionsDuctileDieCasting.pdf, 07. 05. 2012.

[20] TILLOVA, E., CHALUPOVA, M., HURTALOVA, L., BONEK, M., DOBRZANSKI, L. A.: Structural Analysis of Heat Treated Automotive Cast Alloy. *J. of Achievements in Materials and Manufacturing Engineering,* 47/1, (2011), pp. 19–25.
[21] TILLOVA, E., CHALUPOVA, M., HURTALOVA, L.: Evolution of Phases in a Recycled Al-Si Cast Alloy During Solution Treatment. *The Scanning Electron Microscope,* 2011, pp. 411–438, INTECH.
[22] SKOCOVSKY, P.: *Colour Contrast in Metallographic Microscopy.* Slovmetal, Zilina 1993.
[23] PARAY, F., GRUZLESKY, J. E.: Microstructure-mechanical Property Relationships in 356 Alloy. *Cast Metals,* 7, No.1, 1994, pp. 29–40.
[24] VASKO, A., BELAN, J.: Applications of Methods of Quantitative Metallography in Materials Engineering, Intern. *J. of Applied Mechanics and Engineering,* vol. 15, No. 2, 2010, pp. 405–410.
[25] BELAN, J.: *Study of Advanced Materials for Aircraft Jet Engines Using Quantitative Metallography.* Recent Advances in Aircraft Technology, IN-TECH - Open Access publisher of Scientific Books and Journals, 2011, pp. 49–74.
[26] VASKO, A.: Influence of Transformation Temperature on Structure and Mechanical Properties of Austempered Ductile Iron. *Acta Metallurgica Slovaca,* vol. 17, No. 1, 2011, pp. 45–50.

https://doi.org/10.26552/com.C.2012.4.19-25

Zuzanka Trojanova – Zoltan Szaraz – Oksana Padalka – Talant Ryspaev – Pavel Lukac *

STRUCTURAL (SUPER)PLASTICITY OF MAGNESIUM MATERIALS

Superplastic behaviour of two magnesium alloys QE22 and EZ33 having a grain size of ~ 1μm was studied at a temperature of 420 °C and in the strain rate interval from 1×10^{-4} to 1×10^{-3} s^{-1}. The substructure of samples was analysed by the transmission electron microscope before and after deformation. The substructure of samples exhibits an existence of particles in the grain boundaries. These precipitates are very stable even at high deformation temperature and they are reason for the relatively high ductility of alloys. Observed ductility of the WE54/SiCp composite is much lower due to the existence of ceramic particles in the grain boundaries. They inhibit the grain boundary sliding and are the reason for the cavitations and early fracture of the composite.

Keywords: *Magnesium alloys, Magnesium alloy based composite, Strain rate sensitivity, Electron microscopy, Superplasticity, Threshold stress*

1. Introduction

Low density of magnesium alloys and relatively high specific strength are the main advantages of these materials. Magnesium alloys and composites are used in different industrial applications. As magnesium is recyclable, its extensive usage can minimize the negative impact on the environment due to non-degradable plastic wastes. Magnesium materials have low ductility at ambient temperature. This is a consequence of the hexagonal close-packed (hcp) crystal structure with a limited number of operative slip systems. The plasticity of magnesium alloys and composites increases at elevated temperatures where additional slip systems become active. However, low ductility of magnesium alloys prevents their application hence; the enhanced ductility of magnesium materials is of a special interest [1–4]. It is known that the fine grain size ($d \leq 10$ μm) stable at higher temperatures is a main structural requirement for the occurrence of superplasticity. All characteristics of superplasticity (relative elongation to failure ε_f, flow stress σ, strain rate sensitivity of flow stress m, optimum strain rate for superplasticity and optimum deformation temperature for superplasticity) depend on the grain size. Fine grain structure with the grain size less than 10 μm may be obtained by various methods such as phase transformation, recrystallisation, forming of the microduplex structure or severe plastic deformation (equal channel angular pressing, reciprocating extrusion) [5–10]. Structural superplasticity was estimated in several magnesium alloys especially in alloys of the AZ series [11–13] or Mg-Li alloys [14–15]. The superplasticity phenomenon was also observed in ZK60 alloy [16], WE54 alloy [17] and QE22 alloy [18].

In papers [18, 19] the influence of preliminary thermomechanical treatment (hardening, overageing and hot extrusion) on the grain size was investigated. This prior thermomechanical treatment influences the number of recrystallisation nuclei and so the resulting grain size.

The aim of this work is to study the microstructure and substructure of two magnesium alloys containing rare earth elements (RE) and Zr, which exhibited better superplastic properties in comparison with alloys containing Al. The aim is also to find the main features influencing the superplastic behaviour and limiting factors for lower plasticity of particles reinforced composite with the Mg alloy matrix.

2. Materials and experimental methods

QE22 (Mg-2Ag-2RE-Zr), EZ33 (Mg-2.5Zn-3RE-Zr) magnesium alloys and WE54 (Mg-4Y-4RE) reinforced with SiC particles were used in this study. Cylindrical QE22 and EZ33 specimens with a diameter of 72 mm and a length of 80 mm were cut from ingots and exposed to homogenisation treatment at 470 °C for 10 h with the subsequent cooling on the air. Due to low diffusion rates of solute atoms in the magnesium matrix the alloys were simultaneously quenched. Precipitation ageing was conducted in the temperature range from 200 to 380 °C for 10 hours. After that, the aged specimens were preheated at 350 °C and then hot extruded. This device consists of the press with the rated strain of 4000 kN and the tube furnace which heats instrumental rigging

* **Zuzanka Trojanova[1], Zoltan Szaraz[1], Oksana Padalka[1], Talant Ryspaev[2,3] and Pavel Lukac[1]**
[1] Department of Physics of Materials, Faculty of Mathematics and Physics, Charles University in Prague, Czech Republic,
E-mail: ztrojan@met.mff.cuni.cz
[2] Institute of Welding Engineering and Cutting Manufacturing Processes (ISAF) Clausthal University of Technology, Clausthal-Zellerfeld, Germany
[3] Kyrgyz State Technical University, Kyrgyz-German Technical Institute, Bishkek, Kyrgyzstan

(container with a diameter of 75 mm, matrix and punch). Hot extrusion was performed in two steps with the extrusion ratio of 20 and 26. Samples for deformation experiments were machined from the extruded bars.

Composite WE54/SiC containing 13 vol. % SiC particles was processed by a powder metallurgy method (PM). Extrusion billets were prepared by mixing of the matrix powder with SiC particles in an asymmetrically moved mixer with subsequent milling in a ball mill. The powder was encapsulated in Mg containers and extruded to rods at 400 °C. The composite samples were not thermally treated. Tensile specimens with a gauge length of 10 mm and a gauge diameter of 6 mm were machined with the tensile axis parallel to the extrusion direction.

The strain rate sensitivity parameter $m = \left(\frac{d\ln\sigma}{d\ln\dot{\varepsilon}}\right)_T$ was estimated by the abrupt strain rate changes (SRC) method [20]. SRC tests and tensile tests with a constant strain rate ($\dot{\varepsilon}$) were performed at temperatures from 300 to 500 °C and strain rates from 10^{-4} to 10^{-2} s^{-1}. Experiments with the constant strain rate, where the cross-head speed continuously increases, significantly reduces the test time at low strain rates. The best conditions for superplasticity of the alloys were found at a temperature of 420 °C.

Foils for Transmission electron microscopy (TEM) from QE22 and EZ33 alloys were thinned by the electro-polishing method using the TENUPOL 3. The specimens were etched in the solution of 15.9 g of LiCl, 335 g of Mg perchlorate, 1500 ml of methanol, and 300 ml of butoxy-ethanol in the temperature range −55 to −40 °C. After electro-polishing, the foils were washed in methanol. To prevent the formation of an oxide surface layer, TEM foils of all experimental materials had to be stored in vacuum. Investigations of substructure of the materials were carried out with JEOL 2000FX. The transmission electron microscope operating at 200 kV was equipped with an energy dispersive X-ray analyzer (EDAX), which provides the analysis of individual phase composition. Microstructure of WE54/SiC composite was studied using a light microscope Olympus and scanning electron microscope JEOL.

3. Results and discussion

3.1. Microstructure of materials

The grain size of the QE22 and EZ33 alloys was measured in the both as-cast and after thermo-mechanical treatment states. The average grain sizes of the as-cast alloys are higher than 100 μm while in the QE22 and EZ33 alloys after the thermo-mechanical treatment, the grain sizes were reduced to 0.7 μm (QE22) and 1.2 μm (EZ33), respectively.

The substructure of QE22 and EZ33 alloys was investigated in the as-cast and after thermo-mechanical treatment states. Microstructure of the as-cast QE22 alloy consists of α-grains decorated in the grain boundaries by the second phase particles. TEM revealed chains of smaller particles; containing Nd and Ag located at grain

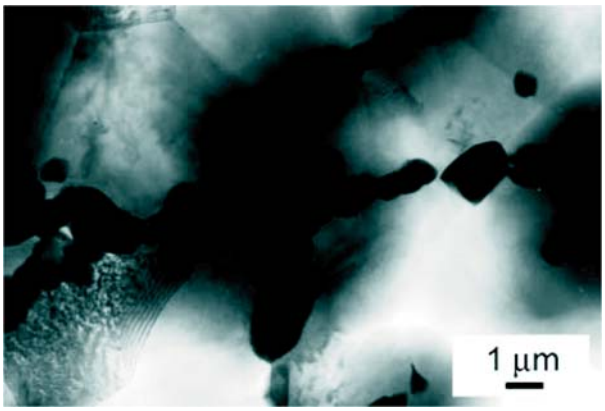

Fig. 1 TEM micrograph of the as-cast QE22 magnesium alloy showing particles of Mg_3 (Ag, Nd) phase situated in grain boundaries

boundaries (see Fig. 1). These particles were dissolved during homogenisation annealing. TEM showed only groups of smaller and bigger non-dissolved zirconium particles which are visible in Fig. 2a. These Zr particles are very stable and they were not influenced by the homogenisation treatment. Dislocations pinned at

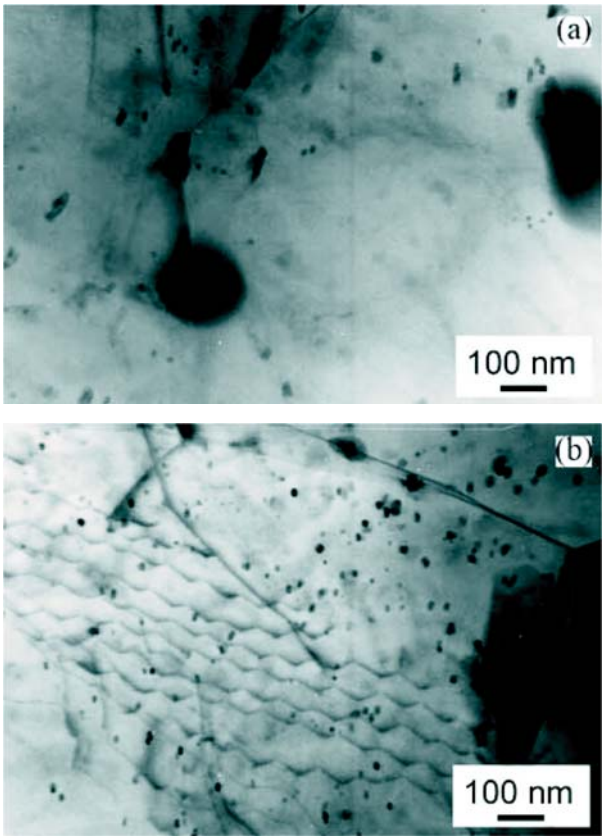

Fig. 2 TEM micrographs of the QE22 magnesium alloy after the homogenisation treatment: (a) fine Zr particles, (b) Zr particles in partially visible dislocation network

Zr particles are also visible in Fig. 2b. After thermo-mechanical treatment (age annealing at 350 °C for 10 h and hot extrusion) the particles at grain boundaries appeared again (see Fig. 3) and they were found again together with the smaller Zr particles also after deformation at 420 °C.

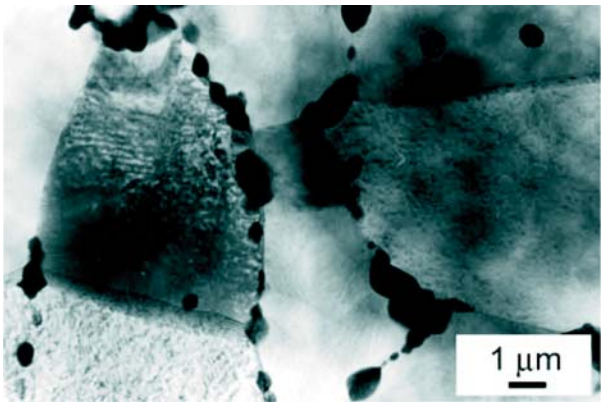

Fig. 3 TEM micrographs of the QE22 magnesium alloy after thermo-mechanical treatment showing chain of particles of Mg_3 (Ag, Nd) phase in grain boundaries

The interior of grains after deformation at 420 °C was clear without dislocations. Round particles appearing after the thermo-mechanical treatment were identified as Mg_3 (Ag, Nd) phase. There are two kinds of round particles of Mg_3 (Ag, Nd) phase: bigger particles with an average diameter of 0.2–0.5 µm lying along the grain boundaries and in the triple points and the smaller particles with an average diameter of 50–100 nm situated in the grains interior. The obtained results of the Mg_3(Ag,Nd) phase distribution agree with results in the paper [21] where similar two particle sizes were found in QE22 alloy after T6 temper (annealing for 5.5 h. at 520 °C and ageing 8 h. at 205 °C). Particles placed at grain boundaries contribute to the microstructure stability hereby they hinder the grain growth during heating in the deformation machine and the self deformation. Precipitates in the grain boundaries were found also after the high temperature deformation practically unaffected.

The electron micrograph of the EZ33 alloy is shown in Figure 4 in the as-cast state. Fine Zr particles are visible. These particles remained unaffected by the thermo-mechanical treatment. The microstructure of EZ33 alloy after thermo-mechanical treatment exhibits small α grains containing fine ZnNd particles in the grain boundaries, very probably particles of T phase (Figure 4a). Wei et al. studied the solidification path and phase constituents of alloys in the magnesium rich corner of the Mg-Zn-misch metal system [22]. They found that the T phase having a c-centred orthorhombic crystal structure exhibits a wide range composition of Mg, Zn and RE depending on the alloy composition. The Zr particles (200-100 nm) were observed in the whole volume. In the sample of EZ33 after high temperature exposition during deformation the same particles were found, i.e. T phase in the grain boundaries and small Zr particles in the grains interior (Fig. 4b). While dislocations in this material were present after the thermomechanical treatment (see Fig. 5), after the high temperature deformation no dislocations were detected. The average grain size of EZ33 alloy is relatively small (1.2 µm), though it is even smaller (0.7 µm)

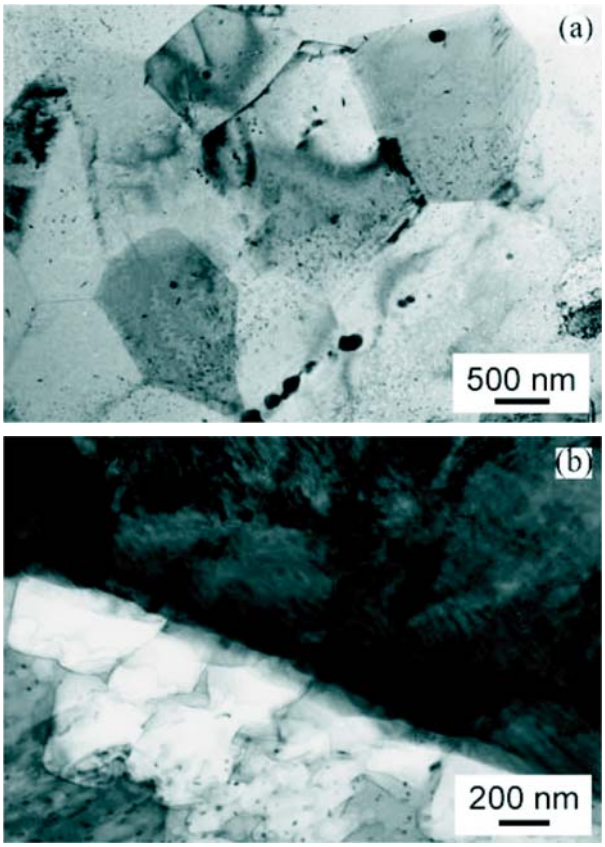

Fig. 4 TEM micrographs of the EZ33 magnesium alloy: after thermomechanical treatment (a) and after high temperature exposition during the deformation process (b)

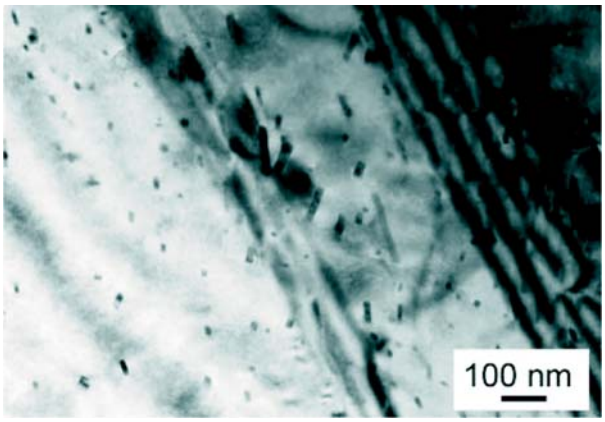

Fig. 5 TEM micrographs of the EZ33 magnesium alloy after thermo-mechanical treatment showing resistance to dislocation motion by the Zr particles

in QE22 alloy. Such a difference between the grain sizes in the alloys can be caused by the presence of alloying element Nd besides Zr. QE22 alloy contains mainly Nd among rare earth elements. Furthermore, fine precipitates of Mg_3 (Ag, Nd) phase are uniformly located also inside of grains. As such Zn (and rare earth) containing alloys are the major Mg alloy group where Zr is used as the grain refiner [23]. Although Zr has long been used as a notable grain refiner for Mg alloys [24] the mechanism of grain refinement by Zr is not yet completely understood. In the alloys, which do not contain Al, small Zr particles remain unsolved in the α-matrix and influence the grain nucleation during solidification or recrystallisation.

Figure 6 shows the microstructure of the WE54/SiC_p composite. The as-extruded bar appears mainly constituted of very small equiaxed grains. The corresponding average grain size was found to be about ~3 μm. The SiC particles (mean particle size ~9 μm) were not uniformly distributed in the matrix; in many cases they formed clusters.

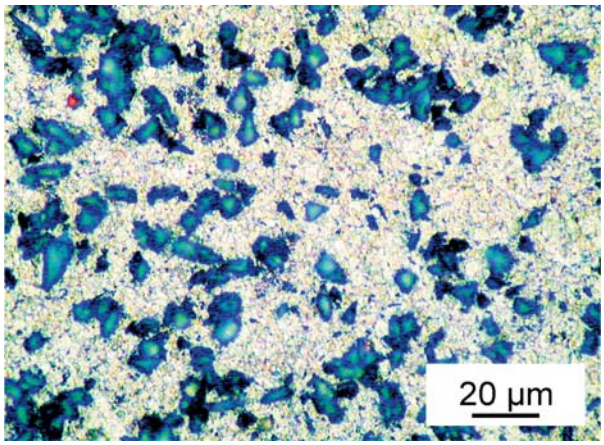

Fig. 6 Microstructure of WE54/SiCp composite

3.2. Superplastic behaviour of alloys

Values of the elongation to failure ε_f introduced in Table 1 together with values of m-parameter were estimated at 420 °C. The highest values of the elongation to fracture $\varepsilon_f = 780\%$ (QE22) and 710% (EZ33) were estimated at a strain rate of $\dot{\varepsilon} = 3 \times 10^{-4}\ s^{-1}$. These values correspond to the highest values of the strain rate sensitivity $m = 0.75$ (QE22) and 0.73 (ZE33) which were estimated at the same deformation conditions. As it follows from Table 1, the tensile elongations of all samples exceeded 200%, which represents a substantial improvement over the poor room-temperature ductility, typical for magnesium alloys. The strain rate of materials deformed at high temperatures is done by a relationship of the following form:

$$\dot{\varepsilon} = A\frac{Gb}{kT}\left(\frac{b}{d}\right)^{p}\left(\frac{\sigma}{G}\right)^{n} D\,, \qquad (1)$$

where A is a dimensionless material constant, G is the shear modulus, b is the Burgers vector, d the grain size, d is the grain size exponent, $n = 1/m$ is the true stress exponent. kT has its usual meaning.

Elongation to failure and strain rate sensitivity values estimated at 420 °C — Table 1

$\dot{\varepsilon}$ (s^{-1})	QE22		EZ33	
	ε_f (%)	m	ε_f (%)	m
1×10^{-4}	720	0.62	700	0.65
3×10^{-4}	780	0.75	710	0.73
5×10^{-4}	450	0.50	420	0.50
1×10^{-3}	360	0.42	340	0.48
5×10^{-3}	300	0.38	280	0.35
0.01	240	0.32	230	0.30

D is the appropriate diffusion coefficient ($= D_0 \exp(-Q/RT)$, where D_0 the frequency factor, Q the activation energy for the diffusion process and R the gas constant). The steady state plastic flow of coarse-grained metals at high temperatures, above $0.4T_M$ (T_M being the melting temperature), is usually described by dislocation motion and storage on obstacles. These obstacles may be either of non-dislocation type or of dislocation type. Grain boundaries or incoherent precipitates are considered as the obstacles of the non-dislocation type. Dislocation type obstacles are formed by reactions between various types of dislocations. Steady state character of deformation is provided with the dislocation cross slip and also by climbing of dislocation edge segments. In the fine grained materials two other independent mechanisms – grain boundary sliding accommodated by slip and directional diffusional flow may be considered [25-27]. Each of the three deformation mechanisms has specific values of n, p and Q by which the mechanism can be uniquely defined. For the plastic flow by slip of dislocation the high values of the stress exponent ($n = 5$ or higher) are characteristic and the activation energy is close to values for the activation energy of the lattice diffusion or for the pipe diffusion. The grain size exponent p is close to zero [28]. Grain boundary sliding accommodated by dislocation slip or diffusional flow is characterised by the low values of the stress exponent (lower than 3, in the case of ideal superplasticity 1) and the activation energy is equal to the lattice or grain boundary diffusion or combination both. As no dislocations were observed by means of TEM and the estimated values of the stress sensitivity parameter are 1.33 (QE22) and 1.37 (EZ33) we may conclude that the main deformation mechanism during the superplastic flow is the grain boundary sliding accommodated by lattice and grain boundary diffusion.

3.3 Plasticity of WE54/SiCp composite.

The strain rate sensitivity parameter m was measured in SRC tests. The values of m estimated for different strain rates and tem-

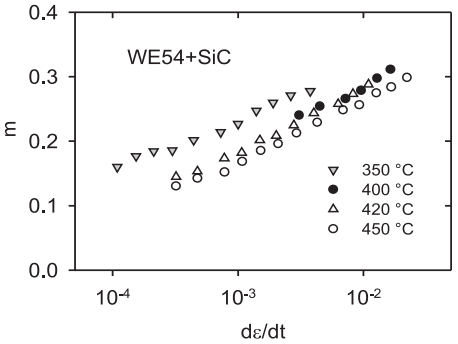

Fig. 7 Strain rate dependence of m-parameter

peratures are introduced in Fig. 7. The strong strain rate dependence of the m-parameter is obvious from the figure. With increasing temperature the dependence is shifted to the higher strain-rates. However, the m parameter slightly increases with temperature; the maximum values are in the vicinity of 0.3 as it is obvious from Table 2. The maximum recorded elongation to failure was 99%, which shows an evidence of the enhanced plasticity, nevertheless this value remains below the bottom limit for superplastic region. The SEM micrograph of the sample exhibiting the highest elongation is shown in Fig. 8 documenting the microstructure after deformation at 450 °C. Numerous cavities formed during the high temperature deformation are visible in Fig. 8. The cavitation primarily occurred at the reinforcement/matrix interfaces which are

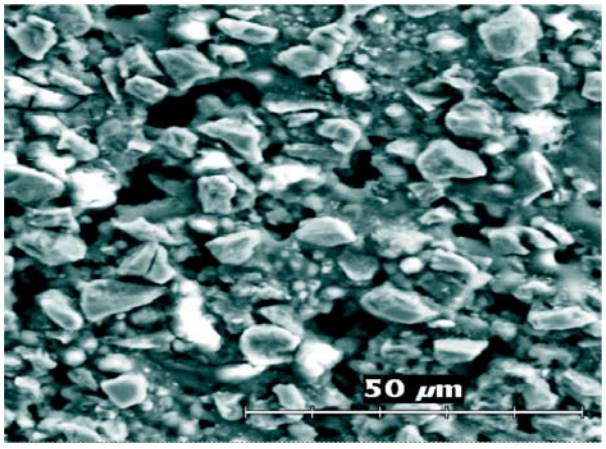

Fig. 8 Micrograph showing cavities formed during high temperature deformation

the preferential sites for the nucleation of cavities. The density of cavities was higher near the fracture surface where elongated cavities were found. Since many of these cavities were fairly large, it is reasonable to assume that the growth and subsequent coalescence and interlinkage of the cavities led to a premature failure.

As it is obvious from Fig. 8 the m−values decrease with decreasing strain rate at low strain rates down to ~ 0.1. Low *m*-values in the low strain rate regime were generally reported for PM magnesium alloys and Mg based composites [29–32]; they are probably associated with the existence of the threshold stresses σ_{th} [33]. Considering the threshold stress, eq. (1) can be rewritten as

$$\dot{\varepsilon} = A\frac{Gb}{kT}\left(\frac{b}{d}\right)^{p}\left(\frac{\sigma-\sigma_{th}}{G}\right)^{n} D \qquad (2)$$

The σ_{th} may be determined by adopting a plot of steady state stress σ against $\dot{\varepsilon}^{1/n}$ (n = 1, 2, 3, 5) in a double linear scale [34]. The best linear fit in the entire temperature range was found for n = 3. By extrapolation to zero strain-rate (see Fig. 9) the threshold stress values were estimated for various temperatures and are introduced in Table 2.

Maximum values of m-parameter and elongation to failure estimated for three temperatures and corresponding strain rates for WE54/SiC composite — Table 2

Temperature	m_{max}	$\dot{\varepsilon}$ (s^{-1})	ε_f (%)	σ_{th} (MPa)
350 °C	0.28	4x10-3	66	11.2
420 °C	0.30	2x10-2	95	6.6
450 °C	0.29	5x10-2	99	4.7

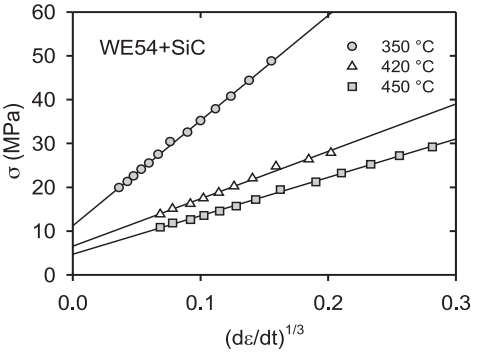

Fig. 9 Estimation of the threshold stress

From Table 2 it follows that the threshold stress decreases with increasing temperature. The temperature dependence of the normalised threshold stress may be expressed by an Arrhenius-type relationship in the form [35]

$$\frac{\sigma_{th}}{G} = B\exp\left(\frac{Q_0}{RT}\right). \qquad (3)$$

Here B is constant and Q_0 is an energy term which appears to be associated with the deformation process. The activation energy Q_0 was estimated from the plot $\ln \dot{\varepsilon} T/G$ vs $1/T$ (Fig. 10), measured at a constant normalized flow stress $(\sigma - \sigma_{th})/G$ ($\sigma - \sigma_{th}/G$ = $= 1.7\times10^{-3}$). The activation energy was found to be $Q \approx 114$ kJ/mol. The activation energy estimated for volume diffusion is 135 kJ/mol and for grain boundary diffusion 92 kJ/mol [36]. Comparing with the experimental value of 114 kJ/mol (using rule of mixture), we may conclude that the measured activation energy

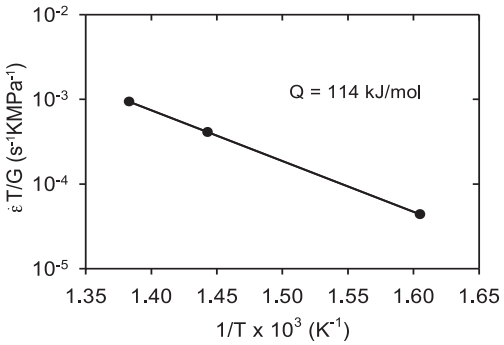

Fig. 10 Estimation of the activation energy

consists of approximately 50% volume and 50% grain boundary diffusion. The threshold stress is very probably necessary for the dislocation slip in the basal planes dependent on cross slip into non-basal slip planes (pseudo-Peierls mechanism), and/or grain boundary sliding.

Observed formation and growth of cavities relaxes the stress concentration caused at the particles on sliding grain boundaries. Cavities, created by vacancy clustering, may nucleate if the stress concentration is not relieved sufficiently rapidly. Local tensile stress caused by sliding at interfaces may be written in the form [4]

$$\sigma_{slid} = \frac{0.92kTd_p\dot{\varepsilon}dV_f}{\Omega D_L\left(1 + 5\frac{\delta D_{GB}}{d_p D_L}\right)}, \qquad (4)$$

where d_p is the particle diameter, $\dot{\varepsilon}$ is the strain rate, d is the grain size, D_L is lattice diffusion and D_{GB} the grain boundary diffusion coefficient, δ is grain boundary width, Ω is atomic volume and V_f is the volume fraction of particles. The insufficiently accommodated grain boundary sliding process is the reason for cavitation and early failure of samples

4. Conclusions

1. Magnesium alloys QE22 and EZ33 exhibit superplastic behaviour at 420 °C and the strain rates in the interval $1-3 \times 10^{-4}$ s^{-1}.
2. The grain size refinement in alloys may be attributed to very stable Mg_3(Ag,Nd) phase and *T* phase in grain boundaries formed in both materials during the preparation process.
3. Small addition of Zr particles significantly influences the resulting grain size.
4. SiC particles very probably inhibit the grain boundary sliding and they are reason for the premature failure of the WE54/SiC_p composite.
5. The threshold stress values found at temperatures 350 – 450 °C may be interpret as the stresses necessary for the glide of dislocations in the compact and non-compact planes and grain boundary sliding.

Acknowledgements.

The work is a part of activities of the Charles University Research Center "Physics of Condensed Matter and Functional Materials". The authors are grateful also for the financial support of the Czech Grant Agency under the contract P108/12/J018.

References

[1] MOHRI, M., MABUCHI, T. M., SAITO, N., NAKAMURA. M.: *Mater. Sci. Engn.* A 257, 1998, 287.
[2] KAIBYSHEV, O. A. *Superplasticity of Alloys, Intermetallics and Ceramics.* Berlin Heidelberg: Springer Verlag; 1992.
[3] KIM, J. W., CHUNG, S. W., CHUNG, C. S., KUM, D.: *Acta Mater.* 49, 2001, 3337.
[4] MABUCHI, M., HIGASHI, K.: *Acta Mater.* 47, 1999, 1915.
[5] ROSOCHOWSKI, A.: *Solid State Phenomena* 101–102, 2005; 13.
[6] ZHU, Y. T., LANGDON, T. G.: *JOM*; 58–63, 2004, 58.
[7] ZEHETBAUER, M. J.: *Adv. Eng. Mater.* 5, 2003; 265.
[8] FIGUEIREDO, R. B., LANGDON, T. G.: *Mater. Sci. Eng.* A, 430, 2006, 151.
[9] MATSUBARA, K., MIYAHARA, Y., HORITA, Z., LANGDON, T. G.: *Acta Mater.*, 51, 2003, 3073.
[10] LEE, S. W., CHEN, Y. L., WANG, H. Y., YANG, C. F., YEH, J. W.: *Mater. Sci. Eng.* A, 464, 2007, 76.
[11] TAN, J. C., TAN, M. J.: *Mater. Sci. Eng.* A 339, 2003, 81.
[12] WANG, Y. N., HUANG, J. C.: *Mater. Trans.* 44, 2003, 2276.
[13] WEI, Y. H., WANG, Q. D., ZHU, Y. P., ZHOU, H. T., DING, W. J., CHINO, Y., MABUCHI, M.: *Mater. Sci. Eng.* A 360, 2003, 107.
[14] KAWASAKI, M., KUBOTA, K., HIGASHI, K., LANGDON, T. G.: *Mater. Sci. Eng.* A 429, 2006, 334.
[15] SIVAKESAVAM, O., PRASAD, Y. V. R. K: *Mater. Sci. Eng.* A323, 2002, 270.
[16] YIN, D. L., ZHANG, K. F., WANG, G. F., HAN, W. B.: *Mater. Letters* 59, 2005, 1714.
[17] NAKASHIMA, K., IWASAKI, H., MORI, K. T., MABUCHI, M., NAKAMURA, M., ASAHINA, T.: *Mater. Sci. Eng.* A 293, 2000, 15.
[18] WESLING, V., RYSPAEV, T., SCHRAM, A.: *Mater. Sci. Eng.* A 462, 2007, 144.
[19] SZARAZ, Z., TROJANOVA, Z., RYSPAEV, T., WESLING, V.: *Kovove Mater.* 46, 2008, 285.

[20] BOOESHAGHI, F., GARMESTANI, H.: *Scripta Mater.* 40, 1999; 509.
[21] SVOBODA, M., PAHUTOVA, M., MOLL, F., BREZINA, J., SKLENICKA, V.: In: *Magnesium Alloys and their Applications.* Weinheim; Wiley-VCH Verlag; 2000, p. 234.
[22] WIE, LlY., DUNLOP, G.L., WESTENGEN, H.: J. *Mater. Sci.* 32, 1995, 3335.
[23] EMLEY EF.: *Principles of Magnesium Technology.* Oxford: Pergamon Press; 1966, p. 127.
[24] DAS, A, LIU, G, FAN, Z.: *Mater. Sci. Eng.* A 419, 2006; 349.
[25] MUKHERJEE, A. K.: *Mater. Sci. Eng.,* 8, 1971, 83.
[26] METENIER, P., GONZALEZ-DONCEL, G., RUANO, O.A., WOLFENSTINE, J., SHERBY, O.D.: *Mater. Sci. Eng.* A 12, 199, 195.
[27] BUSSIBA, A., BEN ARTZY, A., SHTECHMAN, A., IFERGAN, S., KUPIEC, M.: *Mater. Scie. Eng.* A302, 2001, 56.
[28] MUKHERJEE, A. K., BIRD, J. E., DORN, J. E.: *Trans. Am. Soc. Met.*, 62, 1969, 155.
[29] MABUCHI, M., ASAHINA, T., IWASAKI, H., HIGASHI, K.: *Mater. Sci. Technol.* 13, 1997, 825.
[30] WATANABE, H., MUKAI, T., NIEH, T. G., HIGASHI, K.: *Scripta Mater.* 42, 2000, 249.
[31] WATANABE, H., MUKAI, T., MABUCHI, M., HIGASHI, K.: *Acta Mater.* 49, 2001, 2027.
[32] HIGASHI, K., MABUCHI, M., LANGDON, T. G.: *ISIJ Int.* 36, 1996, 1423.
[33] MOHAMED, F. A.: *J. Mater. Sci.* 18, 1983, 582.
[34] LI, Y., LANGDON, T. G.: *Acta Mater.* 47, 1999, 3395.
[35] MOHAMED F. A., PARK, K.-T., LAVERNIA, E. J.: *Mater. Sci. Eng.* A 150, 1992, 21.
[36] FROST, H.J., ASHBY, M. F., *Deformation-mechanism Maps.* Pergamon Press, Oxford, UK, 1982, 44.

https://doi.org/10.26552/com.C.2012.4.26-30

Filip Pastorek – Branislav Hadzima – Pavel Dolezal *

ELECTROCHEMICAL CHARACTERISTICS OF Mg-3Al-1Zn MAGNESIUM ALLOY SURFACE WITH HYDROXYAPATITE COATING

Electrochemical characteristics of Mg-3Al-1Zn alloy surfaces after grinding and/or coating by hydroxyapatite were investigated by voltamperometric tests in 0.9 % NaCl solution. The hydroxyapatite treatments were realised by electrochemical method in water solution of $Ca(NO_3)_2 . 4H_2O$, $(NH_4)_2HPO_4$ and H_2O_2. The influences of various types of hydroxyapatite treatment processes on corrosion potentials, corrosion current densities and characteristics of passive state were evaluated. Basic potentiodynamic curves obtained from the electrochemical tests were analysed by Tafel analyses. The improvement of short-time electrochemical behaviour after hydroxyapatite treatment of tested alloy surface was reported.

1. Introduction

Traditional biomedical implant materials such as stainless steels and Ti alloys play an important role in repairing the damaged bone tissue. If these implants exist in the human body for a long time, they will always release toxic elements to impair human body's health. The application of biodegradable implants can solve this problem. The biodegradable implants can gradually be dissolved, absorbed, consumed or excreted after the bone tissue healing. Current biodegradable implants made from polymers have an unsatisfactory mechanical property [1–2]. In comparison, magnesium and its alloys are potential biodegradable materials due to their attractive biological performances [3–5]:

(1) metal magnesium is biodegradable in body fluids by corrosion;
(2) Mg^{2+} is harmless to human body;
(3) magnesium can accelerate the growth of new bone tissue;
(4) the density, elastic modulus and yield strength of magnesium are closer to the bone tissue than that of the conventional implants [2].

However, poor corrosion and fatigue resistance of magnesium and its alloys limit their applications [6–9]. Hydrogen gas evolution in the corrosion reaction causes sometimes the formation of cavities (bubbles) around the implanted alloy [4, 7]. In the case of subcutaneous gas pockets of rats, the adsorption rate of hydrogen in the tissue was determined as 0.954 $ml.h^{-1}$ based on the diffusion coefficient of hydrogen in the tissue [7]. Song et al estimated that the tolerated level of hydrogen evolution rate was 0.01 $ml.cm^{-2}.day^{-1}$ based on the size of subcutaneous bubbles in guinea pigs [3–4]. Thus, the improvement of corrosion resistance of magnesium alloys by protective coatings has been a crucial issue to promote the practical use of the alloys [10].

To reduce the biodegradation (corrosion) rate of Mg alloys, further bulk alloying is one option [5, 11–13], however this can potentially lead to the introduction of toxic elements. Biocompatible protective coatings are a practical option to moderate biodegradation allowing functional implant deployment [14]. Hydroxyapatite (HA, $Ca_{10}(PO_4)_6(OH)_2$), is a well-known biocompatible and bioactive material with close chemical and structural resemblance to human bones and teeth [15].

HA coating can be deposited on different substrates by various methods such as plasma spraying [16, 17], sputtering [18], sol–gel [19], pulse laser deposition [20], electrophoretic [21] and electrodeposition [22]. Among them, electrodeposition has received much attention due to its versatility, cost effectiveness, and ability to control the thickness and chemical composition of HA by varying the conditions employed for deposition [23–25]. Deposition of HA coating on titanium and its alloys has been studied by many researchers [23, 26, and 27]. However, the degradation behaviour of HA-coated Mg and its alloys has not been studied much [28]. Actually, some magnesium alloys containing Zr, Cd, rare earth elements and heavy metals are not suitable for biomaterials application from the medical aspect [29–30]. But the mechanical and corrosion properties of pure magnesium are unsatisfactory. In comparison with other magnesium alloys, AZ31 magnesium alloy, with low Al content, good mechanical properties and corrosion resistance, is suitable to act as biodegradable material [30]. Even though the biocompatibility of aluminium is limited [31], it

* **Filip Pastorek[1], Branislav Hadzima[1], Pavel Dolezal[2]**
[1] Department of Materials Engineering, FME, University of Zilina, Slovakia, E-mail: filip.pastorek@fstroj.uniza.sk
[2] Institute of Material Science and Engineering, FME, Brno University of Technology, Brno, Czech Republic

seems to be a valid alloying element for magnesium alloys in body contact, as it is known to diminish the magnesium corrosion rate by stabilizing hydroxides in chloride environments [32–33]. The addition of Zn to Mg alloy results in improved mechanical properties thanks to grain refinement, and shows a reduced corrosion rate compared with pure Mg [34–35].

For these reasons, the aim of this study is to electrodeposit HA coating on magnesium alloy AZ31 surface and to improve its corrosion properties this way.

2. Experimental material and methods

The tested AZ31 magnesium alloy was continually casted at Brandenburgische Universität in Cottbus, Germany and chemical composition was analysed at the Magnesium innovation centre MagIC GKSS Geesthacht, Germany. The chemical composition of AZ31 alloy is in Table 1.

Chemical composition of AZ31 alloy Table 1

Component	Al	Zn	Mn	Si	Cu	Ni	Fe	Mg
wt. %	2.96	0.828	0.433	0.004	0.004	<0.001	0.002	bal.

The samples for metallographic observation were prepared by conventional metallographic procedures. For visualization of the magnesium alloy microstructure, etchant consisting of 2.5 ml acetic acid + 2.1 g picric acid + 5 ml H_2O + 35 ml of ethanol was used [36]. The microstructure of AZ31 alloy (Fig. 1) was observed by the CARL ZEISS AXIO Imager.A1m light metallographic microscope in the laboratories of Department of Materials Engineering, University of Zilina. The microstructure is created by polyedric grains of solid solution of aluminium, zinc and other alloying elements in magnesium. The average grain size is 220 μm.

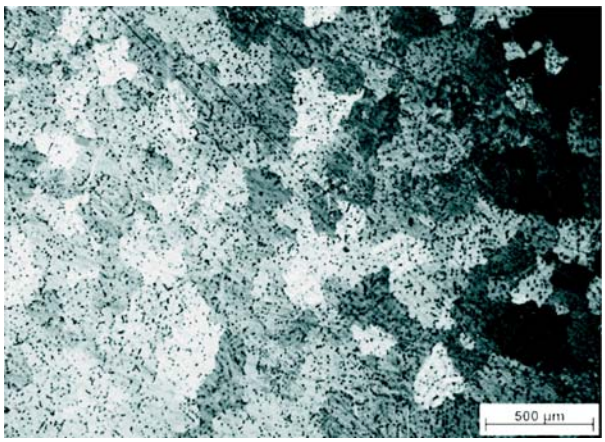

Fig. 1 Microstructure of AZ31 Magnesium alloy, light microscopy, etch. picric acid + ac. acid + ethanol + water

2.1 Experimental material surface preparation

For the evaluation of hydroxyapatite surface treatment influence on electrochemical characteristics the specimen surfaces were grinded with 1000 grit SiC paper to ensure the same surface roughness, then rinsed with demineralised water and ethanol, and dried using a stream of air. After described pre-treating the hydroxyapatite was deposed on the specimens' surfaces. Treatment electrolyte solution was prepared with 0.1 M $Ca(NO_3)_2 . 4H_2O$, 0.06 M $(NH_4)_2HPO_4$, 10 ml.l^{-1} of 30 vol.% H_2O_2. Solution pH was 4.7 and the electrodeposition was carried out at room temperature 22 ± 2 °C. Grinded AZ31 sample was used as the cathode, while a platinum electrode served as the anode. Electrodeposition was performed with constant potential 100 mV vs saturated calomel electrode (SCE) for 1 h on a laboratory apparatus VSP (producer BioLogic SAS France).

After HA deposition the surface of samples was immediately rinsed with demineralized water and dried using a stream of air and then immersed in various environments: 1 M NaOH (22±1 °C) solution for 2 h, demineralized water (22±1 °C) for 2 h and dry air (22±2 °C) for 2 h.

2.2 Experimental methods

The surface morphology of the treated samples was assessed by a stereomicroscope Nikon AZ100 with a digital camera using NIS Elements software. The corrosion characteristics of the untreated and HA-coated AZ31 in 0.9% NaCl were evaluated by potentiodynamic polarization using a potentiostat/galvanostat/frequency response analyser VSP from BioLogic SAS France. All the corrosion experiments were performed at 22±1 °C. A saturated calomel electrode and a platinum electrode served as the reference and auxiliary electrodes, respectively. Treated and untreated AZ31 samples formed the working electrode in such a way that only 1 cm² area of the working electrode surface was exposed to the electrolyte solution in corrosion cell.

Potentiodynamic polarization tests were carried out from −200 to +500 mV vs SCE with respect to the OCP (open circuit potential) at a scan rate of 1 mV.s^{-1}. Measured potentiodynamic curves were analysed using Tafel fit by EC-Lab software. The Stern and Geary equation predicts that for $E > E_{corr}$ (where E is the open circuit potential and E_{corr} is the corrosion potential) the anodic reaction predominates and that for $E < E_{corr}$ the cathodic reaction predominates [37]:

$$I \approx I_{corr} 10^{\frac{E-E_{corr}}{\beta_a}} \text{ for } E > E_{corr}$$

$$I \approx -I_{corr} 10^{\frac{E-E_{corr}}{\beta_c}} \text{ for } E < E_{corr},$$

where I is the current, I_{corr} is the corrosion current and β_a and β_c are the Tafel constants.

So, in a log I versus E representation, one should see two linear parts for $E > E_{corr}$ and $E < E_{corr}$:

$$\log I \approx \frac{E - E_{corr}}{\beta_a} + \log I_{corr} \text{ for } E > E_{corr}$$

$$\log I \approx \frac{E_{corr} - E}{\beta_c} + \log I_{corr} \text{ for } E > E_{corr}$$

The Tafel graph is displayed in log i(i is the corrosion current density) vs E where two linear regressions are automatically made using the least square method and the software deduces the corrosion potential (E_{corr}) to linear regressions intersection, the corrosion current density value (i_{corr}) and the Tafel constants (β_a and β_c) [37 and 38]. These β_a and β_c coefficients express the slope of the anodic and cathodic region of potentiodynamic polarization curve in log i vs E representation. The potentiodynamic polarization measurements were repeated at least three times so that reproducibility of the test results was ensured.

3. Results and discussion

Surface morphology after hydroxyapatite deposition is shown in Fig. 2. As can be seen, transparent irregular units with a width of 10 to 300 μm, which were homogeneously distributed throughout the sample surface, were reached by HA electrodeposition.

Fig. 3 shows the measured potentiodynamic curves of untreated and treated AZ31 Mg alloy samples using hydroxyapatite electrodeposition combined with sealing in various environments. All measured curves except the curve of non-treated surface consist of two parts. First one is a transition between an immune state and active state (characterized by corrosion potentials and corrosion current densities) and second one is a passive state of the surface finished by transpassivation potential. The curve of untreated surface has only transition between immune and active states. The thermodynamic (corrosion potentials E_{corr}, transpassive potential E_t) and kinetic (corrosion current density icorr, corrosion rate r_{corr}, anodic steady state current density in passive state i_a) characteristics obtained from the measured curves are in Table 2.

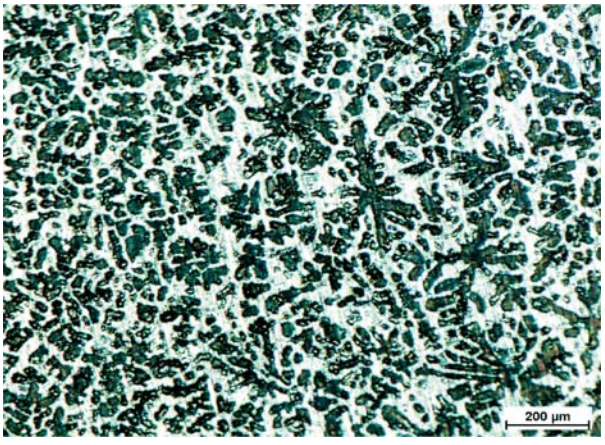

Fig. 2 Surface morphology of AZ31 after HA electrodeposition

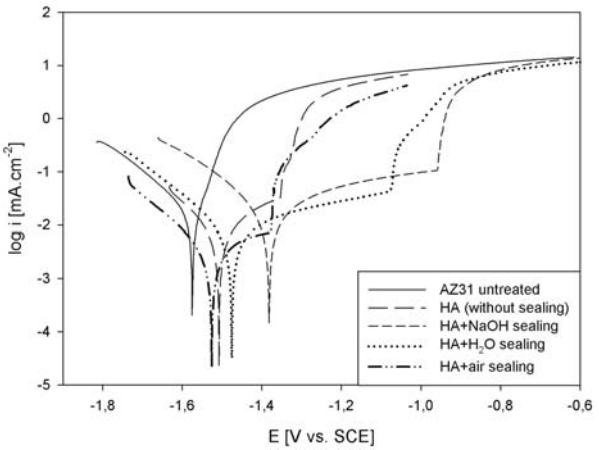

Fig. 3 Potentiodynamic curves of untreated and treated surfaces of AZ31 Mg alloy in 0.9% NaCl

Creation of the hydroxyapatite layer on the specimen's surface causes changes in both thermodynamic and kinetic characteristics. The hydroxyapatite layer is nobler and, therefore, the corrosion potential moves to more positive values. Air sealing does not change the corrosion potential; the layer is from the thermodynamic point of view similar to the layer after a hydroxyapatite process. However, the sealing in water or in 1M NaOH solution causes increase of corrosion potential values. The state is the result of magnesium hydroxide creation in pores of the hydroxyapatite layer. The thermodynamic stability of this layer is better on the surface after NaOH sealing and, therefore, the corrosion potential of this specimen reached the most positive value.

Corrosion rate in the passive state is proportional to the value of anodic steady state current density (i_a). This kinetic characteristic depends on the ability of the passive layer to slow the corrosion process. Significantly the lowest value of ia was observed on the surface of HA + air sealing samples. However, this value is reached only in a relatively narrow range of passivity ($E_t - E_{corr}$). The surface modified by HA without sealing has approximately the same value of ia as HA + H_2O sealing surface, but H_2O sealing extended interval of the layers passive behaviour nearly threefold. Sealing in 1M NaOH resulted in such changes on the HA surface that there was a substantial increase of i_a compared to the state

Electrochemical characteristics of AZ31 Mg alloy surface after various treatments Table 2

Surface treatment	E_{corr} [mV_{SCE}]	i_{corr} [$\mu A.cm^{-2}$]	r_{corr} [$mm.y^{-1}$]	i_a [$\mu A.cm^{-2}$]	E_t [mV_{SCE}]	$E_t - E_{corr}$
grinded	−1575	19.0	0.87	–	–	–
HA without sealing	−1506	5.8	0.27	~ 21	−1353	153
HA + NaOH sealing	−1381	16.8	0.77	~ 56	−957	424
HA + H_2O sealing	−1475	7.3	0.33	~ 20	−1077	398
HA + air sealing	−1526	3.0	0.14	~ 5.6	−1370	156

without sealing. A possible reason of this fact is the reduction in thickness of the HA layer by reactions running in alkaline medium. The surface is thus more protected by created $Mg(OH)_2$ areas than by an initially intended HA layer.

Another important thermodynamic indicator of corrosion resistance of material surface layers is the width of the passive state area represented by the interval between E_{corr} and E_t, where the corrosion products with a relatively good protective effect against corrosion are formed on the sample. This means that the wider this interval is, the more convenient it is. As it is shown in Fig. 3, just grinded sample does not have passive state at all. Width of the passive state of the samples HA without sealing and HA + air sealing is 153 mV and 156 mV, respectively. These nearly identical values confirm the argument that the air sealing does not change the nature of the sample's surface layer from the thermodynamic point of view. Probably a film of magnesium oxide grows on the surface that is not covered by hydroxyapatite. The largest passive state interval was measured on samples which were after HA process sealed in H2O (398 mV) and NaOH (424 mV). These environments were able to create Mg hydroxides on the sample`s surface which are stable even at higher potential.

The third important electrochemical characteristic is the corrosion current density i_{corr} that assesses the corrosion process in terms of kinetics. It is proportionally related to the corrosion rate rcorr that expresses weight losses of material in certain environment over time. The highest and, therefore, in terms of corrosion the least desirable current density value (i_{corr} = 19 $\mu A.cm^{-2}$) was obtained on just grinded surface. The process of HA caused decrease by two thirds compared with just grinded samples that is reflected in two thirds reduction of corrosion rate. Formed HA layer thus largely contributes to slowing the corrosion process. The use of an additional sealing in H_2O and thus creation of protective magnesium hydroxides in this way had no additive effect on further reduction of the corrosion current density (i_{corr} = 7.3 $\mu A.cm^{-2}$). On the contrary, sealing in NaOH after HA process caused dissolution of created HA layer and formation of Mg hydroxides on the sample's surface. It resulted in an increase of the corrosion current density to values approaching those obtained for just grinded samples.

Overall, the lowest value of i_{corr} was reached at HA + air sealing samples where the air filled the gaps in HA by MgO oxides which resulted in reducing the corrosion current density by half compared with the HA samples without sealing.

5. Conclusions

On the basis of the measured data and analyses we concluded:

1. The bioactive hydroxyapatite (HA) coating was successfully obtained by electrodepostion on magnesium alloy AZ31 to improve in combination with different sealings the corrosion properties of the surface.
2. The highest Ecorr value and the widest passive state interval were reached by treatment process consisted of HA + NaOH sealing and the lowest current density was measured at HA + air sealing samples.
3. Taking into account electrochemical corrosion resistance criteria (thermodynamic and kinetic), the most appropriate process consisting of HA electrodeposition and H_2O sealing was considered.

Acknowledgements

The research is supported by the European regional development fund and Slovak state budget by the project ITMS 26220220048 (call OPVaV-2008/2.2/01-SORO). The authors are grateful for the support in experimental works to project VEGA No. 1/0100/11.

References

[1] LIU, C. L., XIN, Y. C., TANG, G. Y.: *Mater. Sci. Eng.* A 456, 2007, 350–357.
[2] SONG, Y. W., SHAN, D. Y., HAN, E. H.: *Mater. Lett.* 62, 2008, 3276–3279.
[3] SONG, G.L.: *Corr. Sci.* 49, 2007, 1696–1701.
[4] WITTE, F., KAESE, V., HAFERKAMP, H.: *Biomater.* 26, 2005, 3557–3563.

[5] WITTE, F., FISCHER, J., NELLESEN, J.: *Biomater.* 27, 2006, 1013–1018.
[6] HADZIMA, B., PALCEK, P.: *Mater. Eng - Mater. inz.* 8, 2001, 67–74.
[7] WITTE, F., HORT, N., VOGT, C., COHEN, S., KAINER, K.U., WILLUMEIT, R., FEYERABEND, F.: *Curr. Opin. Solid State Mater. Sci.* 12 (5–6), 2008, 63–72.
[8] STAIGER, M.P., PIETAK, A.M., HUADMAI, J., DIAS, G.: *Biomater.* 27, 2006, 1728–1734.
[9] NOVY, F., JANECEK, M., SKORIK, V., MULLER, J., WAGNER, L.: *Int. J. Mater. Res.* 100, 2009, 288–291.
[10] HIROMOTO, S., TOMOZAWA, M.: *Surf. Coat. Technol.* 205, 2011, 4711–4719.
[11] KIRKLAND, N.T., LESPAGNOL, J., BIRBILIS, N., STAIGER, M.P.: *Corr. Sci.* 52, 2010, 287–291.
[12] BIRBILIS, N., EASTON, M. A., SUDHOLZ, A. D., ZHU, S.M., GIBSON, M. A.: *Corr. Sci.* 51, 2009, 683–689.
[13] GU, X.-N., ZHENG, Y.-F., CHENG, Y., ZHONG, S.-P., XI, T.-F.: *Biomater.* 30, 2009, 484–498.
[14] GRAY, J. E., LUAN, B.: *J. Alloys Compd.* 336, 2002, 88–113.
[15] CHEN, X.-B., BIRBILIS, N., ABBOTT, T. B.: *Corr. Sci.* 53, 2011, 2263–2268.
[16] SOUTO, R. M., MARIA, M. L., RUI, L. R.: *Biomater.* 24 (23), 2003, 4213–4221.
[17] SOUTO, R. M., MERCEDES, M. L., REIS, R. L.: J. *Biomed. Mater. Res.* 70A (1), 2004, 59–65.
[18] YAMAGUCHI, T., TANAKA, Y., IDE-EKTESSABI, A.: *Nucl. Instrum. Methods* B 249 (1–2), 2006, 723–725.
[19] AKSAKAL, B., GAVGALI, M., DIKICI, B.: *J. Mater. Eng. Perform.* 19 (6), 2004, 894–899.
[20] MAN, H. C., CHIU, K. Y., CHENG, F. T., WONG, K. H.: *Thin Solid Films* 517 (18), 2009, 5496–5501.
[21] YOUSEFPOUR, M., AFSHAR, A., CHEN, J., ZHANG, X.: *Mater. Sci. Eng.* C, 27 (5–8), 2007, 1482–1486.
[22] KAR, A., RAJA, K. S., MISRA, M.: *Surf. Coat. Technol.* 201 (6), 2006, 3723–3731.
[23] SOBIESZCZYK, S.: *Adv. Mater. Sci.* 10 (1), 2010, 19–28.
[24] LIU, X., CHU, P. K., DING, C.: *Mater. Sci. Eng.* R47 (3–4), 2004, 49–121.
[25] SAMEER, R. P., NARENDRA, B. D.: *Mater. Sci. Eng.* R66 (1–3), 2009, 1–70.
[26] BAN, S., HASEGAWA, J.: *Biomater.* 23 (14), 2002, 2965–2975.
[27] HU, H. B., LIN, C. J., HU, R., LENG, Y.: *Mater. Sci. Eng.* C20 (1–2), 2002, 209–214.
[28] JAMESH, M., KUMAR, S., SANKARA NARAYANAN, T. S. N.: *J. Coat. Technol. Res,* 2011, DOI 10.1007/s11998-011-9382-6 (on-line).
[29] SONG, G. L.: *Corr. Sci.* 49, 2007, 1696.
[30] SONG, Y., SHAN, D., CHEN, R., ZHANG, F., HAN, E. H.: *Mater. Sci. Eng.* C29 (3), 2009, 1039–1045.
[31] LOTHAR, T.: *Labor und Diagnose,* 5th ed., TH-Books, Frankfurt 2000.
[32] HADZIMA, B., BUKOVINA, M., DOLEZAL, P.: *Mater. Eng. - Mater. inz.* 17(4), 2010, 14–19.
[33] WITTE, F., KAESE, V., HAFERKAMP, H., SWITZER, E., MEYER-LINDENBERG, A., WIRTH, C. J.: *Biomater.* 26, 2005, 3557–3563.
[34] DAS, A., LIU, G., FAN. Z.: *Mater. Sci. Eng.* A419 (1-2), 2006, 349–356.
[35] KIRKLAND, N. T., STAIGER, M. P., NISBET, D., DAVIES, C. H. J., BIRBILIS, N. B.: *JOM* 63(6), 2011, 28-34.
[36] ASM Handbook, vol 9: *Metallography and Microstructures.* Ed: VANDER VOORT, G.F., ASM International, New York, 2004.
[37] EC-Lab Software User's Manual, version 10.1x – February 2011.
[38] LIPTAKOVA, T.: *Pitting Corrosion of Stainless Steels (in Slovak),* EDIS ZU v Ziline, 2009.

https://doi.org/10.26552/com.C.2012.4.31-36

Ivo Cerny – Dagmar Mikulova – Jiri Sis *

SHORT FATIGUE CRACK GROWTH IN A RESIDUAL STRESS FIELD IN A 7075 AL-ALLOY AFTER SHOT PEENING

The paper contains results of an investigation of effects of shot peening on growth of physically short fatigue cracks in a 2.4 mm thick sheet of an aircraft V-95 Al-alloy (a type of a 7075 alloy), clad with a 7072 Al-alloy (Al-Zn1). Using an improved and verified experimental methodology, particularly direct current potential drop (DCPD) method, short fatigue cracks of the length from 0.2 mm to more than 3 mm, most of them between 0.8 - 1.5 mm, were prepared under high cycle fatigue repeated tensile loading of the constant nominal stress range 160 MPa, load asymmetry R = 0. Edges of the specimens with already existing short fatigue cracks were then shot peened using two different groups of parameters. Some reference specimens without cracks were shot peened with the same parameters. Microhardness measurement and informative measurement of residual stresses near the peened edges were carried out. Significant retardation of crack growth was observed particularly in case of cracks shorter than 2 mm. The work was completed by a unique measurement of actual crack growth rate throughout the peened area with residual stresses starting with crack length less than 0.2 mm. Different stages of the growth are discussed.

Keywords: *Fatigue crack growth, short cracks, shot peening, residual stresses, 7075 Al-alloy*

1. Introduction

Shot peening is one of surface treatment methods applied to various metallic materials either separately or in a combination with other surface treatments like plating, hard anodising etc., in order to locally improve the performance of mechanical components under fatigue loads [1, 2]. This treatment creates compressive residual stresses that usually increase the operating life of the component. In order to perform an effective and reliable design, it is not namely adequate to consider only the in-service stress of the component. Unforeseen cracks can occur due to the fact that tensile residual stresses added to the in-service stress decrease the component life. On the contrary, a strong improvement can be achieved, if compressive residual stresses are induced in the components.

The final effect of shot peening on fatigue resistance depends on numerous parameters and material which the technology is applied to [3, 4]. If the technology parameters are not optimised for a specific material and for its basic structural and mechanical properties, shot peening may not be beneficial, fatigue resistance can even be deteriorated [5, 6]. Recent advanced approaches are based on the hypothesis that compressive residual stresses are able to slow down or stop crack propagation instead of preventing their initiation, and, therefore, they are based on main concepts of fracture mechanics. This approach is conditioned by the use of sophisticated experimental methods, particularly preparation of physically short fatigue cracks in specimens of reasonable dimensions suitable for shot peening applications and exact measurement of actual crack length including not only surface path but also an estimation of crack profile inside the specimen. Length of short cracks is usually measured optically (e.g. [7]), which however does not enable to assess the subsurface length. Complex crack growth measurement including subsurface profile, which is an essential condition of application of fracture mechanics approaches, is not an easy task, particularly if specimens are of quite big dimensions.

In the paper, results and analyses of an extensive experimental programme aimed at an evaluation of effects of shot peening applied to clad V-95 Al-alloy (7075 Al-alloy) sheets on growth and retardation of existing short fatigue cracks are presented and discussed.

2. Experimental material

The work was addressed to potential use in aircraft industry with the aim to investigate conditions of retardation of short or physically small cracks or crack-like defects using shot peening. Therefore, a V-95 Al-alloy, clad with Al-Zn1 (7072 Al-alloy) surface layers was selected as the experimental material.

The V-95 material is a Russian Al-alloy of Al-Zn-Mg type and due to its high mechanical properties and fatigue resistance, it has been widely used for aircraft structures, such as wings and fuselages, already for many years [8]. According to Russian GOST standard, the typical chemical contents of Zn is 5–7 weight %, Mg 2–3 %, Cu approximately 1.5 % and Mn 0.35–0.6 %, whereas chemical composition affects quite strongly the material harden-

* **Ivo Cerny, Dagmar Mikulova, Jiri Sis**
SVUM a.s., Praha, Czech Republic, E-mail: Ivo.Cerny@seznam.cz

ability [9]. A similar US type of the material is represented by a 7075 Al-alloy with just slightly lower content of Zn and Cu. Typical values of basic mechanical properties of this material at heat-treated conditions are: strength up to 550 MPa and yield stress up to 480 MPa.

The V-95 alloy was available in the form of sheets of the total thickness 2.4 mm including both cladding layers (both surfaces) of the thickness 0.07 mm each in Aeronautical Research and Test Institute in Prague, where specimens also were manufactured.

3. Experimental programme

The experimental programme contained the following steps:

- preparation of series of a sufficient, representative number of specimens with physically short fatigue cracks of different lengths from 0.35 mm to 3.6 mm,
- shot peening of the specimens with short cracks, using two groups of parameters,
- characterisation of bulk material and shot peened layers in terms of deformation of the microstructure, microhardness and informative assessment of residual stresses,
- evluation of residual fatigue life of the shot peened specimens with pre-existing short fatigue cracks,
- evalution of fatigue life of specimens with no pre-cracking, both shot peened and without peening and, eventually,
- evaluation of actual growth rate of a short crack growing throughout the peened area with residual stresses.

The specimens were of quite big dimensions given by material availability, namely material sheets of the thickness 2.4 mm, and technological reasons of the shot peening application. Flat specimens of the total thickness 2.4 mm, total length 200 mm and basic width at gripping area 48 mm were manufactured. To localise the area of crack initiation and to enable subsequent shot peening of specimen edges, shallow necking was made from both the specimen sides. The necking radius was 28 mm; the minimum width at the specimen centre was 24 mm.

Using the adapted and verified methodology of short crack measurement by DCPD method, described in [10–13], fatigue cracks of different length between 0.35 mm and 3.6 mm were prepared in 17 specimens, whereas the length of most of the cracks was between 0.87 mm and 1.49 mm (9 specimens). The work programme was performed on the resonance SCHENCK PVQA machine. The loading was of sinusoidal repeated type (load asymmetry $R = 0$) of the constant nominal stress range 160 MPa, load frequency around 17 Hz. These load conditions were uniform for all the specimens. Artificial microscopic notches of dimensions less than 0.05 mm were made on the specimen edges to accelerate the microscopic crack initiation period.

After pre-cracking, the specimens were divided into two groups, each of them containing a similar spectrum of cracks lengths so that the groups could be compared to each other. Shot peening of two different parameters was applied at Technometra Radotín a.s. to the first and second group, respectively. Parameters of the shot peening were: Shot sizes 0.43 – 0.7 mm and 0.21 – 0.32 mm for the first group and second group, respectively, Almen intensity $A = 0.25$ and $A = 0.14$ for the first and second group respectively. Shot peening angle was 60° and coverage 200% for both the groups. Both edges in the central area of specimens were shot peened from both sides to the distance of 4 – 4.5 mm or so from the edge. Shot peening area can be seen in Figs. 1 and 2.

The shot peened layers were characterised using metallographic analysis with an optical microscope Neophot 32 with a digital image processing, microhardness measurement using Hanemann device and informative measurement of residual stresses performed on the basis of a gradual measurement of strain changes with a Hottinger Baldwin Messtechnik strain gauge unit HBM UPM 60 during a gradual grinding material layers off.

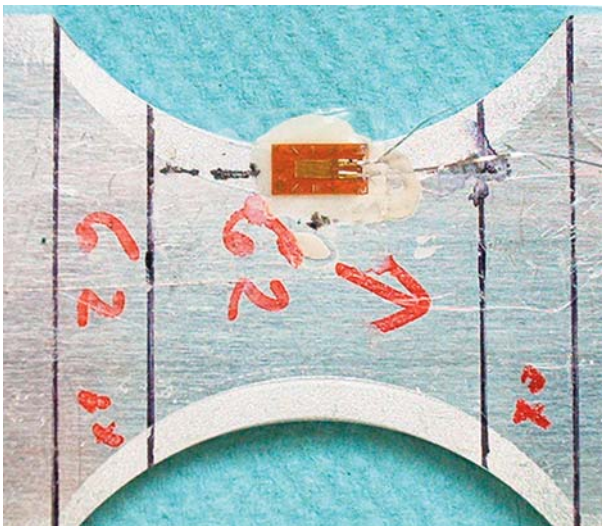

Fig. 1 Position of strain gauge at the centre of specimen with more severe shot peening

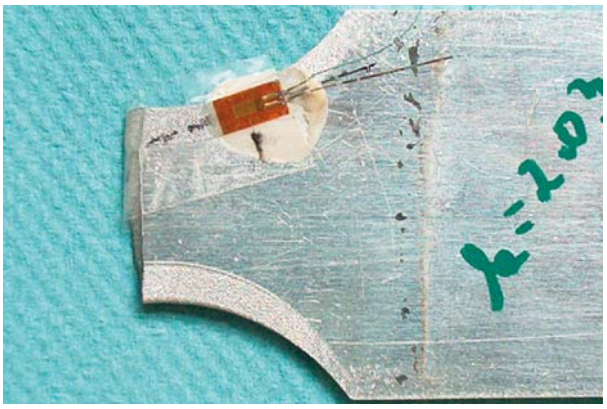

Fig. 1 Inclined position of strain gauge outside the centre of specimen with less severe shot peening

The microhardness measurement HV 0.04 was performed in cross sections of two selected specimens treated with the two different peening parameters in the following areas: (i) near the shot peened clad specimen surfaces, i.e. at four different areas near each of the shot peened bands, (ii) near both the specimen edges where the cladding layer was absent and (iii) near the untreated clad surface for a comparison.

The method of assessment of the residual stress has to be described more in detail. Two specimens representing the two groups of shot peening parameters were equipped with a single strain gauge glued either in the centre of the shot peened area in the longitudinal direction – Fig. 1 (specimen with less severe peening parameters) or near the specimen centre in the inclined angle – Fig. 2 (more severe parameters), since no uncracked specimen was available in the latter case. After connecting the strain gauge device, the strain value was set to zero. The opposite surface of the specimen, which also contained the shot peened area, was then gradually ground off with steps of approximately 0.2 mm followed by strain recording. The remaining thickness of the material at the last step only was about 0.15 mm. It could be therefore anticipated that original surface stresses were almost completely released and the final measured strain corresponded to this relaxation. It should be noted that the complex residual stress state near the edge, which was shot peened at both surfaces, was very complicated. Therefore, using the described simplified strain measurement, it could be assessed just informatively. However, the measurement provided at least some qualitative and partially quantitative results in terms of longitudinal residual stresses, most important from the viewpoint of fatigue crack initiation and early stages of growth.

Residual fatigue life of specimens containing the physically short fatigue cracks after shot peening was evaluated using the same loading conditions as those used for the precracking. Eventually, a sophisticated measurement of actual short crack growth throughout the shot peened area from its beginning was carried out.

4. Results and discussion

Microstructure analyses were carried out particularly in order to characterize the surface layers after shot peening. As expected, the shot peening effect on local surface and subsurface microstructure deformation was stronger for the first group of parameters, i.e. higher Balottini sizes and higher Almen intensity. A boundary area between shot peened and untreated surface is shown in specimen cross section in Fig. 3. It is evident that particularly the cladding layer was strongly deformed and compacted by the peening, resulting in numerous microscopic dimples, pits and also microcracks. On the other hand, it looks that the kinetic energy of the Balottini particles was accumulated through the plastic deformation in the cladding layer – no deformation of the microstructure under the layer was observed either in case of more severe or less severe peening. Some deformation of grains of the basic material, just slight, was observed just near the edges where cladding layer was absent – Fig. 4.

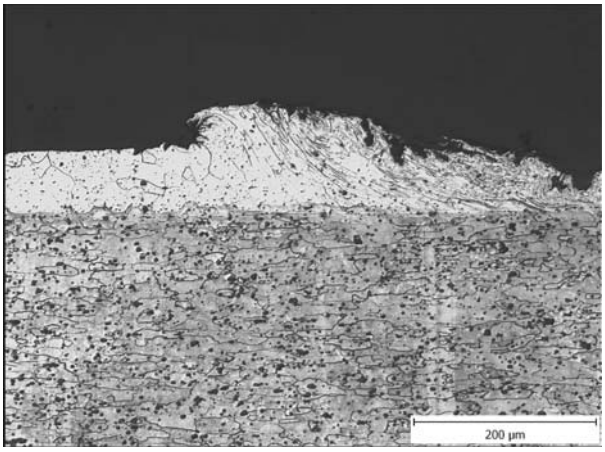

Fig. 3 Microstructure near boundary area between shot peened and untreated surface, more severe peening

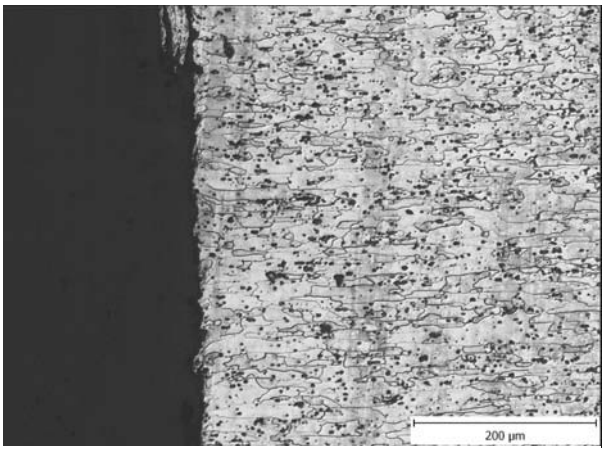

Fig. 4 Slight deformation of grains near the specimen edge, more severe peening

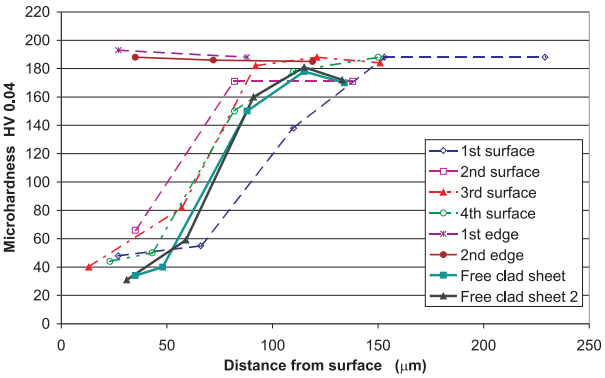

Fig. 5 Dependencies of microhardness on depth in specimen peened with more severe parameters

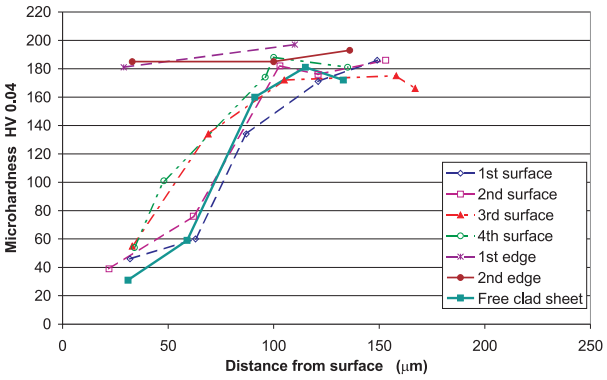

Fig. 6 Dependencies of microhardness on depth in specimen peened with less severe parameters

Results of microhardness measurement in specimens treated with the more and less severe parameters are shown in Figs. 5 and 6, respectively. The fact that there is no distinct surface or sub-surface hardening caused by the shot peening, either near the clad surface or near the specimen edge without the cladding layer, is rather surprising – shot peening usually does result in surface hardening, particularly in steels [14].

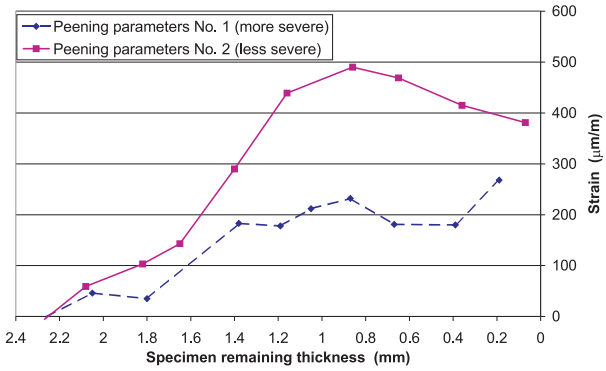

Fig. 7 Strain values recorded as a dependence on specimen remaining thickness during grinding material off

The diagram of strain values recorded as a dependence on the specimen remaining thickness, when the material was ground off from the surface opposite to that with the strain gauge, is in Fig. 7. One could expect that the more severe treatment will result in higher strain values. Some explanation could be found in the fact that the measurement was not carried out at the same surface point – the position of the strain gauge on the specimen peened with the more intensively was outside the centre as mentioned above (Fig. 2).

As regards the strain values after the material relaxation (stress release) at the final step (residual thickness 0.15 mm) namely 270 and 380 μm/m, respectively, considering the E-modulus 72 GPa, the strain values would correspond to compressive stresses of 19 and 27 MPa, respectively, if the simplified conditions are accepted. It is not too much, but on the other hand, considering the fact that the applied maximum stress of 160 MPa was quite close to the material fatigue limit [15], even small changes of surfaces residual stresses to negative values resulting eventually in a reduction of the overall maximum stress can affect fatigue life quite significantly. It should be mentioned once more that the quantitative assessment can be considered just as informative.

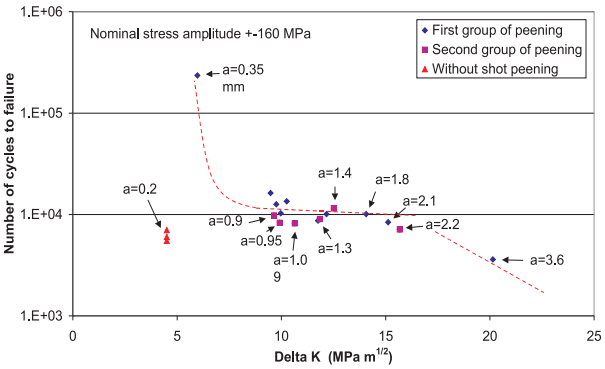

Fig. 8 Residual fatigue life as a dependence on stress intensity factor range and crack length

Survey of residual fatigue life of the pre-cracked specimens after application of shot peening in comparison with untreated specimens is shown as a dependence on stress intensity factor range ΔK in Fig. 8. The K-factor was calculated disregarding the short crack effects, i.e. the standard formula for long cracks was used. As regards the fatigue life of specimens without shot peening, tested to failure at the same stress amplitude, the total life was much longer, not only between 5000 and 8000 cycles as shown in Fig. 8. The experimental points of these three specimens namely correspond just to the crack growth stage starting with the length 0.2 mm, i.e. $\Delta K = 4.5$ MPa $m^{1/2}$, which could be reliably detected and measured by the DCPD method.

It follows from Fig. 8 that the retardation effect resulting from shot peening was quite significant. In the region of crack length between 1 and 2 mm, ΔK between 10 and 15 MPa $m^{1/2}$, the residual life is always longer than that of the unpeened specimens with the crack length just 0.2 mm. The slightly higher retardation effect of the more severe shot peening (the first group in Fig. 8) particularly on short crack of length less than 1.5 mm can be attributed to the more homogeneous distribution of the compressive residual stresses indicated in Fig. 7.

Similar effects of strong retardation of short fatigue cracks in compressive residual stress fields were described e.g. in [16 and 17]. In [17], shot peened Al 7475 alloy under fatigue loading was studied. Retardation of physically short fatigue cracks in the field of compressive residual stresses was also described in [18], though the cracks initiated by fretting fatigue in that case.

There is another interesting effect in Fig. 8, namely the plateau between ΔK 10 and 15 MPa $m^{1/2}$ (crack length between 0.8 and 2.0 mm), where the residual fatigue life is almost constant. The detailed measurement of actual crack growth rate from its beginning in the field of residual stresses indicated some reasons for this phenomenon – Fig. 9.

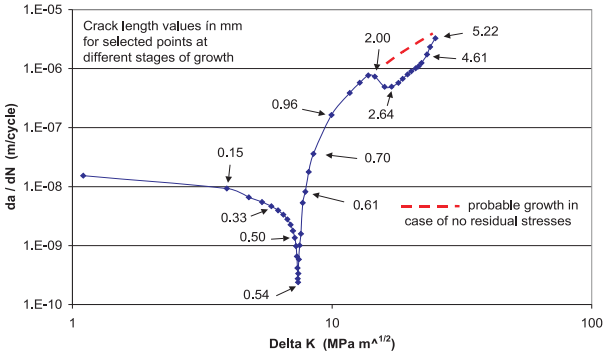

Fig. 9 Short crack growth rate in the field of residual stresses

The measurement in Fig. 9 was performed on a specimen peened with the less severe parameters. In spite of that the modified DCPD method, suitable for short cracks was used to record the short crack growth [10–13, 19], DCPD values were recorded continuously to eliminate scatter and make the measurement even more precise. There was no artificial initiator at the edge, the crack initiated spontaneously. The growth process in Fig. 9 can be divided into four stages: (i) initiation and growth of physically short crack, ending at the crack length approximately 0.6 – 0.7 mm, (ii) relatively short period of a more or less regular growth up to the length 1.9 – 2.0 mm, (iii) retardation period ending at the length 4.5 mm and (iv) final acceleration approaching the regular long crack growth again. It can be anticipated that the first progressive retardation with the minimum growth rate at the length 0.54 mm (ΔK = 7.4 MPa $m^{1/2}$) is caused more by the short crack phenomenon than by compressive residual stresses – it corresponds to the transient period between crystallographic and K_I mode of growth. This transient period ends at the crack length approximately 0.7 mm (ΔK = 8.5 MPa $m^{1/2}$). The second significant retardation is likely caused by compressive residual stresses, which are probably greatest in the shot peened area, near the boundary between the peened and unpeened areas. The shift of effective ΔK value in the diagram corresponds to 30 %. Considering the stress range $\Delta\sigma$ = 160 MPa and load asymmetry R = 0, the compressive residual stresses would correspond to – 50 MPa. It is about 65% more than the longitudinal residual stresses, which were actually measured. It is, however, likely that the point at the centre of the shot peened band, where the strain gauge was bonded (Fig. 1), is not exactly identical to the point of maximum residual stresses near the peened boundary line according to Fig. 9.

5. Conclusions

An experimental investigation of an effect of quite severe shot peening with two different groups of parameters on subsequent retardation and further growth of physically short fatigue cracks to failure in 2.4 mm thick aircraft V-95 Al-alloy sheets (a type of a 7075 alloy), clad with a 7072 Al-alloy (Al-Zn1) was carried out. The significant part of the work was a measurement of actual growth rates of a crack growing throughout the peened area from its beginning, from the length less than 0.2 mm. The main conclusions can be summarised as follows:

- Physically short fatigue cracks of the length from 0.2 mm to more than 3 mm, most of them between 0.8 – 1.5 mm, were prepared under high cycle repeated fatigue loading (load asymmetry R = 0) of the constant maximum stress 160 MPa. Crack growth after shot peening was measured and compared with crack growth in specimens without shot peening. Retardation of crack growth was significant particularly for cracks shorter than 2 mm. Some minor differences between the two groups of shot peening parameters were ascertained.
- Metallographic analyses of surface and subsurface microstructure confirmed an extensive plastic deformation of the peened layer localised in the cladding layer. The bulk material microstructure remained undeformed. The basis microstructure was slightly deformed just in the area of the absence of the cladding layer.
- No surface and subsurface hardening was observed either in the cladding layer or basic material. The increase of residual fatigue life of specimens with preliminary cracks and total fatigue life of specimens without cracks was therefore attributed just to the compressive residual stresses.
- A simplified residual stress measurement indicated significant differences in the through thickness residual stress relief between specimens peened with the two different parameters. A presence of surface or subsurface compressive residual stresses was confirmed.
- There were two retardation periods in the short fatigue crack growth rate diagram, the first one caused probably mostly by the short crack phenomenon, the second one, when the crack front approached the boundary line between the shot peened and unpeened areas, probably by longitudinal compressive residual stresses.

Acknowledgements

The work was carried out under the support of Ministry of Education, Youth and Sports of Czech Republic, grant MSM 2579700001.

References

[1] VOORWALD. H. J. C., SILVA, M. P., COSTA, M. Y. P., CIOFFI, M. O. H.: *Fatigue Fract. Eng. M.*, 32, 2009, 2, 97
[2] CAMARGO, A., VOORWALD, H. J. C.: *Fatigue Fract. Eng. M.*, 30, 2007, 11, 993
[3] RODOPOULOS, C. A., CURTIS, S. A., DE LOS RIOS, E. R., SOLIS, R. J.: *Int. J. Fatigue,* 26, 2004, 8, 849
[4] HATAMLEH, O., LYONS, J., FORMAN, R.: *Fatigue Fract. Eng. M.*, 30, 2007, 2, 115
[5] NOVY, F., CHALUPOVA, M., CINCALA, M., BOKUVKA, O.: *Acta Mech. Slovaca,* 11, 2007, 4, 189
[6] NOVY F., BOKUVKA, O., CHALUPOVA, M., VALOVICOVA, V.: *Acta Mech. Slovaca,*12, 2008, 4-B, 209
[7] KUBENA, I., KRUML, T., HUTAR, P., NAHLIK, L., SEITL, S., POLAK, J.: *Fatigue Properties of Eurofer Steel Developed for Fusion Application.* In: Proc. of the 18th Int. Conf. on Metallurgy and Materials METAL 2009 – Symposium C, Tanger s.r.o. Ed., Ostrava, 2009, 125
[8] KARLASHOV, A. V., GAINUTDINOV, R. G., GOLUBNICHII, A.V.: *Mater. Sci+*, 11, 1976, 1, 100
[9] ZAKHAROV, E. D., PETROVA, A. A., ZHIKHAREV, YU. V., SAVELOVA, N. M.: *Met. Sci. Heat. Treat+*, 5, 1963, 12, 696
[10] CERNY, I.: *Eng. Fract. Mech.,* 71, 2004, 4–6, 837
[11] CERNY, I.: *Int. J. Pres. Ves. Pip.*, 78, 2001, 11–12, 893
[12] CERNY, I.: *Procedia Engineering,* 10, 2011, 3411
[13] CERNY, I., SIS, J., MIKULOVA, D.: *Surf. Coat. Technol.,* 2012, doi:10.1016/ j.surfcoat.2012.06.008 (in press)
[14] AZAR, V., HASHEMI, B., YAZDI, M. R.: *Surf. Coat. Technol.,* 204, 2010, 21–22, 3546
[15] ASM Aerospace Specification Metals Inc., Aluminum 7075-T73; 7075-T735x, http://asm.matweb.com/search/SpecificMaterial.asp?bassnum=MA7075T73
[16] MAJZOOBI, G. H., AHMADKHANI, A. R.: *Surf. Coat. Technol.*, 205, 2010, 1, 102
[17] GAO, Y. K., WU, X. R.: *Acta Mater.,* 59, 2011, 9, 3737
[18] LINHART, V., CERNY, I.: *Eng. Fract. Mech.,* 78, 2011, 5, 731
[19] CERNY, I.: *The Use of DCPD Method for Measurement of Growth of Physically Short Fatigue Cracks.* In: Proc. of the 1st Int. Conf. on Recent Trends in Structural Materials COMAT 2010, COMTES FHT a.s. Ed., Plzen, 25–26 November 2010, 242.

https://doi.org/10.26552/com.C.2012.4.37-42

Tatiana Liptakova – Jozef Jandacka – Milan Malcho – Michaela Vojsovicova *

CORROSION-EROSION WASTE OF METALS IN THE DUCT SYSTEM OF THE RECYCLING ALUMINIUM FURNACE

The corrosion aggressiveness of the environment in the recycling aluminium furnace duct system is very high. Temperature is in the range from 300 to 900 °C and chemical composition of combustion varies according to treated aluminium waste and flue gas flow is turbulent. These conditions are very complicated for construction metal selection. The aim of the work is to investigate corrosion-erosion behaviour of various construction metals in the operating conditions of the duct system. The metals with different chemical composition (unalloyed construction steel, stainless steel and nickel based alloy) were tested by long time experiment in the real work conditions of the recycling aluminium furnace. The character and intensity of the materials corrosion attack after one year exposition are evaluated by gravimetric and metallographic analysis.

Keywords: *High temperature corrosion, fuel gas, recycling furnace, erosion*

1. Introduction

The corrosion aggressiveness of the environment in the duct system of the recycling aluminium furnace is caused by fluctuation of combustion chemical composition. It is because aluminium waste contains remains of various materials (oxygen, carbon oxides, steam, sulphides, halides etc.). At high temperature can very diverse compounds can be created and it makes impossible to define chemical composition of environment. This fact very strong restricts choice of metal and prediction of their corrosion behaviour [1].

Corrosion rate of metals is expressly influenced by temperature and chemical composition of environment because both factors affect character of corrosion products. The average temperature throughout the duct system is from 800 °C to 300 °C. The heat flux influences oxidation behaviour of metals. Fast oxidation produces thicker oxides with more pores and worsens adhesion [2–3]. The function of deposits is not negligible too. The higher temperature region experienced severe deposit-induced corrosion or hot corrosion, where the melting temperature of the deposits was 524–683 °C. A thick deposit could decrease corrosion rates by reducing surface temperatures, protecting it from further active oxidation and preventing the volatilization of metal chlorides. However, this is valid only if the deposit has not melted [2]. Also structural changes of materials can occur in these conditions, e. g. precipitation of carbides or other phases in stainless steels increases sensitization to intergranular corrosion, decarburization of surface layers in unalloyed steel changes their mechanical properties [4–6]. The corrosion damage is supported by solid particles erosion in flue gas. The average rate of the turbulent flue gas flow is approximately 5 m. s^{-1}.

The chemical composition of environment is responsible for character of resultant corrosion products. Present oxygen creates with Fe alloys (low or high alloyed) oxides mostly with protective character and especially with the elements Cr, Al, Si. The sulphur compounds (H_2S, SO_2) are unwanted because sulphides do not have protective properties, create eutectics and increase corrosion rate. Halides (Cl-, F-) freeing during Al waste combustion are very aggressive corrosive agents and support corrosive effect of sulphur compounds too [7 and 1]. During the reclaim process, besides the mentioned agents, other components present can produce e. g. carbon and nitrogen oxides, dust gases, organic compounds (VOC – volatile organic compound, dioxin). The mentioned compounds increase corrosion aggressiveness of the work environment. The next factors affecting corrosion and mechanical properties of Fe and Ni alloys in the duct system are hydrogen, CO, hydrocarbons [6, 1 and 8]. Consequently high-temperature corrosion in so complicated conditions can be amplified by a range of factors: chemical composition of flue gas erased in the Al produced furniture; fluctuations in the flue gas flow; the high velocity, particle-bearing flue gas; and finally deposit (combustion residues) accumulation [9 and 11].

2. Experimental part

Experimental material

Because of impossibility to specify exactly the chemical composition of the work environment in the duct system of the recycling Al furnace, three types of alloys were chosen for the experiment in the real conditions. The experimental material was chosen according to actual science references [2, 9 and 10] and experiences of

* **Tatiana Liptakova[1], Jozef Jandacka[2], Milan Malcho[2], Michaela Vojsovicova[1]**
[1] Department of Materials Engineering, Faculty of Mechanical Engineering, University of Zilina, Slovakia, E-mail: tatiana.liptakova@fstroj.uniza.sk
[2] Department of Power Engineering, Faculty of Mechanical Engineering, University of Zilina, Slovakia

Chemical composition of the experimental material Tab. 1

Element (wt. %)	Cr	Ni	Mo	Mn	N	Ti	C	Si	P	S	W	Co	Fe
AISI 316Ti	16.5	10.6	2.12	1.69	0.012	0.41	0.04	0.43	0.026	0.002			rest
STN 41 1357					0.009		0.17		< 0.045	0.045			rest
Ni based alloy	1.88	71.47	7.30	0.09		1.075	< 0.001	< 0.001			9.5	7.98	rest

operator: unalloyed steel (STN 41 1357.21), stainless steel (AISI 316Ti) and Ni based alloy. The chemical composition of experimental material is in Tab. 1.

Experimental specification

The experimental samples were fastened to the wall of the duct system and exposed one year in real operating conditions of the aluminium furnace. Before the experiment the samples were mechanically cleaned, ungreased by ether and after drying weighed with the accuracy 10^{-5} g. The first sample set was situated in the duct system inlet where temperature varies from 650 to 850 °C, and the second sample set was situated in the duct system exit where the temperature varies from 250 to 300 °C as it can be seen in Fig 1. The direction of flue gas flow is marked by arrows in the same picture. The real temperature history during operation in the duct system is in Fig. 2.

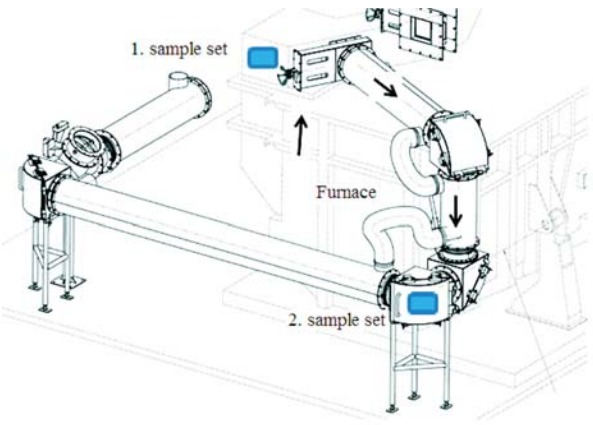

Fig. 1 Scheme of the furnace, location of samples and direction of gas flow

3. Results and discussion

After one year exposition the weight losses were measured and corrosion rate calculated. Character and intensity of corrosion attack was investigated by light microscopy and visually.

Weight loss analysis

The results of our experiment confirmed very high aggressiveness (chemical composition, flow and temperature) in the duct system inlet of the alumina furnace. The samples localized in the duct system inlet after 1 year of exposition disappeared and it means that in this part of the duct system the metal is very strongly damaged by corrosion and erosion. Only negligible rest of unalloyed steel remained under the fixing screw. The damage of the metals tested in the same condition for 30 days confirmed higher corrosion – erosion effect in the duct system inlet in comparison with outlet too [10]. Norling et al [9] investigated the erosion-corrosion behaviour of two steels AISI 304, 353 MA) and one Ni-based super alloy (Inconel 625). The alloys were exposed in a test rig at 550 °C in air for 1 day, 1 and 3 weeks. The particle velocity was 1.2 m/s. The measured wastage of the alloys was in the range 58–270 μm/1000 h. [9]. According to our investigation the original thickness of the unalloyed steel was 8 mm, stainless steel 3 mm and Ni based alloy 4 mm. It means that in the duct system inlet is cor-

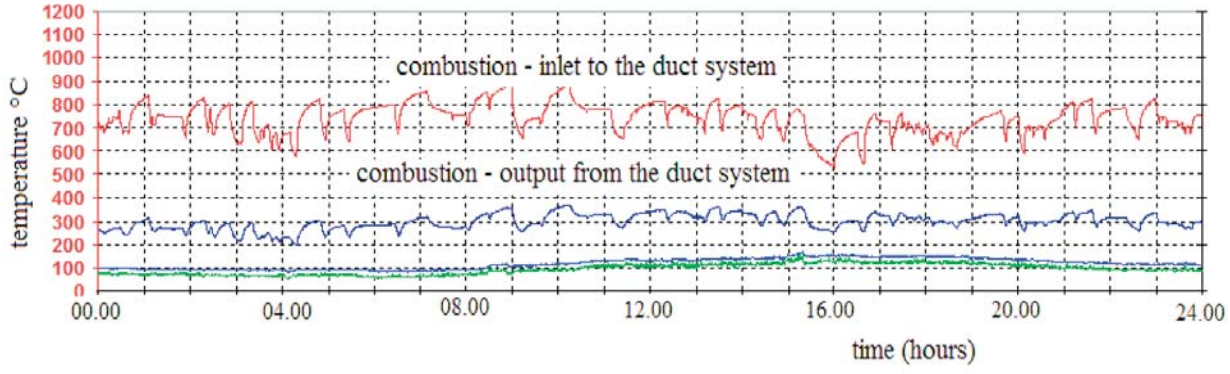

Fig. 2 Time diagram of temperature history during 24 hours operation in the duct system

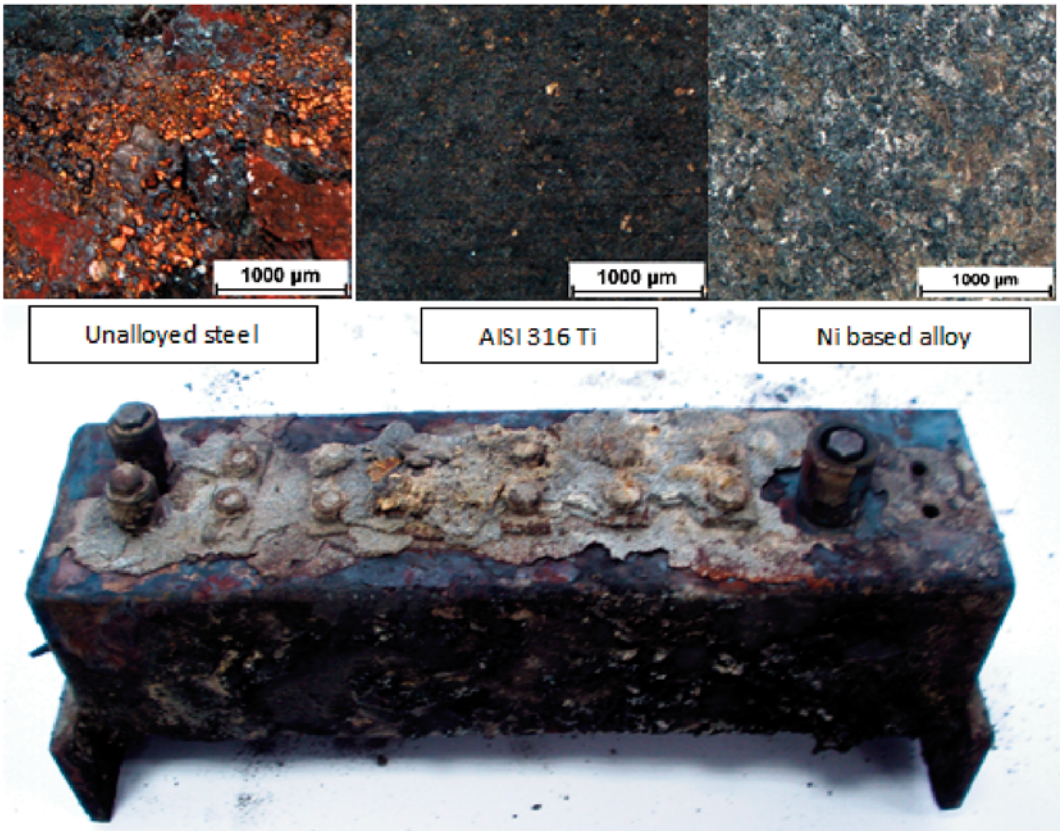

Fig. 3 Deposits on the tested sample in the duct system after exposition and surfaces of the tested metals after deposit removing

rosion-erosion wastage of unalloyed steel 913 µm/1000 h. and Ni based alloy 456 µm/1000 h. According to the results in the outlet, the stainless steel corrosion-erosion wastage is approximately 600 µm/1000 h. The samples fixed in the duct system outlet were covered by the thick layer of deposits (Fig 3). The deposits in this part of duct system create a partial protection mainly to erosion because the deposits content pores and cracks where corrosion agents have access. But they are during furnace operation two times in a year removed for heat transfer. The surfaces of the tested materials after deposit removing are in Fig. 3.

After removing the deposits of unalloyed steel under the inhomogeneous deposits there were strong adhering dark grey-brown corrosion products. Corrosion products created at high temperature have protective effect. The deposits were mechanically removed and the corrosion products were chemically eliminated in the solution of the 20% HCl + 3.5 g hexamethylenetetramine per dm^3 of the solution for 3 minutes at temperature of 22 °C. The samples were in the initial shape and it demonstrates that on the both sites of the duct system there were different operating conditions. The cleaned and dried samples were weighted again. From the weight differences before and after exposition the weight losses per the area were calculated (v_k). The corrosion attack depth is substantiated from metalography investigation. The gravimetric analysis results are presented in Tab. 2 as well as average depth of attack

Weight losses of unalloyed steel are higher in order in comparison to stainless steel and high Ni based alloy. But the total depth of the stainless steel and high Ni alloy corrosion is not clear from the weight analysis. To take the weight analysis results into consideration it can be said that corrosion resistance of the tested metals is significantly different.

Rate and depth of corrosion attack after exposure Tab. 2

Sample	v_k (g. $m^{-2}y^{-1}$)	Depth of corrosion attack (µm)
STN 426317.31 41 1357	144.00	10
AISI 316Ti	24.00	20
High alloy Ni	11.40	15

Microscopic analysis

The samples were cross-cut, sealed to resin, grinded, polished and etched. On the prepared samples the structure, character and intensity of corrosion attack are investigated. s. The corrosion attack after 1 year exposition in the aluminium furnace was investigated on the etched samples (the unalloyed steel by the Nital,

the stainless steel by the Rollings ($CuCl_2$ + HCl + ethanol/, the Ni based alloy by the BR (HNO_3 + HF + glycerine). The differences of corrosion attack intensity determined by gravimetric and microscopic analysis are caused by different corrosion behaviour of the tested metals.

The samples of unalloyed steel are attacked by general corrosion started on the grain boundaries. The high temperature oxides are brittle and during operation cracks are created and it makes possible access of corrosion agents to bare metal [12]. Corrosion damage of the unalloyed steel surface is supported by mechanical effect of the flue flow containing solid particle (Fig. 4). In the depth about 100 μm from the surface light decarburization is observed. In Fig. 5 it can be compared damage of the same material after 30 days in the duct system inlet. Higher temperature causes stronger corrosion attack, decarburization (about 200 μm) and increment of the grains in the place where the sample was deformed. High temperature can change in the metals: structure, various phase formation, corrosion thermodynamics and kinetics, character of corrosion products and deposits. The actualities intensively worsen corrosion-erosion damage of material in the duct system inlet.

The corrosion products of the AISI 316Ti after one year exposure in the duct system outlet were inhomogeneous of dark grey colour with good adhesiveness. By microscope analysis the general inhomogeneous corrosion was identified (Fig. 6a). The corrosion attack of the steel AISI 316Ti after 30 days of exposition in the duct system inlet is shown in Fig 6b. Under the deposits the passive layer ability of renovating is reduced and the cracks are present in oxide film The corrosion starts on the grain boundaries and the grains are removed by corrosion-erosion effect. The changes in the oxide layers during high-temperature oxidation were determined by Norling et al [9]. They identified oxide crushes and cracks on the surface of oxide layers. It is concluded that only the oxide scale is eroded and that the erosion takes place by chipping of small fragments from the oxide surface. The energy of the bombarding particles is not high enough to remove the oxide down to the oxide/metal interface. The thin oxide is free of cracks and pores and covers the

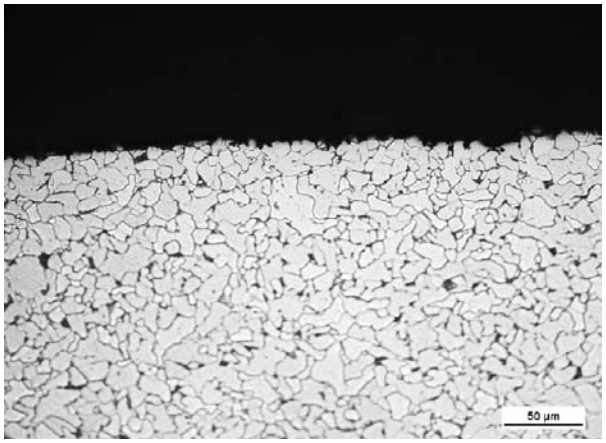

Fig. 4 Surface of the steel STN 41 1357.21 in the duct system outlet after 1 year exposition, mag.400, etch.Nital

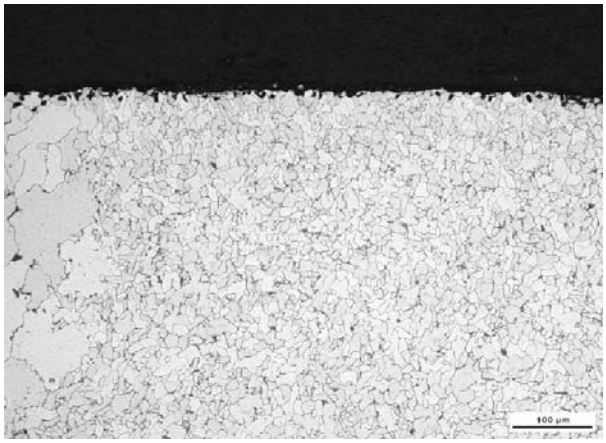

Fig. 5 Surface of the steel STN 41 1357.21 in the duct system inlet after 30 days exposition, mag. 200, etch.Nital

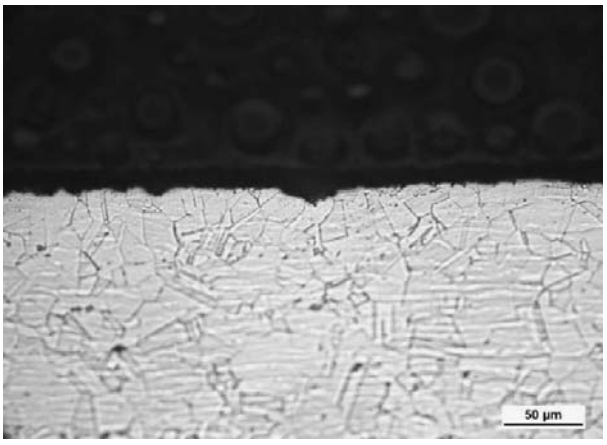

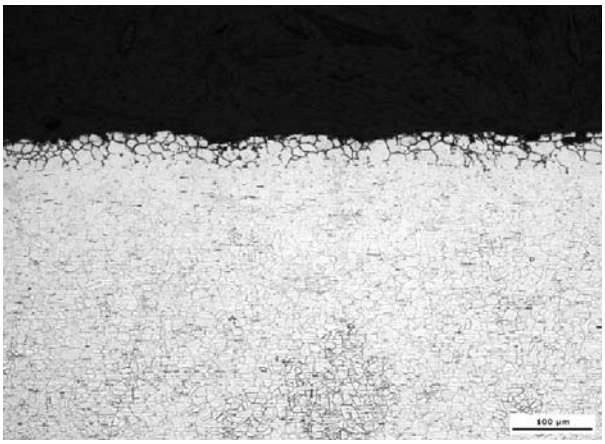

Fig. 6 Damage of the AISI 316Ti after 1 year exposition in the duct system outlet (a), mag. 400, and after 30 days in the duct system inlet (b), mag. 200, etch. Rollings

surface entirely [9 and 3]. It is supposed that the aggressive agent from the flue gas penetrates to the bare metal and it starts corrosion preferentially in the grain boundaries area.

The nickel-based alloys had lower corrosion rates than the iron-based alloy in combustion environment at higher temperature. They were, however, more prone to localised corrosion, most notably from alkali-metal chlorides, and had a lower resistance against pits and crevices [9]. The Ni based alloy shows after our experiments the best corrosion-erosion properties in comparison with unalloyed and stainless steel. The corrosion products of the Ni based alloy are dark grey colour with good adhesiveness. Local corrosion reaches only a few μm under the surface as it can be seen in Fig. 7. Occasionally in subsurface the grain boundary oxidation was observed. Our results are in very good agreement with the results published in [9] and [11] where authors investigated wastage of similar materials at high temperature.

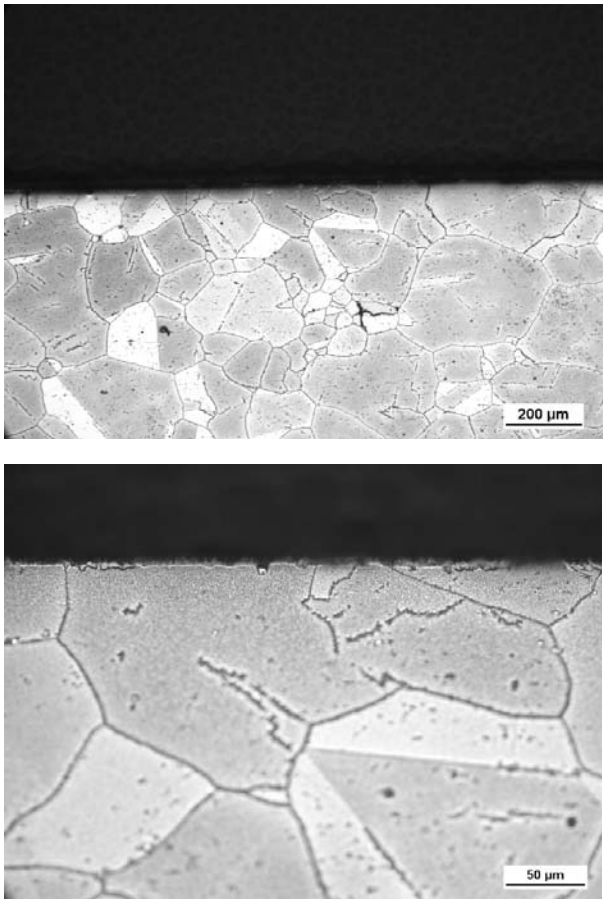

Fig. 7 Corrosion-erosion damage of the high Ni alloy after 1 year exposition in the duct system outlet, mag. 100, and mag. 400 etch. BR

4. Conclusions

On the basis of realized experiments and analyses, we concluded:

- All the tested materials were damaged by various intensity of corrosion-erosion in the duct system inlet and outlet. In the duct system inlet the average temperature is about 800 °C and it enhances corrosion rate and changes behaviour of the deposits. The samples from the inlet with the thickness between 3 and 8 mm were completely damaged. This fact indicates the very high aggressiveness of the environment in the duct system inlet.
- The temperature drop in the duct system outlet (about 300 °C) presents decreasing of the testing metal materials wastage lower by two orders.
- According to the weight analysis results the best corrosion-erosion resistance has the Ni based alloy, Cr-Ni alloyed steel has two times lower and unalloyed steel has about ten times lower than stainless steel.
- Corrosion-erosion attack depth of the tested materials in the duct system outlet evaluated by microscopy is negligible after one year of exposition.
- The different corrosion-erosion damage in the inlet and outlet of the duct system suggest variouscorrosion mechanism and kinetics caused by different temperature.
- Grain thickening at the surface areas occurred only in unalloyed materials in the duct systeminlet, especially in steel deformation locality. Strain tension in this area is reduced by recrystallization at high temperature.

The experimental results can help as an effective tool for duct system material selection. The metals selection for the duct system construction has to be made with respect to production efficiency. Therefore it is necessary to take into consideration not only corrosion-erosion resistance but the price of material too.

Acknowledgement

This research was supported partially by the grant VEGA No. 1/0066/11. Authors gratefully acknowledge this support.

References

[1] MOLNAR, L., VIRCIKOVA, E.: Charakteristika emisii znecistujucich latok z technologie pretavovania hlinikových odpadov [*Characteristics of Pollutant Emission from the Remelting Aluminium Waste Technology*], *Acta Montanistica Slovaca,* vol. 10, No. 1, 2005, pp. 220–23.

[2] HOWES, T. E., ROGERS, P. M., LITTLE, J. A., HUTCHINGS, I. M.: Erosion-corrosion of Mild Steel in a Temperature Gradient, *Wear1 86187*, 1995, pp. 316–324

[3] ENTWISLE, M. J., GIBB, J., HUTCHINGS, I. M., LITTLE, J. A., MEADOWCROFT, D. B., NINHAM A.J., OAKEY J. AND SIMMS N.: In E. Bachelet et al. (eds.), The Laboratory Simulation of Fluidized Bed Tube Wastage, *High Temperature Materials for Power Engineering,* Kluwer, Dordrecht, 1990, pp. 239-248.
[4] PHONGPHIPHAT, A, RYU, CH, YANG, Y. B. A, FINNEY, K. N., LEYLAND, A., SHARIFI, V. N., SWITHENBANK, J., DAVIS, J. R: *ASM Speciality Handbook, Heat Resistant Materials,* USA, ISBN 0871705966, 1997.
[5] BIRKS, N. et al: *High Temperature Oxidation of Metals,* 2nd edition, Cambridge University Press, 2006, ISBN-13 978-0-521-48042-0
[6] KHANA, A., S.: *High Temperature Oxidation and Corrosion,* ASM International, USA 2002, ISBN 0-87170-762-4.
[7] HADZIMA B., LIPTAKOVA, T.: *Zaklady elektrochemickej korozie kovov* [*Fundamentals of Electrochemical Metal Corrosion*], EDIS ZU Zilina, 2008. ISBN 978-80-8070-876-4.
[8] CERNY M. et al: *Korozni vlastnosti kovovych konstrukcnich materialu* [*Corrosion Properties of Metal Construction Materials*], SNTL Praha, 1984.
[9] NORLING, R., OLEFJORD, I.: *Erosion–Corrosion of Fe- and Ni-based Alloys at 550 °C*, Wear 254, 2003, pp. 173–184.
[10] LIPTAKOVA, T., MALCHO, M., JANDACKA, J.: Corrosion Behaviour of Chosen Construction Metals in the Duct System of the Recycling Aluminium Furnace, *Material Engineering*, vol. 17, No. 3, 2010, pp. 28–34.
[11] PHONGPHIPHAT, A., CHANGKOOK, RYU YAO, BIN, YANG, FINNEY, K. N., LEYLAND, A., SHARIFI, V. N., SWITHENBANK, J.: Investigation into High-temperature Corrosion in a Large-scale Municipal Waste-to-energy Plant, *Corrosion Science* 52, 2010, pp. 3861–3874.
[12] HIDAKA Y., ANRAKU, T., OTSUKA, N.: Deformation of Iron Oxide Scales Upon Tensile Tests at 700–1280°, In: *Abstract Booklet of 5th Intern. Symposium on High Temperature Corrosion and Protection of Materials,* Les Embiez, France, 2000 (pp. 4-A115).

https://doi.org/10.26552/com.C.2012.4.43-47

Petr Jonsta – Zdenek Jonsta – Katerina Konecna – Miriam Gabcova – Karel Hrbacek *

MICROSTRUCTURAL ANALYSIS OF NICKEL SUPERALLOY MAR-M247

This paper presents the results of a microstructural phase analysis of the nickel superalloy MAR M247 after casting and different modes of dissolving annealing in the range of 900°C – 1240°C with cooling in water. The alloy in question presents a polycrystalline nickel creep-resistant alloy usable especially for highly stressed components in the aerospace and rocket industries. The analysis was performed using a JEOL JSM 6490LV scanning electron microscope with an Oxford Inca x-act x-ray microanalyzer. The presence of minority phases was identified. The study is focused on their possible changes after the application of different modes of thermal treatment.

Keywords: *superalloy, phase analysis, annealing.*

1. Introduction

The demanding requirements placed on materials working in extreme conditions encourage the use of nickel-based superalloys. The significance of these superalloys for such demanding applications lies primarily in their ability to maintain almost unchanged strength even after long-term exposure to temperatures exceeding 650 °C. One of the most demanding applications is the use of these materials for the hot parts of turbines. The important position of superalloys in this area is reflected in the fact that they currently represent more than 50 % of the mass of modern aircraft engines. The widespread use of superalloys in turbines is supported by the fact that the thermodynamic efficiency of turbines increases with increasing temperatures at the turbine inlet; this has been one factor driving efforts to increase the maximum usable temperature of high-alloyed alloys [1, 2].

The increase in the maximum usable temperature has been enabled particularly by advanced processing techniques which have led to increased purity of alloys and thus to their increased reliability, together with developments in the technique of directional crystallisation and subsequent production technology for products based on single crystals. An equally important factor has been the development of alloys with higher usable temperatures achieved mainly by alloying, especially with Re, W, Ta and Mo [3].

This paper reports on a detailed microstructural phase analysis of the cast nickel superalloy MAR M247 in as-cast condition and after dissolving annealing within the temperature interval of 900 °C – 1240 °C for 2 hours with cooling in water.

The objective of the presented microstructural phase analysis was to achieve a more detailed understanding of this nickel superalloy from the viewpoint of its technical applicability.

2. Material and experimental technique

A microstructural phase analysis was performed on the nickel superalloy MAR-M247in as-cast condition and then after dissolving annealing at temperatures within the interval of 900 °C – 1240 °C. Table 1 gives the chemical composition of the alloy and Table 2 shows modes of dissolving annealing.

The microstructural analysis of the nickel superalloy was performed on the samples in an initial state and after the above-mentioned modes of heat treatment followed by chemical etching. The microstructure was analysed using a light metallographic microscope (Olympus GX51).

Chemical composition in wt. % Table 1

C	Cr	Mo	Al	Ti	Fe	W	Ta	Zr	Co	Hf	B	Ni
0.16	8.60	0.80	5.60	1.00	0.20	10.00	3.00	0.06	10.00	1.50	0.02	rest

* **Petr Jonsta[1], Zdenek Jonsta[1], Katerina Konecna[1], Miriam Gabcova[1], Karel Hrbacek[2]**
[1] VSB-Technical university of Ostrava, Faculty of Metallurgy and Materials Engineering, Czech Republic, E-mail: petr.jonsta@vsb.cz
[2] Prvni brnenska strojirna Velka Bites, a.s., Czech Republic

Modes of dissolving annealing Table 2

Sample	Temperature / duration of annealing	Cooling
MA VS	as-cast state	water
2MAW	900 °C/2h	water
4MAW	1040 °C/2h	water
13MAW	1200 °C/2h	water
15MAW	1240 °C/2h	water

An electron-microscopic investigation was carried out with a JEOL JSM 6490LV scanning electron microscope equipped with an INCA x-act energy dispersive spectral analyzer. The microstructure was documented in the mode of secondary electrons (SEI) and back-scattered electrons (COMPO – material contrast). Individual phases were identified by high quality X-ray microanalysis. Semiquantitative X ray microanalysis was performed only for the particles bigger than 1 μm, when the results were not distorted significantly by an X-ray signal from the surrounding matrix.

3. Results and discussion

The analysed nickel superalloy MAR-M247 is an alloy which is strengthened by the γ' phase in basic austenitic matrix (γ). The γ matrix in the basic type of this alloy contains approx. 60 vol. % of the phase γ'. Alloying by Co, W, Mo, Ti and other admixtures leads to further substitutive or precipitation strengthening of the matrix and thus to a reinforcing effect of the phase γ'. The addition of C within the interval of 0.05 – 0.2 % leads to the formation of carbides of the type $M_{23}C_6$, MC and M_6C [4]. These carbides are not stable phases. Under the influence of working temperature they may change, including their size and morphology, and by this they influence the properties of the alloy at high-temperature exposure. The microstructure of the as-cast sample (MA VS) was characterised by a typical dendritic character. Segregation processes in the microstructure during solidification lead to the formation of distinct chemical heterogeneities. Very frequent formations of eutectics $\gamma + \gamma'$ were segregated in interdendritic spaces – see Fig. 1. These spaces also contain areas that are richer in tungsten. In the areas of eutectics which were the last to solidify, large particles of γ' richer in hafnium were formed. The γ' particles form regular cubes, which are somewhat larger in interdendritic spaces (Fig. 2). Fig. 3 shows a detailed picture of this area.

Particles of primary carbides of the MC type were also identified in the basic matrix which contained variable quantities of carbides of tantalum, titanium, tungsten and hafnium. These carbides are created in the structure as a result of eutectic reaction in the form of larger irregular particles with cubic morphology, and they can be situated randomly both inside the grains and at their boundaries. At high temperature exposure these carbides tend to change into carbides of the type $M_{23}C_6$ or M_6C, in case of higher content of molybdenum, tungsten and chromium in the alloy. The influence of a higher content of niobium, which stabilises MC carbides up to the temperature of 1260 °C, plays no role in this case, since this element is not present in the given alloy – see Table1.

Table 3 below gives chemical composition of identified minority phases.

During solidification, MC carbides are formed into the structure of "Chinese script characters" composed of three different parts [5, 6]. The central part and extended arms contain carbides of the type MC (Ti, Hf, Ta, W) C. The ends of the extended arms are broadened, forming angular "heads". These heads contain carbides of titanium, hafnium, tantalum and tungsten and have an increased content of hafnium in comparison with the central part and the arms. Due to the fact that hafnium strongly segregates to the rest of the solidifying interdendritic melt, interdendritic carbides contain more hafnium than intradendritic carbides [7]. Volume fraction of carbides, their fixation and behaviour during growth are related to their growth rate. Their volume fraction drops a slower growth rate [8], which is caused by their reduced ability of fixa-

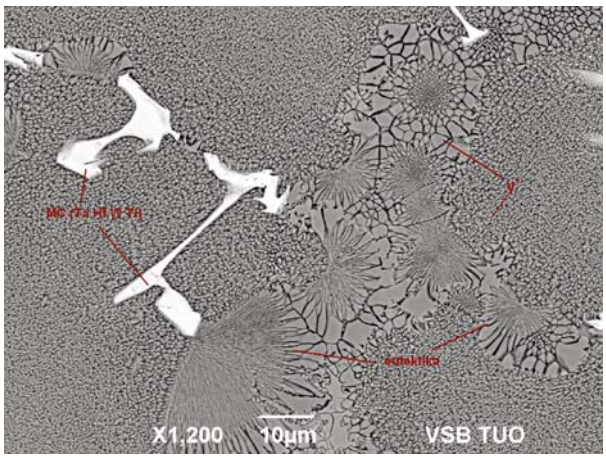

Fig. 1 Microstructure-sample MA VS (BEC)

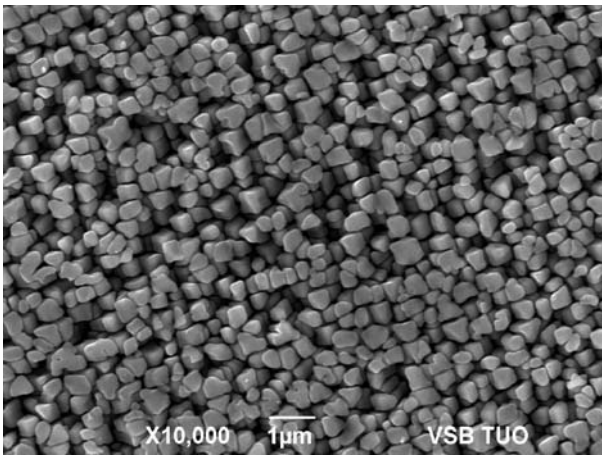

Fig. 2 Phase γ' in matrix (SEI)

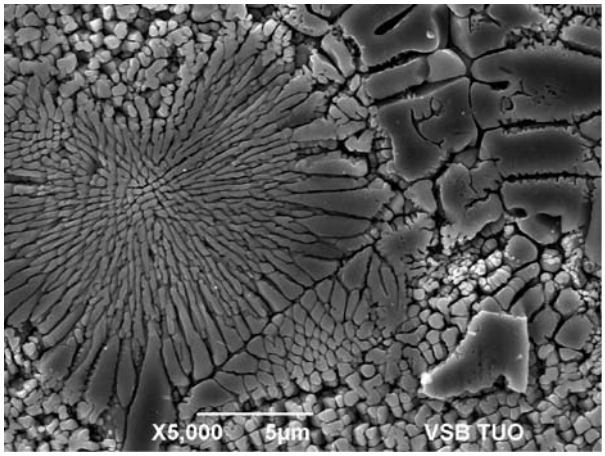

Fig. 3 Formation of eutectics (SEI)

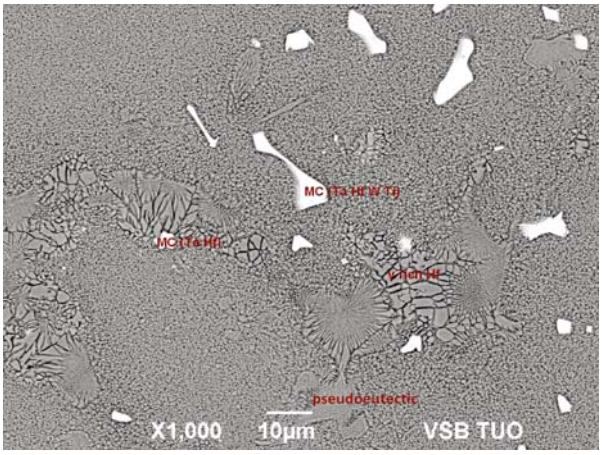

Fig. 4 Microstructure-sample 2MAW (BEC)

Chemical composition of individual phases in wt. % Table 3

Name	Al	Ti	Cr	Co	Ni	Hf	Ta	Mo	W
gamma prime	7.9	2.0	4.2	7.0	64.5	5.5	4.4		4.6
gamma prime Hf-rich	7.1	1.7	3.5	6.4	62.6	10.3	3.8		4.5
eutectics	7.7	1.8	5.6	7.3	64.9	3.3	3.9		5.4
pseudo-eutectics	6.9	1.1	6.2	8.5	60.3	2.2	3.0		11.7
MC (Ta Hf W Ti)		10.3	0.9	0.6	3.6	16.8	53.7		14.1
MC (Hf Ta)		2.7	0.5	0.7	3.9	56.6	32.0		3.6
$M_{23}C_6$		0.7	36.0	3.3	8.1			9.9	41.9

tion to the solidus – liquidus interface. At slow growth rates the growing carbides become enriched by hafnium and titanium while at rapid growth rates their diffusion is suppressed and carbides contain more tungsten.

After the application of dissolving annealing in the mode of 900 °C/2h/water (sample 2MAW), no important changes occurred in the microstructure as can be seen from Fig. 4 above. During the modes working with higher temperatures of dissolving annealing more significant changes in composition, distribution and morphology of minority phases take place. After dissolving annealing in the mode of 1040 °C/2h/water (sample 4MAW) the hafnium carbides begin to precipitate in the area of eutectics between large particles of γ'. A minority phase rich in Mo, W, Cr, probably carbides $M_{23}C_6$, is also present. At the same time particles in interdendritic spaces begin to coagulate and to become coarser (Fig. 5).

In the structure of the sample 13MAW treated by the mode 1200 °C/2h/water, it is already possible to see a significant precipitation of carbides rich in hafnium or tantalum.

In the areas of large γ' particles a dissolution of eutectics takes place, as well as a change of size of the γ' particles both inside dendrites and in interdendritic spaces. Bimodal distribution is evident here. Areas containing segregated very fine γ' particles are present in the matrix around the residues of eutectics – Fig. 6.

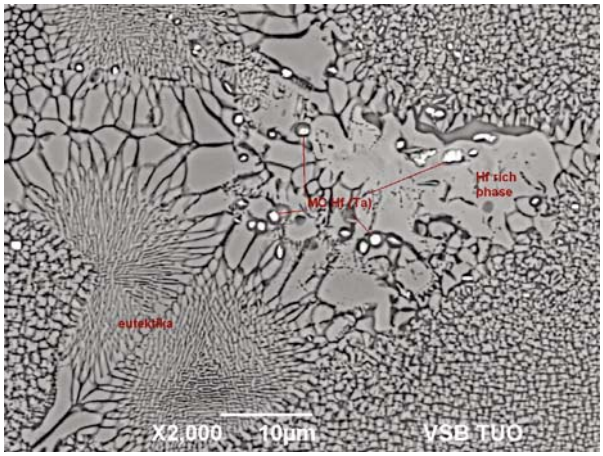

Fig. 5 Microstructure-sample 4MAW (BEC)

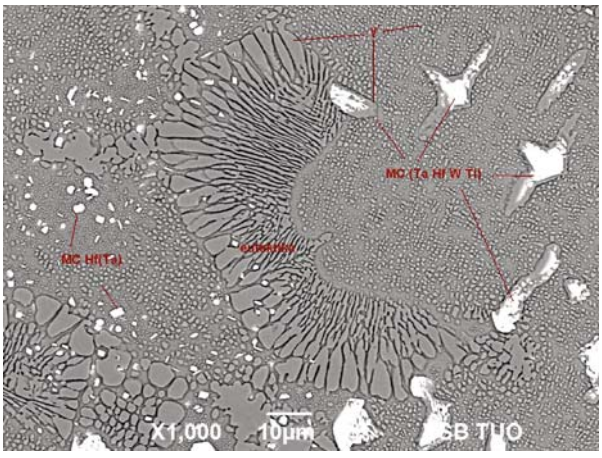

Fig. 6 Microstructure-sample 13MAW (BEC)

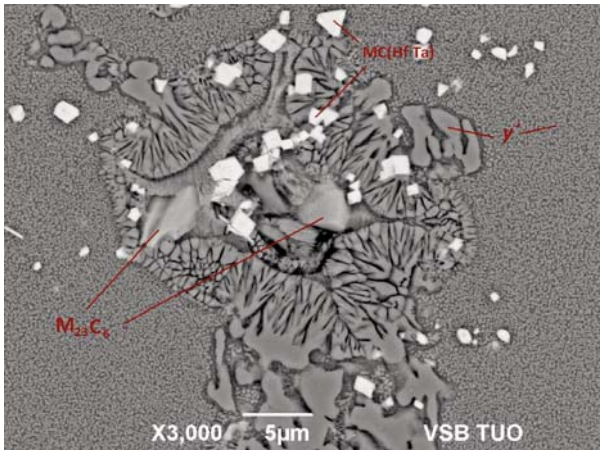

Fig. 7 Microstructure-sample 15MAW – carbides $M_{23}C_6$ in the centre of residue of eutectic formation (BEC)

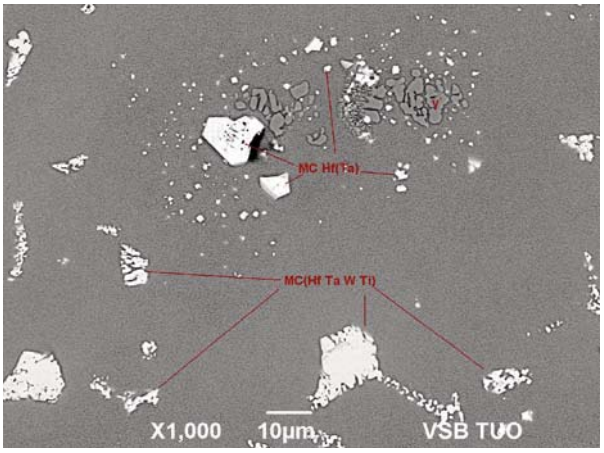

Fig. 8 Microstructure-sample 15MAW – disintegrating primary carbides (BEC)

In the case of the highest temperature of dissolving annealing, namely at the mode of 1240 °C/2h/water in the sample 15MAW, all the γ' particles in the matrix are fine; no bi-modal distribution is observed here. Eutectics are almost dissolved and areas with small carbides of hafnium and tantalum are present at their place. In a few isolated cases residues of eutectics are present, in the centre of which are particles of the carbides $M_{23}C_6$.

Large primary carbides disintegrate, and new sharp-edged carbides rich in hafnium and tantalum grow – see Figs. 7 and 8.

4. Conclusions

This paper presented microstructural phase analysis of the nickel superalloy MAR-M247 in as-cast condition and after various modes of dissolving annealing within the temperature interval of 900 – 1240 °C with dwell of 2 hours and cooling in water. It may be stated that changes in the structure of the investigated alloy took place from the temperature of dissolving annealing of 1040 °C.

The increasing temperature of dissolving annealing brought gradual precipitation and increasing frequency of occurrence of hafnium carbides, dissolution of eutectics, and a change of shape and size of γ' particles both in interdendritic spaces and also inside dendrites. Bimodal distribution was gradually suppressed.

On the basis of X-ray microanalysis (see Table 3) it was possible to observe changes in the percentage representation of individual alloying elements in minority phases.

A quite important fact was that the microstructural phase analysis did not prove the presence of undesirable TCP phases, particularly of the phase σ, which significantly contributes to the degradation of this alloy.

The presented analysis contributes data and serves to deepen knowledge of the investigated alloy for purposes of industrial application.

Acknowledgement

This paper was created in the project No CZ.1.05/2.1.00/01.0040 "Regional Materials Science and Technology Centre" within the frame of the operation programme "Research and Development for Innovations" financed by the Structural Funds and from the state budget of the Czech Republic. The work was also realized under the support of the research project FR-TI3/077.

References

[1] HERNAS, A., JONSTA, Z., et.al: *Zarupevne oceli a slitiny* [*Refractory Steels and Alloys*]. 2nd ed. ES VSB-TU Ostrava, 2009, 392 p. ISBN 978-80-248-2187-0.

[2] HRBACEK, K.: *Vyzkum a vyvoj technologie presneho liti lopatek stacionarnich plynovych turbin, umoznujici nahradu kovanych lopatek za lopatky lite* [*Research and Development of Technology of Precision Casting of Blades for Stationary Gas Turbines, Enabling Replacement of Forged Blades by Cast Blades*]. Research Report, PBS Velka Bites, 2005, 40 p.

[3] HRBACEK, K.: *Soucasny stav vyzkumu a vyvoje superslitin na bazi niklu pouzivanych v nasi republice na casti plynovych turbin, turbodmychadel a odlitky pro sklarsky prumysl* [*Current State of Research and Development of Nickel-based Superalloys used in the Czech*

Republic for Components of Gas Turbines, Turbo-blowers and Castings for Glass Industry]. Research Report, PBS Velka Bites, 2004-10–15, 26 p.

[4] LIAO, J., H., et al: Effects of Rhenium on Microstructure and Phase Stability of MAR-M247 Ni-Base Fine-Grain Superalloy. *Mat. Trans,* vol. 51, No. 4 2010, pp. 810–817.

[5] DONACHIE, M., J., DONACHIE, S., J.: *Superalloys: A Technical Guide,* 2nd ed. USA, 2002, 439 p. ISBN 0- 87170-749-7.

[6] BOR, H., Y., HSU, C., WEI, C., N.: Influence of Hot Isostatic Pressing on the Fracture Transitions in the Fine Grain MAR-M247 Superalloys, *Materials Chemistry and Physics,* vol. 84, No. 2-3, 2004, pp. 284–290.

[7] CHEN, J. et al: MC Carbide Formation in Directionally Solidified MAR – M247 LC Superalloy. *Mat. Sci Eng.* A247, 1998, pp. 113–125.

[8] ROKOSZ, S., STASZEWSKI, M., CVAJNA, J. A Complex Procedure for Describing Porosity in Precision Cast Elements of Aircraft Engines Made of MAR-M247 and MAR-M509. *Mat. Characterization* 56, 2006, pp. 405–413.

https://doi.org/10.26552/com.C.2012.4.48-53

Agata Wronska – Agata Dudek – Jacek Selejdak *

SURFACE REMELTING OF MULTI-PHASE SINTERED STEEL

This study presents the results of the investigations of the effect of surface remelting using arc welding (GTAW) on the microstructure and selected properties of surface layer of sintered steels 304L and 434L. It was found that in order to improve surface quality in these sinters, remelting should be carried out at lower current intensities, i.e. 30A and 40A. The surface treatment carried out in the study allowed for obtaining an uniform cellular-dendritic microstructure in surface layer. X-ray examinations demonstrated the effect of compressive stress in surface layer, which reduces the risk of cracking on the surface.

Keywords: *sintered stainless steel, arc surface remelting*

1. Introduction

Among the group of corrosion-resistant steels, duplex steels are characterized by particularly good combination of the properties typical of chromium ferritic steels and chromium-nickel austenitic steels. They exhibit high mechanical strength, elasticity, weldability and very high corrosion resistance and oxidation in different environments and operating conditions. However, manufacturing of two-phase steels using conventional methods is complicated from the technological standpoint and thus expensive [1, 2]. Recent years have seen a dramatic increase in interest in alternative methods of manufacturing of these steels, offered by powdered metallurgy. This technology allows for large-scale production of components with complex shapes, ensuring high precision of dimensions and surface quality even for small parts [3]. Manufacturing duplex steel by means of powder metallurgy is carried out through sintering of the mixture of alloy powders with chemical composition corresponding to duplex steel, mixture of ferritic and austenitic steels and the mixture of ferritic, austenitic or martensitic steel with the elements which destabilize the resultant phase, which allows for creation of the two-phase structure [4]. Moreover, powder metallurgy uses 97% of burden material, which makes it a nearly waste-free technology, thus more economical and ecological compared to conventional procedures. The technology also allows stainless steels to be used in control devices, household equipment, medicine, tools as well as in aviation and automotive industries which are the recipients of over 70% of sintered products [5].

A major limiting factor in broader use of sintered austenitic-ferritic steels is its worse mechanical and corrosion properties compared to their cast counterparts. This is caused by the presence of porosity. Although powder metallurgy allows for precise determination of chemical composition of sinters and controlling the conditions of sintering, limitation of porosity is possible only to some extent [2, 6]. Presence of empty holes in the material might generate cracking during the use of these materials, whereas porosity adversely affects corrosion resistance as it increases the surface area of the material which is exposed to direct contact with corrosion environments [7÷9]. Given that sintered duplex steels are typically designed for using in automotive industry, e.g. exhaustion systems elements which operate under corrosion conditions, the authors of the present study focused on the improvement in the properties of surface layer.

Recent two decades have seen an increasing interest in surface remelting. Previous scientific output in this field provides evidence that surface remelting in sintered stainless steels using concentrated heat sources favourably affects the improvement in functional properties of these materials [10÷12]. A particular popularity has been observed in application of laser techniques. They are characterized by high precision, while a stable and focused laser beam, coupled with dynamic cooling, allows for obtaining the remelted layers with the fine-crystalline structure [13÷15, 18]. The obtained surface layer is characterized by insignificant surface roughness and total reduction in open porosity, i.e. the places which are conducive for creation of corrosion nuclei [16]. Moreover, remelting of sintered alloy steels is a particularly justified surface treatment since it does not affect the chemical composition of the material [17]. It can be expected that the properties of the sinter that result from chemical composition and sintering parameters will not deteriorate. Laser remelting offers a range of benefits. However, from the economic standpoint, this process is very expensive. The present study proposes the use of a cheaper but relatively effective TIG (GTAW) method. The opportunities of monitoring of a number of parame-

* **Agata Wronska[1], Agata Dudek[1], Jacek Selejdak[2]**
[1] Czestochowa University of Technology, Faculty of Process & Materials Engineering and Applied Physics, Institute of Materials Engineering, Czestochowa, Poland, E-mail: agataw@wip.pcz.pl
[2] Czestochowa University of Technology, Faculty of Management, Institute of Production Czestochowa, Poland

ters e.g. current type and intensity, arc voltage, surface scanning rate and selection of the electrode material/diameter make it easier to control the quality and properties of the modified surface layer. The arc method might be considered as an alternative solution to the laser technologies. Using TIG devices, the remelted layers with the structure and properties similar to the laser-modified layers are obtained [18÷21].

The study presents the results of the investigations of the effect of remelting by means of GTAW method on the microstructure and selected properties of surface layer in sintered multi-phase steel, obtained from the mixture of powders of austenitic and ferritic steel.

2. Research material and methodology

The examinations were carried out for the specimens of sinters of stainless steel powders (304L and 434L), manufactured by Hoganas AB (Sweden). The mixture of powders was prepared using the following proportions: 20% 304L: 80% 434L (marked as 20A-80F). The specimens were compressed with pressure of 720 MPa and sintered at temperature of 1250 °C for 30 minutes in the atmosphere of dissociated ammonia (75% H_2: 25% N_2) and cooled at cooling rate of 0.5 °C/s. Table 1 presents chemical compositions of individual powders.

Density of the sinters amounted to 6.96 g/cm^3. Porosity was determined by means of microstructural examinations and software for computer image analysis. The porosity on the surface and in the cross-section amounted to 3.06 ± 0.7% and 2.68 ± 0.4%, respectively. The sinter showed the multiphase microstructure with the presence of austenite, ferrite and martensite (Fig. 1).

The diagram of the GTAW method and the dimensions of the remelted specimens are presented in Fig. 2. Table 2 presents the parameters of remelting operations.

Parameters of arc remelting of sinter 20A-80F Table 2.

No.	Current Intensity I [A]	Arc Voltage [V]	Total Arc Power qc [W]	Linear Energy E [kJ/m]	Scan Rate V [mm/min]	Type and Flow Pattern of the Inert Gas
1.	30	10	300	39.47	460	Argon ~10 l/min
2.	40	10.5	420	35.92		
3.	50	10	500	42.76		
4.	60	10.5	630	53.88		

The effect of remelting on the quality and microstructure of surface layer was evaluated based on microscope observations of the remelted surface and metallographic sections. Geometry of the remelted zone (depth and width of remelting) was also determined.

Chemical composition of sinter 20A-80F and steel powders 304L and 434L [wt%] Table 1.

Powder	Cr	C	Ni	Si	Mn	Mo	N	O	S	Fe
304L(A)	18.9	0.013	11.2	0.9	0.1	–	0.02	0.28	0.005	rest
434L(F)	16.2	0.015	–	0.8	0.1	0.98	–	–	–	rest
20A-80F	16.74	0.015	2.24	0.82	0.1	0.78	0.004	0.056	0.001	rest

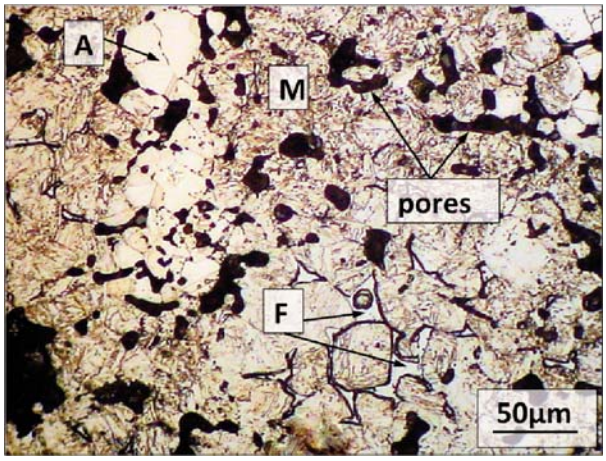

Fig. 1 Microstructure of 20A-80F sinter, magnification 200x

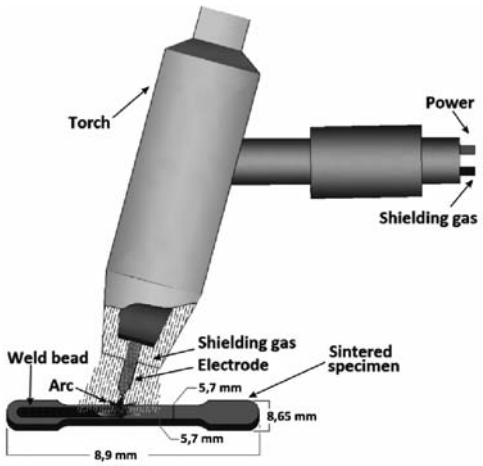

Fig. 2 Surface remelting using GTAW method

Furthermore, the authors evaluated surface topography and measured roughness parameters for each sample by means of profilometer Hommel T1000. The measurements were carried out in contact with the examined surface through coupling of the indenter with differential measurement system.

Parameters of stress measurement by means of $\sin^2\psi$ method — Table 3.

Angle 2θ	59.9°
(hkl)	(022)
Peak Slope	0; 24.095; 35.264; 45.00°
Young's Modulus	$220*10^3$ MPa
Poisson's Ratio	0.28
X-Ray Lamp	Co; λ_{Co} = 0.17902 nm

The state of residual stresses in surface layer was determined by an X-ray method ($\sin^2\psi$) using Seifert XRD-3003 diffractometer. Dedicated software (Rayflex-Stress Analyzer) was used for determination of angular positions of diffraction peaks from austenitic phase. The parameters of the measurement are presented in Tab. 3.

Microhardness tests in remelted zone and the adjacent zones were carried out using Vickers method with the load of 490 mN by means of microhardness tester Future- Tech FM-7.

3. Discussion

The density of the modified sinter of 6.96 g/cm^3 suggests that remelting might have caused shrinkage due to a local change in volume. This phenomenon is unfavourable as it generates stress in surface layer and cracking of the surface [22, 23]. Using the arc method (GTAW) allows for limitation of the volume of liquid in the remelted zone through opportunities of monitoring of a number of process parameters. Application of different current intensities led consequently to obtaining remelted layers with varied surface geometry. Figures 3 and 4 present macroscopic effects of selected variants of the treatment used. The best surface quality was found for the specimens remelted with current intensity of 30 A and 40A. Presence of small areas of scales was found on the surface, which was easily removed through polishing. Heat impact zone was characterized by a colourful deposit formed by a thickening of the natural oxide layer. The open porosity was totally eliminated. Current intensities of 50 A and 60 A were too high and numerous fusions were observed on the surface of the sinter. Higher current intensity affected surface geometry in the specimens unfavourably as it was characterized in both cases by considerable waviness. The results of profilometric examinations revealed that application of current intensity of 30 A reduces the roughness in the sinters studied. As results from Table 4 and Fig. 5, the value of Ra parameter increases after arc remelting at current intensity of 40 A to 0.26 μm compared to the initial state. The values of roughness parameters for the surface of the specimen remelted using 60 A

Comparison of roughness parameters for remelted surface and input material — Table 4.

Roughness parameter	Substrate material	30A	40A	50A	60A
Ra	2.99	2.27	3.25	9.14	25.96
Rz	31.03	17.32	23.80	64.71	113.42
Rmax	48.74	23.91	27.81	106.65	145.47

R_a – arithmetic mean roughness deviation from mean line,
R_z – maximum height of the profile,
R_{max} – maximum distance of profile peak from the lowest valley.

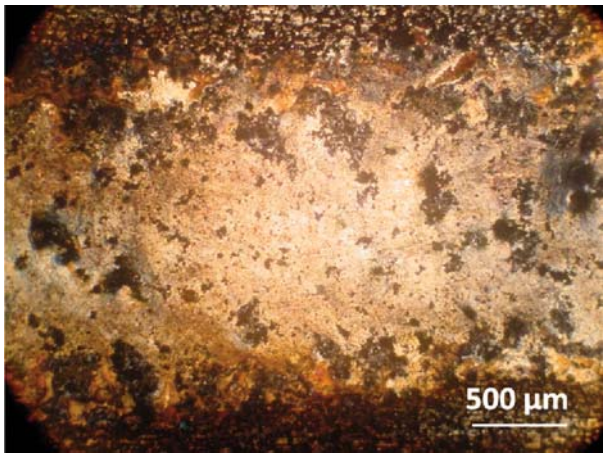

Fig. 3 Macroscopic effects of remelting sinters 20A-80F at current intensity of 40A

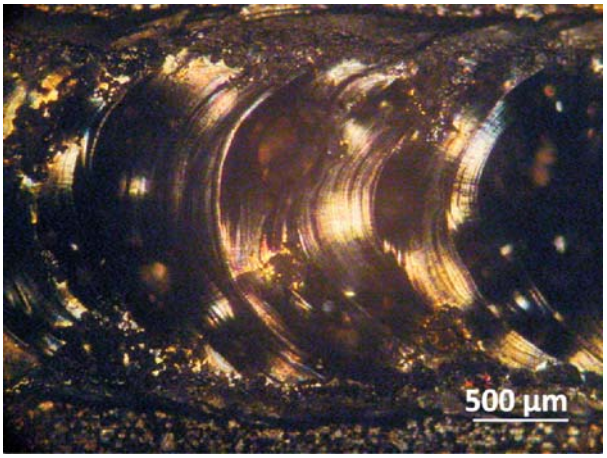

Fig. 4 Macroscopic effects of remelting sinters 20A-80F at current intensity of 50A

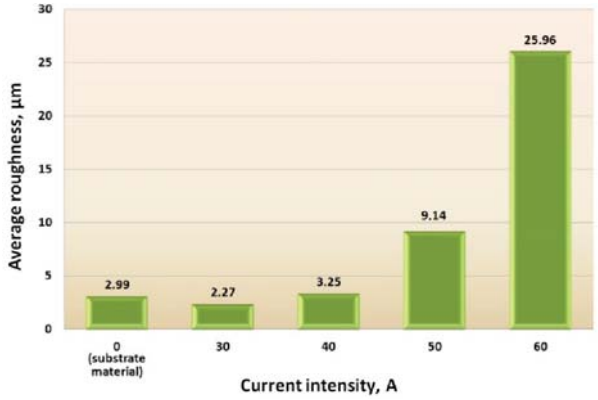

Fig. 5 Ra parameter vs. current intensity

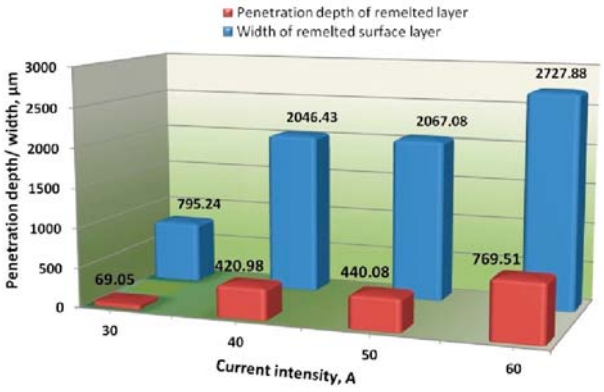

Fig. 6 Geometry of remelted layers vs. current intensity

current intensity exceeded the measurement error of the profilometer, which causes that the recorded data might contain errors.

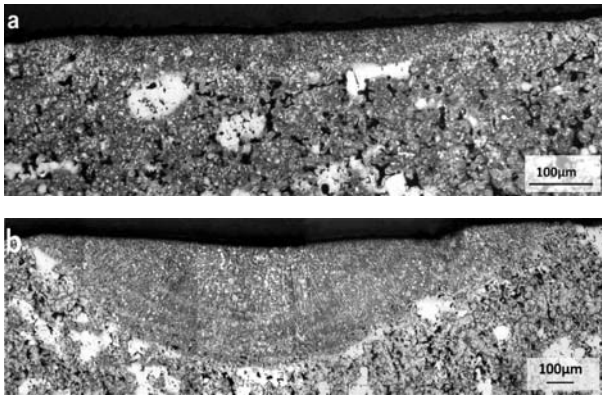

Fig. 7 Microstructures of surface layer of the sinter after remelting at the current intensities: a) 30 A, b) 40 A

Macroscopic examinations were employed to determine the width and depth of remelted layers. The results of the measurements were presented in the form of the chart (Fig. 6). Both parameters which characterize the geometry of surface layer are directly proportional to the value of current intensity. The highest depth of remelting and the widest path (769.5 µm and 2727.88 µm, respectively) was obtained after remelting with current intensity of 60 A. For intensities of 40 A and 50 A, the obtained remelted layers have similar geometry, whereas in the case of the treatment with current intensity of 30 A, changes were found in the insignificant volume of material.

Figures 7a and 7b present microstructures of surface layers after remelting with current intensities of 30 A and 40 A. Examinations by means of optical microscope revealed a primary character of microstructures for the obtained remelted layers. Using the formula (1) based on chemical constitution of the sinter; the authors calculated the ratio of Cr and Ni equivalents. The obtained value amounts to 6.84, which points to a ferritic character of solidification [24].

$$\frac{R_{Cr}}{R_{Ni}} = \frac{Cr + Mo + 1.5Si + 0.5Nb}{Ni + 30C + 0.5Mn} \quad (1)$$

Ferrite was formed during cooling, between dendritic grains of austenite. Furthermore, the authors found that ferrite fraction is the lowest in the layer remelted with current intensity of 60 A. This might be caused by the fact that in the case of higher linear energy or arc, solidification and cooling rates are lower, which allows dendritic cells to grow and take more volume of the material. Therefore, the column grains were observed mainly in the areas located at the contact with substrate (Fig. 8), whereas on the surface, where the heat is transferred much faster, a fine grain structure was formed.

Figure 10 presents a microhardness profile for surface layer of the sinter after remelting. The highest hardness in remelting zone was observed for the sinter remelted with current intensity of 60 A. The surface treatment caused that the microstructure of surface layer was homogenous, which was suggested by similar values during measurements performed in the remelting zone for individual cases. A considerable dispersion of the values of microhardness results from non-homogenous microstructure of the sinter which in its input state contains martensite, ferrite and austenite (Fig. 1). Microscopic examinations did not reveal a distinct transient zone between the remelted material and the core. However, a decline in microhardness was found in all the cases in the remelted zone near the substrate. Unequivocal explanation of this phenomenon is yet to be researched.

Table 5 presents fundamental parameters and results of stress measurements in remelted surface layers. Figure 9 shows diffraction peaks depending on the variable slope ψ with the example of a specimen remelted with current intensity of 30 A. Since the level of residual stress considerably affects strength properties of the material, it seems beneficial to generate compressive stress in the remelted layer, which might reduce the risk of cracking. The mea-

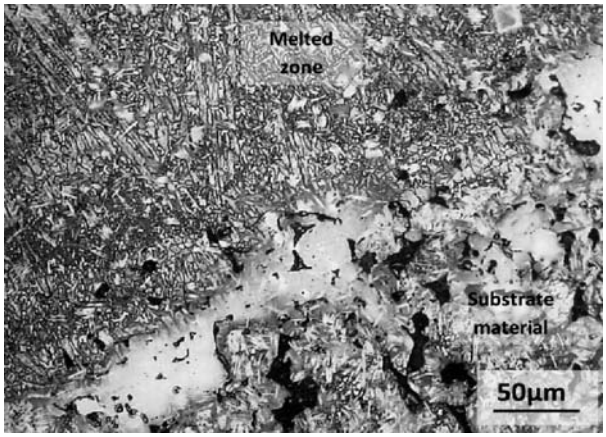

Fig. 8 Microstructure of remelted layer near substrate material (I = 40 A)

surements demonstrated that compressive stress is generated in the remelted areas analysed in the study.

Stress in remelted surface layers Table 5.

Current Intensity I, A	Stress for 2θ = 59.9	
	σ	τ
30	778.4	769.2
40	734.3	−688.0
50	963.0	−298.1
60	81.7	−357.9

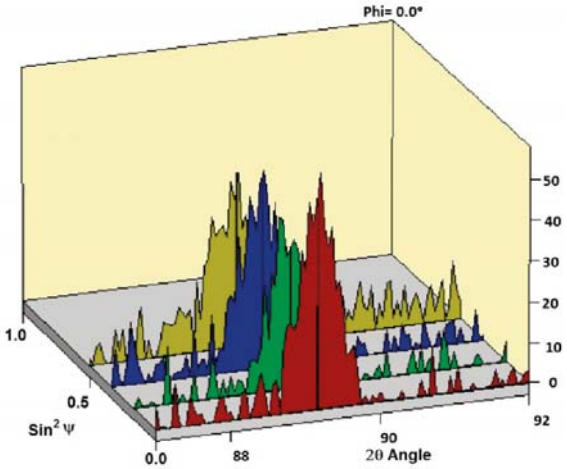

Fig. 9 3D diffraction peaks for variable slope ψ

4. Conclusions

The results of the investigations focused on the evaluation of the effect of surface remelting on the microstructure and selected properties of surface layer of multi-phase sinter 20A-80F lead to the following conclusions:

- Application of arc method (GTAW) allowed for formation of a fine grain cellular-dendritic microstructure in surface layer.
- Both width and depth of remelting are directly proportional to the values of the used current intensity. The highest values of these parameters (2727.88 µm and 769.5 µm, respectively) were obtained after remelting at current intensity of 60 A,
- Remelting of the surface of the sinter 20A-80F at the current intensity of 30 A and 40 A allowed for elimination of open poros-

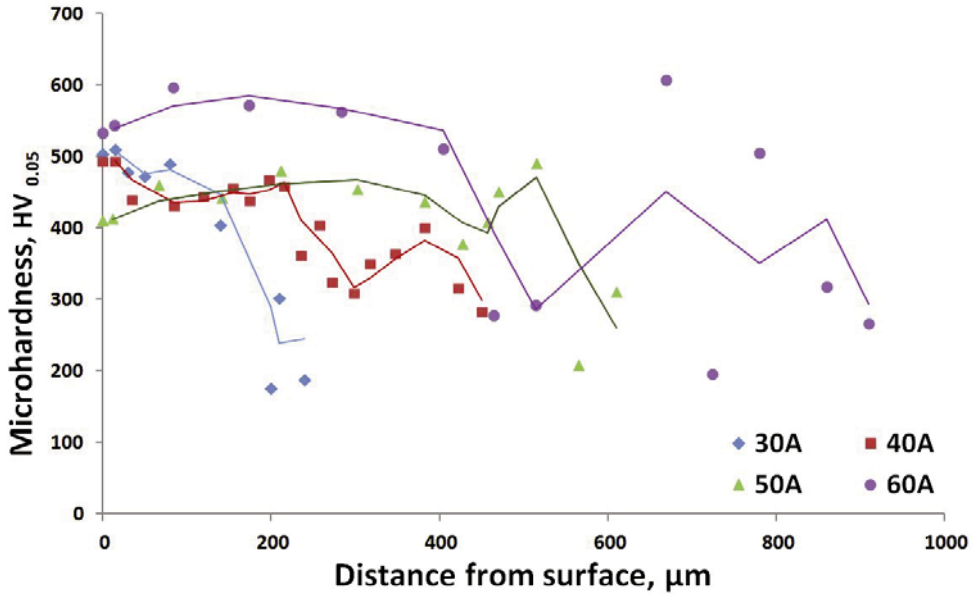

Fig. 10 Distribution of Vickers microhardness in surface layer of the sinter 20A-80F after remelting with different current intensities

ity and reduction of roughness. Sinter surface after remelting with current intensity of 50 A and 60 A was characterized by considerable waviness and presence of fusions,
- Compression stress was present in the obtained remelted layers
- The highest microhardness in the remelted layers was obtained after remelting with current intensity of 60 A
- Optimum current intensity used during remelting of multi-phase sinters studied amounted to 40 A. The obtained surface layer had suitable depth and width and was characterized by good quality and insignificant surface roughness.

References:

[1] DOBRZANSKI, L. A., BRYTAN, Z., ACTIS GRANDE, M., ROSSO, M.: Influence of Sintering Parameters on the Properties of Duplex Stainless Steel, *Archives of Materials Science and Engineering,* vol. 20, 2007, pp. 231÷234

[2] MARTIN, F., GARCIA, C., BLANCO, Y.: Effect of Chemical Composition and Sintering Conditions on the Mechanical Properties of Sintered Duplex Stainless Steels, *Materials Science and Engineering* A 528, 2011, pp. 8500÷8511

[3] GARCIA, C., MARTIN, F., BLANCO, Y., DE TIEDRA, M. P., APARICIO, M. L.: Corrosion Behaviour of Duplex Stainless Steel Sintered in Nitrogen, *Corrosion Science* 51, 2009, pp. 76÷86

[4] MUNEZ, C. J., UTRILLA, M. V., URENA, A.: Effect of Temperature on Sintered Austeno- Ferritic Stainless Steel Microstructure, *J. of Alloys and Compounds* 463, 2008, pp. 552÷558

[5] GARCIA, C., MARTIN, F., DE TIEDRA P., GARCIA CAMBRONERO, L.: Pitting Corrosion Behaviour of PM Austenitic Stainless Steels Sintered in Nitrogen-Hydrogen Atmosphere, *Corrosion Science* 49, 2007, pp. 1718÷1736

[6] GARCIA, C., MARTIN, F., BLANCO, Y., TIEDRA, M. P., APARICIO, M. L.: Corrosion Behaviour of Duplex Stainless Steel Sintered in Nitrogen, *Corrosion Science* 51, 2009, pp. 76÷86

[7] ROSSO, M., ACTIS GRANDE, M.: High Density Sintered Stainless Steels with Improved Properties, *JAMME*, vol. 21, 2007, pp. 97÷102

[8] KAZIOR, J., NYKIEL, M., PIECZONKA, T., MARCU PUSCAS, T., MOLINARI, A.: Activated Sintering of P/M Duplex Stainless Steel Powders, *J. of Materials Processing Technology* 157–158, 2004, pp. 712÷717

[9] GARCIA, C., MARTIN, F., DE TIEDRA, P., GARCIA CAMBRONERO, L.: Pitting Corrosion Behaviour of PM Austenitic Stainless Steels Sintered in Nitrogen–Hydrogen Atmosphere, *Corrosion Science* 49, 2007, pp. 1718÷1736

[10] BRYTAN, Z., DOBRZANSKI, L.A., PAKIELA, W.: Laser Surface Alloying of Sintered Stainless Steel with SiC Powder, *JAMME*, vol. 47, 2011, pp. 42÷56

[11] BRYTAN, Z., BONEK, M., DOBRZA, L. A.: Microstructure and Properties of Laser Surface Alloyed PM Austenitic Stainless Steel, *JAMME*, vol. 40, 2010, pp. 70÷78

[12] BRYTAN, Z., DOBRZANSKI, L. A., PAKIELA, W.: Sintered Stainless Steel Surface Alloyed with Si3N4 Powder, *Archives of Materials Science and Engineering,* vol. 50, 2011, pp. 43÷55

[13] DOBRZANSKI, L. A., DOBRZANSKA–DANIKIEWICZ, A. D.: Obrobka powierzchni materialow inyynierskich [Surface Treatment of Engineering Materials], *Open Acces Library,* vol. 5, Gliwice, 2011, pp. 80÷84

[14] SOO KIM, J., CHUNG, C. M., BAIK, S. H., LEE, S. B.: Study on Laser- Surface Melting to Enhance Intergranular Corrosion Resistance of SUS 304 Weld, *Metals and Materials International,* vol. 17, No. 1, 2011, pp. 77÷82

[15] KWOK, C. T., CHENG, F. T., MAN, H. C.: Laser Surface Modification of UNS S31603 Stainless Steel, Part I: Microstructures and Corrosion Characteristics, *Materials Science and Engineering* A290, 2000, pp. 55÷73

[16] PANEK, D., BONEK, M.: Obrobka laserowa warstwy wierzchniej stali austenitycznej [Laser Treatment of the Surface Layer of Austenitic Stainless Steel], *PSKN zeszyt* No. D., 8, Gliwice, 2006, pp. 101–108

[17] D'OLIVEIRA, A, PAREDES, R., WEBER, F., VILAR, R.: Microstructural Changes Due to Laser Surface Melting of an AISI 304L Stainless Steel, *Materials Research,* vol. 4, No. 2, 2001, pp. 93÷96

[18] IWASZKO, J.: *Kształtowanie struktury i składu fazowego przetapianych powłok tlenkowych ZrO_2 i Al_2O_3* [*Shaping of the Structure and Chase Composition of the Remelted ZrO_2 and Al_2O_3 Oxide Coatings*], Wyd. PCz, Częstochowa, 2008, pp. 9÷22

[19] NITKIEWICZ, Z., DUDEK, A., KUCHARSKA, B.: Wstępne badania nad modyfikowaniem warstwy wierzchniej stali 40H [Introductory investigation of 40H steel surface layers modification], *Inzynieria Materialowa*, No. 5, 1999, pp. 447÷449

[20] DUDEK, A., NITKIEWICZ, Z., STOKLOSA, H.: The Crystallization of the Remelting Surface Layer of Steel with Ceramic Layer, *Archives of Foundry*, vol. 6, No. 22, 2006, pp. 158÷163

[21] DUDEK, A., NITKIEWICZ, Z.: The arc Plasma Shape in the Structural Changes Aspect after Remelting Process, *Archives of Foundry*, vol. 6, No. 21, 2006, pp. 199÷206

[22] PIECZONKA, T.: Procesy spajania w metalurgii proszkow [Welding Processes in Powder Metallurgy], *Rudy i Metale Niezelazne,* No. 9, 2003, pp. 435-447

[23] KLAR, E., SAMAL, P. K.: PM Stainless Steels: Processing, Microstructures and Properties, *ASM International,* 2007, pp. 173÷182

[24] http://a-g-h.freehost.pl/struktury_spoin_austenitycznych.pdf dostep z dn. 04.05.2012.

https://doi.org/10.26552/com.C.2012.4.54-59

Marian Kokavec – Radomila Konecna – Gianni Nicoletto *

FATIGUE STRENGTH OF NODULAR CAST IRON WITH DIFFERENT SURFACE CONDITIONS UNDER BENDING LOADING

The aim of this study is to evaluate the effects of surface conditions on the fatigue life of nodular cast iron under cyclic plane bending where the maximum stress is reached at the surface of interest. In order to evaluate the effect of surface conditions, fatigue tests were carried out on five sets of specimens with different surfaces. The surface conditions were as-cast, sand blasted, fine ground, nitrided and carbonitrided. The results show differences in fatigue strength, which are associated with the surface conditions. The characteristics of the surface layers in the different test specimens were examined by metallography. The fracture surfaces were fractographically analyzed to find places of fatigue crack initiation and to explain different fatigue life.

Keywords: *Nodular cast iron, fatigue, defects, surface layers, plane bending*

1. Introduction

Nodular cast irons (NCI) are technologically important materials and are used extensively in automotive industry. Defects produced during casting process often play a dominant role in limiting mechanical properties and fatigue life under cyclic loading in cast alloy components [1]. Besides the microstructural aspects such as chemical composition, nodule count and graphite shape, casting defects such as small shrinkage voids, porosities or dross defects play a dominant role in determining fatigue life and fatigue limit of cast irons [2]. Such defects make cast irons susceptible to brittle fracture and play the role of microscopic stress concentrators to promote the processes of nucleation and growth of cracks. NCI has been tested in fatigue with the aim to analyze the role of cast defects on fatigue crack initiation and propagation [3–6]. Many approaches to fatigue resistance evaluation for defect containing materials consider that a crack initiation stage is negligible and therefore fatigue crack propagation composes the whole fatigue process [7, 8]. Casting defects are inherent in the foundry processes and can be found in different cast alloys: aluminum alloys [7, 8], various steels [9, 10] or cast irons [4] for instance. Size, type and population of encountered casting defects depend on the alloy type and casting process [11]. Thermo-chemical surface treatments are frequently adopted with ferrous materials because they promote the formation of a hard and strong surface layer and of a system of compressive residual stress. Therefore, treatments, such as nitriding, simultaneously improve the fatigue endurance and the wear resistance [12, 13].

This paper presents and discusses the influence of surface conditions on fatigue behavior of pearlite/ferrite NCI. The dependence of the fatigue behavior on a specific surface condition is highlighted using prismatic specimens tested under cyclic plane bending with maximum stress reached at the surface of interest. The characteristics of the surface layers in the different test specimens are examined by metallography. The fracture surfaces were studied under inspection of SEM to explain the differences in fatigue lives.

2. Experimental material and methods

The experimental material was prepared as synthetic melt from 2000 kg of pig iron, 300 kg of steel scrap, and 1500 kg of cast iron scrap. The melting was performed using an arched alkaline furnace with basic lining and 35 kg of FeSi was added to the melted metal as an additive to increase the content of Si, [14, 15]. Chemical composition of the pearlite/ferrite NCI is given in Tab. 1. The cast material was supplied in the form of 140 × 100 × 20 mm plates.

Chemical composition of pearlite/ferritic NCI (in wt. %) Tab. 1

C	Si	Mn	S	P	Mg	Cr	Cu	Ni
3.68	2.62	0.51	0.005	0.05	0.034	0.2	0.02	0.01

No annealing treatment was performed before machining the specimens used for tensile and fatigue testing. The tensile tests performed according to the ASTM E8 standard of the present NCI gave a tensile strength R_m = 576 MPa and an elongation to the rupture A = 6 %. The fatigue specimen geometry, see Fig. 1, were prepared by machining cast plates. The role of different surface

* **Marian Kokavec[1], Radomila Konecna[1], Gianni Nicoletto[2]**
[1] Department of Materials Engineering, Faculty of Mechanical Engineering, University of Zilina, Slovakia, E-mail: marian.kokavec@fstroj.uniza.sk
[2] Department of Industrial Engineering, University of Parma, Italy

conditions was investigated. Therefore, a set of specimens was obtained with an as-cast surface condition, Fig. 2, (the opposite face was in all cases fine ground). A second set of specimens had the as cast test surface sand blasted, Fig. 2, by compressed air pressure (i.e. 1 MPa) and a SiC sand abrasive (i.e. grain size 250–300 μm). A third set of specimens had the test surface fine ground, Fig. 2, with a smooth finish achieved by removing the casting surface layers on a vertical milling machine and finishing by soft grinding on a disk sander. The final soft grinding was conducted by ceramic aluminum oxide wheel under the conditions of the grinding speed of 30 m/s, down feed 0.020 mm/pass.

Other two specimen sets with fine ground surfaces were subjected to thermo-chemical treatment, either nitriding or carbonitriding, to investigate the role of surface hardening on the fatigue behavior.

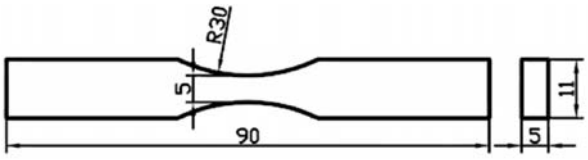

Fig. 1 Shape and dimensions of fatigue specimens

The structural analysis of NCI was performed on polished and etched specimens taken from cast plates. Structure details were analyzed in the light metallographic microscope according to the EN STN 42 0461 standard and by the methods of quantitative metallography [15]. Fig. 3 shows a typical microstructure of experimental material. The matrix was pearlite/ferritic with ferrite around the graphite nodules. Ferrite volume percentage of about 36 % was calculated using image analysis obtained from low magnification images. The nodule count (the number of graphite particles per unit area of mm^2) for studied nodular cast iron were in range 80 – 123. The graphite nodules were observed in fully (VI) and partly not fully globular (V) shape. Size was predominately ranging from 30 to 60 μm (6) and with a small number of nodules ranging in the size from 15 to 30 μm (7).

The nitrided and carbonitrided layers were analyzed using methods of color etching because a high chemical heterogeneity characteristic for this region. Microhardness (HV 0.02) was measured on nitrided and carbonitrided specimens at different distances starting from the surface down to the core of material. The hardness profile characterizes the effectiveness of the nitriding treatment and is used to define an effective nitrided or carbonitrided depth.

Fatigue tests were performed on specimens using a fatigue test machine for cyclic plane bending with loading ratio $R = 0$ and 25 Hz frequency. The tests were interrupted at 2.10^6 cycles if the specimen did not fail. The ratio $R = 0$ allowed to apply a cyclic tensile loading (the most critical in fatigue) to the surface of interest, either *as-cast, sand blasted, fine ground, nitrided and carbonitrided*. The initial stress range was associated to a fixed displacement range. A load-cell monitoring the specimen stress during the test allowed the determination of the evolution of specimen compliance. It was observed that the fixed initial stress range remained constant for a substantial part of the test followed by a continuous stress reduction in the final part because of fatigue crack initiation and propagation.

Fig. 2 Surface condition of specimens (from left as-cast, sand blasted, fine ground)

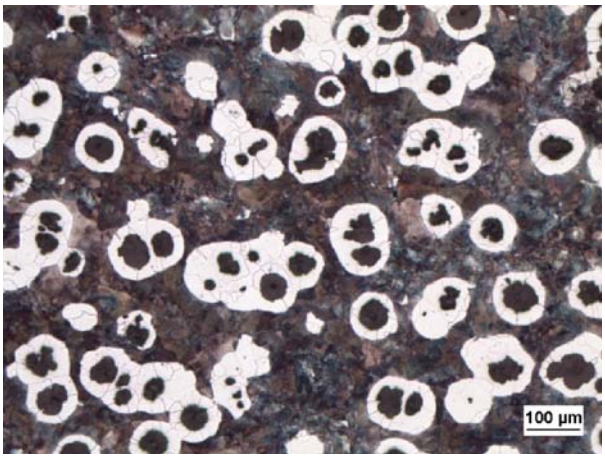

Fig. 3 Characteristic microstructure of experimental nodular cast iron, etched with 3% Nital

3. Results and discussion

The results of fatigue tests for all specimens are presented in Fig. 4. Trends of the S/N dependence for different surface conditions were identified. A ranking of the five surface conditions in fatigue is experimentally obtained with the best performance associated to the thermo-chemical surface treatment. At 10^6 cycles,

the fatigue strength shows a decrease of approx. 20 % going from a fine ground to a sand blasted surface and of approx. 30 % going from nitrided or carbonitrided to a fine ground surface.

The scatter of results for specimens with as-cast surface was very large and estimation of the fatigue limit of these specimens from the trend of S/N dependence was difficult. The large scatter of results can be explained by the presence of many defects in the cast surface layer, from which the fatigue cracks can initiate very quickly [16]. The specimens with as-cast and sand blasted surfaces showed very similar response in fatigue behavior. The thermo-chemical surface treatments showed the best fatigue behavior compared to the non-treated materials. Nitrided and carbonitrided NCI specimens showed quite similar fatigue behavior.

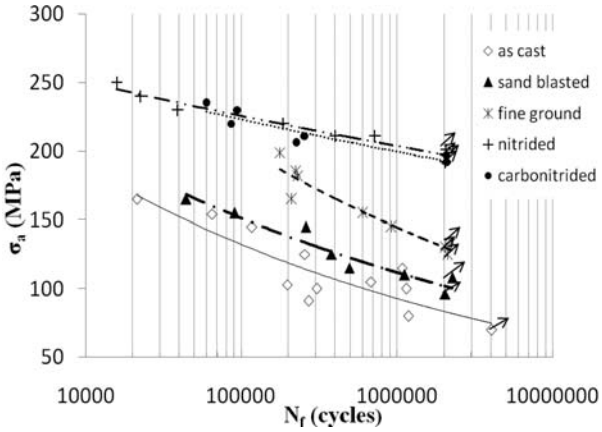

Fig. 4 S/N fatigue data after cyclic plane bending

Fatigue life of castings strongly depends on the surface condition. Only a few studies, [1, 4, 5, 17, 18], have been conducted on NCI castings with as-cast surfaces. In the presented case fatigue fracture initiation in as-cast and sand blasted specimens was observed with a scanning electron microscope (SEM) and these defects were found as fatigue crack initiation places (Fig. 6). However, the surface condition is expected to influence the fatigue crack initiation considerably with a strong effect associated to high surface roughness or by surface defects.

The surface and subsurface characteristics were metallographically investigated on cross sections perpendicular to the fracture surface and are discussed with reference to Fig. 5. Typically, the as-cast surface (Fig. 5a) is covered by a thin cast layer containing pores and cavities which negatively affect fatigue crack initiation. Just below this surface layer, a pearlitic layer with variable thickness, formed due to rapid solidification and cooling rate was found. Below these two layers and for the rest of the cross-section, the base NCI structure was found, see Fig. 3. The thickness of cast layer was approx. 36 µm and pearlitic layer was variable in the range from 80 to 110 µm. The sand blasting treatment removes the thin cast layer of oxides and pores and locally deforms the metal but cannot remove pearlitic layer. Fig. 5b shows that in the sand blast specimens the pearlite layer contains lamellar graphite, which gradually turns into vermicular and finally nodular shape going from the surface to the core of material. The combination of lower strength of pearlite matrix because of the presence of the lamellar graphite is expected to negatively affect the surface layer strength in case of fatigue loading because it results in early crack initiation compared to the presence of nodular graphite. Only fine grinding reduced significantly the surface roughness (i.e. by one order of magnitude) by complete elimination of the surface layers (formed by a thin cast layer of oxides and pores and layers with different structure than the core of material). The typical surface structure is shown in Fig. 3. The average surface roughness of fine ground specimens was $Ra = 2.3$ µm.

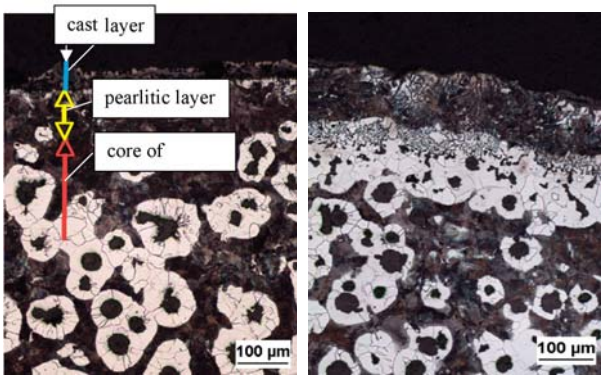

a) *b)*

Fig. 5 Typical structures of a) as-cast layer surface, b) sand blasted surface, etched 3% Nital

The investigation of the thermo-chemically treated NCI specimens showed that both nitriding and carbonitriding produced layers formed by a thin white layer (WL) on the specimen surface and diffused zone (DZ) below, Fig. 7. The white layer was continuous with thickness about 21 µm for nitrided surface and about 15 µm for carbonitrided surface and with the local presence of graphite nodules in both cases. Thicker nitrided and carbonitrided layer and diffused zone were identified in areas where graphite particles presence was observed and WL was found below the graphite nodules.

Vickers microhardness profiles of the nitrided or carbonitrided layers are presented in Fig. 8. The hardness decreases with distance from the surface, following the decreasing nitrogen diffusion in the diffused zone to the basic material. Fig. 8 shows that the trend of the hardness measurements on the cross sections of the two types thermo-chemical treated specimens is similar. The highest value of HV 0.02 = 978 was found in the white layer of nitrided specimens and HV 0.02 = 1088 in the white layer of carbonitrided specimens. The values of microhardness decreases with increasing distance from surface and 348 HV 0.02 is hardness of pearlite in core region.

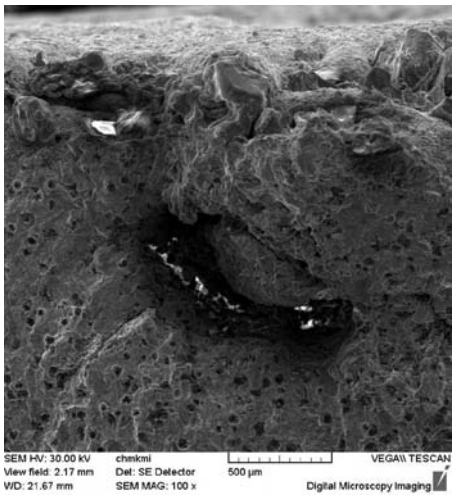

a) lustrous carbon film

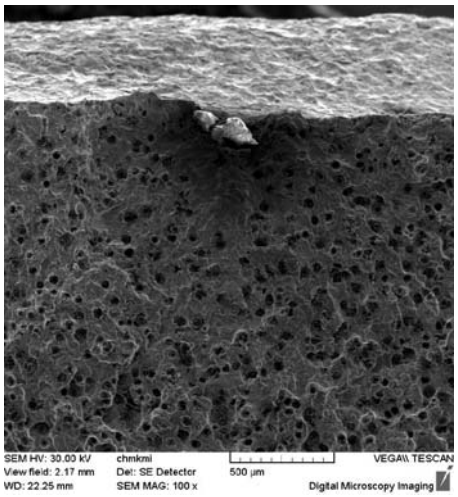

b) slag

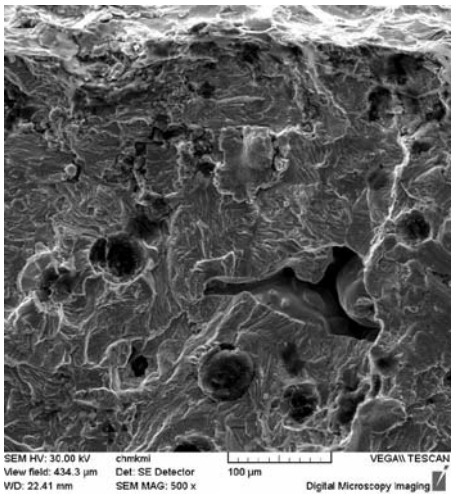

c) shrinkage

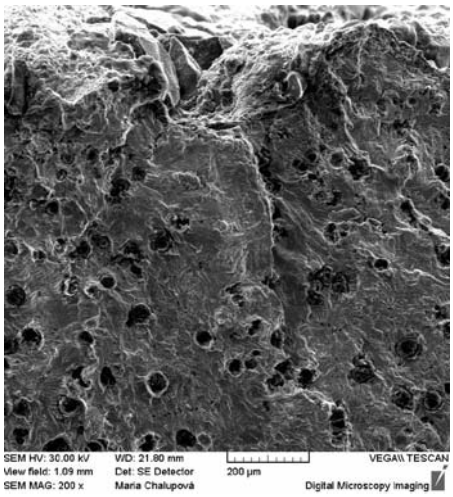

d) casting sand

Fig. 6 Fatigue crack initiation places in as-cast and sand blasted specimens, SEM

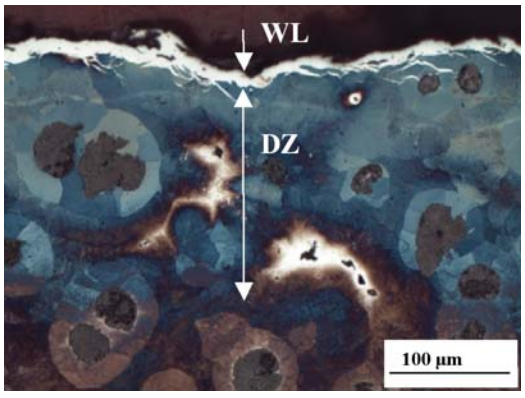

a)

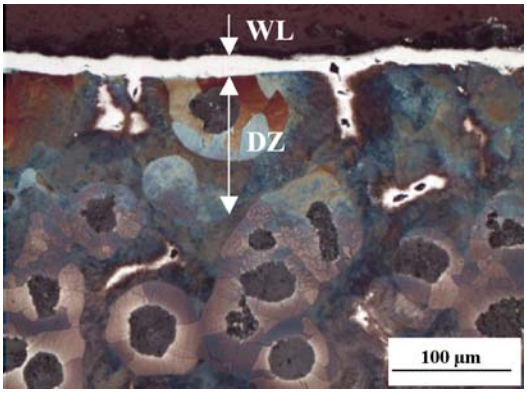

b)

Fig. 7 Structure of a) nitrided layer, b) carbonitrided layer, etched with Klemm II

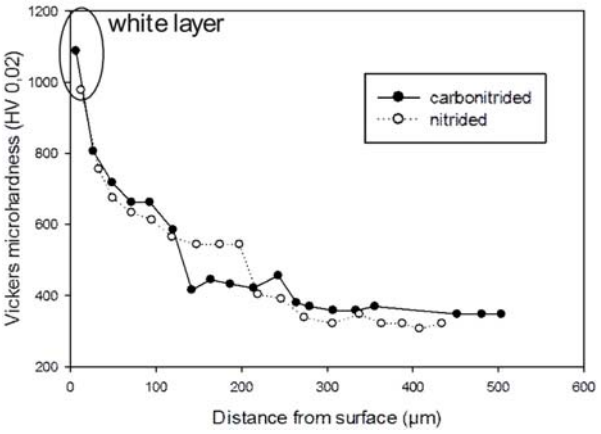

Fig. 8 Vickers microhardness measurements across the surface hardened layer

4. Conclusions

The surface characteristics of five different pearlite/ferritic NCI specimen sets and their fatigue behavior were investigated. From this study, the following conclusions can be drawn:

- The as-cast and sand blast surface condition produce similar and low fatigue strength of NCI specimens (70 MPa at 4.10^6 cycles for as-cast surface and 90 MPa at 2.10^6 cycles for sand blast surface) compared to the fine ground surface condition. Fine grinding of the NCI increases the fatigue strength of roughly 100 % (134 MPa at 2.10^6 cycles).
- Thermo-chemical treatment of smooth NCI specimens increases further the fatigue strength because of the hardened surface layer and the residual stress system. Carbonitriding and nitriding treatments achieve similar and considerable fatigue strength improvements (i.e. 50 %) compared to the untreated case (196,5 MPa at 2.10^6 cycles for carbonitrided surface and 201 MPa at 2.10^6 cycles for nitrided surface).
- Fatigue fracture origins of nodular cast iron with as-cast and sand blasted surface are largely attributed to the surface roughness and defects existing in the vicinity of the surface and sub-surface. The as-cast surface layers are characterized by the presence of many defects and a brittle surface structure due to the presence of lamellar graphite, which is very different from the base pearlite/ferritic metal microstructure with nodular graphite.

Acknowledgements

The research was supported by project VEGA grant No. 1/0196/12.

References

[1] CHAKHERLOU, T. N., MAHDINIA, Y.V., AKBARI, A.: Influence of Lustrous Carbon Defects on the Fatigue Life of Ductile Iron Castings Using Lost Foam Process. *Materials and Design,* 2011, vol. 32, pp. 162–169.
[2] MURAKAMI, Y.: *Metal Fatigue: Effect of Small Defects and Non-Metallic Inclusions.* Elsevier, 2002.
[3] YAACOUB AGHA, H., BERANGER, A. S., BILLARDON, R., HILD, F.: High-Cycle Fatigue Behavior of Spheroidal Graphite Cast Iron. *Fatigue Fracture of Eng. Materials Structures,* 1998, vol. 21(3), pp. 287–296.
[4] NADOT, Y., MENDEZ, J., RANGANATHAN, N., BERANGER, A. S.: Fatigue Life Assessment of Nodular Cast Iron Containing Casting Defects. *Fatigue Fracture of Eng. Materials Structures,* 1999, vol. 22, pp. 289–300.
[5] YAMABE, J., KOBAYASHI, M.: Influence of Casting Durfaces on Fatigue Strength of Ductile Cast Iron. *Fatigue Fracture of Eng. Materials Structures,* 2006, vol. 29, pp. 403–415.
[6] CHANTIER, I., BOBET V., BILLARDON, R., HILDA, F.: A Probabilistic Approach to Predict the very High-Cycle Fatigue Behavior of Apheroidal Graphite Cast Iron Structures. *Fatigue Fracture of Eng. Materials Structures,* 2000, vol. 23, pp. 173–180.
[7] TING, J. C., LAWRENCE JR., F. V.: Modeling the Long Life Fatigue Behavior of a Cast Aluminum Alloy. *Fatigue1 Fractures of Eng. Materials Structures,* 1993, vol. 16(6), pp. 631–47.
[8] GRANDT, A. F., SCHEUMANN, T. D., TODD, R. E., HINKLE, A. J.: Modeling the Influence of Initial Material Inhomogeneities on the Fatigue Life of Notched Components. *Fatigue Fractures of Engineering Materials Structures,* 1993, vol. 16(2), pp. 199–213.
[9] JAYET-GENDROT, S., GILLES, P., MIGNE, C.: Behavior of Duplex Stainless Casting Sdefects under Mechanical Loadings. *Nuclear Engineering and Design,* 2000, vol. 197 (1-2), pp. 141–153.
[10] HEULER, P., BERGER, C., MOTZ, J.: Fatigue Behavior of Steel Castings Containing Nearsurface defects. *Fatigue Fractures of Engineering Materials Structures,* 1992, vol. 16(1), pp. 115–36.
[11] NADOT, Y., DENIER. V.: Fatigue Failure of Suspension Arm: Experimental Analysis and Multiaxial Criterion. *Engineering Failure Analysis,* 2004, vol. 11(4), pp. 485–499.
[12] DAVIS, J.: *Cast Irons/Metallurgy and Properties of Ductile Cast Irons.* ASM Specialty Handbook, The Materials Information Society, USA 1996.
[13] NICOLETTO G., TUCCI, A., ESPOSITO, L.: Sliding Ear Behavior of nitrided and nitrocarburized cast irons. *Wear,* vol. 197, 1996, p.38–44.
[14] KOKAVEC, M., KONECNA, R., NICOLETTO G.: Influence of Surface Quality on Fatigue Behavior of Nodular Cast Iron. *Acta Metallurgica Slovaca,* 2011, No. 2, pp. 99–105.

[15] KONECNA, R., ZAHOROVA, B., MATEJKA, M.: Vplyv prisady SiC na porusovanie tvarnej liatiny [Influence of SiC Additives on Fracture of Nodular Cast Iron]. *Materialove inzinierstvo* 7 (4), 2000, p. 27–34.
[16] KUNZ, L.: *Experimentalni stanoveni unavovych charakteristik materialu* [*Experimental Determination of Fatigue Characteristics of Materials*], EDIS, Zilina, 2003 (in Czech).
[17] COSTA, N., MACHADO, N., SILVA, F. S.: A New Method of Prediction of Nodular Cast Iron Fatigue Limit. *Intern. J. of Fatigue,* 2010, vol. 32 (7), pp. 988–995.
[18] COLLINI, L., PIRONDI, A., BIANCHI, R., COVA, M., MILELLA, P. P.: Influence of Casting Defect on Fatigue Crack Initiation and Fatigue Limit of Ductile Cast Iron. *Procedia Engineering,* 2011, vol. 10, pp. 2898–2903.

https://doi.org/10.26552/com.C.2012.4.60-64

Katarina Istenikova – Dagmar Faktorova – Adriana Savin – Branislav Hadzima *

METAMATERIAL STRUCTURES AND POSSIBILITY OF THEIR APPLICATION IN MICROWAVE APPLICATOR OPTIMIZATION

Metamaterials are special one-, two- or three-dimensional artificial structures with electromagnetic properties generally not found in nature. Due to the simultaneous negative values of permittivity (ε) and permeability (μ), the wave vector and the vectors of electric- and magnetic-field intensity form a left-handed triplet with the result of antiparallel phase and group velocity and backwave propagation. These unique properties of the left-handed materials have allowed novel applications and devices to be developed. In this paper the metamaterial structures based on the split ring resonator approach for optimization of microwave applicator characteristic are used. The main field of the study is absorption of microwave-frequency field in human arm model and improvement of microwave applicator properties such a directivity and gain by means of simulations performed in CST Microwave Studio environment.

Keywords: *Metamaterial structure, waveguide, microwaves, human arm model.*

1. Introduction

Directive radiation pattern from open waveguide as a microwave applicator is strongly desirable to achieve high radiation power gain. This waveguide property is important for many technical and medical applications, which need to control the accurate electromagnetic (EM) beam focusing and maximum power gain achievement, e.g. in microwave hyperthermy therapy.

In the past few years, new methods for improving the microwave applicator gain by metamaterials were proposed [1–3] and theoretically discussed [4, 5]. Metamaterials, which are defined as effectively homogeneous electromagnetic structures exhibiting unusual electromagnetic properties, especially the backward wave and negative refraction not readily available in nature, represent a new paradigm in electronics and photonics [6]. In those works, various metallic structures are used as metamaterials to achieve certain unusual characteristics, which are suitable for high gain design [7]. However, most of those former works are suitable for high frequency applications, such as X-band or millimeter waves.

In this paper we describe approach with implementation of metamaterial structures (MMS) with negative permeability over the microwave applicator represented by open waveguide in order to increase the gain and achieve the optimal radiation pattern in microwave X-band to improve the control of electromagnetic field focusation in microwave hyperthermy therapy.

The paper is organized as follows. The paper presents the principle of interaction of electromagnetic field with layered human body tissues and principle of proposed metamaterial structure. Next simulated results for irradiation of human arm model using conventional and tuned open waveguide are presented.

2. Human body tissues and their interaction with electromagnetic field

Complex relative permittivity ($\dot{\varepsilon}_r$) is a parameter which is characterized by the interaction between the electric field and the bound charges in the material. Due to bound charges for lossy materials the permittivity is complex variable with both real (ε_r') and imaginary (ε_r'') components

$$\dot{\varepsilon}_r = \varepsilon_r' - j\varepsilon_r''.$$

Interaction between the electric field and the bound charges in tissue results in an oscillatory motion of the bound charges. The part of the motion that is 90° out of phase with the electric field is characterized by the real part of the permittivity (ε_r') and is described as a lossless interaction. But as the bound charges oscillate, they also heat up due to friction-like forces within the molecule and from molecules nearby. This motion component is in phase with the electric field and is represented by the imaginary part of the permittivity (ε_r'').

Thus, biological tissues are lossy materials and this loss changes the way how the wave interacts with the material and its propagation behavior. The energy will be accumulated in the lossy mater-

* **Katarina Istenikova[1], Dagmar Faktorova[1], Adriana Savin[2], Branislav Hadzima[3]**
[1] Department of Measurement and Applied Electrical Engineering, FEE, University of Zilina, Slovakia, E-mail: katarina.istenikova@fel.uniza.sk
[2] National Institute of Research and Development for Technical Physics, Iasi, Romania
[3] Department of Materials Engineering, FME, University of Zilina, Slovakia

ial as wave passes through it, thus causing loss of the propagating wave energy. EM energy causes the increasing of temperature in the material [8].

2.1 Reflection and transmission characteristics in layered body structures

If there are several layers of different tissues, the reflection and transmission characteristics of EM waves become more complicated [9]. Due to the different permittivity of the various layers a wave impinging on the human body suffers different reflections at each boundary between two organs with different value of the permittivity, Fig.1.

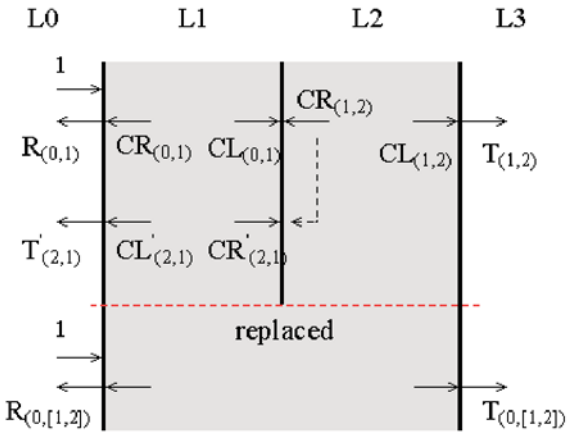

Fig. 1 Two-layered model with corresponding coefficients. CR and CL represents total sum of multiple reflections within sample, respectively

Hence, in the *i*-th layer, the electrical field is given by the sum of the incident field and of the reflected field from the $(i + 1)$-th layer

$$E_i = E_i^{inc} + E_i^{ref}$$

The propagation constant in the *i*-th layer is

$$\dot{k} = j\sqrt{\omega^2 \dot{\varepsilon}\dot{\mu}} = \frac{j\omega}{c}\sqrt{\varepsilon_r' - j\varepsilon_r''}$$

and hence, the attenuation in the *i*-th layer is

$$\alpha_i = \frac{\omega}{c}\mathrm{Im}\sqrt{\dot{\varepsilon}_r}$$

where $\dot{\varepsilon}_r$ and $\dot{\mu}_r$ represent relative permittivity and permeability of the layer separately, ω is angular frequency, c is velocity of light in vacuum [10] and for biological tissue $\mu_r = 1$. According to that, if a classical antenna for medical purposes is matched to the air, almost all radiated field is back reflected at the air/skin interface (approximately 70% of the radiated signal). From these results it follows that proper microwave hyperthermy applicators optimized for in-body transmission are an imperative task [10].

3. Metamaterials structure

The currently available artificial structures are realized by using planar structures with specific topology in x–y plane. These planar structures provide enhanced permeability only in the direction normal to the plane of the MMS and enhanced permittivity in the directions tangent to the plane [10]. In our paper we study the influence of negative permittivity and permeability medium on the performances of a microwave generator represented by waveguide.

Metamaterial structure used for waveguide antenna tuning consists on one side of substrate of arrays of split rectangle resonators unit cells (SRR), which were designed by Pendry et al. [10]. SRR can be described as LC resonant circuits which can be excited by a time-varying electromagnetic field with a non-negligible component applied parallel to the SRR axis. SRR structure behaves like magnetically active material in the microwave frequency range. The complex effective relative permeability of SRR structure is given by [10], [11]

$$\dot{\mu}_{eff} = 1 - \frac{f_{mp}^2 - f_0^2}{f^2 - f_0^2 - j\gamma f},$$

where f is the frequency of microwave signal, f_{mp} is the magnetic plasma frequency, f_0 is resonant frequency of SRR structure, γ is conductivity.

On the other side of the substrate the disrupted wires array is placed, which behaves like electrically active material in the microwave frequency range. The array of parallel disrupted wires exhibits the high-pass properties for plane wave with electric vector intensity parallel to the wires. In the case when the distance between wires is smaller than the wave length of incident electromagnetic wave, the array can be taken as continuous plasma. The complex effective relative permittivity of wire structure is given by [11, 12]

$$\dot{\varepsilon}_{eff} = 1 - \frac{f_{ep}^2}{f^2 - j\gamma f},$$

where f_{ep} is plasma frequency, which generally depends on the geometry of wire structure like a wire radius and wire lattice constant.

Metamaterial placed in the radiation area of the open waveguide which functions as an antenna plays a role of controlling the EM wave propagation direction. In the far-field view, the sideward radiation will be reduced and forward radiation can be enhanced in the radiation patterns. As a result, a more directional and higher waveguide gain will be obtained.

The SRR structure is strongly resonant around the magnetic plasma frequency ω_{mp}, which is induced by the currents and split which imitates magnetic poles. This resonant behavior is due to the capacitive element such as splits and in turn results in very high positive and negative values of permeability close to the magnetic

plasma frequency. The SRR would yield a negative value of permeability in the case when $\omega < \omega_{mp}$. The disrupted wire structure is strongly resonant around the electric plasma frequency ω_{ep}. Structure of thin wires of conductors periodically placed into dielectric substrate results a well defined plasmonic behavior also at microwave range. The wire structure yields a negative value of permittivity in the case when $\omega < \omega_{ep}$ [13].

To investigate the focusing and gain upping effect of SRR structure in this work the waveguide with metamaterial structure was tuned. The region of metamaterial structure negative permeability was proposed to embody the working frequency 12 GHz of designed conventional waveguide WR-90.

4. Numerical simulations

4.1 Model creation in CST microwave studio software

Numerical simulations were performed with assistance of the CST Microwave Studio environment which is suitable for electromagnetic simulation of high frequency components. Metamaterial structure with double SRR with outer dimensions 5×5 mm and thickness of the copper 35 μm, Fig. 2, was designated for conventional waveguide WR-90 tuning. The SRR are placed on the high frequency laminate Rogers RT/Duroid 5870 with relative permittivity $\varepsilon_r = 2.33$ and thickness of the dielectric substrate $h = 0.508$ mm in the form of a 2–D and provide negative reflection of phase. The number of unit resonant cells along the x and y axis was chosen 7×7 to fit waveguide dimensions. On the other side of the substrate the disrupted wires are placed. The incident EM wave propagates along the z direction, while the vector of electric intensity E is oriented along the y direction, and magnetic intensity H is oriented along the x direction.

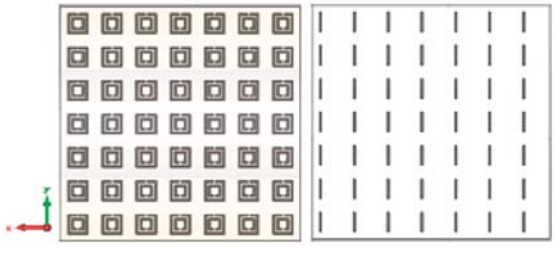

Fig. 2 Design of the metamaterial structure (front and back side)

Waveguide WR-90 working at the X-band frequency region was designed from PEC material (perfect electric conductor) with symmetry planes shown in Fig. 3; in *yz* plane there is a magnetic symmetry and in *xz* plane the electric symmetry. The whole simulated structure and waveguide are surrounded with vacuum.

Distance between the open waveguide and metamaterial structure influences the performance of the waveguide. Therefore this parameter was numerically optimized. The simulation results in Fig. 4 have shown how this distance influences the gain of the waveguide. According to numerical results the optimal distance of metamaterial structure and conventional open waveguide was set on 18 mm.

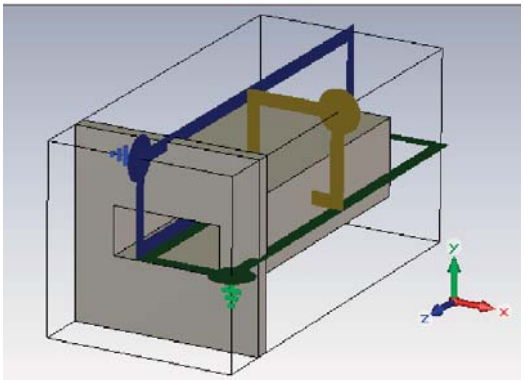

Fig. 3 Symmetry planes of the waveguide (magnetic symmetry in yz plane, electric symmetry in xz plane)

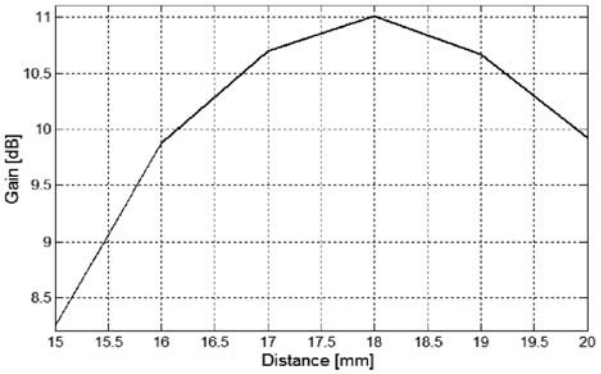

Fig. 4 Dependence between the gain of the tuned open waveguide and waveguide/metamaterial structure distance

In case that metamaterial structure is placed in 18 mm distance in front of the open waveguide, the gain at the frequency 12 GHz increased from 8.23 dB to 10.95 dB. According to calculation the directivity of tuned open waveguide was after metamaterial structure incorporation increased from 8.28 dBi to 11.01 dBi.

Finally, to investigate power loss density as a main measure used in numerical dosimetry, the model of human arm consisting of four different biological structures in isothermal conditions of background was processed, Fig. 5.

Dielectric parameters used for different layers of biological sample were loaded from material library of CST Microwave Studio Suite. These data are presented in Tab. 1.

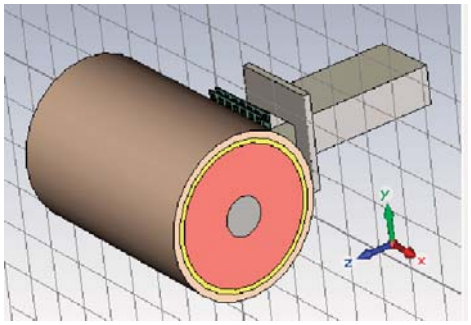

Fig. 5 Arrangement of the numerical simulations

Dielectric properties of biological layers Table 1

	Radius (d mm)	Permittivity εr (-)	Conductivity σ (S/m)
skin	3	41	0.7
fat	2	5	0.04
muscle	20	42.7	10.6
bone	10	12	0.95

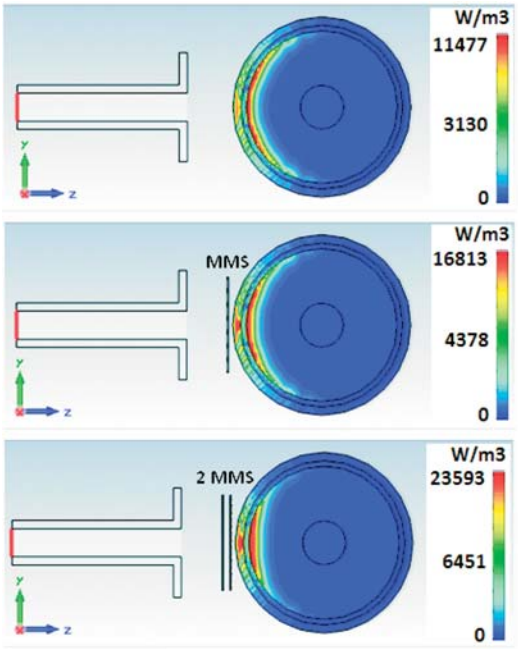

Fig. 6 Influence of the number of metamaterial structures (MMS) on the power loss density in the human arm model

Besides the sufficient sampling of the fields, it was very important to obtain a good approximation of the structure within the mesh. The simulated structure and the electromagnetic fields were mapped to hexagonal mesh. For the spatial discretization with a hexahedral grid, the Finite Integration Method in conjunction with the Perfect Boundary Approximation (PBA) was used, which maps the structure from the continuous world into the mesh of the discrete world. For a good compromise between the need of an accurate structure and field discretization and a short simulation time the number of meshcells was set on 10 millions.

4.2 Results of the numerical simulations

Power loss density closely connecting with SAR parameter was demonstrated at the frequency 12 GHz which falls into the X-band frequency range. The electric field vector was parallel to longitudinal axis of the models.

Power loss density value for presented human arm model at frequency 12 GHz is shown in Fig. 6. Local power loss density was given as a numerical value per volume element and becomes a space distribution function.

In the first case the human arm model by waveguide WR 90 was irradiated. The maximum value of the power loss density reaches 11477 W/m3 and was scattered in the muscle layer in direction radiation pattern from the waveguide. In the second simulation the suggested metamaterial structure between the open waveguide and human arm model was placed. As was shown in the color range, metamaterial structure causes increasing value of power loss density in irradiated area of the model in comparison with non-tuned open waveguide case from 11477 to 16813 W/m3. In the third simulation the additional metamaterial structure was added between the open waveguide and model, so that optimal distance 18 mm between the structure and waveguide was hold. The additional metamaterial structure caused subsequent increasing of the directivity which led into the doubled focusation of electromagnetic energy (23593 W/m3) in comparison with non-tuned open waveguide case and the electromagnetic energy was much more concentrated in the impact area of the metamaterial structure.

However, in Fig. 6 it can be seen that used EM field in the fat layer created subdermal hot spots which are complicated to treat and thus, must be avoided. A common way of mitigating this effect is to place a layer of water between the microwave source and the irradiated part of human body.

5. Conclusions

The experimental and numerical results connected with the study of dielectric properties of biological materials and, on the other hand the influence of dielectric properties of biological materials on electromagnetic wave propagation gives us the information very useful in medical therapy using microwaves.

In this work the appropriate metamaterial structure was suggested by using CST Microwave Studio software for operating waveguide frequency in the negative region metamaterial structure permeability. The numerical simulations were used at the designing of both, microwave applicator and metamaterial structure.

Also for the calculation of microwave applicator parameters such gain and directivity with numerical simulation using commercial software was done.

The simulation results showed that appropriate design of metamaterial structure improves the constitutive properties of microwave applicator – gain and directivity. The presented numerical results are useful at the microwave applicator parameters optimization used for microwave hyperthermia at malignant tumors treatment. The obtained numerical results can be also useful at microwave tomography of chosen human body parts.

Acknowledgements

This work has been supported from Slovak Research and development agency APVV Bilateral project SK-RO-0015-10 and Tatra banka grand program "Studenti do sveta" as the project 11sds046. The authors are grateful for the support of experimental works by project VEGA No. 1/0100/11 and No. 1/0743/12.

The author would like to thank Technische Universitat Ilmenau in Germany for support of this work by international program IPID – International Promovieren in Deutschland.

References

[1] TAJEH, G. et al.: *Compact Directive Antennas Using Metamaterials.* 12th Intern. Symposium on Antennas, 2002, pp. 101–104.
[2] LEI, Z. et al.: Directive Emissions from Subwavelenght Metamaterial – Based Cavities. *Appl. Phys. Lett,* 2005, vol. 53, pp. 1–3.
[3] ALICI, K. B. F. et al.: Optimization and Tenability of Deep Subwavelenght Resonators for Metamaterial Applications: Complete Enhanced Transmission through a Subwavelenght Aperture. *Opt. Express,* 2009, vol. 17, pp. 5933–5943.
[4] ALU, A. ET AL.: Metamaterials Covers Over a Small Aperture. *IEEE Trans. on Antenna and Propagation,* 2006, vol. 54, pp. 1632–1642.
[5] FAKTOROVA, D.: *Mater. Eng. - Mater. inz.* 16, 2009, 9–13.
[6] BAENA, J. D., BONACHE, J., MARTIN, F. et al.: Equivalent-Circuit Models for Split-Ring Resonators and Complementary Split Ring Resonators Coupled to Planar Transmission Lines. *IEEE Transactions on Microwave Theory and Techniques,* 2005, vol. 53, pp. 1451–1461.
[7] LAI, A., CALOZ, C., ITOH, T.: Composite Right/Left-Handed Transmission Line Metamaterials. *IEEE Microwave Magazine,* 2004, vol. 5, pp. 34–50.
[8] PEYMAN, A.: *Dielectric Properties of Tissues, Variation with Structure and Composition.* Proc. of Conference ICAA, 2004, pp. 863–864.
[9] KOZLIKOVA, K., MARTINKA, J.: *Zaklady spracovania biomedicinskych merani - cast II.* [*Basics of Biomedical Measurements Processing - part II.*]. ASKLEPIOS, Bratislava 2009, ISBN 978-80-7167-137-4, 202 p.
[10] PANCERA, E., BARBA, H., LI, X., JALILVAND, M., ZWICK, T.: *UWB Antennas Optimization for In-Body Radiation.* Proc. of the 6th German Microwave Conference, 2011.
[11] PENDRY, J. B.: Magnetism Covers Over a Small Aperture. *IEEE Trans. Microwave Theor. Tech.,* 1999, vol. 47, pp. 2075–2084.
[12] LIU, Y. H., ZHAO, X. P.: Investigation of Anisotropic Negative Permeability Medium Cover for Patch Antenna. *IET Microwave, Antennas and Propagation,* 2008, vol. 2, pp. 737–744.
[13] FAKTOROVA, D., OMELKA, P., ISTENIKOVA, K.: Antenna Parameters Enhancement by Using Artificial Magnetic Structure. *J. of Electrical Engineering,* 2010, vol. 61, pp. 156–159.

https://doi.org/10.26552/com.C.2012.4.65-72

Vincent Kvocak – Pavol Beke – Renata Vargova *

T- JOINTS – EXPERIMENTAL AND NUMERICAL ANALYSIS

The article presented focuses on the comparison of the measurement results obtained in laboratory experiments on joints of a lattice girder. Because of the geometric variety of joints, the article presented concentrated selectively on hinged T-joints only. The geometry of this type of joint consists of two fundamental members: the chord and the brace member. The T-joints examined were always composed of the rectangular chord member in combination with a variety of types (rectangular, circular and open) and dimensions of brace members. The scientific research results and evaluations presented characterize the correlations regarding the global resistance of joints in lattice structures in the light of the latest scientific knowledge that should be responsibly taken into consideration in their reliable and cost-effective design.

Keywords: *T-joints, circular hollow sections, rectangular hollow sections, HEA-sections, vertical and horizontal deformation.*

1. Introduction

The gradual increase in the production range of hollow sections has resulted in their more common application in various areas and types of construction. This type of section can find a number of applications in the construction industry, especially in structures where attractive general appearance of the whole structure is required [1].

From the point of view of a structural designer, the application of hollow section joints presents relatively effective utilisation of the material. The distribution of the material and its mass in hollow section joints brings several advantages for various kinds of load. Their application is one of the best design solutions in members under compression, with respect to their buckling, as well as in members loaded in bending, with respect to their lateral-torsional buckling as well.

As far as strain is concerned, joints present the most exposed areas in structures composed of such types of section. Joints composed of rectangular hollow sections have recently received quite close attention. Our experimental research programme concerns the hollow-section joints combined with other kinds of section [2].

The article presents the results of the experimental programme that has been carried out at the Faculty of Civil Engineering of the Technical University in Košice. Attention is paid to the joints composed of rectangular and circular hollow sections, and HEA-type open sections. These are all T-joints where the continuous chord member is made of a rectangular hollow section in each type of specimen. The brace members vary in section in terms of type and dimensions. Due to a large variety of combinations of sections in terms of their type and dimensions, the authors of the article are planning to extend their research and supplement the results gradually by using some other combinations and types of section in the future.

2. Experimental analysis

2.1 Experimental plan

Hollow sections are applicable particularly in the construction of lattice structures. In the design of such structural members the essential loading component is an axial force – either in tension or in compression. Given these facts can be concluded that the joint in a lattice structure belongs to one of the most exposed areas. When designing the joint itself it is necessary to take into consideration a number of factors having an impact on its stiffness, such as geometrical data, the stiffness and strength ratios between the chord and brace members, and similarly, the slenderness ratios of web sections, material properties and, last but not least, the magnitude of action [4].

On the basis of the mentioned above requirements, an experimental programme was drawn up whose purpose was to verify and supplement the acquired knowledge on the actual behaviour of joints in lattice structures with rectangular hollow sections, also depending on combinations of various types of hollow section and hollow and open sections [4–5].

As the scope of the problem under investigation is so vast, attention was focused on and limited to T–joints. The angle between the chord and brace members was identical in all cases, i.e. 90°. For the chord member of the joint under investigation, the upper compression member of a lattice structure was selected, while the

* **Vincent Kvocak, Pavol Beke, Renata Vargova**
Faculty of Civil Engineering, Technical University of Kosice, Slovakia, E-mail: vincent.kvocak@tuke.sk

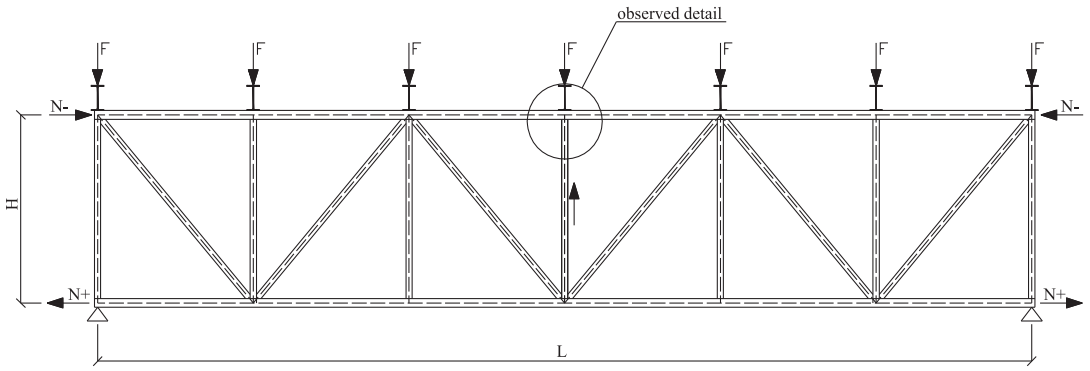

Fig. 1 Arrangement of joint members and their mutual action

brace member was the vertical compression member in a lattice structure. The arrangement of the joint members and their mutual action is shown in the following Fig. 1.

From the geometrical point of view, three types of joint were compared. In the first type, both the chord and brace members were composed of rectangular hollow sections. In the second type of joint, the chord member consisted of a rectangular hollow section, whereas the vertical brace member was made of a circular hollow section. In the third variant of joint, similar to the previous types, the chord member was composed of a rectangular hollow section and the brace member was represented by an open HEA-section. For the purpose of mutual comparison of the results obtained for the individual types of section, the dimensions and the cross-section of the chord member always remained equal [5].

The brace member varied both in size and shape of section. The ratio of the mean diameter or width of the vertical brace member, to that of the horizontal chord is called the β−parameter. In rectangular and circular sections was applied β = 0.43 (60/140), 0.71 (100/140) and 1.0 (140/140) respectively. HEA-sections are an exception where the experimental programme had to be adjusted to the rolling mill plan for such types of section. In this type of joint, β−parameters were 0.71 (100/140), 0.86 (120/140) and 1.0 (140/140) respectively. Thus, for rectangular hollow sections, the following sections were selected: RHS 140 × 140 × 4, RHS 100 × 100 × 3, RHS 60 × 60 × 3, for circular bracing members: CHS 140 × 5, CHS 100 × 5, CHS 60 × 4 and for open sections: HEA 140, HEA 120, and HEA 100. The chord member for each type of joint composed of RHS 140 × 140 × 4. The β−parameter was one of the most significant factors in the comparison and evaluation of the resulting effects of action of joints of circular, rectangular and open rolled-steel HEA sections. The goal of the research was to cover the greatest possible spectrum of β−parameters [6].

The above parameters made it possible to create a total of nine experimental types of joint (three joints consisting of circular sections, three joints consisting of square sections, and finally, three joints with open brace members). For each test type/set of joints there were subsets of three identical test specimens. Geometry of test specimens and shape of loading test assembly is shown in Fig. 2.

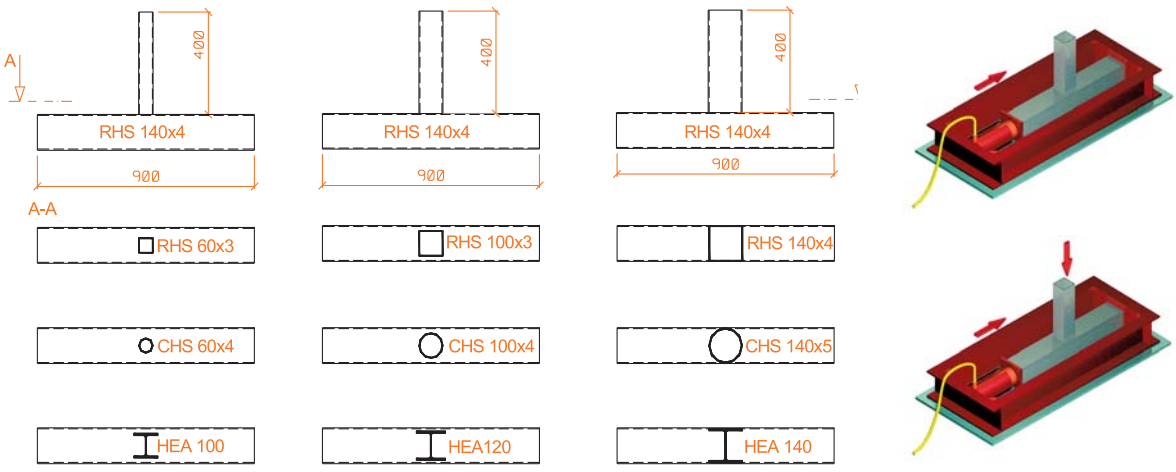

Fig. 2 Geometry of test specimens

All models were made of steel S235 and a specimen of each model was taken to analyse its material characteristics. The yield strength in all specimens did not exceed the one declared by the steel manufacturer and it varied between 290 and 320MPa.

To simulate the real behaviour of the joint in a lattice structure, the chord member was assumed to act in horizontal compression, while the brace members were compressed in a vertical direction. Horizontal compression was actuated by means of an additional frame and pneumatic press (see Fig. 2). The numerical value of horizontal load remained constant during the whole loading period. Each specimen type was tested at three horizontal force levels: 68 kN, 115kN and 192kN. Vertical load imposed on the specimens by the main hydraulic press was gradually increased until the total failure of the specimen. With respect to the complexity of the task, the length of the brace member was designed so as to prevent buckling of the member.

Measurement points on the individual specimens were then selected. Strain gauges were used to measure stress in the specimens and inductive sensors to determine horizontal and vertical deformations. During the strain-gauge measurements attention was focused on the chord member as, based on the calculation model, the joints under investigation collapsed due to the failure of the chord member in particular. Stresses were examined both in the horizontal and vertical webs of the chord and the strain gauges were attached in both longitudinal and transverse directions. Arrangement of strain gauges is shown in Fig. 3a. As can be seen from Fig. 3b, deformation was measured mainly in the chord members, specifically in the upper horizontal and vertical webs of the chord member section.

tions and to this end – to simulate such conditions – the above mentioned software seemed to be the most suitable.

The process of constructing a theoretical model with the aid of the mentioned above software package consists of several steps. The external CAD description of the structure's geometric features is fundamental to the construction of such a model. The structure's geometry was imported into the Ansys software package by means of an external pre-existing SAT file. Once the finite element geometric model was created and checked, the joint to be analysed was divided into finite elements. After generating and refining the mesh network in the model, the structural simulation module was activated. Here, the simulation module serves the purpose of determining the type of computation and thus imposing proper boundary conditions – support and loading constraints. In the joint analysis a static structural analysis module was applied.

The most complex issue in the construction of a theoretical model is the proper specification of constraints. The constraints were imposed with special attention paid to the real behaviour of the joint in the course of the experiment. The correctness of the support constraints was verified by comparison with the theoretical and real deformation curves.

The simulation of loading conditions was compatible with the experimental measurements, and the load was applied on both chord and brace members. The horizontal load was considered to be constant, while the vertical load was gradually increased.

Material non-linearity was taken into account by using Young's modulus with linear strain hardening in the model. The yield strength

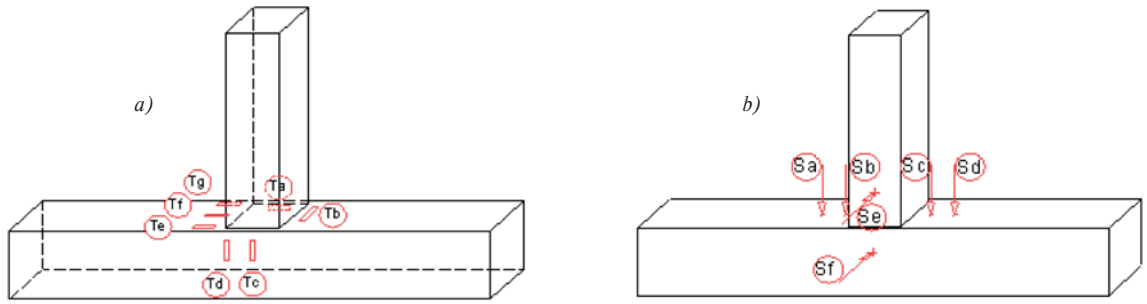

Fig. 3 Arrangement of (a) strain gauges, (b) inductive sensors and deformeters

2.2 Theoretical Finite Element Analysis model

For the purpose of verifying and confirming the experimental measurements theoretical models of the joints under investigation were constructed using the software package Ansys 11, specifically its graphical upgrade Workbench 11 [7–8].

In order to obtain the most credible results, it was necessary to consider both geometric and material non-linearity in the calculacorresponded to its true value that was obtained in tensile tests. Geometric non-linearity was taken into consideration by activating the function of large deflections.

After the input of all necessary characteristics the computation itself was conducted. The evaluation of the joint was carried out on the basis of deformations/strains or stresses. Considering the fact that the stresses (strains) could not be compared with the

experiment in a precise manner, the deformations of the joint were essential for the comparison. Although it was not possible to pinpoint precisely where strains were evaluated in the experimental measurement, the theoretical stress analysis provides an overall view of the joint behaviour. From the stress-related point of view, it made possible the evaluation of the points that could not be included for practical reasons, especially those on the interior webs of the chord member. In conclusion, the construction of the theoretical model confirmed the experimental results and facilitated the analysis of other joints.

3. Obtained results

The types of joints selected were observed for both stress and deformation. In the following section of the article, attention will be directed to the deformation of the joints. The following sections provide an exact view of the real behaviour of the individual types of joint. The figures presented compare both vertical and horizontal experimentally measured deformations of the joints.

3.1 Comparison of deformations in the joints consisting of the identical type of the brace member

The joints with the identical type of the brace member are compared (Fig. 4 – RHS sections, Fig. 5 – CHS sections and Fig. 6 – HEA sections). First, when there is linear deformation, the joint is in the elastic range. Later, as the load is increased, the joints deviate from this linear proportionality and the deformation goes through the elasto-plastic and eventually into its plastic range of action.

Of all the types of brace members, the most resistant certainly seem to be those with $b_0 = b_1$ ($\beta = 1$). From the deformation point of view, the joints with a width of 60 mm are the least suitable. These exhibited excessive deformations even under minimal load.

3.2 Comparison of deformations in the joints with the same widths of chord and brace members

The stiffness of the joint does not depend only on its dimensions but also on the type of the brace member used. The comparisons are presented in the form of the following Figs. 7–9.

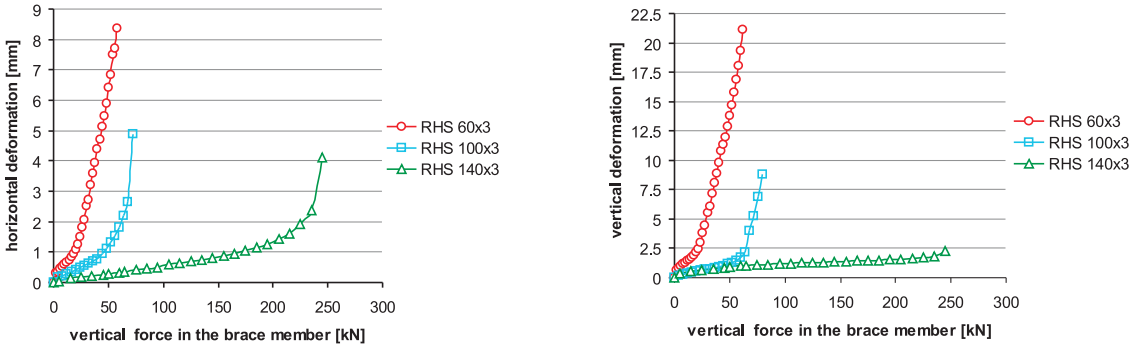

Fig. 4 Comparison of the experimentally measured horizontal and vertical deformations in the joints composed of the brace members with rectangular hollow sections

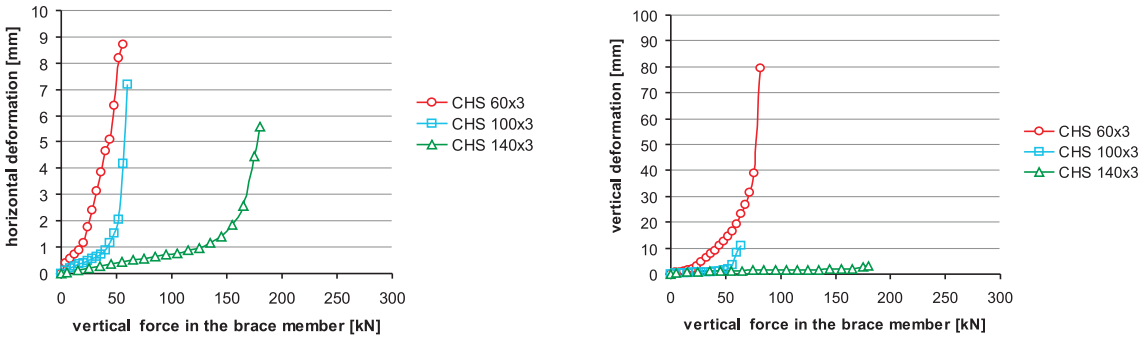

Fig. 5 Comparison of the experimentally measured horizontal and vertical deformations in the joints composed of the brace members with circular hollow sections

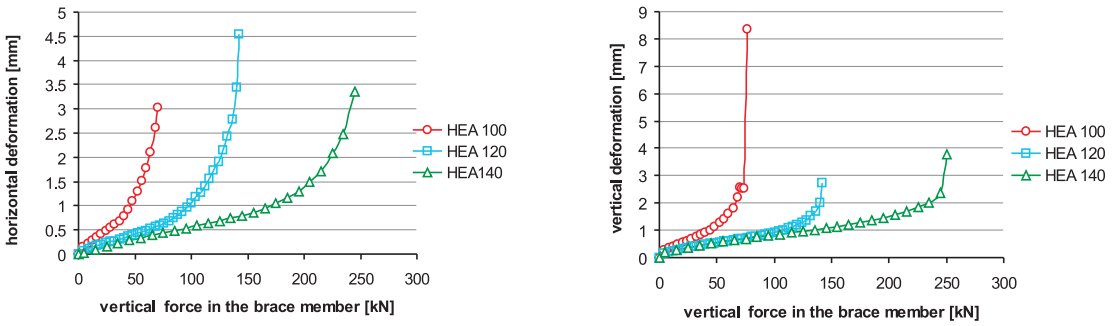

Fig. 6 Comparison of the experimentally measured horizontal and vertical deformations in the joints composed of the brace members with open HEA-sections

In the first type of joint ($\beta = 1$), the stability of the chord web was crucial for the overall resistance of the joint. Figure 7 presents the distribution of values of vertical and horizontal deformation. Significant deformation of the vertical chord web occurred even under a relatively light vertical load. The joint collapsed completely with the gradual increase in load due to the buckling of the vertical web of the horizontal chord member. When the resistance of rectangular, circular and open sections was compared, the rectangular sections proved to be the stiffest.

As can be seen from Fig. 8, the buckling effect of the chord web on the overall resistance of the joint can be observed also in the joints with $\beta = 0.714$. The overall resistance of the joint was influenced by the loss of stability of the vertical web although the difference between the vertical and horizontal deformation was less significant than in the first case. When comparing the types of brace member used, the rectangular section appeared to be the most resistant of all. However, the difference between the rectangular and open HEA-section was minimal regarding vertical and horizontal deformations.

In the third type of joint (Fig. 9) with the most slender brace members, the overall resistance of the joint was to a great extent affected by the stiffness of the horizontal chord web. The difference

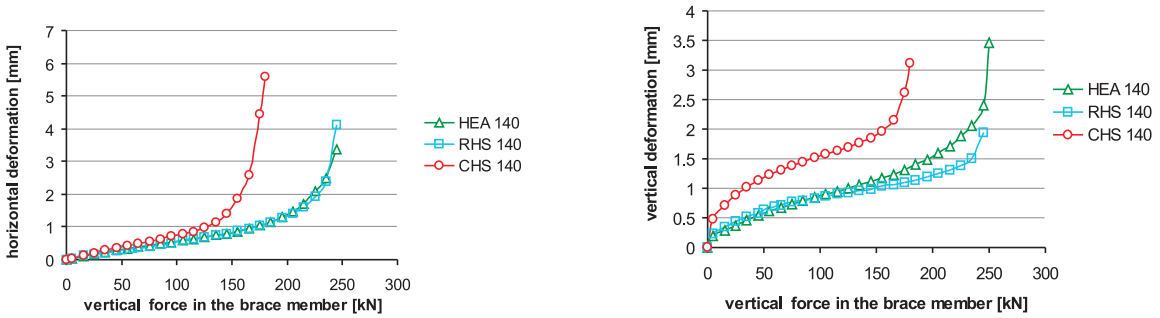

Fig. 7 Horizontal and vertical deformation of the T-joint with β = 1.00 depending on the type of brace member used

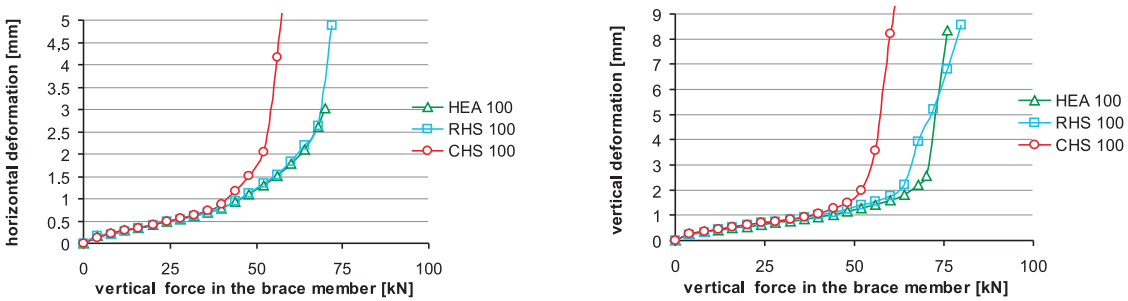

Fig. 8 Horizontal and vertical deformation of the T-joint with β = 0.714 depending on the type of brace member used

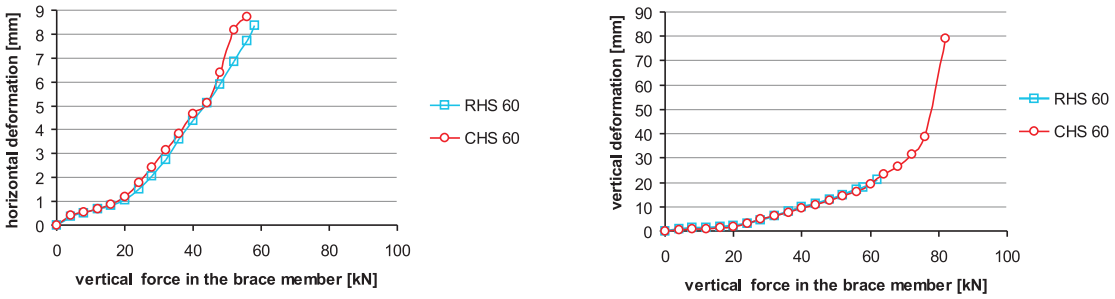

Fig. 9 Horizontal and vertical deformation of the T-joint with β=0.428 depending on the type of brace member used

between the horizontal and vertical deformation in this type of joint is the biggest and the vertical deformation the greatest. The influence of the type of the brace member used on the overall resistance of such joints is virtually negligible. Due to the limited possibilities of the HEA rolling programme, only circular and rectangular hollow sections were compared. For $\beta = 0.714$ the behaviour of open sections was identical to that of rectangular sections and, obviously, it does not change for lower β-parameters.

4. Resistances of the individual types of joints

Two essential loading states were recorded during the entire loading cycle: one represented the resistance of the joint and the other at which the joint failed.

The resistance of the joint is the loading point at which, without increasing the load, deformation continues to rise. This point is the state when the joint departs from its elastic range and gradually goes from the elasto-plastic into the plastic range of behaviour. The resistances of the joints in horizontal compression in the chord of 192kN are given in Table 1.

The table above compares the experimental values of resistances with the resistances determined using different calculation techniques. For the determination of the experimental resistances the joints with the most subtle brace members seemed to be most problematic. With this type of joint, it was impossible during the loading cycle to specify the load that would correspond to the resistance of the joint. No plastic flow occurred even during the heaviest vertical load, nevertheless, the joints exhibited excessive deformations even during the smallest vertical loads. Therefore, the resistance was determined on the basis of the limit of deformation (Table 2). The vertical deformation of 1.5 mm that occurred at the vertical load of 20 kN was considered as the limit of deformation. The limit deformation of 1.50 mm corresponds to measured points Sb and Sc (see Fig. 3). The given resistance corresponds to the joints with both rectangular and circular brace member sections.

Comparison of the resistances of various joints determined using different calculation techniques — Table 1.

	Joint resistances [kN]				
	Experiment	STN EN 1993-1- 8	ANSYS	Exp/STN EN	Exp/Ansys
RHS 60	21	21	19	1.00	1.11
RHS 80	–	35	30	–	–
RHS100	56	54	55	0.96	1.02
RHS120	–	146	141	–	–
RHS140	170	165	167	0.97	1.02
CHS 60	21	16	20	0.80	1.00
CHS 80	–	27	26	–	–
CHS100	49	42	46	0.86	1.07
CHS120	–	109	109	–	–
CHS140	130	129	120	0.99	1.08
HEA 60	–	–	20	–	–
HEA 80		–	34	–	–
HEA 100	42	–	44	–	0.95
HEA 120	101	–	102	–	0.99
HEA 140	191	–	195	–	0.98

Resistances of the individual specimen types together with the horizontal and vertical deformations at the ultimate limit state

Table 2.

Brace member section	Experiment resistance [kN]	Vertical deformation [mm]	Horizontal deformation [mm]
RHS 60×3	21	1.50	0.74
RHS 100×3	56	1.29	1.39
RHS 140×4	170	0.59	0.91
CHS 60×4	20	1.51	0.86
CHS 100×4	49	1.47	1.69
CHS 140×5	130	0.89	1.04
HEA100	42	0.72	0.72
HEA120	101	0.82	1.00
HEA140	191	1.06	1.24

In the determination of the design resistance values, according to the standards, the resistances of the joints with open HEA brace member sections are omitted. The relevant standard, on the basis of which the resistances were determined, makes provisions for such types of joint but takes a different joint geometry into account (providing that the brace member is rotated by 90°).

The following Fig. 10 represents the resistances for the individual types of joint. The values obtained in the experimental measurements, those determined in compliance with the standard requirements set by STN EN 1993-1-8 [9], those determined using the FEA computation models are compared.

5. Conclusion

The article presented points to the significance and actuality of the issue of investigating the joints in lattice structures. The priority of the research was to acquire knowledge of the real behaviour of the joints and supplement it with more effective methods for the design of joints composed of rectangular and circular hollow sections, and open HEA-sections. Because of the geometric variety of joints, the work presented concentrated selectively on hinged T-joints only. T-joints along with other basic uniplanar joints create basic members in lattice structures. The geometry of this type of joint consists of two fundamental members: the chord and the brace member. The T-joints examined were always composed of the rectangular chord member in combination with a variety of types (rectangular, circular and open) and dimensions of brace members.

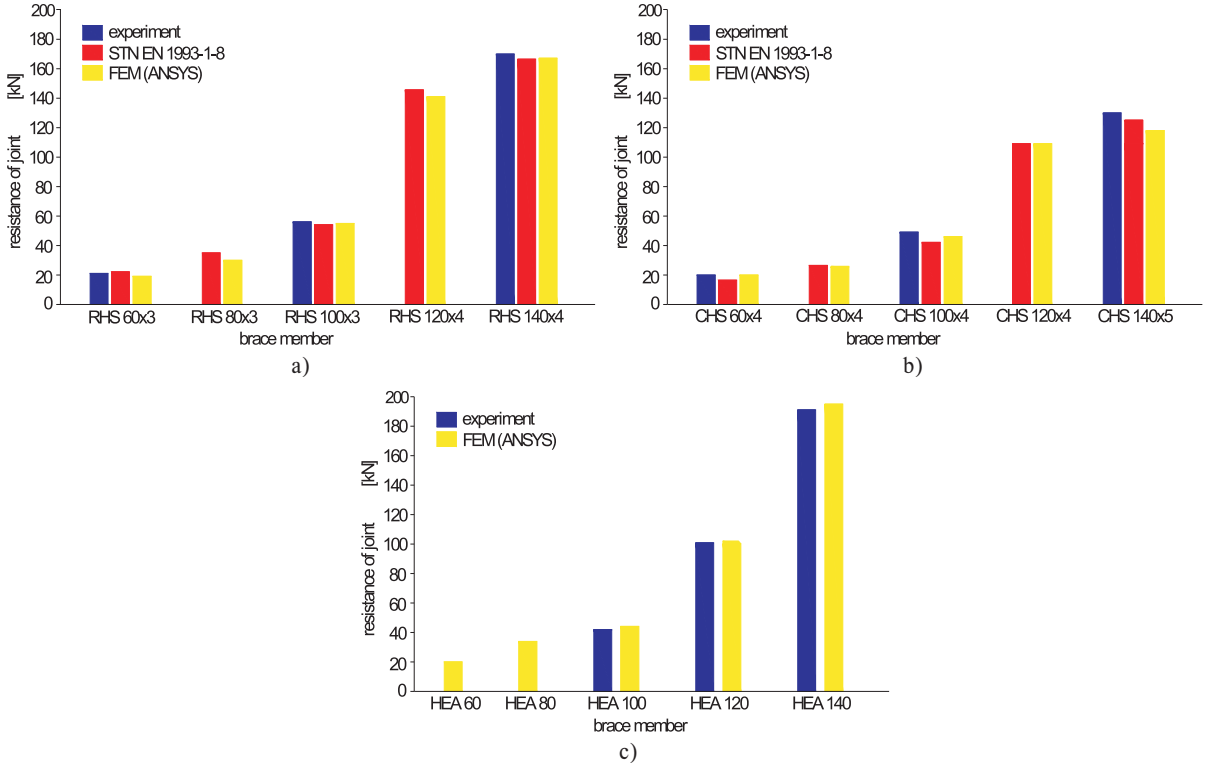

Fig. 10 Resistances comparison of the joints composed of a) rectangular hollow section brace b) circular hollow section and c) open HEA-section brace members

From the results obtained some patterns of behaviour of T-joints may be identified. With respect to the geometry and type of section, it can be concluded that the resistance of a joint with $\beta = 1.00$ is greatly influenced by the type of brace member. This influence sharply diminishes with the decreasing value of a β-parameter. With very low β-parameters, the influence of the type of brace member becomes virtually negligible and unimportant.

The application of joints composed of hollow sections is encouraged in the standards for the design of steel structures currently in force. The standards; however, make no provisions for combinations of hollow and open sections. The research presented in the article underlines the need for the re-evaluation of the criteria set in the current standards. These should be supplemented with new perfectly legitimate normative requirements for the resistances of the above-mentioned joints according to the presented results. Nowadays authors prepared the analysis of such joints, while the main emphasis is placed on the verification of the obtained results using an appropriate finite model for the joints in question.

Acknowledgment

This research has been carried out in terms of the project NFP 26220120037 "Centre of excellent research of the progressive building structures, materials and technologies", supported from the European Union Structural funds and Grant VEGA No. 1/0788/12: "Theoretical and Experimental Analysis of Stability and Strength of Composite Members in Compression and Bending" of the grant agency VEGA of the Ministry of Education of the Slovak Republic and the Slovak Academy of Science.

References

[1] PACKER, J.A., WARDENIER J., KUROBANE Y., DUTTA D., YEOMANS N.: *Design Guide for Rectangular Hollow Section (RHS) Joints under Predominantly Static Loading.* Verlag TUV Rheiland

[2] RADIC, I., MARKULAK, D., MIKOLIN, M.: Design and FEM Modelling of Steel Truss Girder Joints. **Strojarstvo**, vol. 52, ISSN 0562-1887, pp.125–135

[3] NIKOLIC, R., VELJKOVIC, J., VICAN, J.: Design of Columns Centrically Loaded in Compression. *Communications - Scientific Letters of the University of Zilina.* vol. 9, No. 3, 2007, ISSN 1335-4205, pp. 51–55

[4] WARDENIER, J., KUROBANE Y., PACKER J.A., DUTTA D., YEOMANS N.: *Design Guide for Circular Hollow Section (CHS) Joints under Predominantly Static Loading.* Verlag TUV Rheiland

[5] BEKE, P.: *Analyza zvaranych stycnikov z pravouhlych dutych prierezov* [*Analysis of Welded Joint Composed of Rectangular Hollow Section*]. Dissertation work, Kosice, 2009, 135 p.

[6] BEKE, P.; KVOCAK, V.: *Analysis of Joints Created from Various Types of Sections.* Proc. from 5th European Conference on Steel and Composite Structures, Eurosteel 2008 Graz, Brussels- ECCS, ISBN 92-0147-000-90, pp. 531–536

[7] FREITAS, A. M. S., MENDES, F.C., FREITAS, M. S. R.: *Finite Elements Analyses of Welded T-Joints.* Proc. from 5th European Conference on Steel and Composite Structures, Eurosteel 2008, Graz, Brussels- ECCS, ISBN 92-0147-000-90, pp. 555–560

[8] VICAN, J., SYKORA, M.: Design of Compression Members for Durability. *Communications - Scientific Letters of the University of Zilina.* vol. 11, No. 4/2009, ISSN 1335-4205, pp. 9–14

[9] EN 1993-1-8 Eurocode 3: Design of Steel Construction. Part 1–8 Design of joints.

https://doi.org/10.26552/com.C.2012.4.73-78

Miloslav Rezac – Iveta Skotnicova *

NOISE ATTENUATION FROM TRAMWAY TRAFFIC

The article describes course and results of experiment, which provided influence of change of acoustic absorption properties of concrete tram track surface by using the recycled rubber on traffic noise attenuation. The experiment was carried out in cooperation of the Faculty of Civil Engineering, VSB-TU Ostrava with the companies: the Ostrava Transport Company Plc, ODS – the Transport Constructions Plc, INTERTECH plus, Ltd. and with the Faculty of Mechanical Engineering, VSB-TU Ostrava [2].

Keywords: *Sound absorption coefficient, concrete tiling panel, recycled rubber cover, traffic noise*

1. Introduction

In recent years, the Ostrava Transport Company has applied a number of noise elimination features that demonstrably reduce noise and vibrations from the tramway traffic. Nevertheless, a suitable element that would significantly reduce the level of noise in the construction of tram tracks with a cover (concrete tiling panels) has not been found yet. Hence it came the need to develop and validate such a track line cover that would produce better absorption properties and higher attenuation of emitted noise in comparison with existing covers (of reinforced concrete panels, asphalt concrete). At the request of the Ostrava Transport Company, the Faculty of Civil Engineering VSB-TU Ostrava conducted a two-year experiment whose aim was to test the influence of a change of acoustic absorption properties of the concrete tiling panel of tram track on the noise from tramway traffic [1].

2. Concept of modification of concrete tiling panel

Concrete tiling panel is one of the sound reflective materials. One of the possibilities to verify the influence of reflective surface of tram tracks on noise load generated by tramway traffic is to change the absorption properties of the concrete panel surface. Based on requirements of the Ostrava Transport Company, an option to improve the absorptive properties of the surface of the concrete tiling panel by the use of layers of recycled rubber was examined.

2.1 Properties of concrete panel

ODS – the Transport Constructions is the manufacturer of concrete panels (tiling). Concrete panels are rectangular 1240 × 1980 mm (type B – internal, inter-rail) and 1430 × 1980 mm (type C – external, inter-track). Longer sides are beveled so that the panel could follow the edge of the rail seating. The current height of panel is 170 mm. Panels are made of concrete C-/40 sap3b and reinforced by welded mesh reinforcement of 10 505 (R), ∅8/∅8 – 150/100 at the lower surface with a longitudinal lining pitch of 100 mm. The coverage on both surfaces is 45 mm. The panels are seated on the tram line ties with the pitch of 600 mm and can be loaded also by road transport (Fig. 1).

Due to the clearance zone of a tram car it was impossible to increase arbitrarily the height of the existing panel by an additional layer. A prerequisite for the realization of the modification was to reduce the height of existing concrete panel and its consequent topping by designed thickness of a rubber layer. The maximum thickness of the rubber layer was designed 40 mm. Given that the concrete inner panel is designed for the potential burden on road transport, it was necessary to execute a static computation of the change in the panel's height first.

Within the modification of the concrete panel, the way of mutual fusion between the rubber layer and concrete panel was also elaborated. The variant of sticking, which is commonly used, for instance, on concrete walls with acoustic absorbing coating consisting of a recycled rubber, was excluded. Due to the potential shear stress of the panel caused by vehicles' acceleration and braking forces, the variant of the treatment of contact surfaces of both materials was chosen in order to ensure better adhesion of the rubber layer to the substrate. This variant was also a subject of static computation.

Static assessment proved that weakening section of the panel will not affect its mechanical properties. It should, however, be considered the possibility of panel's damage during transport and assembly.

* **Miloslav Rezac[1], Iveta Skotnicova[2]**
[1] Department of Transport Constructions, Faculty of Civil Engineering, VSB-Technical university of Ostrava, Czech Republic,
E-mail: miloslav.rezac@vsb.cz
[2] Department of Building Environment and Building Services, Faculty of Civil Engineering , VSB-Technical university of Ostrava, Czech Republic

2.2 Acoustic properties of boards made from recycled rubber

Recycled rubber is one of porous materials capable through its porous structure to absorb (consume) the incident acoustic energy. The absorption is expressed by ratio of sound energy that is absorbed during the impact and irreversibly transformed into heat to the total incident sound energy. Acoustic energy absorption occurs:

Fig. 1 Tramway track with concrete panels cover

- by multiple reflections of the sound beam in the pores of the material,
- by friction of air transmitting acoustic energy against the pore walls,
- by conversion of acoustic energy to the expansion work of periodically compressing air in the pores.

Quantity that expresses the ability of structure to absorb part of acoustic power of the incident sound wave is the sound absorption coefficient α [–] in a frequency band, defined as:

$$\alpha = \frac{W_a}{W_i} \tag{1}$$

where:
W_a is the acoustic power absorbed by material [W],
W_i is the net acoustic power incident on the material [W].

The sound absorption coefficient of the material depends on the relation of its thickness d, the frequency of the incident sound f and the pore size of material. Generally, at low frequencies the sound absorption coefficient increases with increasing thickness of the material. It attains its maximum at the thickness d when:

$$d = \frac{c}{4f} \tag{2}$$

where:
c is velocity of sound in air [m/s],
f is frequency of falling sound [Hz].

The goal of the experiment was to verify the optimal thickness and shape of the surface, which would ensure maximum absorption of acoustic energy while providing adequate strength and durability of the material in given conditions.

The shape and size of the spatial surface layout of rubber plates are limited by the manufacturing production. The thickness of the rubber layer is limited by the clearance zone of a tram car.

Four variants of a design were carried out in order to achieve the optimal comparison of acoustic properties of various thicknesses and shapes of the upper surface layer of recycled rubber.

- variant A – rubber plate with smooth surface, thickness 20 mm,
- variant B – rubber plate with smooth surface, thickness 40 mm, with reduced edges to 20 mm,
- variant C – rubber plate with shaped surface - traverse waves, thickness max. 40 mm,
- variant D – rubber plate with shaped surface – spatial bulges, thickness max. 40 mm.

A greater durability is assumed for plates with smooth surface and greater sound absorption is assumed for the shaped surface plates.

Acoustic properties of all variants of the rubber plate shapes were verified on the basis of the sound absorption coefficient whose values were measured in a reverberation chamber. The test was performed by an accredited testing laboratory CSI, Inc. Zlin. According to the standard CSN EN 1793-1:1998, evaluation of the absorption effects is carried out on the base of the coefficient of sound absorption measurement in laboratory conditions stated in the standard CSN EN ISO 354:2003.

The measurement results of sound absorption coefficient of all investigated variants of the shape of the rubber layers are presented in Fig. 2.

Based on the evaluation of acoustic properties of all variants of rubber plates, one can conclude that the optimal solution appears to be the variant of C – plate with waves of maximum thickness of 40 mm, and the D variant – plate with bulges of maximum thickness of 40 mm, which absorbs the sound even at higher frequencies (around 1600 Hz). Reducing noise levels at higher frequencies is more favourable to the human organism, since these noises are perceived as more intrusive. Based on these observations the variant of D was selected from all the investigated variants as a pattern for the modification of concrete tiling and, consequently, for its further usage on the test section.

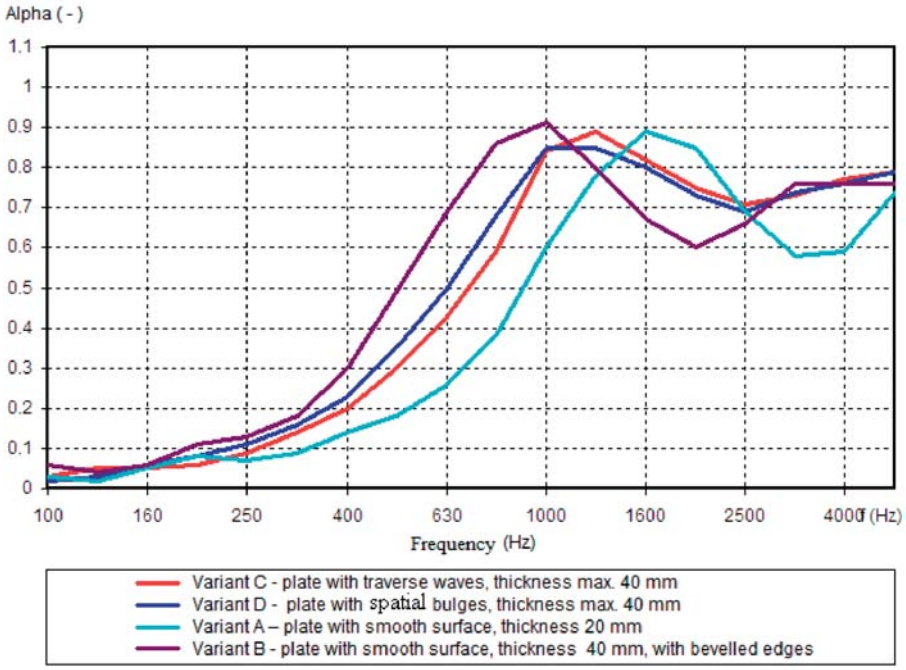

Fig. 2 Measured values of sound absorption coefficient of all examined variants of rubber plates

3. Implementation of the test section

A straight section of the two-lane tram track on Zavodni Street in Ostrava-Hrabuvka (see Fig. 3) was chosen as a test section to verify the properties of proposed modification of concrete tiling panel. The Zavodni Street is classified as collector, there are two-lane road (the width is 7.0 m), two-lane tram track (the width is 6.2 m) and two parking lanes (the width is 5.0 m). The tram track is separated from travel lanes by a physical barrier (concrete curb). The test section of the two-lane tram track is lined on both sides by a single-lane road, grass strips and fences of gardens of separate houses on one side, and by a fence of a town cemetery on other. The total length of the test section is 50 m.

Fig. 3 The test section of the tram line with modified tiling on Zavodni street in Ostrava

The exchange of panels took place in September 2008. The replacement of a tram line paving was carried out by the company DPO, Inc. The basic prerequisite for the final assessment of the impact related to the changes of the surface of panels on the noise level was the exchange of panels only, without any other noise feature elimination.

Existing panels were pulled out, the original sub-base was extracted to the ties and gravel bed. The geotextile separation layer was newly laid and covered by a sub-base from aggregate of fraction 0–4. Next, new panels were put in a bed. Filling of cement mortar was injected by a pump in order to minimize mortar spilling into the porous structure surface of panel.

4. Measurement of tramway traffic noise on test section

Noise measurement on the test section on Zavodni Street in Ostrava-Hrabuvka was carried out on 28 August and 8 October 2008. The first measurement was performed for the initial state of the tram track, the second, after the original tiling panels were replaced by the panels coated with a rubber layer (variant D).

The objective of the measurement was to verify the impact of the changes of absorption properties of tiling panels surface (coated with recycled rubber) on the noise from tramway traffic.

4.1 Principle of the noise measurement from tramway traffic

Noise measurements were conducted by the Department of Machine Parts and Mechanisms, Faculty of Mechanical Engineering, VSB-TU Ostrava [2]. Sound-level meter, type 2250B of firm Brüel&Kjaer was used for the noise measurement. Instant values of acoustic pressure pA [Pa], with frequency weighting A, were measured and recorded during the whole interval of passage of the reference tramway throughout the test section. A total length of recording of the acoustic pressure was $T = 8$ s. Records of each individual traversal were stored in computer memory with a sampling frequency of 10 kHz.

The sound-level meter was placed on a tripod in a horizontal plane at a height of 1.1 meters above the ground and surrounding terrain with no obstacles between the sound-level meter and the reference tramway during each of measuring sessions. The sound-level meter microphone was wind shielded by a soft PUR membrane.

Five passages of the reference tram (see Fig. 4) over the test section were measured at two tram speeds (40 a 50 $km.h^{-1} \pm 2\ km.h^{-1}$) and at two different distances between sound-level meter and the axis of measured track (7.5 a 15 meters). The tramway drove through the measured section by inertia, without acceleration pedal engaged.

In accordance with the Government Regulation no. 148/2006 Coll., on protection of health against the negative impacts of noise and vibrations, as amended, and the Methodological guidance for the measurement and evaluation of noise in non-working environment (RN. HEM-300-11.12.01-34065), the background noise in the idle state, before and after measurement, was also recorded. Its value was always about more than 10 dB lower.

The measurements always took place at night, from about 23.30 hours, when traffic on surrounding roads was very sparse. Only passages of the reference tram undisturbed by other traffic on the test section of Zavodni street were measured.

Fig. 4 Reference tramway

4.2 Evaluation of measurement results

From the recorded instantaneous value of acoustic pressure $p_{A,\,8s}$ the sound pressure level L_{Afast} [dB] was subsequently evaluated and the equivalent sound pressure level $L_{Aeq,4s}$ [dB] was computed from 15 highest values (in time interval of 4 s). Afterwards, the equivalent sound pressure level $L_{Aeq,4s}$ [dB] was evaluated as an average value of five records. The reference value of acoustic pressure $p_0 = 2.10^{-5}$ Pa.

Further, the amplitude spectrum (FFT) of representative records of acoustic pressure (without A-weighting filter) in the frequency bands from 0 to 5000 Hz and from 500 to 5000 Hz was evaluated in order to assess the effects of noise in terms of the ergonomic and hygiene criteria. In these frequency ranges the equivalent levels of sound pressure $L_{Aeq,4s}$ a $L_{Aeq,4s,cut}$ (equivalent level of sound pressure from the record of acoustic pressure with upper-pass filter of 500 Hz) were determined as well.

Table 1 and Fig. 5 represent the recorded results and their evaluation by two methods, by means of:

- the equivalent sound pressure level,
- the spectral analysis of sound pressure level (or acoustic pressure).

The equivalent sound level is a single-valued evaluation of noise related to the equivalent, maximal, or any other characteristic sound level for the given time interval. This classification is appropriate from the health perspective to assess the noise climate of living or working environment. However, a single value does not have sufficient explanatory power for the evaluation of acoustic properties of structures and is, therefore, not suitable for a separate assessment.

The spectral analysis of sound levels is a frequency analysis of sound level. It is suitable for technical evaluation of structures (for determination of significant frequency components and the design of appropriate protective measures). It is possible, by means of the spectrum of sound levels with a sufficient number of readings, to assess the frequency range at which the changes in the tram line construction will appear. These changes can be caused by the influence of inserted damping element or grinding the tram rails.

There was used a spectral analysis of the acoustic pressure in this paper, which is more accurate in the case of technical comparison of two states (in our case – panels with and without rubber layer). The conversion of the acoustic pressure in Pa to the sound pressure levels in dB causes proportional changes in the processed record. For our intention of technical comparison it was preferable to use the original measured values in Pa.

When comparing the measured single-valued values of the levels of sound pressure $_{LAeq,4s}$ we can see just a little impact of the

The resulting equivalent sound levels $L_{Aeq,4s}$ [dB] for frequency bands from 0 to 5000 Hz — Table 1

Transit speed of reference tramway [km/hour]	Initial conditions of tramway track		Conditions after exchange of modified panels with rubber layer	
	$L_{Aeq,4s\ cut}$ [dB]		$L_{Aeq,4s\ cut}$ [dB]	
	7.5 m from axis	15 m from axis	7.5 m from axis	15 m from axis
50	81.34	78.03	81.34	77.98

The resulting equivalent sound levels $L_{Aeq,4s\ cut}$ [dB] for frequency bands from 500 to 5000 Hz — Table 2

Transit speed of reference tramway [km/hour]	Initial conditions of tramway track		Conditions after exchange of modified panels with rubber layer	
	$L_{Aeq,4s\ cut}$ [dB]		$L_{Aeq,4s\ cut}$ [dB]	
	7.5 m from axis	15 m from axis	7.5 m from axis	15 m from axis
50	78.81	75.56	76.01	73.21

modified panels on the sound levels. Although during the actual measurement, a discernible decline of noise during passing of reference tram was audible. This effect is caused by the change of frequency pattern of noise levels due to changes of absorptive properties of the surface of tiling panel.

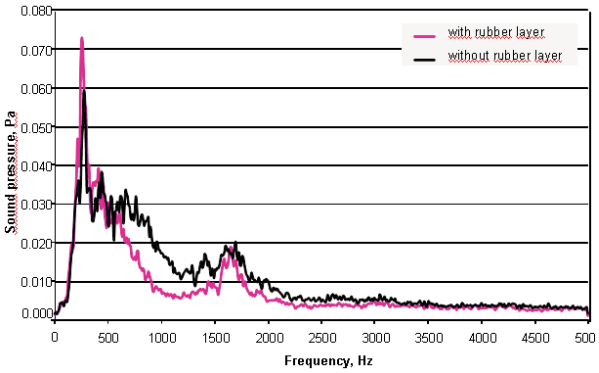

Fig. 5 Average spectra of sound pressure at the distance of sound-level meter of 7.5 m and reference tram passing speed 50 km.h^{-1} [2]

From the above chart of the average measured spectra of sound pressure is apparent noticeable decrease in sound pressure in the case of new modified panels. Absorptive properties of the top rubber layer are more apparent in the frequency ranges from 500 to 5000 Hz.

At low frequency ranges, the impact of changes in absorption capacity of panel surface is not reflected. On the contrary, the values of sound pressure appear to be higher than in the case of initial state. The reason for this probably lies in the fact that measurement of new layout took place shortly after deposition of new panels to the ballast.

In order to define more accurately the amplitude of attenuation of sound levels for new modified panels, the resulting equivalent sound levels $L_{Aeq,4s\ cut}$ [dB] for frequency bands from 500 to 5000 Hz only were assessed (Table 2). Further, the amplitude spectra (FFT) of sound pressure p_{Acut} [Pa] in the frequency bands from 500 to 5000 Hz were evaluated for representative passage records (Fig. 6).

When comparing the measured single-valued values of sound pressure $L_{Aeq,4s\ cut}$ in frequency range from 500 to 5000 Hz (which is the most perceptive range to the human ear), we can see a noticeable difference of measured levels of 2.2 to 2.8 dB between the initial tramway track layout and the new layout after panels being replaced. Such a difference is just perceptible to the human ear.

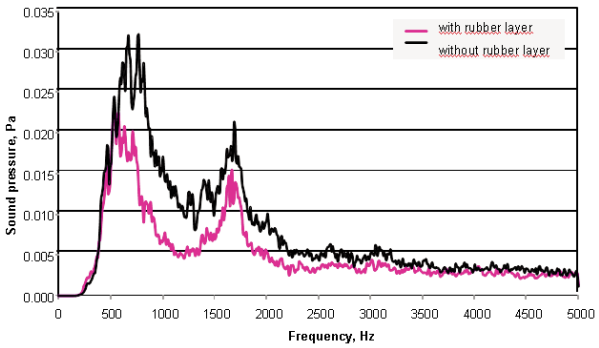

Fig. 6 Average spectra of sound pressure at the distance of sound-level meter of 7.5 m and reference tram passing speed 50 km.h^{-1} for frequency bands from 500 to 5000 Hz [2]

From the figure above there is an obvious significant decrease of the measured average spectra of the sound level in the case of newly modified panels, particularly in the frequency bands from 500 to 5000 Hz.

5. Conclusion

Based on the research and measurement we can conclude that the modification of surface absorption of the concrete tiling panel by using the recycled rubber can lead to reduction of the noise from tramway traffic. However, wider application of this system in practice will require further measures.

The positives, which the use of tiling panel coated by the recycled rubber will bring, can be summarized as follows:

- significant noise level reduction in the range of maximum sensitivity of human hearing, up to 2.8 dB,
- easy constructional replacement of existing panels by newly modified panels,

- still remains possibility of driving on the tram track for emergency vehicles, which have the right of way (and others, if necessary),
- easy tram track maintenance (during the winter period only a higher attention has to be required while working with a snow plow),
- short time of the technological implementation,
- availability of supplier, a good supplier-customer relationships.

But there are also some negatives:

- a failure to record attenuation of low threshold values of the noise (around 250 to 300 Hz),
- necessity of further investment for resolving the attenuation in the field of low threshold values of the noise,
- insufficient data to determine the final life-cycle of a new element (for now, after two years of operation without defects),
- drainage of rainwater,
- lack of data to determine the failure probability of the new element,
- a possible decrease of the absorption capacity of the panel caused by infiltration of dirt (unverified yet),
- higher implementation costs (currently the biggest obstacle to wider application).

References

[1] SKOTNICOVA, I., REZAC, M., OZANOVA, E., HUDECEK, L.: *Soundproofing of Tram Track with Cover: Final Report HS 229/702.* Ostrava : VSB-Technical university of Ostrava, Faculty of Civil Engineering, 2008. 180 p.

[2] HRUDICKOVA, M.: *Report on the Noise Measurement on the Street Zavodni: Annex 1 of final report HS 229/702.* Ostrava : VSB-Technical university of Ostrava, Faculty of Mechanical Engineering, 2008. 12 p.

https://doi.org/10.26552/com.C.2012.4.79-82

Marcela Malindzakova – Jozef Futo *

TUNNEL BORING MACHINE DESIGN AND RELIABILITY PARAMETERS OF A DYNAMIC ROCK-INDENTOR SYSTEM

The article deals with the calculation of reliability indicators of system dynamics, between the tunnel boring machine and the rock during the tunnel boring of the exploratory tunnel Branisko. The background deals with a design of a tunnel boring machine as a whole where the observed parts are rolling chisels in relation to the length of tunnel boring, as well as physical and technological properties of disintegrated rock.

Keywords: *tunnel boring machine, rock disintegration, reliability parameters, maintenance*

1. Introduction

The theoretical justification and explanation of the processes of disintegration of rocks and the mechanism of their disintegration are based on the theory of elasticity (the area of continuum mechanics) [1, 2]. This is because the vast majority of rocks during the mechanical disintegration acts as a quasi-elastic and brittle material and the ongoing processes can be interpreted by the foundations of this theory. However, by formulating new hypotheses and conclusions, the usage of additional simplifications must be considered. This model describes the behaviour of rocks interacting with the tool until disintegration occurs.

2. Construction of tunnel boring machine

Full-profile tunnel boring machine (TBM) is a complex set of machinery and equipment units, that allows a mechanical boring into rock mass, creating an opening of a circular shape of a specified size, that is secured against collapse. Tunnel boring machine consists of:

- supporting skeleton,
- tunnel boring head,
- engine,
- telescopic hydraulic press mechanisms,
- transport trailer.

The TBM equipment automatically loads and transports removed rock from the tunnel into the transport trailer. The transport trailer is several tens of meters long. During the extraction this trailer is attached behind the TBM, and is pulled on rails. The transport trailer is equipped with all the distribution and support mechanism that are necessary for continuous and fully balanced operation of the tunnel boring machine [3, 4].

The excavation performance of TBM machine is significantly influenced by the design of the tunnel boring head, of its torque and by the design of rolling chisels. Rolling chisels for TBM are specifically designed for tunnel boring in hard rock conditions.

The performance of installed engine drive depends on the required torque and speed. Torque is significantly influenced by geological conditions. Soft, easily drillable rocks allow by the same chisel pressure a greater penetration. As a result, more rotation resistance requires more torque power than for hard rocks (low penetration). In soft rocks, it is not possible to use the full value of penetration, achieved by pushing force, otherwise it would uneconomically increase the necessary torque parameters. On the other hand, in hard rocks, even at the maximum thrust only a relatively small penetration can be achieved, therefore a relatively small torque is necessary.

In soft rocks the necessary high torque level can be compensated by reducing the number of revolutions. The corresponding high level of torque and thrust must be adapted and all bearings must be sturdily constructed. That ensures sufficient durability and reliability of the entire plant.

Rock disintegration by full-profile tunnelling boring machines is a very complex process. The price for a standard meter length of such underground works is determined by a number of factors. These are: design and operational parameters, construction of disk chisels, chisels deployment at the tunnelling boring head, their shape and material composition, and last the applied tunnel boring regime [5]. So in terms of the total work cost, the process of disintegration especially in its optimal mode throughout the tunnelled section has the most impact, as well as the design of the tunnelling boring machine. Therefore, it is important to collect all important data about the ongoing tunnelling process, about the current mode

* **Marcela Malindzakova, Jozef Futo**
Institute of Control and Informatization of Production Processes, Faculty of Mining, Ecology, Process Control and Geotechnology, TU Kosice, Slovakia, E-mail: marcela.malindzakova@tuke.sk

and machine status. A significant challenge for this kind of monitoring is the rapid transfer of real time data. After proper analysis, the results can be implemented for better control of this challenging process in real time [6–10].

One way to evaluate the effectiveness of the tunnelling boring process is to monitor the reliability indicators of used chisels or reliability of models that take into account the impact of the machine regime on its design elements, depending on the tunnel boring regime.

Reliability indicators used in this article are quantitative. They show the impact of static and dynamic properties of tunnel boring machine-rock system for transition through different geological sections of the gradual attrition of tunnel boring chisels [3, 4].

3. The monitoring of the tunnelling boring indenter – rock system

Monitoring system for tunnel boring machine allows capturing and storing the following variables: thrust, speed, torque, power and length of extracted rocks (henceforth called extract). In addition to those variables, for this study, also the frequency of chisels replacements was monitored, along with corresponding material composition. Fig. 1 shows a tunnel boring head with roller chisels.

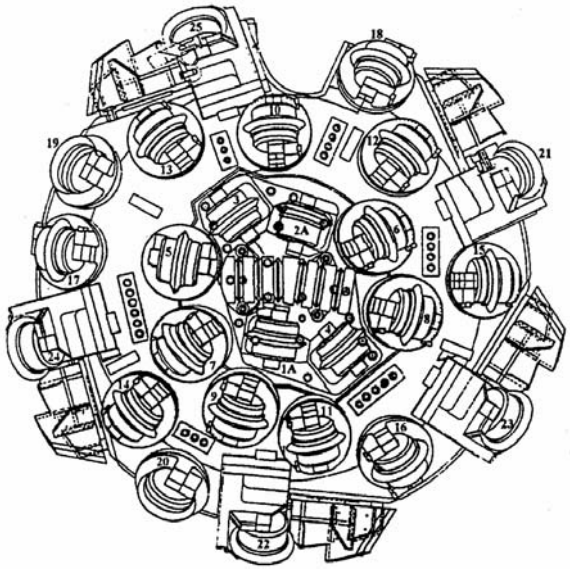

Fig. 1 Tunnel boring head with roller chisels

Based on the values measured during the monitoring of the tunnel boring process we can create models for monitoring of static and dynamic properties of tunnel boring heads. Input variables include the thrust and speed; the output variables include power and torque of the tunnel boring head (Fig. 2).

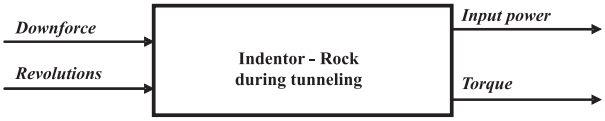

Fig. 2 Process flow diagram of disintegration input / output

The static properties of this system include:
- design parameters of a tunnel boring machine, e.g. dimensions of the head, the installed capacity,
- number and shape of chisels,
- properties of rocks, which are "homogeneous" in different geological sections.

Whilst the static properties of this system during tunnelling do not change, the dynamic properties of this system change over time as they depend on parameters that change during tunnelling.

Changing the parameters affects the technical state of the system and ultimately affects the final price of the tunnelling works. One way to assess the dynamic properties of tunnel boring systems is to investigate the transient characteristics. Examples of these transitions are shown in Fig. 3. It implies not only different torque values, but also the trend [11, 12] and [13].

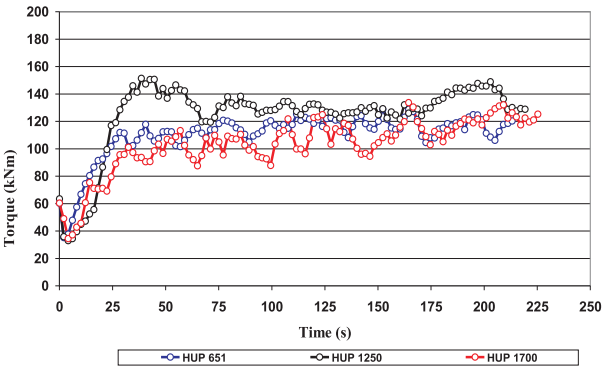

Fig. 3 Trends of transient characteristics in different types of rocks

Based on the transient characteristics it can be assumed that the wear and tear, damage and also the number of replaced rolling chisels will greatly affect the dynamic stress of a tunnel boring head. The trends of rolling chisels replacements across section stations can be observed in Fig. 4, where HUP lines describe drilling in three different geological sections

The replacements begun at a distance of 452 meters from the entrance portal when 2 chisel pieces are replaced and then from 780 meters to 835 meters further 6 chisels had to be replaced. Gradually, at a distance of 958 meters, 18 chisels had to be replaced. After that we can observe a replacements stabilization at the distance of about one hundred meters, followed again by a dramatic increase of replacements at a distance of 1092 meters, when first

17 and then 30 meters further 9 more chisels had to be replaced. This fact can be described also by reliability indicators such as, for example, by the rate of replacement probability (Fig. 5) or the intensity of replacements (Fig. 6).

Reliability indicators help designers and technologists more accurately determine the time and cause of the damage for the subsequent chisels replacement. There is a number of theories that describe the wear and dulling of rolling chisels, but the values obtained from monitoring can reveal new connections between input variables and the number of replaced chisels [14–17].

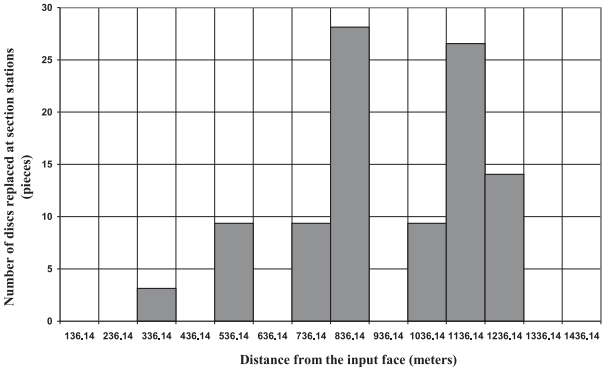

Fig. 4 Number of discs replacements at section stations

Mathematical formulas describing the used indicators are based on the probability theory [18–20]. The statistical estimates of indicators for a failure-free operation, it is not necessary to record the number of chisels $\Delta B_t(\Delta T)$ that are damaged in short time ΔT after time interval t.

$$\Delta B_t(\Delta T) = B(t + \Delta T) = B(t + \Delta t) - B(t). \quad (1)$$

Because in an estimate the following is valid:

$$\Delta B_t(\Delta T) \cong N f_E(t)\Delta T, \quad (2)$$

where N stands for total number of samples, the point estimate $f_E(t)$ of the rate of a defects probability in the interval $\langle 0,t \rangle$ given by formula:

$$f_E(t) = \frac{\Delta B_i(\Delta T)}{N\,\Delta T}. \quad (3)$$

then the replacements intensity can be described by:

$$\lambda_E(t) = \frac{\Delta B_i(\Delta T)}{N(t)\Delta T}. \quad (4)$$

4. Conclusion

Life expectancy of rolling chisels or tools usage converted to 1 cubic meter of desintegrated rock is a very significant cost

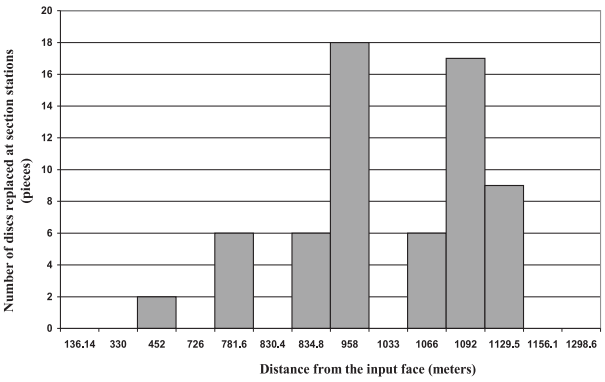

Fig. 5 Drilling distance when chisel replacements at section station occured

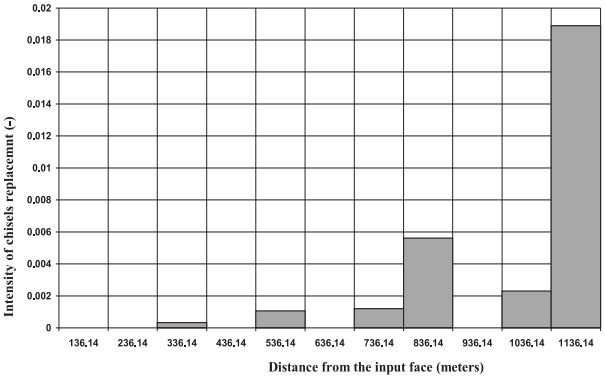

Fig. 6 The intensity of chisels replacements at section stations

characteristic. It affects significantly the total cost of TBM excavation, directly or indirectly:

- the price of used rolling chisels directly affects the cost of TBM excavation,
- indirectly, it causes the loss associated with the necessary downtime needed for replacement of a blunt rolling chisel.

The cost of tunnel boring chisels are mainly influenced by:

- properties of rocks (hardness, abrasion resistance, brittleness)
- shape and diameter of the tunnel boring head
- the required rate of tunnel boring,
- construction of a rolling chisel.

Modern roller chisels have properly sealed and lubricated bearings, which greatly extends their life expectancy. The edge of tunnel boring chisel that is made of carbide can be replaced independently and rolling chisels can be written off after a few replacements of the tunnel boring edge, which significantly reduces the tunnelling costs. The cost of tunnelling boring tool based on the rocks hardness are considerably higher than the figures stated by the Wirth firm in the first half of the 90ies:

- for hard rock (amphibolite, granodiorite) at the tunnel boring speed of 1.5 meter per hour, the price of tunnel boring chisels varies from 7.5 to 10 EUR/m^3 of disintegrated rock,

- for medium-hard rock (sandstone and limestone) at the tunnel boring speed of about 3.5 meter per hour, the price of tunnel boring chisels is about 5 EUR/m^3 of disintegrated rock.

For further research it is necessary to pay closer attention to the monitoring of dynamic properties of the rock-indenter system. It is possible, for example, by constructing a suitable simulation model of these dynamic processes, taking into account mainly the wear and damage to chisels on the tunnel boring head. Subsequent description of those experimental processes, implementing suitable mathematical models and resolving the rapid transfer of data problem, could represent a suitable solution for better control and management of this complex process. Also the data obtained in real time provide an opportunity to predict dangerous operating conditions.

References

[1] KRUPA, V.: *Hypotheses, Models, Theories and the Verification of the Full-profile tunneling* [H*ypotezy, modely, teorie a ich verifikacie pri plnoprofilovom razeni*], Dizertation thesis, Kosice, UGt SAV, 1998.

[2] KRUPA, V., PINKA, J.: *Rock Disintegration* [*Rozpojovanie hornin*], Stroffek, Kosice, 1997.

[3] KLEPSATEL, F. et al.: *Construction of the Tunnels in the Rock* [*Vystavba tunelu ve skalnich horninach*], Vydavatelstvi Jaga group, v. o. s., Bratislava, 2003, ISBN 80-88905-43-5.

[4] LAZAROVA, E., KRUPA, V.: Experiences from Full-profile Exploration Excavation of Tunnels construction [Skusenosti z plnoprofiloveho razenia prieskumnych stolni pre tunelove stavby], *Acta Montanistica Slovaca,* vol. 11, 2006, special No. 2, pp. 330–334, ISSN 1335-1788.

[5] FUTO, J., IVANICOVA, L., KREPELKA, F.: *Statistical Evaluation of Reliability of Disc Roller Bits on Tunnel Boring Machines.* Proc. of 34th Seminar ASR 09 Instruments and Control, 2009, VSB TU : Ostrava, 2009. p. 16, ISBN 978-80-248-2011-8.

[6] BARANOVA, V.: *Measurement and Evaluation of Parameters to Support the Management of Steel in Oxygen Converters* [*Meranie a vyhodnotenie parametrov na podporu riadenia vzroby ocele v kyslikovych konvertoroch*], Kosice, Technicka univerzita, F BERG, Bachelor thesis, 2008.

[7] BARANOVA, V.: *The Impact of Quality of Input Material for the Converter Process* [*Vplyv kvality vstupnych surovin na konvertorovy proces*], Kosice, Technicka univerzita, F BERG, Diploma thesis, 2010.

[8] BENKOVA, M.: *Quality Assurance Processes* [*Zabezpecovanie kvality procesov*], Kosice, Technicka univerzita, F BERG, 2007.

[9] BENKOVA, M., FLOREKOVA, L., BOGDANOVSKA, G.: Variability of Quality Parameters and the Loss Function [Variabilita parametrov kvality a stratova funkcia], In: *Acta Montanistica Slovaca,* vol. 10, No. 1, 2005, pp. 57–61.

[10] FUTO, J., IVANICOVA, L., KREPELKA, F.: *Hydraulics and Pneumatics – parts 1–2* [*Hydraulika a pneumatika 1–2*], 2010, pp. 9–13.

[11] KACUR, J., LACIAK, M., DURDAN, M.: Measurement of Relevant Variables in the Process of Underground Coal Gasification [Meranie relevantnych velicin v procese podzemneho splynovania uhlia], *AT&P journal,* 2010, vol. 17, No. 11, pp. 51–55, ISSN 1335-2237.

[12] KRUPA, V., LAZAROVA, E.: Assessing the Reliability of Rolling Disk Chisels Full-Profile Tunneling Machine Drilling of Exploration Gallery for Tunnel Tubes [Hodnotenie spolahlivosti diskovych valivych dlat plnoprofilovych raziacich strojov pri razeni prieskumnych stolni pre tunelove rury], *Q magazin, internetovy casopis o jakosti.* Ostrava: VSB-TU, 2009, vol. 4, fmmi10.vsb.cz/639/magazin.htm, ISSN 1213-0451.

[13] LESSO, I., FLEGNER, P.: *Specification of Symptom Process of Disintegration of Rocks by Rotary Drilling for the Purpose of Process Management* [Specifikacia priznakov procesu rozpojovania hornin rotacnym vrtanim pre ucely riadenia procesu], In: *Sbornik vedeckych praci Vysoke skoly banske – Technicke univerzity Ostrava : Rada stavebni,* vol. 9, No. 2, 2009, pp. 155-165, ISSN 1213-1962.

[14] HOROVCAK, P., TERPAK, J.: *Web Services in Comparison with Other Technologies.* In: ICCC 2004: Proc. of intern. Carpathian control conference, Zakopane, Poland, 2004, Krakow, ISBN 83-89772-00-0.

[15] KACUR, J., LACIAK, M., DURDAN, M.: *Remote Monitoring and Control of the UCC Process.* In: ICCC 2011, Proc. of the 12th Intern. Carpatian Control Conference, Velke Karlovice, Czech Republic, pp. 180–184, ISBN 978-1-61284-359-9.

[16] KOCI, P.: *Computer Science* [*Vypocetni technika*]. VSB-TUO,1. vyd. Ostrava, VSB-TU Ostrava, 2007, ISBN 978-0-248-1515-2.

[17] TUMA, J., WAGNEROVA, R. FARANA, R. LANDRYOVA, L.: *The basis of automation* [*Zaklady automatizace*], 1. vyd. Ostrava, VSB-TU Ostrava, p. 280, ISBN 978-80-248-1523-7.

[18] MYKISKA, A.: *Reliability of Automation Systems* [*Spolehlivost automatizacnich systemu*], CVUT, Praha, 1996, ISBN 80-01-01466-5.

[19] O'CONNOR, P., D., T. et al.: *Practical Reliability Engineering,* John Wiley & Sons, Chichester, Wiley, 2006, ISBN 978-0-470-84462-5.

[20] PAVLICKOVA, M., BOGDANOVSKA, G.: The Position of Metrology and Measurement to Support Quality Products [Pozicia metrologie a merania pre podporu kvality vyrobkov], *Manazment v teorii a praxi: On-line odborny casopis o novych trendoch v manazmente,* vol. 3, No. 4 (2007), pp. 79–85.

https://doi.org/10.26552/com.C.2012.4.83-87

Mohamad Al Ali – Michal Tomko – Ivo Demjan – Vincent Kvocak *

ANALYSIS OF THE INITIAL IMPERFECTIONS EFFECT ON THE THIN-WALLED COLD-FORMED COMPRESSED STEEL MEMBERS

The paper deals with the influence of initial imperfections and presents fundamental information about experimental and theoretical-numerical research to determinate the load-carrying capacity of thin-walled cold-formed compressed steel members. The investigated members had closed cross-sections made of homogeneous material. The theoretical-numerical analysis in this paper is oriented on the investigation and modeling of initial imperfections effects, caused by production process, on the load-carrying capacities of mentioned members, while the experimental investigation is to verify the theoretical results and to investigate the behavior of mentioned members during the loading process.

Key words: *initial imperfections, thin-walled cold-formed profiles, steel structure, load-carrying capacity, plasticity, modeling, experiment*

1. Introduction

Theory and design development of steel thin-walled cold-formed members and profiles creates a certain knowledge base for their practical application in the civil engineering. However, this fact does not mean that all the complicated and challenging processes of their behavior, during the strain, transformation and failure are sufficiently investigated. From the material and geometric point of view, the thin-walled cold-formed profiles have specific specialties, which must be responsibly taken into account in their design [1]. From this aspect, the local stability requirements related to unfavorable buckling effects of their compressed parts are very significant. Favorable effects, related to membrane stresses and post-critical behavior are also important. Different calculation procedures in different standards (STN 73 1402:1988, STN EN 1993-1-3: 2006), reciprocal comparison of the results and their comparison to with existing experimental results indicate the need for further theoretical and experimental investigation of the post-critical behavior and elastic-plastic resistance of thin-walled profiles.

2. Description of the testing members

In general, the experimental research program included 18 thin-walled cold-formed testing members with closed cross-sections. The testing members were divided into two cross-sectional groups:
- Group A: with square cross-sections,
- Group B: with rectangular cross-sections; see Fig. 1.

Different dimensions of closed cross-sections and tested members were chosen to reflect the post-critical behavior of their several thin webs during strain, transformation and failure processes.

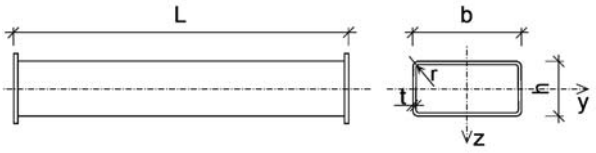

Fig. 1 Scheme of testing members, Group B

The obtained results are very extensive; therefore the paper deals only with group B, Tab. 1, Tab. 2.

Geometrical dimensions of the designed members, group B — Tab. 1.

Testing members			Geometrical dimensions [mm]					Steel
Cross-sectional group		Marking	b	h	t	r	L	
B	1	B11, B12, B13	150	100	2	3	450	S235
	2	B21, B22, B23	200	100			650	
	3	B31, B32, B33	200	150			600	

In the terms of local-stability classification, the webs of individual members are thin-walled at the compressive strain. The members' lengths were designed from the global stability point of view, in order to decide of the members' local (cross-sectional) resistance.

* **Mohamad Al Ali, Michal Tomko, Ivo Demjan, Vincent Kvocak**
Technical University, Faculty of Civil Engineering, Institute of Structural Engineering, Kosice, Slovakia, E-mail: mohamad.alali@tuke.sk

Basic geometrical characteristics of the designed testing members, group B — Tab. 2

Cross-sectional group		STN EN 1993-1-3:2006				STN 73 1402:1988			
		β_b	β_h	λ_y	λ_z	β_b	β_h	λ_y	λ_z
B	1	73.12	48.12	10.70	7.87	71.00	46.00	10.74	7.89
	2	98.12	48.12	15.01	8.84	96.00	46.00	15.05	8.85
	3	98.12	73.12	9.58	7.71	96.00	71.00	9.60	7.72

All testing members were made out from steel sheets with nominal thickness 2 mm (steel S235). Three material pieces were taken from each used steel sheet to make normative shaped testing specimens. The testing specimens underwent a tension tests to find out the stress-strain diagrams and the actual material characteristics of applied steels.

Detailed dimension measuring of the testing members was done before the loading tests, in order to achieve consistent evaluation and analyses of the experimental knowledge and results. The dimensions of cross-sections: width b, height h, and thickness t, were measured at the top, middle and bottom of each member. The radius r was measured at each curved corner and the length L was measured at each member's side. The average values of the measured dimensions were considered as actual; see Tab. 3.

Average dimensions values and actual material characteristics — Tab. 3.

Member	b	h	t	r	L	f_y	f_u
	[mm]					[MPa]	
B21	207.93	103.08	2.12	3.0	650.00	242.33	360.00
B22	207.47	103.18	2.10	3.0	649.88	242.33	360.00
B23	207.35	102.62	2.16	3.0	649.25	242.33	360.00

3. Testing methodology and limit loads

During the consecutive programmed loading of the tested members, the strains ε were measured using resistive strain gauges in the middle cross-sections and the deflections (buckling) of the webs w were measured using inductive sensors at different places, according to the members lengths. The resistive gauges and inductive sensors were connected to the computer for direct evaluation. The loading process of each member was regulated close to its real behavior, measured strains ε and deflections w. The test continued up to the total failure defined by the beginning of continuous increasing of strains ε and deflections of the webs w.

According to the research targets, the initial buckling shapes of all tested members' webs were measured on previously drawn raster, by means of inductive sensors before testing start. The final buckling shapes, after test finishing were also obtained [2].

Taking into account real-measured dimensions and yield stresses, the limit loads of all tested members were calculated according to relevant standards [3 – 5]. Theoretical and experimental limit loads are presented in Tab. 4. It is evident from Table 4 that the experimental limit loads are smaller than the expected theoretical values. This serious fact may incur in consequence of the unfavorable development of initial imperfections. This unfavorable influence of the initial imperfections is analyzed in detail in the following section.

In Table 4 the following notation was used:

N_{pl} – the local plastic limit load of full cross-section, defined by attaining the yield stress fy,

$N_{ul,el}$ – the local (post-critical) elastic limit load of effective cross-section, defined by attaining the yield stress f_y,

The above mentioned theoretical limit loads with indices (STN) were calculated according to the Slovak technical standard STN 73 1402:1988, considering chapter 6/6.8.1 of the Slovak technical standard STN 73 1401:1998. Theoretical limit loads with indices (EN) were calculated according to the European standard STN EN 1993-1-3:2006, considering chapters 4/4.1 – 4/4.4 of the standard STN EN 1993-1-5:2006 and chapter 6/6.3.1 of the standard STN EN 1993-1-1:2006.

Theoretical and experimental limit loads — Tab. 4

Member	$N_{pl,STN}$	$N_{pl,EN}$	$N_{ul,el,STN}$	$N_{ul,el,EN}$	$N_{u,y,STN}$	$N_{u,y,EN}$	$N_{u,z,STN}$	$N_{u,z,EN}$	$N_{u,exp}$
	[kN]								
B21	312.08	309.4	229.3	194.45	229.3	194.45	229.3	194.45	171.15
B22	309.28	306.62	226.3	191.76	226.3	191.76	226.3	191.76	173.27
B23	316.63	313.93	234.79	200.55	234.79	200.55	234.79	200.55	164.77

4. Calculation models and the experiment simulation

Calculation models of the testing members, described in Tab. 3, were created using software based on FEM – ANSYS [6, 7 and 8]. The target of the FEM analysis was to obtain more accurate data about the post-critical behavior of the mentioned members, to determine their limit loads and to compare them with the experimental results. In this paper, the obtained analysis results are compared to the theoretical and experimental limit loads of the actual testing members B21, B22 and B23.

The volume shell elements SOLSH190 were applied to create the calculation models. The finite element SOLSH190 is usually used for the simulation of shell structures with wide range of thicknesses (from thin to medium thickness). This element, with eight connecting nodes, has three degrees of freedom at each node. The element may be used to solve the geometrical and physical nonlinear problems. This type may be also used for the composite multilayer modeling (up to 250 different material's layers).

The modeling was carried out with considering the initial imperfections. Fig. 2 illustrates the arrangement of the tests with some views on the member after the test finishing. The values of the measured initial imperfections in individual grid points were considered in the 3D models [2].

Each of the 3D calculation models (B21, B22 and B23) contains 4 182 nods and 4 100 shell elements. Boundary conditions of the modeled, axially compressed members were defined by the two-sided hinged connections.

Two types of calculation models were used to verify the initial imperfections effect:
- With the consideration of the webs' initial deviation,
- Without the consideration of the webs' initial deviation.

Elastic-plastic material with hardening was considered with the use of the plastic zones method. This material is characterized by a bilinear approximation of the strain-stress diagram of steel with yield stress f_y = 242.33 MPa and hardening modulus E_{hard} = 2800 MPa [2].

The modeling of testing members was carried out according to above mentioned description. Fig. 3 illustrates the 3D model with generated grid for initial imperfections defining (a – b) and finite element mesh of volume shell elements SOLSH190 (c).

The analysis was carried out with sequentially increasing the applied load until the first appearance of plastic zones locations. The applied load was transformed to the middle-plane of the shell elements. The model was analyzed using the geometrical and physical non-linear calculation.

5. Results and their analysis

The final webs' buckling shapes in topographical form, together with the equivalent elastic strain of the modeled member B22 is presented in Fig. 4. Fig. 5 illustrates the equivalent stress and plastic strain of the mentioned member.

The comparison of the several limit loads of tested members B21, B22 and B23, obtained by the theoretical, FEM simulation and experimental investigation are illustrated in Fig. 6.

From Fig. 6 is evident that the experimental limit loads of individual tested members are smaller than the limit loads obtained by relevant standards. Fig. 6 also presents the influence of initial imperfections through the process of the 3D FEM simulations.

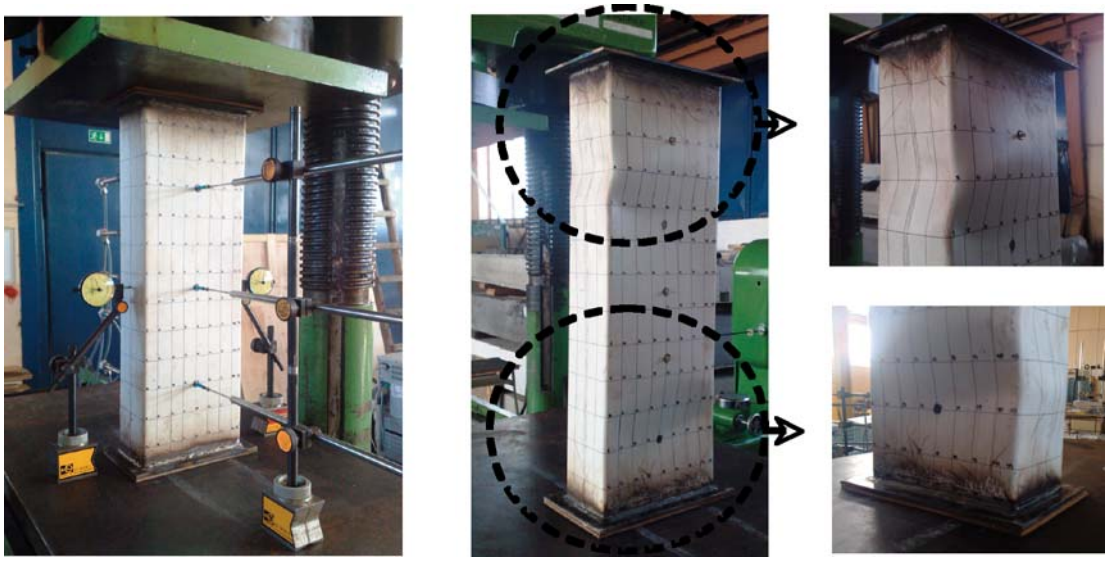

Fig. 2 Arrangement of the tests and the member failure shape

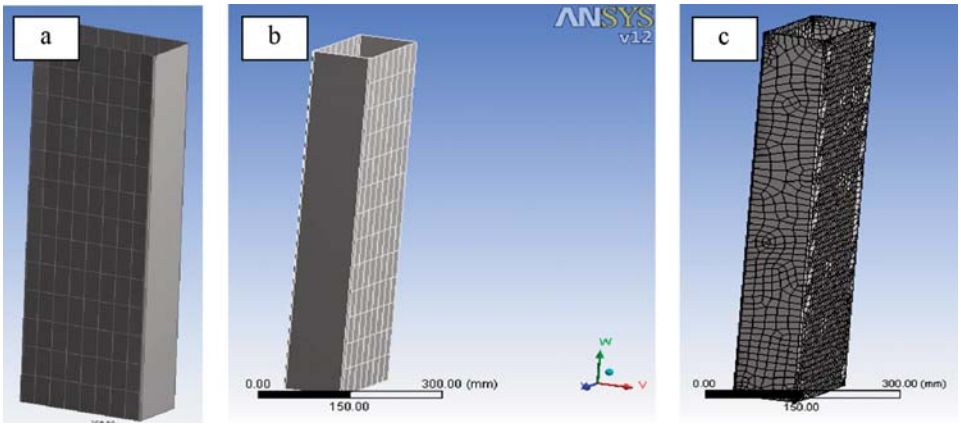

Fig. 3 Configuration of the calculation model, member B22

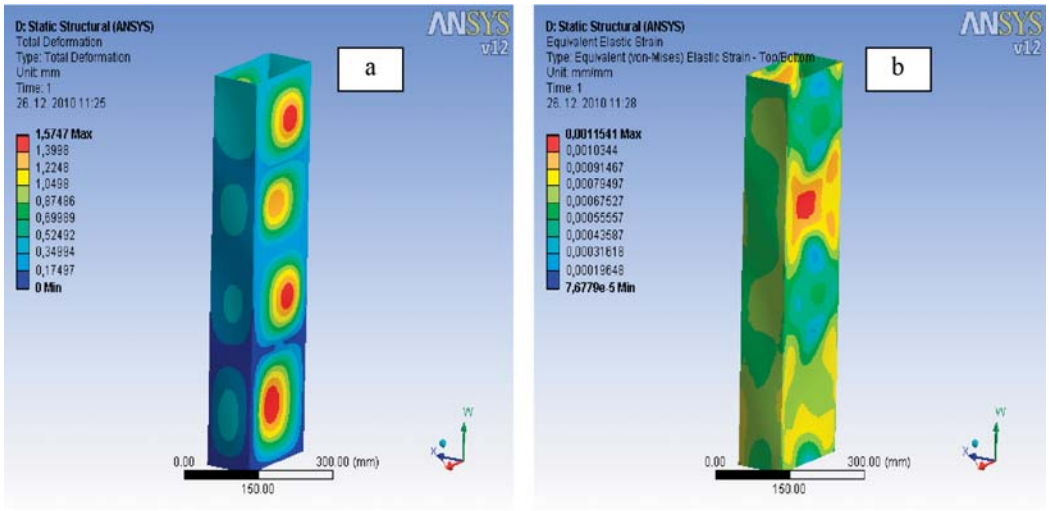

Fig. 4 Final deformation (a) and equivalent elastic strain (b), member B22

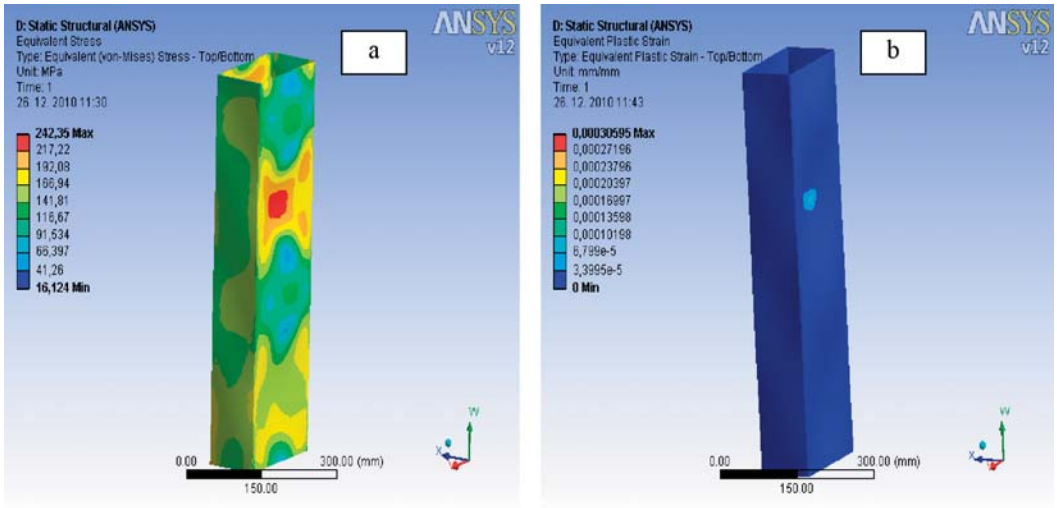

Fig. 5 Equivalent stress (a) and equivalent plastic strain (b), member B22

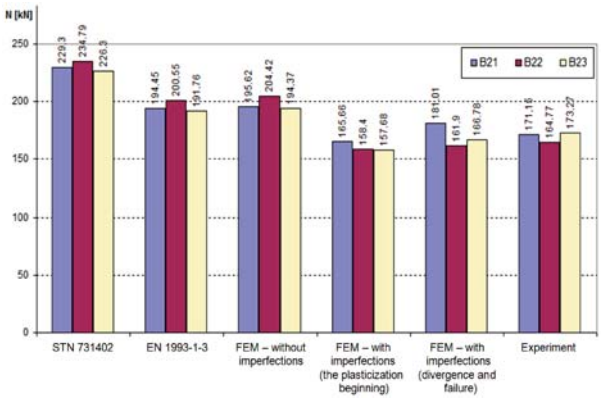

Fig. 6 Comparison of several limit loads; B21, B22 and B23

6. Conclusion

The resistances of the tested members, together with their post-critical behavior were investigated by means of theoretical-numerical analysis and experimental verification. Based on obtained experimental results, results acquired from the calculation models and analysis, it is evident that the resistances of the compressed thin-walled cold-formed steel members are significantly influenced by the initial imperfections and/or by the initial buckling shapes of their individual webs.

Fig. 6 indicates the results' conformity between the FEM simulation and theoretical calculation according to EN 1993-1-3:2006 – without considering the initial imperfections. This Figure also indicates the results' conformity between the FEM simulation and experiment results – with considering the initial imperfections. The difference in the results between the standard STN 73 1402:1998 and EN 1993-1-3:2006 is 14.58 %. The FEM simulation proves that the calculation procedures in the relevant standards are not sufficient enough for the consideration of the initial imperfections' influence.

In terms of tolerance values, the maximum measured imperfection of the webs was 1.51mm. This value is smaller than the maximum tolerated imperfection given in the standard EN 1090-2; A1:2012-03 as b/50, which is 4.15mm. Although the condition has been met, the results revealed a serious effect of initial imperfections.

Obtained results enlarge the knowledge base about the elastic-plastic resistance of thin-walled cold-formed steel members, as well as about the influence of initial imperfections. Obtained knowledge and results encourage the more consistent analysis and research, oriented to limiting the tolerance values of initial imperfections for the thin-walled cold-formed profiles and members.

Acknowledgements

The present work has been carried out within the project ITMS 26220120037 "The Support to the Centre of Excellent Integrated Research into Progressive Building Structures, Materials and Technologies", based on the Operational program Research and development, financed by the European Regional Development Fund of the European Union.

References

[1] JUHAS, P. et al.: *The Elastic-plastic behavior and Stress-strain Analysis of Framed and Flat Structural Members Made from Steel and Composite Materials.* Research report VEGA 1/0673/10, Kosice, 2010–2011.
[2] AL ALI, M., TOMKO, M., DEMJAN, I., BADAK, M.: Stress-strain Analysis of Thin-walled Compressed Steel Members with Closed Cross-sections, *SSP - J. of Civil Engineering* 17/1, 2011, pp. 85–96.
[3] AL ALI, M., TOMKO, M., BADAK, M.: *Investigation and Analysis of the Resistance of Compressed Cold-formed Steel Members.* In: The Research of the Institute of Structural Engineering. Kosice, Slovakia 2010, pp. 13–18.
[4] STN 73 1402:1988 *Design of Thin-walled Profiles in Steel Structures.* UNM, Prague 1987.
[5] STN EN 1993-1-3:2006 *Design of steel structures - Part 3: Supplementary Rules for Cold-formed Members and Sheeting.* Brussels 2006.
[6] ANSYS Inc.: *Theory, Release 9.0* [online]. Canonsburg: November 2004, 1062 p. <http://www1.ansys.com/customer/content/documentation/90/ansys/a_thry90.pdf>.
[7] ANSYS Inc.: *Release 11.0 Documentation for ANSYS* [online]. 2011. <http://www.kxcad.net/>.
[8] DANESHJO, N.: Computers Modeling and Simulation*, Advanced Materials Research*, 463/464, 2012, pp. 1102–1105.

https://doi.org/10.26552/com.C.2012.4.88-93

Ivana Pobocikova – Zuzana Sedliackova *

THE LEAST SQUARE AND THE WEIGHTED LEAST SQUARE METHODS FOR ESTIMATING THE WEIBULL DISTRIBUTION PARAMETERS – A COMPARATIVE STUDY

In this paper we study the performance of the least square method and the weighted least square method for estimating the Weibull distribution parameters. In engineering practice these methods are commonly used due to their simplicity. The estimates of the parameters can be calculated easily by the closed-form formula. We consider three estimators of the cumulative distribution function and the weight factor proposed by Bergman (1986). The methods are compared in terms of the root mean square error and sample size. The comparison is based on the Monte Carlo simulation. The comparison shows that the weight factor improves the accuracy of the estimation the Weibull distribution parameters.

Keywords: *Weibull distribution, parameter estimation, least square method, weighted least square method, root mean square error.*

1. Introduction

The Weibull distribution is one of the widely used distributions in engineering practice. It is named after Walodi Weibull (1887–1979), who popularized its use in the theory of reliability, especially for metallurgical failure models. Moreover, the Weibull distribution is useful for description of the life time of the machine components, for description of mechanical properties of the materials as fatigue of materials and strength of materials.

We consider the two parameter Weibull distribution. The probability density function of the Weibull distribution with parameters $c > 0$ and $\delta > 0$, abbreviated $W(c, \delta)$, is given by

$$f(x) = \frac{c}{\delta^c} x^{c-1} \exp\left(-\left(\frac{x}{\delta}\right)^c\right)$$

where $x > 0$, c is the shape parameter and δ is the scale parameter.

The cumulative distribution function of the Weibull distribution is

$$F(x) = 1 - \exp\left(-\left(\frac{x}{\delta}\right)^c\right), \; x > 0\,. \tag{1}$$

The mean μ and the variance σ^2 of the Weibull distribution are

$$\mu = \delta\Gamma\left(1 + \frac{1}{c}\right),$$

$$\sigma^2 = \delta^2\left[\Gamma\left(1 + \frac{2}{c}\right) - \Gamma^2\left(1 + \frac{2}{c}\right)\right],$$

where $\Gamma(a)$ is the gamma function defined by $\Gamma(a) = \int_0^\infty x^{a-1}e^{-x}dx$, $a > 0$.

The failure rate function of the Weibull distribution is given by

$$H(x) = \frac{c}{\delta^c} x^{c-1}.$$

Fig. 1 shows the effect of the shape parameter c on the density function for different values c and $\delta = 1$. Fig. 2. shows the effect of the scale parameter δ on the density function for different values δ and $c = 2$.

In this paper we study the performance of the methods for estimating the Weibull distribution parameters c and δ. The estimates of the parameters c and δ can be obtained in more ways. The commonly used methods are the maximum likelihood method (MLM), the method of moments (MOM), the least square method (LSM) and the weighted least square method (WLSM). The MLM is the most popular for its efficiency and good properties, but the calculation is complicated. The estimates of the parameters can be obtained only numerically. Several authors have studied and compared performance of the methods for estimating the Weibull distribution parameters, e. g. Bergman [1], Chu and Ke [2], Faucher and Tyson [3], Lu, Chen and Wu [4], Trustrum and Jayatilaka [5], Wu, Zhou and Li [6], Zerda [7].

Here, we consider the least square method (LSM) and the weighted least square method (WLSM), each with three estimators of the cumulative distribution function $F(x)$. In engineering practice these methods are commonly used due to their simplicity. The estimates of the parameters can be calculated easily by the closed-form formula. The methods are compared using the Monte Carlo simulation. The comparison is based on the root mean square error (*RMSE*) and the sample size n. Based on the simulation study we recommend the methods which have better performance.

* **Ivana Pobocikova, Zuzana Sedliackova**
Department of Applied Mathematics, Faculty of Mechanical Engineering, University of Zilina, Slovakia, E-mail: ivana.pobocikova@fstroj.uniza.sk

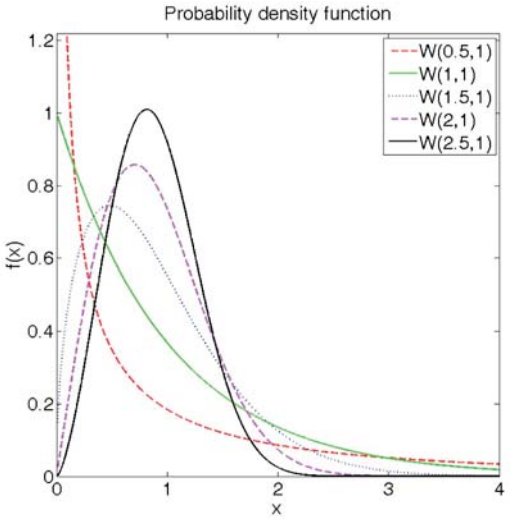

Fig. 1 Shows the effect of the shape parameter c on the density function for different values c and δ = 1

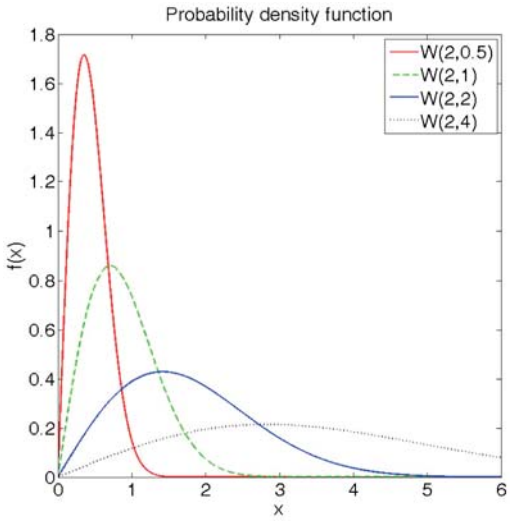

Fig. 2 Shows the effect of the scale parameter δ on the density function for different values δ and c = 2

2. Estimation of the parameters of the Weibull distribution

In this section we introduce the methods for estimating the Weibull distribution parameters. The estimates of the parameters c and δ denote $\hat{c}$ and $\hat{\delta}$, respectively. Let $X_1, X_2, ..., X_n$ be a random sample of size n from the Weibull distribution $W(c, \delta)$ and let x_1, x_2, ..., x_n be a realization of a random sample.

Least square method

Now, the cumulative distribution function (1) will be transformed to a linear function. From (1) by two logarithmic calculations we obtain

$$\ln[-\ln(1 - F(x))] = c \ln x - c \ln \delta \tag{2}$$

Let $Y = \ln[-\ln(1 - F(x))]$, $X = c \ln x$, $\beta_1 = c$ and $\beta_0 = = - c \ln \delta$. Then the equation (2) can be written as

$$Y = \beta_1 X + \beta_0$$

Now let $X_{(1)}, X_{(2)}, ..., X_{(n)}$ be the order statistics of $X_1, X_2, ..., X_n$ and let $x_{(1)} < x_{(2)} < ... < x_{(n)}$ be observed ordered observations. To estimate the values of the cumulative distribution function $F(x)$ we can use the folloving methods

$$\hat{F}(x_{(i)}) = \frac{i}{n+1} \quad \text{(the mean rank)} \tag{3}$$

$$\hat{F}(x_{(i)}) = \frac{i - 0.5}{n}, \tag{4}$$

$$\hat{F}(x_{(i)}) = \frac{i - 0.3}{n + 0.4} \quad \text{(the median rank)} \tag{5}$$

where i denotes the i^{th} smallest value of $x_{(1)}, x_{(2)}, ..., x_{(n)}$, $i = 1, 2, ..., n$.

The estimates $\hat{\beta}_0$ and $\hat{\beta}_1$ of the regression parameters β_0 and β_1 minimize the function

$$Q(\beta_0, \beta_1) = \sum_{i=1}^{n} (Y_i - \beta_0 - \beta_1 X_i)^2 =$$

$$= \sum_{i=1}^{n} (Y_i - \beta_0 - \beta_1 \ln x_{(i)})^2 .$$

Therefore, the estimates $\hat{\beta}_0$ and $\hat{\beta}_1$ of the parameters β_0 and β_1 are given by

$$\hat{c} = \hat{\beta}_1 = \frac{n \sum_{i=1}^{n} \ln x_{(i)} \ln\left[-\ln\left(1 - \hat{F}(x_{(i)})\right)\right] - \sum_{i=1}^{n} \ln x_{(i)} \sum_{i=1}^{n} \ln\left[-\ln\left(1 - \hat{F}(x_{(i)})\right)\right]}{n \sum_{i=1}^{n} \ln^2 x_{(i)} - \left(\sum_{i=1}^{n} \ln x_{(i)}\right)},$$

$$\hat{\beta}_0 = \frac{1}{n} \sum_{i=1}^{n} \ln\left[-\ln\left(1 - \hat{F}(x_{(i)})\right)\right] - \hat{c} \frac{1}{n} \sum_{i=1}^{n} \ln x_{(i)} .$$

The estimate $\hat{\delta}$ of the parameter δ is given by

$$\hat{\delta} = \exp\left(-\frac{\hat{\beta}_0}{\hat{c}}\right) = \exp\left\{-\frac{\sum_{i=1}^{n} \ln\left[-\ln\left(1 - \hat{F}(x_{(i)})\right)\right] - \hat{c} \sum_{i=1}^{n} \ln x_{(i)}}{\hat{c} n}\right\}.$$

Weighted least square method

We suppose that the estimates $\hat{\beta}_0$ and $\hat{\beta}_1$ of the regression parameters β_0 and β_1 minimize the function

$$Q(\beta_0, \beta_1) = \sum_{i=1}^{n} w_i (Y_i - \beta_0 - \beta_1 X_i)^2 =$$

$$= \sum_{i=1}^{n} w_i (Y_i - \beta_0 - \beta_1 \ln x_{(i)})^2$$

where w_i is the weight factor, $i = 1, 2, \ldots n$. Therefore, the estimates $\hat{\beta}_0$ and $\hat{\beta}_1$ of the parameters β_0 and β_1 and are given by

$$\hat{c} = \hat{\beta}_1 = \frac{\sum_{i=1}^{n} w_i \sum_{i=1}^{n} w_i \ln x_{(i)} \ln\left[-\ln\left(1 - \hat{F}(x_{(i)})\right)\right] - \sum_{i=1}^{n} w_i \ln x_{(i)} \sum_{i=1}^{n} w_i \ln\left[-\ln\left(1 - \hat{F}(x_{(i)})\right)\right]}{\sum_{i=1}^{n} w_i \sum_{i=1}^{n} w_i \ln^2 x_{(i)} - \left(\sum_{i=1}^{n} w_i \ln x_{(i)}\right)^2},$$

$$\hat{\beta}_0 = \frac{\sum_{i=1}^{n} w_i \ln\left[-\ln\left(1 - \hat{F}(x_{(i)})\right)\right] - \hat{c} \sum_{i=1}^{n} w_i \ln x_{(i)}}{\sum_{i=1}^{n} w_i}.$$

Then the estimate $\hat{\delta}$ of the parameter δ is given by

$$\hat{\delta} = \exp\left(-\frac{\sum_{i=1}^{n} w_i \ln\left[-\ln\left(1 - \hat{F}(x_{(i)})\right)\right] - \hat{c} \sum_{i=1}^{n} w_i \ln x_i}{\hat{c} \sum_{i=1}^{n} w_i}\right).$$

In this paper we use the weight factor proposed by Bergman [1]

$$w_i = \left[\left(1 - \hat{F}(x_{(i)})\right) \ln\left(1 - \hat{F}(x_{(i)})\right)\right]^2, \; i = 1, 2, \ldots, n.$$

3. Monte Carlo simulation

We generate by the Monte Carlo simulation the random samples from the Weibull distribution and compare the performance of the methods for estimating the Weibull distribution parameters mentioned above. In simulation study we consider the LSM and the WLSM each with three methods for estimating the cumulative distribution function. Thus together we compare six methods. We denote the methods with the estimators of the cumulative distribution function (3) as LSM_1, WLSM_1, with (4) as LSM_2, WLSM_2 and with (5) as LSM_3, WLSM_3.

We consider sample sizes $n = 5$ to 100, $\delta = 1$ and several values of the parameters $c = 0.5, 1.5, 2.5$ representing decreasing, increasing and concave, increasing and convex failure rate functions respectively. All possible combinations of the parameters c, δ and sample sizes n are considered. For each combination c, δ and n we generate by the Monte Carlo simulation $N = 5000$ random samples from the Weibull distribution. For each of six methods we obtain 5000 estimates $\hat{c}_1, \hat{c}_2, \ldots, \hat{c}_{5000}$ of the parameter c and 5000 estimates $\hat{\delta}_1, \hat{\delta}_2, \ldots, \hat{\delta}_{5000}$ of the parameter δ. Then we compute for each method the sample means $\bar{c}$, $\bar{\delta}$ and the sample variances s_c^2, s_δ^2, i. e.

$$\bar{c} = \frac{1}{5000} \sum_{i=1}^{5000} \hat{c}_i, \; \bar{\delta} = \frac{1}{5000} \sum_{i=1}^{5000} \hat{\delta}_i,$$

$$s_c^2 = \frac{1}{4999} \sum_{i=1}^{5000} (\hat{c}_i - \bar{c})^2, \; s_\delta^2 = \frac{1}{4999} \sum_{i=1}^{5000} (\hat{\delta}_i - \bar{\delta})^2.$$

To compare the performance of the various methods we compute the sample root mean square error (*RMSE*) defined by

$$RMSE = \sqrt{\frac{1}{5000} \sum_{i=1}^{5000} \left[(\hat{c}_i - \bar{c})^2 + (\hat{\delta}_i - \bar{\delta})^2\right]}.$$

The estimates with smaller variance and *RMSE* are prefered. The simulations and the calculation are performed in the Matlab system.

4. Comparison of the methods

In this section we summarize the performance of the methods for estimating the Weibull distribution parameters. The methods are compared in terms of the *RMSE* and sample size n.

The results of the comparison for selected sample sizes $n = 5$, 10, 30, 50, 100 are summarized in Tables 1, 2, 3. The tables show the sample means, the sample variances and the sample *RMSE*. Figures 3, 4, 5 show illustrative plots of the *RMSE* for $n = 5$ to 50 (left), for $n = 50$ to 100 (right).

It is evident that the *RMSE* of the least square method is in many cases much larger than the *RMSE* of the weighted least square method for the case studies in this paper. The weight factor improves the accuracy of the estimation the Weibull distribution parameters. When gets larger the *RMSE* of all methods tends to be smaller.

For the sample size $n \geq 10$ and for $c = 1.5, 2.5$ the comparison shows that the *RMSE* of the LSM_1 is in many cases much larger than the other methods. The LSM_2 and the LSM_3 are comparable methods in many cases in terms of the *RMSE*. The *RMSE* of the LSM_3 is slightly larger than the RMSE of the LSM_2. The *RMSE* of the WLSM_2 is larger than the WLSM_1 and the WLSM_3. The *RMSE* of the WLSM_3 is slightly larger than the RMSE of the WLSM_1, both methods are comparable for $n \geq 40$. In general, the WLSM_1 provides the best estimates of the Weibull distribution parameters than the other methods in terms of the *RMSE*.

For the small sample size $5 \leq n < 10$ and for $c = 1.5, 2.5$ the comparison shows that in general the *RMSE* of the WLSM_1 outperforms the other methods. The *RMSE* of the LSM_1 is only slightly larger than the *RMSE* of the WLSM_1. The LSM_1 provides good results in these cases.

For the sample size $n \geq 10$ and for $c = 0.5$ the comparison shows that in general the *RMSE* of the WLSM_2 outperforms the other methods. The *RMSE* of the WLSM_3 is slightly larger than the *RMSE* of the WLSM_2. The RMSE of the LSM_2 and the

Simulation results of the parameter estimation for real parameters $c = 0.5$, $\delta = 1$ — Table 1

Sample size	Method	$\bar{c}$	$\bar{\delta}$	s_c^2	s_δ^2	*RMSE*
n = 5	LSM_1	0.4508	1.6745	0.0745	2.6689	1.7889
	LSM_2	0.6007	1.3947	0.1311	1.8255	1.4568
	LSM_3	0.5271	1.4977	0.1014	2.1039	1.5663
	WLSM_1	0.4319	1.6060	0.0651	2.4445	1.6974
	WLSM_2	0.5485	1.3710	0.1071	1.8767	1.4572
	WLSM_3	0.4940	1.4555	0.0855	2.0588	1.5334
n = 10	LSM_1	0.4363	1.3946	0.0205	0.9475	1.0619
	LSM_2	0.5311	1.2439	0.0298	0.7336	0.9075
	LSM_3	0.4860	1.3034	0.0252	0.8129	0.9645
	WLSM_1	0.4345	1.3256	0.0182	0.8595	0.9939
	WLSM_2	0.5036	1.2197	0.0272	0.7586	0.9132
	WLSM_3	0.4734	1.2595	0.0226	0.7937	0.9403
n = 30	LSM_1	0.4557	1.1618	0.0076	0.2252	0.5108
	LSM_2	0.5048	1.0972	0.0090	0.1957	0.4627
	LSM_3	0.4822	1.1246	0.0084	0.2078	0.4816
	WLSM_1	0.4713	1.1046	0.0066	0.1984	0.4655
	WLSM_2	0.4966	1.0721	0.0079	0.1898	0.4503
	WLSM_3	0.4864	1.0847	0.0073	0.1930	0.4557
n = 50	LSM_1	0.4652	1.1087	0.0047	0.1198	0.3708
	LSM_2	0.5011	1.0637	0.0053	0.1083	0.3430
	LSM_3	0.4848	1.0831	0.0051	0.1131	0.3540
	WLSM_1	0.4823	1.0640	0.0040	0.1108	0.3452
	WLSM_2	0.4976	1.0450	0.0045	0.1080	0.3383
	WLSM_3	0.4915	1.0524	0.0043	0.1091	0.3408
n = 100	LSM_1	0.4760	1.0563	0.0025	0.0533	0.2440
	LSM_2	0.4991	1.0283	0.0027	0.0501	0.2315
	LSM_3	0.4888	1.0405	0.0026	0.0515	0.2363
	WLSM_1	0.4898	1.0258	0.0022	0.0525	0.2355
	WLSM_2	0.4974	1.0166	0.0023	0.0519	0.2333
	WLSM_3	0.4944	1.0202	0.0023	0.0521	0.2341

Simulation results of the parameter estimation for real parameters $c = 1.5$, $\delta = 1$ — Table 2

Sample size	Method	$\bar{c}$	$\bar{\delta}$	s_c^2	s_δ^2	*RMSE*
n = 5	LSM_1	1.3407	1.0925	0.7156	0.1192	0.9320
	LSM_2	1.7878	1.0277	1.2710	0.1060	1.2084
	LSM_3	1.5683	1.0527	0.9784	0.1107	1.0471
	WLSM_1	1.2914	1.0764	0.6761	0.1170	0.9178
	WLSM_2	1.6453	1.0164	1.1606	0.1095	1.1363
	WLSM_3	1.4792	1.0394	0.9075	0.1117	1.0105
n = 10	LSM_1	1.2949	1.0598	0.1758	0.0564	0.5270
	LSM_2	1.5759	1.0202	0.2545	0.0519	0.5590
	LSM_3	1.4421	1.0363	0.2154	0.0536	0.5232
	WLSM_1	1.2884	1.0413	0.1562	0.0554	0.5079
	WLSM_2	1.4920	1.0108	0.2348	0.0542	0.5378
	WLSM_3	1.4033	1.0226	0.1948	0.0545	0.5091
n = 30	LSM_1	1.3653	1.0326	0.0676	0.0185	0.3245
	LSM_2	1.5126	1.0135	0.0801	0.0176	0.3131
	LSM_3	1.4447	1.0217	0.0743	0.0180	0.3095
	WLSM_1	1.4098	1.0162	0.0569	0.0181	0.2888
	WLSM_2	1.4853	1.0059	0.0677	0.0181	0.2932
	WLSM_3	1.4549	1.0099	0.0630	0.0181	0.2885
n = 50	LSM_1	1.3945	1.0218	0.0433	0.0112	0.2570
	LSM_2	1.5022	1.0080	0.0485	0.0107	0.2435
	LSM_3	1.4532	1.0140	0.0462	0.0109	0.2438
	WLSM_1	1.4442	1.0083	0.0369	0.0110	0.2261
	WLSM_2	1.4897	1.0022	0.0412	0.0110	0.2286
	WLSM_3	1.4716	1.0046	0.0394	0.0110	0.2264
n = 100	LSM_1	1.4276	1.0155	0.0240	0.0054	0.1868
	LSM_2	1.4968	1.0065	0.0255	0.0053	0.1755
	LSM_3	1.4657	1.0104	0.0248	0.0053	0.1774
	WLSM_1	1.4711	1.0052	0.0200	0.0054	0.1619
	WLSM_2	1.4938	1.0022	0.0211	0.0054	0.1628
	WLSM_3	1.4847	1.0034	0.0206	0.0054	0.1620

Simulation results of the parameter estimation for real parameters $c = 2.5$, $\delta = 1$ — Table 1

Sample size	Method	$\bar{c}$	$\bar{\delta}$	s_c^2	s_δ^2	*RMSE*
n = 5	LSM_1	2.2223	1.0423	1.5070	0.0387	1.2745
	LSM_2	2.9630	1.0048	2.6661	0.0361	1.7076
	LSM_3	2.5993	1.0194	2.0564	0.0370	1.4503
	WLSM_1	2.1367	1.0329	1.3909	0.0383	1.2498
	WLSM_2	2.7187	0.9975	2.4000	0.0377	1.5764
	WLSM_3	2.4459	1.0112	1.8685	0.0377	1.3816
n = 10	LSM_1	2.1727	1.0325	0.5197	0.0197	0.8047
	LSM_2	2.6437	1.0094	0.7517	0.0188	0.8894
	LSM_3	2.4194	1.0188	0.6367	0.0191	0.8140
	WLSM_1	2.1559	1.0212	0.4450	0.0196	0.7637
	WLSM_2	2.4961	1.0028	0.6570	0.0196	0.8225
	WLSM_3	2.3478	1.0100	0.5497	0.0195	0.7696
n = 30	LSM_1	2.2736	1.0151	0.1894	0.0064	0.4973
	LSM_2	2.5190	1.0038	0.2245	0.0062	0.4807
	LSM_3	2.4060	1.0086	0.2082	0.0063	0.4727
	WLSM_1	2.3494	1.0056	0.1656	0.0064	0.4412
	WLSM_2	2.4747	0.9994	0.1977	0.0064	0.4525
	WLSM_3	2.4243	1.0018	0.1839	0.0064	0.4427
n = 50	LSM_1	2.3228	1.0145	0.1193	0.0040	0.3935
	LSM_2	2.5024	1.0062	0.1332	0.0039	0.3703
	LSM_3	2.4206	1.0098	0.1269	0.0039	0.3704
	WLSM_1	2.4116	1.0065	0.0997	0.0039	0.3339
	WLSM_2	2.4876	1.0029	0.1112	0.0040	0.3396
	WLSM_3	2.4573	1.0043	0.1065	0.0040	0.3350
n = 100	LSM_1	2.3805	1.0082	0.0646	0.0019	0.2844
	LSM_2	2.4960	1.0028	0.0686	0.0019	0.2656
	LSM_3	2.4441	1.0052	0.0669	0.0019	0.2682
	WLSM_1	2.4580	1.0021	0.0539	0.0019	0.2399
	WLSM_2	2.4959	1.0003	0.0568	0.0019	0.2424
	WLSM_3	2.4808	1.0010	0.0556	0.0019	0.2407

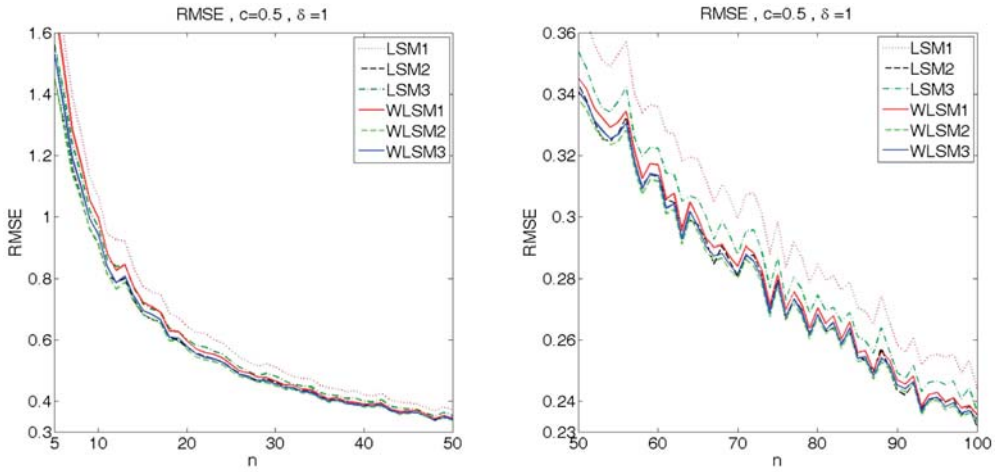

Fig. 3 Root mean square error for real parameters $c = 0.5$, $\delta = 1$

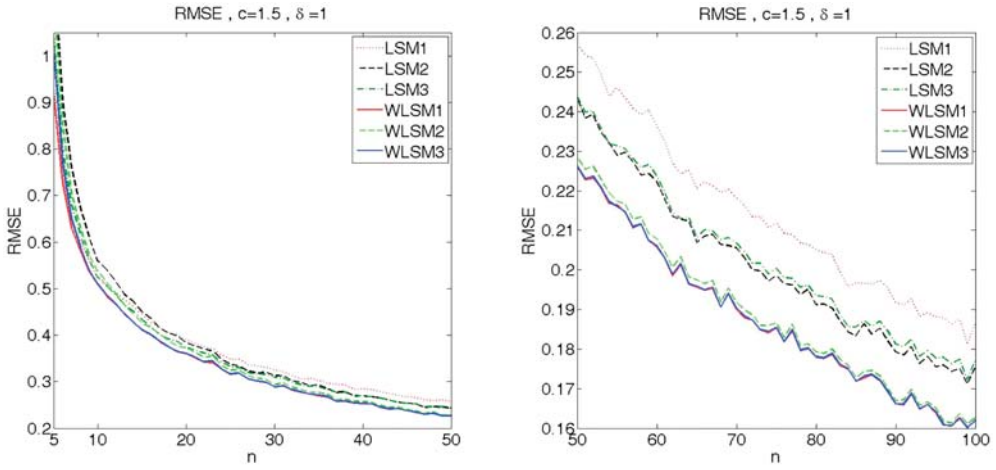

Fig. 4 Root mean square error for real parameters $c = 1.5$, $\delta = 1$

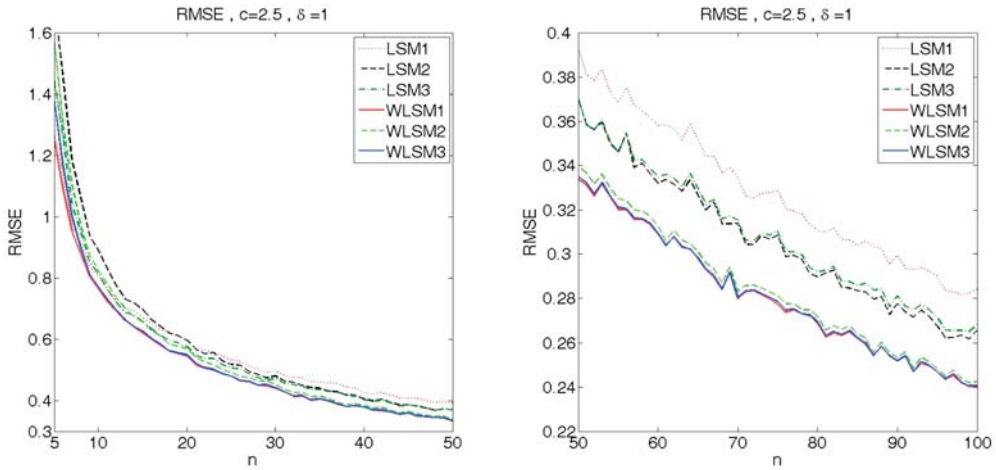

Fig. 5 Root mean square error for real parameters $c = 2.5$, $\delta = 1$

WLSM_1 follow. The *RMSE* of the LSM_1 is in many cases much larger than the other methods.

For the sample size $5 \leq n < 10$ and for $c = 0.5$ the *RMSE* of the LSM_2 is only slightly larger than the *RMSE* of the WLSM_2. The *RMSE* of the WLSM_3 and the LSM_3 follow. The *RMSE* of the LSM_1 is much larger than the *RMSE* of the other methods.

5. Concluding remarks

In this paper we compared the performance of the methods for estimating the Weibull distribution parameters in terms of the *RMSE* and sample size *n*. The comparison was based on the Monte Carlo simulation. The comparison shows that the weight factor improves the accuracy of the estimation the Weibull distribution parameters. The WLSM_1 performs the best in terms of the *RMSE* than the other methods for majority cases studied in this paper and for all sample sizes, the WLSM_3 follows as the second good choice. Except the case when $c = 0.5$, the WLSM_2 performs to be the best for all the sample sizes than the other methods. The good choice is in this case for middle and large sample sizes the WLSM_3.

The advantages of these recommended methods are: simple derivation, easy calculation of the estimates of the parameters by the closed-form formula. And so from this point of view these methods are very useful for engineering practice.

Acknowledgement

This research was supported by the Slovak Grant Agency VEGA through the projects No. 1/1245/12 and No. 1/0797/12.

References

[1] BERGMAN, B.: Estimation of Weibull Parameters Using a Weight Function. *J. of Materials Science Letters* 5, pp. 611–614, 1986

[2] CHU, Y. K., KE, CH., J.: Computation Approaches for Parameter Estimation of Weibull Distribution. *Mathematical and Computational Applications,* vol. 17, No. 1, pp. 39–47, 2012

[3] FAUCHER, B., TYSON, W. R.: On the Determination of Weibull Parameters. *J. of Materials Science Letters* 7, pp. 1199–1203, 1988

[4] LU, H. L., CHEN, CH. H., WU, J. W.: A Note on Weighted Least-squares Estimation of the Shape Parameter of the the Weibull Distribution. *Quality and Reliability Engineering International* 20, pp. 579–586, 2004

[5] TRUSTRUM, K., JAYATILAKA, A. S.: On Estimating the Weibull Modulus for a Brittle Material. *J. of Material Science* 14, pp. 1080–1084,1979

[6] WU, D., ZHOU, J., LI, Y.: Methods for Estimating Weibull Parameters for Brittle Materials. *J. of Material Science* 41, pp. 5630–5638, 2006

[7] ZERDA, I.: An Experimental Comparison of Popular Estimation Methods for the Weibull, Gamma, and Gompertz Distributions. *Schedae Informaticae* 20, pp. 67–82, 2011.

https://doi.org/10.26552/com.C.2012.4.94-98

Katarina Mikova – Mario Guagliano – Otakar Bokuvka – Libor Trsko – Frantisek Novy *

THE ROLE OF SHOT PEENING IN INCREASING X70 STEEL FATIGUE PROPERTIES

The paper presents the authors' results of experimental examination of pipeline steel X70 fatigue properties before and after shot peening application, including relaxation of residual stresses during rotating bendi ng fatigue loading ($f = 30$ Hz, $T = 20 \pm 5$ °C, $R = -1$). The obtained results confirmed the positive effect of surface hardening realized by shot peening. The fatigue properties incl. fatigue limit were higher after shot peening and this effect was visibly higher for notched specimens than for smooth specimens. During rotating bending fatigue loading the residual stresses in subsurface layers relaxes which decreases the strengthening effect after a certain number of cycles.

Keywords: *X70 steel; shot peening; fatigue properties*

1. Introduction

The fatigue of structural materials is a phenomenon which has been continuously investigated more than 170 years. The fatigue properties obtained by experimental techniques are very important, especially with regards to safety, reliability of engineering components and constructions, which is closely connected with economy and ecology of production [1–3].

Natural gas is transported through big distances in pipes under high pressure. Due to the friction of the gas with the pipe and turbulences caused by fittings and bent adapters the value of the pressure inside the pipe decreases. To restore the pressure it is necessary to periodically add compressor stations into the pipe system. Vibrations created by compressors and rapid pressure changes in the pipes cause fatigue damage of used material. Several methods of non – destructive testing as a penetration test, magnetic particle test and so on are used to identify propagating fatigue cracks [4]. Damage of a high pressure gas pipe is usually followed by big explosion which causes devastating disaster. These are the reasons why it is necessary to increase fatigue life of X70 steel used for high pressure gas pipes [5].

Deformation strengthening of the surface layer is one of the methods used to increase time necessary for a fatigue crack initiation. Due to a difficult shape of gas pipes not all the methods of surface hardening can be used. One of suitable methods, which is possible to use on gas pipes is shot peening. Shot peening is a cold – working process of surface treatment, where the surface is bombarded with small and hard spherical media called shots. Impact of every shot causes a plastic deformation of the surface and a dimple is created [6, 7]. Tension deformation necessary for creation of a dimple causes compression residual stress in the subsurface layers of the material. This compression residual stress mainly increases the time necessary for fatigue crack initiation which increases the total fatigue life of a component or a construction.

The measurement of residual stress by X-ray diffraction (XRD) relies on the fundamental interactions between the wave front of the X-ray beam and the crystal lattice. By residual stress measuring using X-ray diffraction (XRD), the strain in the crystal lattice is measured and the associated residual stress is determined from the elastic constants assuming to a linear elastic distortion of the appropriate crystal lattice plane. Since X-rays impinge over an area for about 2 mm^2 on the sample, many grains and crystals will contribute to the measurement. The exact number is dependent on the grain size and beam geometry. Although the measurement is considered to be near surface, X-rays do penetrate some distance into the material: the penetration depth depends on the anode, material and angle of incidence. Hence the measured strain is usually over a few microns depth under the surface of the specimen [8].

In this paper the authors publish their own results of experimental examination of pipeline steel X70 fatigue properties before and after shot peening application including relaxation of residual stresses during rotating bending fatigue loading.

2. Experimental part

Results of quantitative chemical analysis of X70 steel are listed in Table 1. They show that the steel has a very low carbon content

* **Katarina Mikova[1], Mario Guagliano[2], Otakar Bokuvka[1], Libor Trsko[1], Frantisek Novy[1]**
[1] Department of Materials Engineering, Faculty of Mechanical Engineering, University of Zilina, Slovakia, E-mail: katarina.mikova@fstroj.uniza.sk
[2] Department of Mechanics, Politecnico di Milano, Milano, Italy

(because very good weldability is required) and two microalloying elements Nb and V which increase the toughness of material. Microstructure of experimental X70 steel (Fig. 1, Fig. 2) consists of polyedric grains of ferrite and perlite. The microstructure has a very strong deformation texture (ferrite and pearlite grains create rows) which was caused by the rolling of X70 steel during its manufacturing.

Chemical composition of X70 steel (in weight %) Tab. 1

C	Si	Mn	P	S	Nb	V	Fe
0.09	0.30	1.71	0.016	0.002	0.05	0.06	balance

Mechanical properties of X70 steel Tab. 2

R_m (MPa)	R_e (MPa)	A (%)
605	495	21.6

Mechanical properties (Table 2) show medium tensile strength and high elongation which makes a good assumption that shot peening treatment could create strengthened surface layers which would increase the time necessary for fatigue crack initiation. From X70 steel sheet metal of thickness 14 mm were cut pieces in longitudinal direction, which were machined to obtain 21 pieces of round specimens and 21 pieces of notched specimens for rotating bending fatigue tests. Rotating bending fatigue tests with parameters: frequency $f = 30$ Hz, temperature $T = 20 \pm 5$ °C and stress ratio $R = -1$, were carried out on the as - machined and shot peened smooth specimens and on as - machined and shot peened notched specimens with geometry according to ISO 1143 [9], Figs. 3 and 4. The shot peening treatment of specimens [10] was realized with the use of parameters including Almen intensity presented in Table 3.

Parameters of performed shot peening treatment Tab. 3

Shot type and diameter (μm)	Almen Intensity	Coverage (%)
S 170 (steel, ø = 425 μm)	8A	100

Microhardness measurement on the cross section of specimens was carried out by Vickers method at a loading weight 200 g for

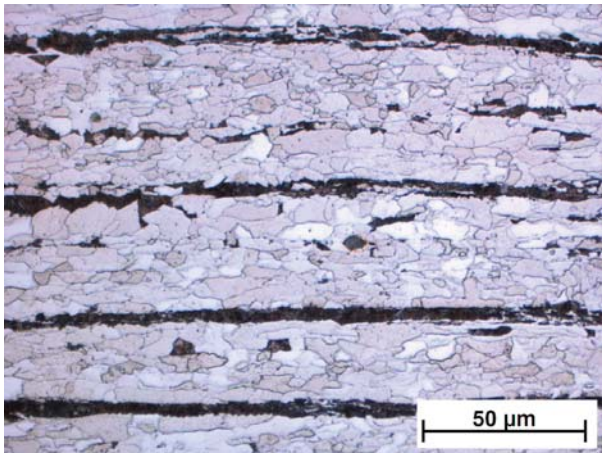

Fig. 1 Microstructure of X70 steel, longitudinal cut, etch. Nital

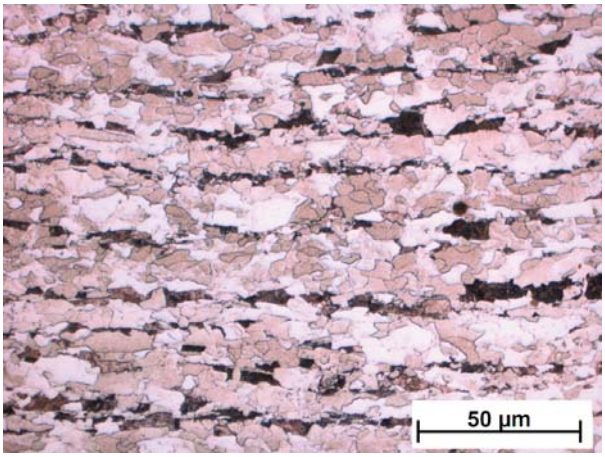

Fig. 2 Microstructure of X70 steel, transversal cut, etch. Nital

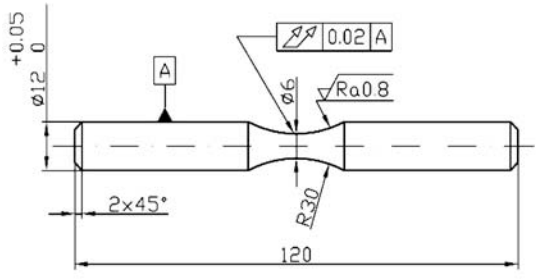

Fig. 3 Shape and dimensions of smooth specimens for fatigue tests

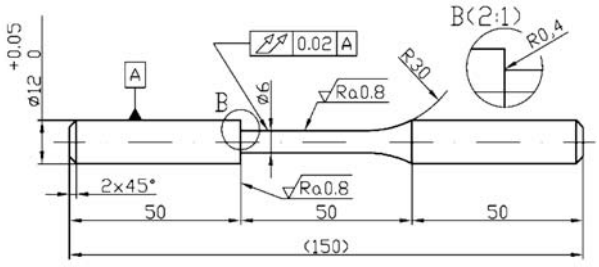

Fig. 4 Shape and dimensions of notched specimens for fatigue tests

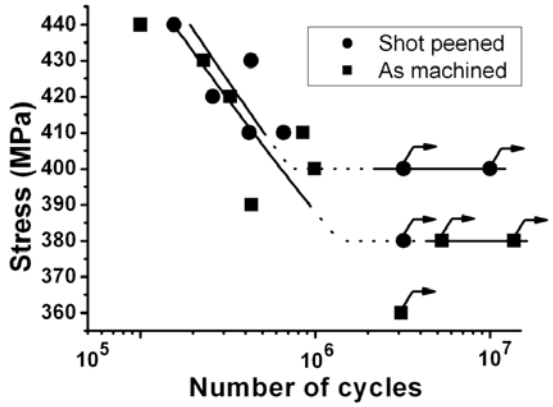

Fig. 5 S – N curves of X70 steel before and after shot peening application (smooth specimens)

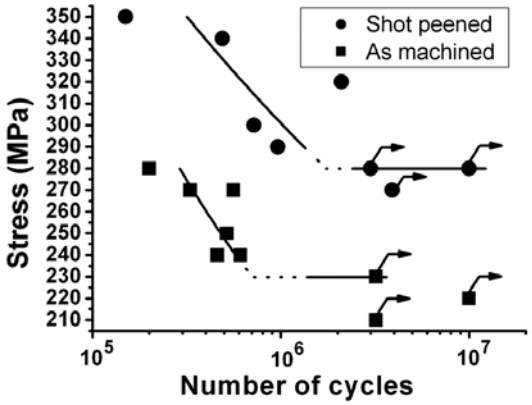

Fig. 6 S – N curves of steel X70 before and after shot peening application (notched specimens)

15 s. To study the state of residual stresses, XRD analysis was performed on all series of specimens using an AST X-Stress 3000 X-ray diffractometer (radiation C_r K_a, irradiated area 2 mm^2, sin2ψ method, diffraction angles (2θ) scanned between −45° and 45°). Measurements were carried out in depth step by step removing a very thin layer of material using an electro – polishing device in order to obtain the in - depth trend of residual stresses. A solution of acetic acid (94 %) and perchloric acid (6 %) was used for electro – polishing.

3. Results and discussion

Results of fatigue tests, the dependence of rotating bending stress vs. number of cycles to failure (or run out), S – N curves, obtained in the region from $N \approx 10^5$ cycles to $N \approx 10^7$ cycles for smooth specimens and notched specimens are shown in Figs. 5 and 6. According to these figures it is obvious that the fatigue life-time continuously increases with the decrease of rotating bending loading. The results after shot peening application obtained for the smooth specimens and notched specimens are also shifted to a higher number of cycles, to the right side of the plot, and it entails better fatigue properties. The fatigue limit σ_{oc} was determined at the run – out number of $N = 3 \times 10^6$ cycles with using a staircase procedure. Fatigue limit σ_{oc} in the case of smooth as machined specimens was σ_{oc} = 380 MPa and for shot peened specimens σ_{oc} = 400 MPa, the increase is 5.26 %, Fig. 5. The fatigue ratio σ_{oc}/R_m increased from σ_{oc}/R_m = 0.628 to σ_{oc}/R_m = 0.661. In the case of notched as machined specimens the fatigue limit σoc was σoc = 230 MPa and for shot peened specimens σ_{oc} = 280 MPa, the increase is 24.73 %, Fig. 6. The fatigue ratio σ_{oc}/R_m increased from σ_{oc}/R_m = 0.380 to σ_{oc}/R_m = 0.462. The influence of shot peening application on the fatigue properties, resistance against fatigue degradation mechanisms is visibly higher for notched specimens than for smooth specimens. These results are in good agreement with works [11, 12], where an increase of fatigue properties

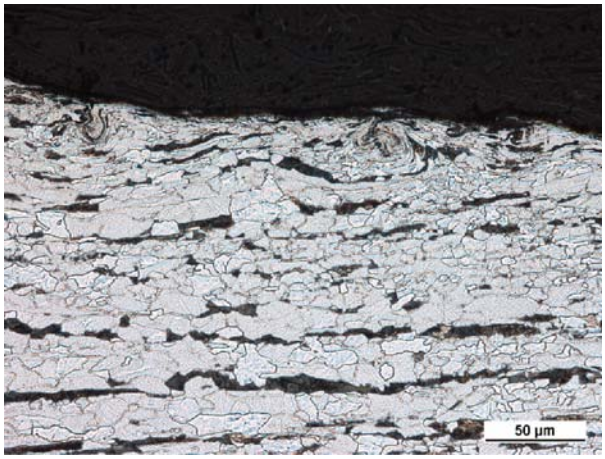

Fig. 7 Surface morphology of X 70 steel after shot peening application, etch. Nital

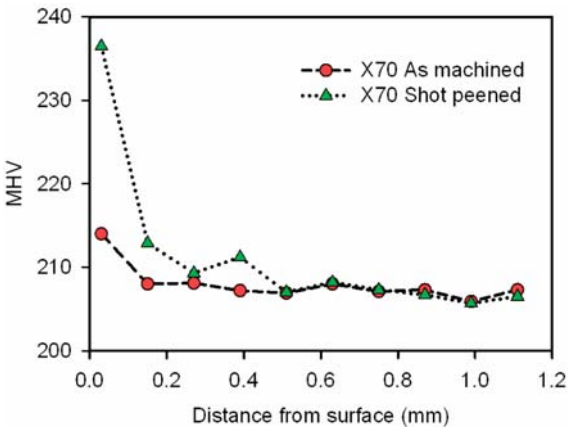

Fig. 8 Surface layers microhardness values, X70 steel, before and after shot peening application

after application of shot peening on the surface of the structural materials is presented; the fatigue properties of structural materials can be increased up – to 20 %. Better fatigue properties of X70 steel after shot peening are the result of quantitative changes in the surface layers; the characteristic surface morphology is created (Fig. 7), mechanical and technological properties are changed, Figs. 8 and 9. The characteristic surface morphology is the result

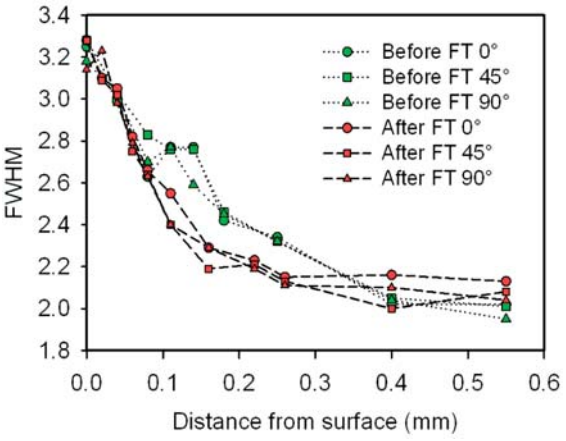

Fig. 9 FWHM profile, X70 steel, before and after fatigue tests

of multiple impacts of the shots on the surface of the specimens, an indentation is created which is surrounded by a plastic region followed by an elastic zone Fig. 7. The surface morphology changes are accompanied usually with increased surface hardness (Fig. 8) and FWHM (Full With at Half Maximum), Fig. 9, due to the cold – working effect of shot peening [13]. Microhardness is higher at the surface (237 MHV) and with gradually increasing depth in a direction to the axis it has a decreasing character (207 MHV for the core of material). The variation of microhardness values is caused by different orientation and deformation of grains. The parameter FWHM shown in Fig. 9, measured by X – ray diffraction (XRD) represents the full width of the diffraction peak at half of the maximum intensity and it is assumed as an index of hardening of the material. As it is observed in Fig. 9 the on – surface amount of FWHM is growing with increasing kinetic energy of the shot peening process. It is to be noted that the thickness of the work – hardened layer can be estimated as the thickness of the layer which shows considerably increased FWHM values in comparison with the core of material. The microhardness is closely related to FWHM and residual stresses which represents resistance of material to local plastic deformation. The decrease of microhardness and FWHM corresponds to the decrease of residual stresses (see Figs. 8, 9 vs. Fig. 10). Relaxation of residual stresses can be observed by comparing the residual stresses of specimens before fatigue test and residual stresses of specimens after fatigue test, Fig. 10.

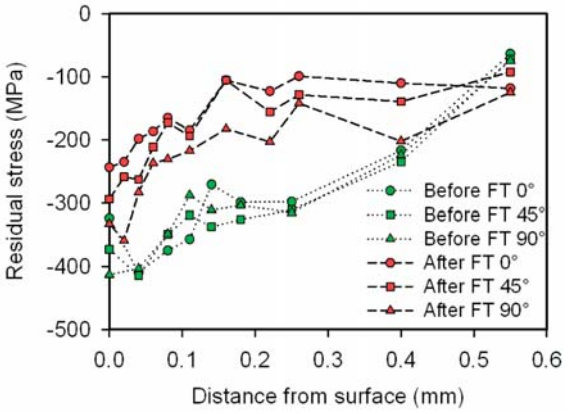

Fig. 10 Distribution of residual stresses, X70 steel, shot peened specimens before and after fatigue tests

Residual stresses of specimens after fatigue tests had comparable values on the surface with the specimens before fatigue tests, but it is obvious that after the fatigue test the values of residual stresses decrease much faster and reach minimum in a smaller depth than specimens before fatigue tests. This means that during cyclic loading the residual stresses in the surface and subsurface layers relax which lowers the strengthening effect and lowers the fatigue lifetime of metallic components [12].

4. Conclusions

With regard to the obtained results of X70 pipeline steel at rotating bending fatigue tests ($f = 30$ Hz, $T = 20 \pm 5$ °C, $R = -1$) it can be stated:

- shot peening application causes deformation strengthening of surface layers of tested steel,
- fatigue limit determined for smooth as – machined specimens was $\sigma_{oc} = 380$ MPa and for smooth shot peened specimens $\sigma_{oc} = 400$ MPa,
- fatigue limit determined for notched as – machined specimens was $\sigma_{oc} = 230$ MPa and for notched shot peened specimens $\sigma_{oc} = 280$ MPa,
- increase of fatigue limit σoc after shot peening application was visibly higher for notched specimens than for smooth specimens,
- during rotating bending fatigue loading the residual stresses in subsurface layers relax, whhich lowers the strengthening effect after a certain number of cycles,
- the role of shot peening as a cold – working process at increasing of X70 steel fatigue properties is positive.

Acknowledgements

The research was supported by the Scientific Grant Agency of the Ministry of Education, Science and Sports of the Slovak Republic and Slovak Academy of Sciences, grant No. 1/0743/12.

References

[1] BOKUVKA, O. et al.: Low and High Frequency Fatigue Testing, EDIS, ZU Zilina, 2000

[2] KUNZ, L.: *Experimentalni stanoveni unavovych charakteristik materialu* [E*xperimental Evaluation of Materials Fatigue Characteristics*], EDIS, ZU Zilina, 2003 (in Czech)

[3] BURSAK, M., BOKUVKA, O.: *Communications - Scientific Letters of the University of Zilina*, 4, 2006

[4] LEITNER, B. et al.: *Nedestruktivne skusanie materialov v plynarstve,* [*Nondestructive Testing of Materials in Gas Industry*], EDIS ZU Zilina, 2003

[5] GAJDOS, L. et al.: *Structural Integrity of Pressure Pipelines,* PRAAM, Prague, 2004

[6] ABADIE, F. et al.: *Shot Peening: A Dynamic Application and its Future – 2. edition,* Wetzikon, Metal Finishing News, 2009

[7] Metal Improvement Company: Shot Peening Applications. 2010. [online]. [cit. 2012-08-14] Available on the internet: <www.metalimprovement.net.cn/documents/english_lit/ MIC_Green_Book_9th_Edition.pdf>

[8] FITZPATRICK, M.E. et al.: *Measurement Good Practice Guide No. 52: Determination of Residual Stresses by X-Ray Diffraction – 2. edition,* Teddington : NPL, 2005

[9] ISO 1143: 1975. Metals - Rotating Bar Bending Fatigue Testing

[10] PEEN SERVICE – NORBLAST GROUP s. r. l.: Surface Engineering – Propagation Handbook of Company, 2011

[11] BAGHERIFARD, S., GHELICHI, R.: Experimental and Numerical Analysis of Surface Nanostructured Materials Obtained by High Energy Shot Peening, *Convegno Nazionale IGF*, 2009

[12] GUAGLIANO, M. et al.: *Influence of Surface Hardening on Fatigue Properties of AISI 16Ti Stainless Steel.* 29th Intern. Colloquium Advanced Manufacturing and Repair Technologies in Vehicle Industry. EDIS, ZU Zilina, 2012

[13] SHAW, L. L. et al.: A Direct Comparison in the Fatigue Resistance Enhanced by Surface Severe Plastic Deformation and Shot Peening in a C-2000 Superalloy. *Materials Science and Engineering,* 2010.

https://doi.org/10.26552/com.C.2012.4.99-105

Ivo Cerny *

FATIGUE CRACK GROWTH IN A 7075 AL-ALLOY WITH EVALUATION OF OVERLOADING EFFECTS

Measurement of fatigue crack growth (FCG) in an Al 7075-T7351 alloy of a particularly high homogeneity was carried out as a part of the Proficiency Test Programme on fatigue crack growth measurement, organised by General Electric Aviation, USA, in collaboration with the company Exova in France. To pass the test programme successfully, a particular attention was paid to improve and verify DCPD (direct current potential drop) method being used for the crack length measurement. Additionally, an investigation of effects of overloads on fatigue crack growth and retardation was carried out. In the CT specimens used, the difference between actual and calculated crack length at the crack starting point was quite significant, approximately 4.3 mm. However, the difference as a function of crack length was almost constant. Results of FCG rates were very self consistent, likely due to the material homogeneity. Values of the parameters C and m measured at the SVÚM a.s. laboratory were evaluated as the third best precise from all the 16 worldwide participating laboratories. Retardation effects of overloads of the magnitudes 2.7-times and 3.0-times of the maximum load in the constant range fatigue loading were significant. The overloads resulted in substantial crack closure effects, which, however, did not occur immediately, but just after further fatigue crack extension, comparable with plastic zone size.

Keywords: *Fatigue crack growth, overloading, crack closure, 7075 Al-alloy, crack retardation*

1. Introduction

Al 7075 alloy is a high strength material usually used for highly stressed components in lightweight structures, typically in aircraft fittings, gears and shafts, fuse parts, meter shafts and gears, missile parts, regulating valve parts, worm gears, keys, aircraft, aerospace and defence applications [1]. It can be applied in different heat treatment conditions, but the T7351 temper state is most widely used because of improved stress-corrosion cracking resistance. The content of alloying element (weight %) is Cu 1.2 – 2, Mg 2.1 – 2.9, Zn 5.1 – 6.1 and Cr 0.18 – 0.28. Typical mechanical properties are R_m = 505 MPa, $R_{p0.2}$ = 435 MPa, elongation at break 13% and fatigue strength (limit) 150 MPa. The T6 or T651 temper state is characteristic by somewhat higher mechanical properties, by 10 – 15% and increased fatigue strength by 6 – 7%, but with a lower ductility and reduced resistance to stress corrosion cracking.

In comparison with an Al alloy widely used in the past and recently, namely Al 2024, the content of Al 2024 alloying elements was Cu 3.8 – 4.9, Mg 1.2 – 1.8 and Mn 0.3 – 0.9, no Zn or just less than 0.25 %. Mechanical properties and fatigue strength were significantly lower in comparison with Al 7075, just elongation at break was higher. These are the main reasons, why the Al 7075 type has been recently used more frequently.

A rather problematic property of Al 7075 alloy may be fracture toughness, which vary from 22 MPa $m^{1/2}$ to more than 30 MPa $m^{1/2}$ according to the temper state and test orientation. This may be a problem in structures using Damage Tolerance design philosophy having been recently more and more used in connection with the necessity to reduce total weight of structures and to exploit their potential service life to the maximum extent not only in such industrial branches like aircraft [2], but also gradually in other fields, e.g. railway structures and components [3–5]. Therefore, exact knowledge about fatigue crack growth rates and various affecting factors is a very important basis for an assessment of residual fatigue life of structures and their in-service safety and reliability.

Measurement of fatigue crack growth rates has become recently a standard test, described in detail in different international standards, e.g. [6, 7]. Though this type of test is being offered by numerous laboratories, correct results are conditioned by a good experience and carefulness of the staff, besides exact methodology and experimental facilities. Results generated at different laboratories may not be therefore correct. That is why serious and big manufacturers like e.g. General Electric Aviation, a worldwide manufacturer of aircraft engines, organise so called Proficiency Test Programmes (a kind of Round Robin Tests) of fatigue crack growth measurement. Strength department of SVUM a.s. with accredited laboratory decided to participate in this test. To pass

* **Ivo Cerny**
SVUM a.s., Praha, Czech Republic, E-mail: Ivo.Cerny@seznam.cz

the test programme successfully, a particular attention was paid to improve and verify DCPD (direct current potential drop) method being used for the crack length measurement. The remaining material was then used for an investigation of effects of overloads on fatigue crack growth or retardation. Results of this comprehensive programme are described and discussed in this article.

2. Experimental programme

The Al 7075-T7351 alloy acquired for the experimental programme was of a particularly high quality. Since it was a material used for the Proficiency Test Programme, it had particularly homogeneous composition, microstructure, mechanical and fatigue properties. Actual proof stress was 445 MPa, somewhat higher than typical average proof stress of this material. The only disadvantage was a very high price, but on the other hand, the characteristics affected reproducibility of experimental measurements very positively.

The fatigue crack growth (FCG) measurement was performed according to the latest issue of the ASTM standard [6] on CT specimens of width $W = 75$ mm – Fig. 1. Loading was of a sinusoidal type, load asymmetry $R = 0.1$, test frequency $f = 11–12$ Hz given by the resonance system of the SCHENCK PVQA fatigue machine.

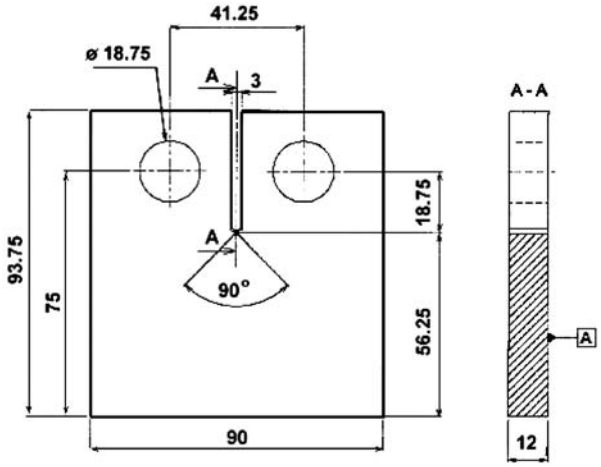

Fig. 1 Scheme and dimensions of CT specimen used for FCG measurement

As already mentioned, particular care was given to improve the precision of the DCPD method and device used. In general, the method corresponded to those described in [8–10]. This method is, however, very suitable for long specimens, where a sufficient length results in a homogeneous direct electric current field in the specimen centre with the growing crack. Unfortunately, in CT specimens being used for FCG measurement very often, the electric current is not sufficiently homogeneous due to insufficient specimen length and presence of attaching pin holes. The modified analytical calibration curve described in [8–10] cannot be therefore directly used, some corrections have to be applied.

The correction function was verified using one of the specimens, where overloading cycles and different load amplitude steps were applied to obtain marking of crack front – Fig. 2. After final braking of the specimen, positions of the crack front markings were exactly evaluated on the microscope. During the measurement, average value of the through thickness crack front, considering inside curvature was evaluated. An example of such the measurement is in Fig. 3.

Effects of overloads on FCG were studied considering just two single overloading cycles and subsequent crack growth at the load amplitude used previously. The overloading cycles were applied at low stress intensity factor ranges ΔK, close to the near-threshold transient area. It was found that FCG rates in the studied material were not sensitive to small overloading cycles – overloading even up to approximately 100% of the constant load amplitude did not have any measurable effect either on the crack acceleration or retardation. Therefore, quite severe overloading was eventually applied – 2.7-times and 3-times, respectively. Before the overloading and at several intervals after the overloading application, COD was carefully measured. The method of measurement on the back edge of the specimen was used [11] – the clip gauge (high resolution semiconductor clip gauge INOVA) was attached at the centre of the edge opposite to the notch.

Fig. 2 "Beach" marking of crack front on specimen fracture surface

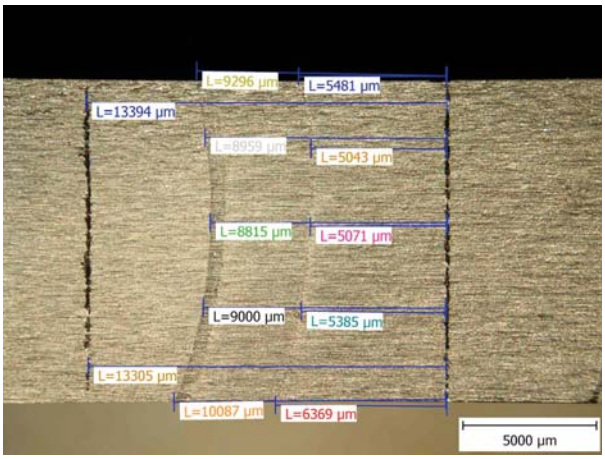

Fig. 3 Example of detailed measurement of crack front considering curvature

3. Results and discussion

3.1. Correction function of DCPD method

Results of the optical measurement of the crack front values were compared with crack length values calculated from measured direct potentials according to [8]. Differences between the calculated and optically measured crack lengths Δa were determined and a diagram of these differences as a dependence on actual crack length elaborated – Fig. 4.

For the specific case of the specimen type, dimensions, but also material of the specimen – Al-alloy and material of the attaching pins – steel, the difference between actual and calculated crack length at the starting point – actual length approximately 7 mm was quite significant, approximately 4.3 mm. There was, however, a very advantageous character of this difference as a function of growing crack length: this difference was almost constant, independent on crack length. It can be therefore concluded that the analytical calibration curve can be used for this specimen with just a very simple correction.

It should be noted that the DCPD correction function shown should not be generalised, the DCPD measurement may need a different correction function in other cases, e.g. in combinations of other materials of specimens and pins. The direct current potential field, determined by Laplace equation, is partially affected not only by the attaching holes in the specimens, but also by the material of the pins, because in the holes, there also is some contact between the specimen and the pins.

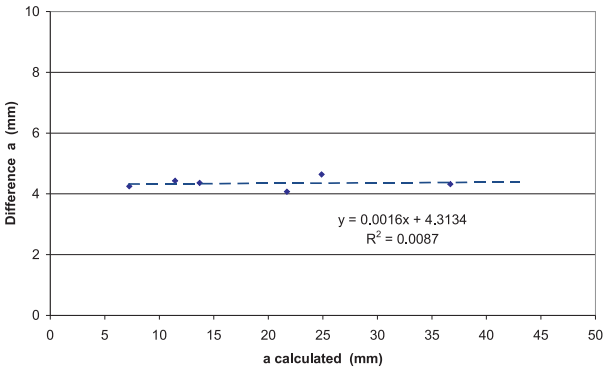

Fig. 4 Differences between actually measured crack length and length calculated from DCPD method

3.2. Fatigue crack growth in Al 7075 alloy

Fatigue crack growth in stable – Paris region was evaluated individually for each tested specimen and then a common regression line (power regression) was calculated using methods of mathematical statistics. Note that the very high material homogeneity resulted in very self consistent results – Fig. 5. The dependencies are almost ideally linear and moreover, differences between individual specimens are negligible either. Parameters C and m of the Paris line were evaluated individually for each specimen and eventually for all the specimens together. The results sent to the company Exova in France, responsible not only for the original distribution of the material, but also for the final evaluation of all results from all participating laboratories.

The final evaluation made by Exova is shown in Figs. 6 and 7. The precision of the measurement carried out at SVÚM a.s. laboratories is very encouraging: Values of the parameters C and m were evaluated with the third best precision from all the 16 worldwide participating laboratories – Figs. 6 and 7. The reproducibility (repeatability) of the parameter m evaluated at SVUM a.s. was even the best one. Note that all the 16 laboratories have been qualified for accreditation testing for GE Aviation aircraft industry according to specific S-400 quality assurance system, which is very severe. So, the laboratories can be considered as better than average. It is just a confirmation that if a special care and attention is paid to the experimental methodology and measurement precision, such the approach brings good fruits, and eventually the effort is worth it.

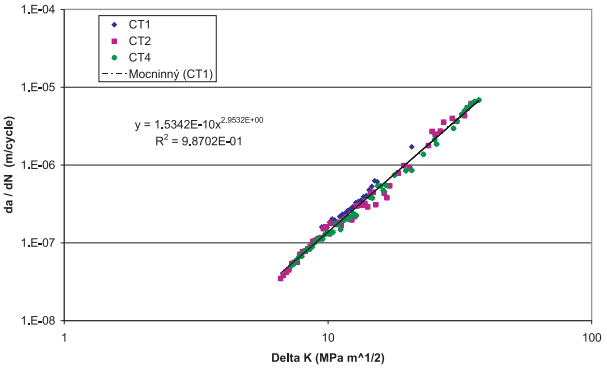

Fig. 5 Fatigue crack growth rates in Al 7075 alloy measured as part of Proficiency Test Programme

3.3. Effect of overloading cycles on FCG

Effects of the huge overloads of the magnitudes 2.7-times and 3.0-times of the maximum load in the constant range fatigue loading were significant. The FCG diagram, which includes the overloading cycles and FCG rates after the overloads, is shown in Fig. 8. FCG rate after the first and second overloading was reduced by approximately one order and two orders, respectively. The dashed line in Fig. 8 represents FCG dependence from Fig. 5 – without overloads. It is clear that after the reduction of FCG rates due to the overloading, after some further growth of the crack by increments, approximately comparable with plastic zone size, the values of

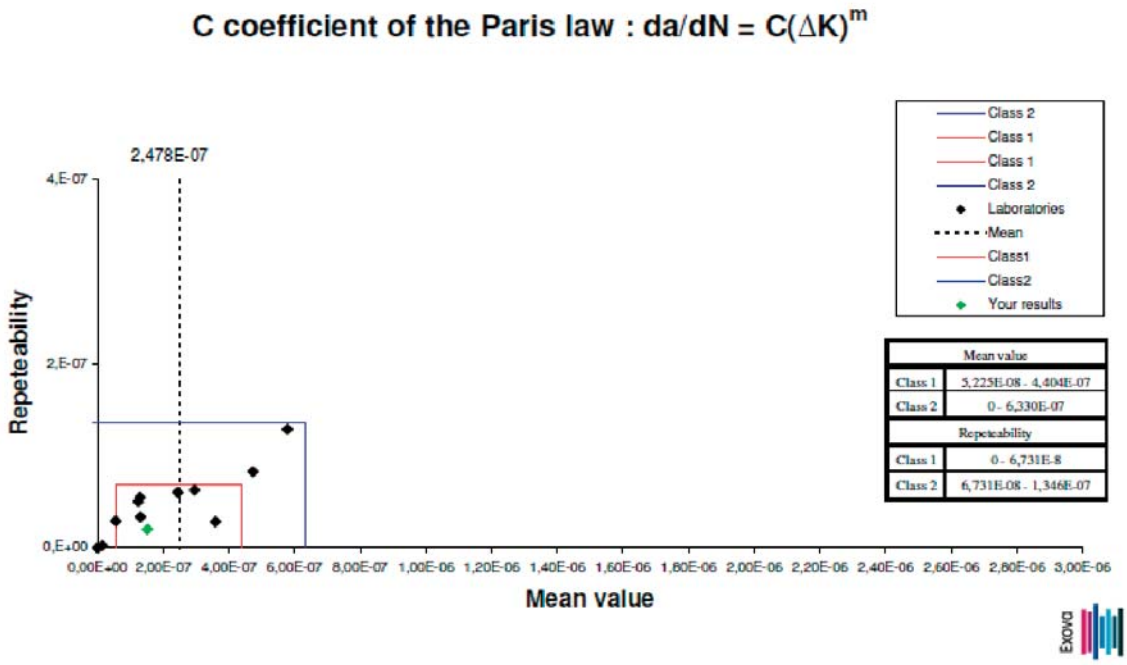

Fig. 6 Values of coefficient C of Paris dependence evaluated at different worldwide laboratories, result measured at SVÚM a,s, highlighted by green colour

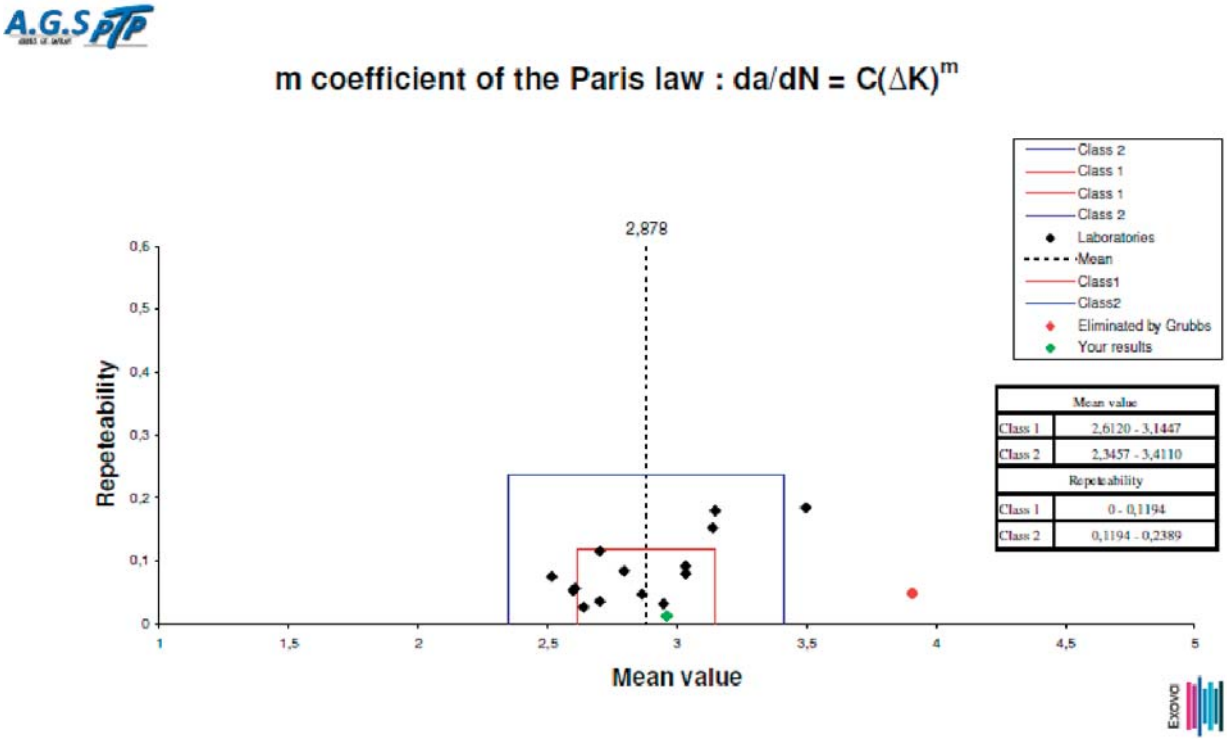

Fig. 7 Values of coefficient m of Paris dependence evaluated at different worldwide laboratories, result measured at SVÚM a.s. highlighted by green colour

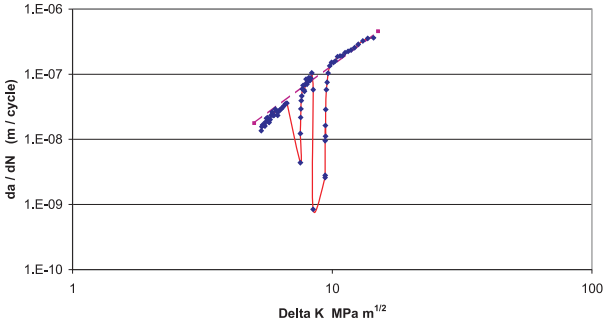

Fig. 8 FCG in Al 7075 alloy including overloading retardation effects

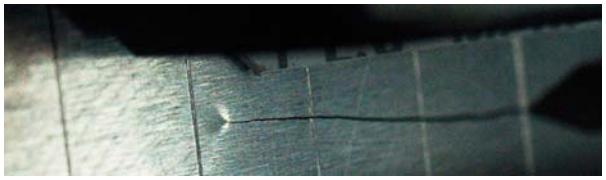

Fig. 9 Plastic zone near crack front during 2.7-times overload, distance between marks being 5 mm

FCG rates gradually, but quite fast rise to their original values. An example of plastic zone after the 2.7-times overload is shown in Fig. 9.

These results are quite comparable with those published in [12], where effects of less severe overloads on FCG rates in the same Al-alloy with a different heat treatment, namely 7075-T651 were investigated besides others. Crack retardation occurred after single overloads, too and crack growth rates also resumed after the crack propagated out of the influencing plastic zone created by the overloads. Similar retardation effects after overloading in a rather different type of Al-alloy, 2124–T351, frequently used particularly in the past but also recently, were described in the literature [13]. In that case like in this work, retardation after a peak overload was observed to extend over the length of the calculated plane strain plastic zone due to the overload.

The evaluation of overloading cycles was completed by measurement of crack closure as a dependence on further crack development. The first group of crack closure measurements was performed already before the first overloading, during the transient period after the last step of load shedding procedure, when FCG was still affected (retarded) by previous, higher load range – approximately the first 10 points in Fig. 8. The second group of measurements was performed after the 3-times overload.

Crack closure forces were evaluated from load/deformation curves recorded during quasi static load cycles, where deformation was measured with clip gauge attached at the specimen edge opposite to the notch ("back edge"), as mentioned in Section 2. Closure force was evaluated as the load value corresponding to the point of declination from the linear part of the curve. An example

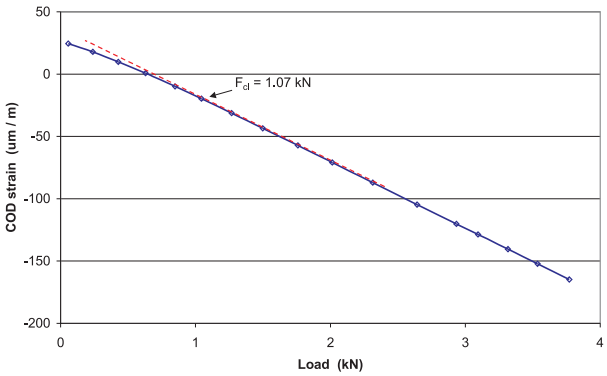

Fig. 10 Example of evaluation of closure force F_{cl} from load/strain curve

is shown in Fig. 10. Note that closure forces evaluated by this method corresponded to plain strain rather than plain stress conditions, as due to fairly big specimen thickness, 12 mm, plain strain conditions predominated near the crack tip, even during the overloading. Crack tip closure forces measured on the specimen surface, at plain stress conditions, would be significantly higher, as shown in [11].

Results of the evaluation of F_{cl} (force corresponding to crack closure) and effective load F_{eff}, $F_{eff} = F_{max} - F_{cl}$ are presented in Figs. 11 and 12. Though the diagrams in Figs. 11 and 12 document different situations, they have quite a similar character. The most important point is some retardation of the crack closure reaction on the overloading. Crack closure did not occur immediately after the application of the overload. As an example, in case of the 3-times overload (Fig. 12), the closure force Fcl remained constant or even slightly decreased. This result might be in an agreement with recently published, quite surprising numerical analysis of plasticity induced crack closure, where the authors have concluded that such the crack closure actually does not exist at all [14]. Note that other publications dealing with plasticity induced crack closure, even recent, definitely do reckon with this phenomenon and its effect on crack growth rates and retardation [15, 16]. Crack closure, namely closure load Fcl, started to increase just after further crack extension by approximately 0.2 – 0.3 mm, whereas the maximum closure occurred after 0.7 mm crack extension after the overload, which is comparable with the end of the plastic zone size. The crack closure returned back to its original value after approximately 1.5 mm of the total increment after the overload. In case of the final step of load reduction during the load shedding process, crack closure effect remained surprisingly even longer, for more than 2 mm of the crack increment, though the load range reduction only was 24 %.

The evaluated effective load F_{eff} does not explain the drastic crack retardation – the first two points after the overloads in Fig. 8. It is likely caused by further mechanisms like crack tip blunting or local residual stresses arising in the plastic zone and near it. On the contrary, after the maximum value of crack closure is reached, results of FCG rates are in a good agreement with effective values

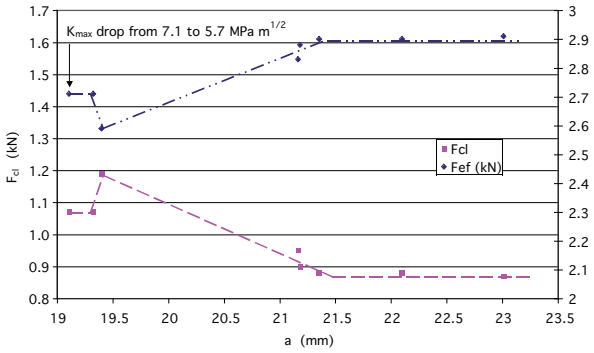

Fig. 11 Closure and effective forces F_{cl} and F_{eff}, respectively, after the last stage of load shedding as a dependence on further crack growth

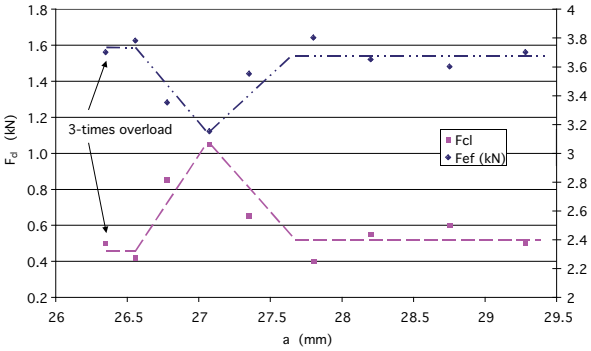

Fig. 12 Closure and effective forces F_{cl} and F_{eff}, respectively, after overloading cycle

of stress intensity factor ΔK_{eff}, like in other recent computational and experimental studies – e.g. [17]. The FCG retardation in the studied case and conditions is caused by the plasticity induced crack closure phenomenon rather than by compressive residual stresses in round bars loaded by rotating bending, described in [18].

4. Conclusions

Using an aircraft Al 7075 alloy, the accredited strength laboratory of SVÚM a.s. passed a Proficiency Test Programme on fatigue crack growth measurement, organised by General Electric Aviation, USA, in a collaboration with the company Exova in France. To pass the test programme successfully, a particular attention was paid to improve and verify DCPD (direct current potential drop) method being used for the crack length measurement. Additionally, an investigation of effects of overloads on fatigue crack growth and retardation was carried out. Results of this comprehensive programme can be summarised as follows:

- For the specific case of the specimen type, dimensions and material the difference between actual and calculated crack length at the starting point were quite significant, approximately 4.3 mm. However, the difference as a function of growing crack was almost constant.
- The very high material homogeneity of the Al 7075alloy provided for the Proficiency Test Programme resulted in very self consistent results. The precision of the measurement carried out at SVÚM a.s. was encouraging: Values of the parameters *C* and *m* were evaluated with the third best precision from all the 16 worldwide participating laboratories. This result shows that the attention paid to the experimental methodology was worth it.
- Effects of the overloads of the magnitudes 2.7-times and 3.0-times of the maximum load in the constant range fatigue loading were significant. The overloads resulted in substantial crack closure effects, which, however, did not occur immediately after the application of the overload, but just after further fatigue crack extension, comparable with the plastic zone size.

Acknowledgements

The work was carried out under the support of Ministry of Education, Youth and Sports of Czech Republic, grant MSM 2579700001.

References

[1] *ASM Aerospace Specification Metals Inc., Aluminum 7075-T73; 7075-T735x,* http://asm.matweb.com/search/SpecificMaterial.asp?bassnum=MA7075T73
[2] *MOSTA - Modernization of small transport aircraft to increase operation effectiveness and economy.* Project FR-TI 2/557 of the programme TIP of the Czech Ministry of Industry and Trade, 2010.
[3] ZERBST, U., SCHODEL, M., BEIER, H. T.: *Eng. Fract. Mech.*, 78, 2011, 5, 793
[4] ZERBST, U., BERETTA, S.: *Eng. Fail. Anal.,* 18, 2011, 2, 534
[5] BERETTA, S., ZERBST, U.: *Eng. Fract. Mech.*, 78, 2011, 5, 713
[6] ASTM E647 – 11. *Standard Test Method for Measurement of Fatigue Crack Growth Rates,* 2011
[7] ISO 12108:2002. *Metallic materials. Fatigue testing. Fatigue crack growth method.* 2002
[8] CERNY, I.: *Eng. Fract. Mech.,* 71, 2004, 4–6, 837
[9] CERNY, I: *Int. J. Pres. Ves. Pip.,* 78, 2001, 11–12, 893
[10] CERNY, I.: *Procedia Engineering,* 10, 2011, 3411

[11] CERNY, I, REMAR, L., CIPERA, M.: *Use of Different Methods of Fatigue Crack Closure Measurement and their Vomparison.* Proc. of the 47th Int. Conf. on Experimental Stress Analysis, Eds. Marvalova, B., Petrikova I., Capek, L., Sychrov, 2009, 74
[12] ZHAO, T., ZHANG, J., JIANG, Y.: *Int. J. Fatigue,* 30, 2008, 7, 1169
[13] ROBIN, C., PELLOUX, R.M.: *Mater. Sci. Eng.,* 44, 1980, 1, 115
[14] TORIBIO, J., KHARIN, V.: *Key Eng. Mat.,* 417–418, 2010, 781
[15] CODRINGTON, J., KOTOUSOV, A., WILDY, S., YING HO, S.: *Key Eng. Mat.*, 417–418, 2010, 201
[16] LI, Y., HE, J., ZHANG, Z.: *Key Eng. Mat.*, 417–418, 2010, 653
[17] SEIFI, R., BAHRAMI R.: *Eng. Fail. Anal.,* 17, 2010, 6, 1475
[18] PURNOWIDODO, A., MAKABE, C.: *Eng. Fail. Anal.,* 2009, 7, 2245

https://doi.org/10.26552/com.C.2012.4.106-108

Rudolf Kampf – Jan Lizbetin – Lenka Lizbetinova *

REQUIREMENTS OF A TRANSPORT SYSTEM USER

This article deals with the problem of basic parameters which influence the selection of a mode of transport by a transport user. The article suggests the use of Saaty's method as a method suitable for the determination of weights of importance of basic parameters (user's requirements).

Key words: *transport system, transport user, Saaty's method.*

1. Introduction

Public transport, neither road nor rail transport in the Slovak Republic has taken the opportunity to increase its share of the division of transport work. On the contrary, the volume of public transport in the Slovak Republic has been decreasing recently which has led to an increased strain on the infrastructure caused by individual car transport (see Table 1 and Fig. 1). The only solution to these problems lies in the increased quality of public transport and in respecting its users' requirements. This can only be achieved by improving the function of the transport system.

2. Basic parametres

The basic parameters which influence the selection of a mode of transport and thus the success of public transport, are [1]:

- time availability – expresses the possibility of using a given mode of transport at the point in time of reaching the point serviced by public transport until the arrival of a suitable connection,
- travel speed,
- price for the users,
- comfort, quality of the fleet and scope of add-on services in the mode of transport,
- inside safety – in relation to the transport process, probability of an accident,
- outside safety – the risk of an unlawful act, protection against terrorism, vandalism and other similar unlawful acts and pathological social phenomena and protection against natural elements,
- reliability – transport system must operate with a high probability of running according to the published time table,
- accessibility of the public transport system to passengers with limited movement and/or orientation ability,
- passenger awareness.

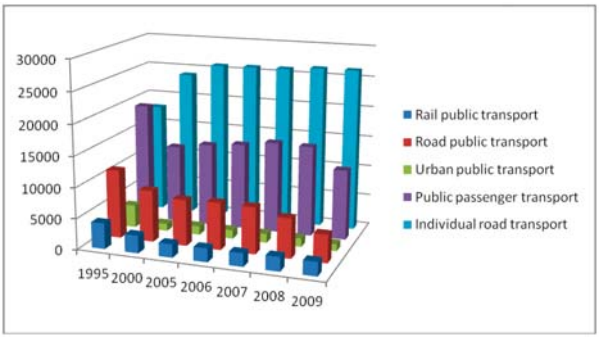

Fig. 1 Total passenger transport performance by mode (mill.pass-km)

In the following part, the article will deal with a suggestion for a method suitable for the determination of weights of importance of basic parameters (users' requirements).

3. Determination of weights of importance

The system of evaluation should be based on the formation of arranged pairs consisting of the weight of importance of a given

* **Rudolf Kampf[1], Jan Lizbetin[2], Lenka Lizbetinova[3]**
[1] Institute of Technology and Businesses in Ceske Budejovice, Department of Transport and Logistics, Ceske Budejovice, Czech Republic, E-mail: kampf@mail.vstecb.cz
[2] Department of Railway Transport, Faculty of Operation and Economics of Transport and Communications, University of Zilina, Slovakia,
[3] Department of Road and Urban Transport, Faculty of Operation and Economics of Transport and Communications, University of Zilina, Slovakia,

Development of public transport share of transport work for passenger transport Table 1

Modal split with regards to passenger transport performance (mill. pass-km)							
	1995	2000	2005	2006	2007	2008	2009
Total passenger transport performance	39578	37390	39614	40184	41050	41281	37971
of which by mode:							
Rail public transport	4202	2870	2182	2213	2165	2296	2264
Road public transport	11191	8435	7525	7665	7596	6446	4538
Urban public transport	3688	1173	1399	1403	1451	1370	1127
Public passenger transport	19274	12733	13575	14113	14915	14765	11433
Individual road transport	17977	23929	25824	25920	25994	26395	26420
Modal split with regards to transport performance between public and individual road transport (% proportion of public transport)	51.74	34.73	34.46	35.25	36.46	35.87	30.20

Source: Statistical Office of SR

parameter which the user evaluates within the framework of transport and the level (value) of this parameter (relation 1) [2, 3]:

$$MH = \sum_{i=1}^{n} v_i \cdot s_i$$

where:
- MH – total multi criteria valuation,
- v_i – relative weight of importance of the i^{th} parameter,
- s_i – level of meeting the requirements of the i^{th} parameter.

In order to determine the weights of importance of a given parameter we use Saaty's method.

The principle of Saaty's method lies in the fact that instead of using a numerical scale, it enables the users to express their preferences verbally which is often a much easier way of expressing themselves. Verbal expression is automatically transferred into a numerical scale.

The level of importance of one parameter before any other is expressed by the user on a whole number scale 1 to 9. The value 1 means that the pair of parameters has the same importance. The value 9 means that the value of one parameter is absolutely higher than the value of the other parameter. If one parameter is less important than the other, the reverse value of the whole numbers of the given scale is used. The information from pairwise comparison can be put into a matrix $S = (s_{ij}, i,j = 1, 2, ..., k)$ known as Satty's matrix. The elements of this matrix sij can be interpreted as estimates of the share of the i^{th} and j^{th} parameters (relation 2) [4 and 5]:

$$s_i \approx \frac{v_i}{v_j} \quad i, j = 1, 2, ..., k.$$

For the elements of Saaty´s method it applies that s_{ii}, $i = 1, 2, ..., k$, ie. units are on the diagonal; it further applies that $s_{ij} = 1/s_{ji}$, $i,j = 1, 2, ..., k$, ie. elements symmetrical according to the main diagonal carry reversed values.

User's preferences are contained in the matrix of pairwise comparisons S. It is important to use the information about these preferences for the estimate of the weight of the parameters. One of the conditions for usability of this information is its appropriate quality. The matrix of pairwise comparisons must be sufficiently consistent. Matrix S is fully consistent if for any index trio i, j, q it applies that $s_{iq} = s_{ij}\, s_{jq}$. For example matrix (relation 3) [4, 5]:

$$S = \begin{bmatrix} 1 & 2 & 6 \\ 1/2 & 1 & 3 \\ 1/6 & 1/3 & 1 \end{bmatrix}.$$

A good estimate of vector v can be obtained as a geometrical average of elements in each line of the matrix. Matrix S normalized so that the sum of its elements is equal to 1 (relation 4) [4, 5]:

$$v_i = \left(\prod_{j=1}^{k} s_{ij} \right)^{1/k} \quad i = 1, 2, ..., k$$

$$v_i = \frac{v_i'}{\sum_{i=1}^{k} v_i'} \quad i = 1, 2, ..., k$$

If the above given method is used, weights of parameters from one transport system user are obtained. In order to determine the objective value of the weights of parameters we need to obtain data from a representative group of users. The total weight of the ith parameter is then the arithmetical average of the weights obtained from individual users.

4. Conclusion

It is important to realize that while researching these basic parameters (users' requirements) it is important to respect the fact that the value of transport service from the point of view of the user depends on the specific type of transport system and it is individual in relation to the specific type of transport system [6, 7].

It is also important to remember that the users' requirements will change in time, especially as a result of increasing living standards, etc. The question of the internal workings of the system is also an important factor. A correct internal functioning of the system is an important prerequisite for high quality work which demonstrates itself externally towards the users [8–10].

References

[1] Ministerstvo dopravy Slovenskej republiky [Ministry of Transport, Construction and Regional Development of the Slovak Republic]. Statistics [online]. Available< http://www.telecom.gov.sk/files/statistika_vud/preprava_ osob.htm#k1/>.

[2] CAJCHAN, J.: *The European Standard of Service Quality in Public Passenger Transport.* Proc. of 7th intern. conference Public Passenger Transport, Bratislava, 2004, ISBN 80-233-0498-4.

[3] GNAP, J., KONECNY, V.: *Quality Assessment of Road & Carriers from Customer's Perspective,* Proc. of 3rd intern. Scientific conference Quality of Traffic and Transport Processes and Services, Pardubice, 2002.

[4] JABLONSKY, J.: *Operations Research, Quantitative Models of Economic Decision Making.* Professional Publishing, Praha, 2002. ISBN 80-86419-23-1.

[5] JABLONSKY, J.: *Operations research.* VSE, Praha, 2001. ISBN 80-245-0162-7.

[6] PRUSA, P.: The Influence of Transport on the Environment as one of the Goals of Transport Policy, *Dopravni politika pro vstup do EU,* pp. 78–82, Univerzita Pardubice, 2003, ISBN 80-7194-556-0.

[7] SOTEK, K., CHLAN, A.: *Theory of Transport Systems, 9th Intern. Conference on Traffic Science 2005,* Portoroz, Slovenia, 2005. ISBN 961-6044-75-3.

[8] KAMPF, R.; HODAS-PAUER, M.: Development of Innovations in Transport Companies SR, LOGI, *Sci. J. on Transport and Logistics*, 1(2): 23–28, 2010. ISSN 1804-3216.

[9] KAMPF, R.; ROUDNA, J.: Slept Analysis of Logistic Centers' Operating in Czech Republic, LOGI *Sci. J. on Transport and Logistic,* 1(1): 79–85, 2010. ISSN 1804-3216.

[10] KOLAR, J.: Logistics Activities in Relation to Tangible and Intangible Operations. *Sci. J. on Transport and Logistics „LOGI"*, 2(1), vol. 1, No. 2, 2010, pp. 29–34, ISSN 1804-3216.

COMMUNICATIONS – Scientific Letters of the University of Zilina
Writer's Guidelines

1. Submitted papers must be unpublished and must not be currently under review for any other publication.
2. Submitted manuscripts should not exceed 8 pages including figures and graphs (in Microsoft WORD – format A4, Times Roman size 12, page margins 2.5 cm).
3. Manuscripts written in good English must include abstract and keywords also written in English. The abstract should not exceed 10 lines.
4. Submission should be sent: By e-mail – as an attachment – to one of the following addresses: komunikacie@uniza.sk or holesa@uniza.sk (or on CD to the following address: Zilinska univerzita, OVaV – Komunikacie, Univerzitna 1, SK-10 26 Zilina, Slovakia).
5. Uncommon abbreviations must be defined the first time they are used in the text.
6. Figures, graphs and diagrams, if not processed in Microsoft WORD, must be sent in electronic form (as JPG, GIF, TIF, TTF or BMP files) or drawn in high contrast on white paper. Photographs for publication must be either contrastive or on a slide.
7. The numbered reference citation within text should be enclosed in square brackets. The reference list should appear at the end of the article (in compliance with ISO 690).
8. The numbered references (in square brackets), figures, tables and graphs must be also included in text – in numerical order.
9. The author's exact mailing address, full names, E-mail address, telephone or fax number, the name and address of the organization and workplace (also written in English) must be enclosed.
10. The editorial board will assess the submitted paper in its following session. If the manuscript is accepted for publication, it will be sent to peer review and language correction. After reviewing and incorporating the editor's comments, the final draft (before printing) will be sent to authors for final review and minor adjustments
11. Submission deadlines are: September 30, December 31, March 31 and June 30.

COMMUNICATIONS

SCIENTIFIC LETTERS OF THE UNIVERSITY OF ZILINA
VOLUME 14

Address of the editorial office:
Zilinská univerzita
Office for Science and Research
(OVaV)
Univerzitna 1
SK 010 26 Zilina
Slovakia

E-mail: komunikacie@uniza.sk

Each paper was reviewed by two reviewers.

Journal is excerpted in Compendex and Scopus.

It is published by the University of Zilina in
EDIS – Publishing Institution of Zilina University
Registered No: EV 3672/09
ISSN 1335-4205

Published quarterly

Single issues of the journal can be found on:
http://www.uniza.sk/komunikacie